UNIVERSIDAD COMPLUTENSE DE MADRID
FACULTAD DE CIENCIAS FÍSICAS

Departamento de Óptica

DIFFRACTIVE OPTICAL ELEMENTS BY NANOSECOND PULSED LASER

MEMORIA PARA OPTAR AL GRADO DE DOCTOR PRESENTADA POR

Francisco Javier Salgado Remacha

Bajo la dirección de los doctores
Luis Miguel Sánchez Brea
Eusebio Bernabeu Martínez,

Madrid, 2011

ISBN: 978-84-695-0767-4

©Francisco Javier Salgado Remacha, 2011

UNIVERSIDAD COMPLUTENSE DE MADRID

FACULTAD DE CIENCIAS FÍSICAS

DEPARTAMENTO DE ÓPTICA

Philosophy Doctorate Thesis / Tesis doctoral

Diffractive Optical Elements by nanosecond pulsed laser

Elementos Ópticos Difractivos mediante láser pulsado de nanosegundo

---

Francisco Javier SALGADO REMACHA

Supervisors/Directores

Dr. Luis Miguel Sánchez Brea

Dr. Eusebio Bernabeu Martínez

Madrid, Abril 2011

A mis padres, José Antonio y María Magdalena, y a mi hermano Ignacio,

que siempre estarán a mi lado.

Nace bárbaro el hombre, redímese de bestia cultivándose. Hace personas la cultura, y más cuanto mayor. En fe de ella pudo llamar Grecia bárbaro a todo el restante universo. Es muy tosca la ignorancia, no hay cosa que más cultive que el saber. Pero aun la misma sabiduría fue grosera, si desaliñada. No sólo ha de ser aliñado el entender, también el querer y más el conversar.

Baltasar Gracián, "Oráculo manual y arte de prudencia".

Saber, pero transformar; conocer, pero obrar: tal es la norma del verdadero hombre de ciencia.

Santiago Ramón y Cajal, "Reglas y consejos sobre investigación científica".

Agradecimientos

Caminante, son tus huellas
el camino y nada más;
Caminante, no hay camino,
se hace camino al andar.
Al andar se hace camino,
y al volver la vista atrás
se ve la senda que nunca
se ha de volver a pisar.
Caminante no hay camino
sino estelas en la mar.

Una vez cumplida esta etapa de mi vida, es justo reconocer y agradecer la ayuda recibida. De todas las personas aquí nombradas, algunas han significado una guía; otras me han insuflado fuerzas para seguir adelante; otras, simplemente, me han acompañado caminando junto a mí. A todas ellas les doy las gracias.

En primer lugar, quisiera agradecer a mis directores de tesis, los profesores Eusebio Bernabeu Martínez y Luis Miguel Sánchez Brea, por su apoyo y atención. En el trabajo diario me han contagiado su espíritu emprendedor, su curiosidad y las ganas de aprender de ambos. Soy consciente de que con ellos he crecido y madurado personalmente, y me han enseñado que la mejor actitud ante un problema es la perseverancia.

Quiero agradecer muy especialmente el apoyo que he recibido por parte del Dr. Tomás Morlanes, de Fagor Automation. Sus sugerencias a lo largo de estos años, así como la confianza mostrada, han sido indispensable para la realización de esta tesis.

Deseo también mostrar mi mayor gratitud a Isidoro Jiménez, sin cuya ayuda totalmente desinteresada este trabajo no se hubiera podido llevar a cabo. Además de ser un inmejorable compañero en el laboratorio, se ha convertido en un gran amigo. Asimismo, quisiera agradecer al profesor Javier Alda por su apoyo a la hora de sacar adelante alguna colaboración conjunta.

No puedo olvidarme de todos mis compañeros y amigos. Una mención aparte merecen Fran y Javi, con los que he compartido piso y trabajo, así como el resto de compañeros que he tenido en La Cueva y miembros del Departamento de Óptica: Chema Rico, Chema Herrera, Infor, Quiroga, Natalia, Mari Cruz, Alfredo, Agustín, Paloma y todo el resto del grupo.

Agradezco también a mi padrino Manuel, que siempre se ha interesado por la marcha de mi trabajo; y a Amancio y Carmen por haberme acogido repetidamente en su casa (¡y por su pacharán!). Recuerdo también en estos momentos a todos mis amigos: Juan y Jesús, a los que tengo la suerte de llamar Amigos desde hace ya mucho tiempo, y a mis compañeros de la universidad en Zaragoza: Ana, Borja, Elena, Estela, Eva, José Antonio y Juanma. Tengo que mencionar también a todo el clan paderborniano, con los que siempre he podido encontrar entretenimiento, diversión y conversaciones realmente constructivas; a Antonio Benayas, con quien he podido charlar (y divertirme) muy a menudo. Y por supuesto, gracias Elena por poner siempre un punto de cordura en medio de esta locura.

He dejado el último lugar de esta larga lista para mi familia: mi hermano Ignacio y mis padres José Antonio y María Magdalena. Con ellos siempre he respirado un ambiente de respeto por el trabajo y aprecio por el saber. El ejemplo que he recibido viéndoles trabajar a diario ha sido, sin duda, el mejor modelo que he podido seguir.

Este trabajo ha sido financiado por el proyecto DPI2008-02391 del Ministerio de Ciencia e Innovación de España.

Resumen

Capítulo 1: Introducción

La difracción es un fenómeno que aparece cuando un haz de luz ve limitada su extensión en el espacio, o cuando encuentra un obstáculo en su camino. Bajo estas circunstancias, el haz deja de propagarse en línea recta. La importancia de los efectos difractivos depende del tamaño de las aperturas: cuanto más pequeñas sean éstas, más notable será el efecto de la difracción. Teniendo en cuenta los fenómenos que rigen la propagación de la luz (tales como la refracción o la reflexión), la difracción (así como los fenómenos interferenciales) procede de la naturaleza ondulatoria de la luz, entendida como un campo electromagnético. En este sentido, la teoría general de los campos electromagnéticos es la base física utilizada para describir los fenómenos difractivos.

Históricamente, la difracción ha sido considerada como un efecto pernicioso desde el punto de vista del diseño de instrumentos ópticos. A partir del siglo XIX comenzó a valorarse las posibilidades que ofrecen los instrumentos difractivos y que no son alcanzables mediante refracción o reflexión (fundamentalmente, la capacidad dispersora de las redes de difracción). Gracias al desarrollo de técnicas de micro-fabricación por parte de la industria electrónica a mediados del siglo XX, así como a los avances en campos como la holografía, los *elementos ópticos difractivos* (DOEs, "Diffractive Optical Elements") han sido capaces de abrirse un hueco en ámbitos científicos e industriales. Para una exitosa aplicación de este tipo de dispositivos, es necesario contar con unas buenas herramientas de diseño y con técnicas rápidas y fiables de prototipado y de fabricación a un coste razonable.

El ámbito de estudio de esta Tesis Doctoral comprende todas las etapas necesarias para la producción de elementos difractivos, desde el diseño hasta la fabricación y evaluación de los dispositivos fabricados. La aplicación más cercana que encontramos para los elementos diseñados y fabricados se enmarca dentro del campo de la codificación óptica de la posición, pero no necesariamente se limita a dicho campo. Además, necesitamos un método de fabricación que nos permita operar con una variedad de substratos de muy diferente naturaleza, haciendo posible fabricar prototipos a bajo coste. En este sentido, el procesado de materiales mediante láser pulsado se perfila como el método idóneo para nuestros intereses, dada su versatilidad.

Planteamos por tanto una serie de objetivos que se pueden resumir en tres apartados principales:

- El desarrollo de diferentes herramientas para el diseño y la evaluación de elementos ópticos difractivos.
- La puesta en marcha de un equipo de ablación láser, y la determinación de los parámetros de funcionamiento apropiados para nuestros intereses. Se comprobará la capacidad de procesado de diferentes substratos.
- La evaluación y caracterización del comportamiento óptico de los elementos fabricados.

Capítulo 2: Diseño y simulación de DOEs

En este capítulo se resumen los principios matemáticos y físicos que se utilizarán a lo largo de la tesis para describir el efecto de la difracción. Partiendo de las ecuaciones de Maxwell, eq. (2.1), una serie de aproximaciones conducen, en primer lugar, al modelo de difracción de Fresnel, eq. (2.19). El rango en el que este modelo es válido define el llamado "campo cercano". Restringiendo aún más las condiciones, es posible obtener la ecuación de la difracción de Fraunhofer, eq. (2.22), que define el llamado "campo lejano". Según esta aproximación, la difracción en campo lejano producida por una apertura que interfiere con un haz es la transformada de Fourier de dicha apertura (añadiendo un factor de escalado). Al mismo tiempo, se explica la *Aproximación de Elemento Delgado* (TEA, Thin Element Approximation), que constituye una herramienta muy útil para modelar diversos elementos difractivos. Esta aproximación consiste en suponer que el DOE puede describirse mediante una función de

transmitancia. Con este marco teórico seremos capaces de describir todos los elementos difractivos utilizados en esta Tesis Doctoral, como veremos en adelante.

Por otro lado, es común el uso de diversas herramientas numéricas para simular la propagación de la luz en el ámbito de la micro-óptica, dada la complejidad de las ecuaciones que rigen dicha propagación. Los algoritmos descritos son la transformada compleja de Fourier (FFT), utilizada en campo lejano, el algoritmo de Rayleigh-Sommerfeld (que considera únicamente propagación en vacío para elementos planos en campo cercano) y el "Beam Propagation Method", que es capaz de simular la propagación de la luz en campo cercano a través de elementos bi- o tridimensionales.

Asimismo, se muestran algunos algoritmos utilizados en el diseño de dispositivos difractivos. El primero de ellos es el "Iterative Fourier Transform Algortihm" (IFTA). Este algoritmo está especialmente concebido para el diseño de DOEs planos en campo lejano, aunque puede aplicarse también bajo otras condiciones. Otros métodos considerados son los Algoritmos de Optimización Global. Estos algoritmos, utilizados en una gran cantidad de ramas de la ingeniería y las matemáticas aplicadas, se utilizan para la optimización de problemas y la búsqueda de mínimos en funciones generales con una gran cantidad de variables. Aunque para el diseño de DOEs el IFTA se comporta mejor, los Algoritmos de Optimización Global pueden utilizarse para otro tipo de tareas de interés en el campo de la micro-óptica.

Capítulo 3: Ablación láser con pulsos de nanosegundos

Durante la interacción de un pulso de haz láser con materia tienen lugar una gran cantidad de procesos. Cuando el haz pulsado es, además, altamente energético y altamente focalizado, los procesos que dominan dan lugar a un rápido calentamiento de la materia, provocando cambios de fase e ionización del material de la muestra. La gran cantidad de energía comunicada a la muestra provoca ionizaciones y cambios de fase a gran velocidad. En función de la duración del pulso, dominarán los fenómenos térmicos o los efectos puramente electrónicos. En general, cuando los pulsos tienen una duración en torno a picosegundos o femtosegundos, los efectos térmicos se minimizan. Por el contrario, con duraciones mayores, los efectos térmicos en el

material son más visibles. Estos efectos térmicos, desde el punto de vista de la fabricación de elementos difractivos, tienden a empeorar la calidad de los dispositivos, especialmente en los bordes de las grabaciones. Al conjunto de procesos, de carácter explosivo, que provocan cambios de fase en escalas de tiempo muy pequeñas, se le denomina por lo general "ablación láser".

En nuestro caso, se ha puesto en marcha un equipo de ablación laser mediante láseres de nanosegundos (que producirá, por tanto, una cierta cantidad de daño térmico en las muestras). Se ha elegido este tipo de equipamiento por su alta disponibilidad en el mercado y su precio competitivo, en comparación con otras tecnologías, que lo convierten en merecedor de un estudio de prospectiva para su aplicación en el ámbitos micro-ópticos. En este capítulo se detallan las características del equipo, y se lleva a cabo una caracterización del funcionamiento del sistema con la intención de fabricar elementos difractantes. Se demuestra la posibilidad de trabajar con substratos de diferente naturaleza: acero (un metal), vidrio (un dieléctrico transparente) o silicio cristalino (un semiconductor con estructura cristalina).

Capítulo 4: Elementos ópticos difractivos en acero mediante ablación láser

Para ciertas aplicaciones (como es el caso de codificadores ópticos de la posición con recorridos mayores que 3 metros), el acero es el substrato más utilizado dadas sus propiedades mecánicas de flexibilidad y resistencia. Sin embargo, en comparación con otros tipos de substratos, como máscaras de cromo sobre vidrio, presenta un peor comportamiento óptico. En este capítulo se estudian ciertos factores que afectan a la utilización del acero como substrato para dispositivos difractantes en campo cercano.

En primer lugar, se estudia el efecto que produce la rugosidad del substrato sobre el proceso de las autoimágenes para redes de difracción fabricadas mediante ablación láser en flejes de acero. Se ha supuesto que los pulsos de radiación láser focalizados sobre los flejes provocan un cambio en la rugosidad superficial del acero. Se ha comprobado que la rugosidad del fleje sin grabar condiciona el comportamiento de estas redes. Cuando esta rugosidad es mayor, el decaimiento en el contraste de los planos de Talbot es más rápido. Este estudio se ha ampliado también a elementos difractivos binarios sobre superficies rugosas. En concreto, se han estudiado placas

zonales de Fresnel (FZPs) con el mismo método, capaces de focalizar la luz a una determinada distancia. Se ha comprobado que, una vez alcanzado un cierto nivel de rugosidad en la zona afectada por la ablación láser, el parámetro más importante es la rugosidad de la zona sin grabar.

Por otro lado, la naturaleza maleable de los flejes hace que estos se curven fácilmente. Se ha realizado por tanto un estudio del efecto de los planos de Talbot con redes de difracción definidas sobre una superficie curva. El efecto de la curvatura es cambiar la periodicidad de las autoimágenes a lo largo del eje longitudinal a la red. Se ha realizado una comprobación experimental de este hecho. Este estudio es de gran utilidad para el diseño de codificadores ópticos anulares, así como para definir las tolerancias mecánicas en codificadores de la posición lineales trabajando con redes sobre acero.

Capítulo 5: Fabricación de DOEs embebidos en vidrio mediante láseres pulsados de nanosegundos

En el caso de dieléctricos transparentes, como es el caso del vidrio, es posible focalizar el láser pulsado en el interior del material, de forma que las grabaciones adquieren un carácter embebido. Este tipo de dispositivos tiene un gran interés, ya que el elemento queda protegido de agentes externos. Los efectos térmicos comentados anteriormente son más visibles en dieléctricos que en metales. En nuestro caso, utilizando un láser con pulsos de nanosegundos, una serie de micro-roturas aparecen rodeando las zonas afectadas por el láser, siendo imposible eliminar dichas roturas. Además de influir negativamente sobre el patrón de difracción de la luz (en términos de eficiencia y de fidelidad respecto al diseño del elemento), disminuyen la vida útil del elemento fabricado ya que, en ocasiones, las roturas se propagan a lo largo del vidrio llegando a destruir la muestra. Sin embargo, el acceso a este tipo de láseres es cada vez más común. Por ello, planteamos la posibilidad de utilizarlos como herramienta de prototipado rápido, o para la generación de DOEs embebidos de bajo coste.

En este capítulo, por tanto, se lleva a cabo una caracterización de las características de la interacción entre pulsos láser de nanosegundos y muestras de vidrio, buscando los parámetros idóneos para la fabricación de elementos difractivos, tales como simetría de las marcas producidas o minimización de los daños térmicos. Se muestra que, a pesar de producir una gran

cantidad de ruido debido a las zonas de fractura, los elementos fabricados tienen una buena relación calidad-precio.

Como extensión, se muestra la posibilidad de grabar elementos apilados (en "stack"). Este tipo de elementos es de gran interés, dado que es posible fabricar elementos difractivos integrados en una única pieza. A modo de ejemplo se muestran una serie de redes de difracción apiladas. Se detecta una serie de discrepancias con la teoría clásica de redes de Ronchi, que se achacan a la incorrecta descripción de las redes fabricadas. Por ello, se hace necesario un estudio en profundidad de redes de difracción binarias bajo un enfoque más amplio que el contemplado por la teoría de Ronchi.

Capítulo 6: Proceso de autoimágenes con redes binarias no de Ronchi

Las redes de Ronchi son redes binarias (es decir, tienen dos niveles de modulación) que operan sobre la amplitud o sobre la fase de la luz. Además, se considera que el factor de relleno de estas redes es del 50% del periodo. En este capítulo planteamos el estudio de redes de difracción binarias que, en principio, modulan al mismo tiempo la amplitud y la fase del haz de iluminación. Además, el factor de relleno puede tomar cualquier valor entre 0% y 100%.

Un desarrollo analítico, utilizando el formalismo de Fresnel, muestra que la separación entre máximos del contraste de las autoimágenes depende exclusivamente del periodo de la red y de la longitud de onda utilizada como iluminación. Sin embargo, la posición de dichos máximos, así como su forma y anchura, dependen del carácter de la modulación (amplitud o fase) y del factor de relleno. Este hecho abre las puertas a la realización de un diseño apropiado de redes de difracción en función de su uso. Por ejemplo, es posible colocar los máximos de contraste a determinadas distancias jugando con los parámetros de configuración de las redes. De la misma forma, es posible aumentar la anchura de los máximos de contraste modificando el factor de relleno, lo que sería de gran interés para su aplicación en codificadores ópticos de la posición. De forma similar, unos máximos de contraste muy estrechos podrían utilizarse como una matriz de fuentes de iluminación cuasi-puntuales, o para marcar distancias (en múltiplos de la separación entre planos de Talbot) con gran exactitud.

Apéndice A: Codificadores ópticos de la posición

Un codificador óptico de la posición (conocido también como "codificador", "encoder óptico" o, simplemente, "encoder") es un dispositivo opto-electrónico utilizado para medir desplazamientos relativos y posiciones con una gran exactitud. Su funcionamiento se basa en el desplazamiento de un fotodetector a lo largo de una red de difracción. La lectura del patrón de difracción proporciona una medida del desplazamiento experimentado por el fotodetector. Sobre el fotodetector se suele colocar una segunda red que se desplaza solidariamente con el fotodetector. De esta forma, de la señal que mide el fotodetector se puede obtener, además de la posición, el sentido de desplazamiento. Además, ciertas marcas en la primera red se utilizan como referencia, de forma que además de desplazamientos relativos se pueden medir también posiciones absolutas.

Pueden medir desplazamientos lineales (codificadores lineales) o angulares (codificadores rotatorios o anulares). En general se suelen utilizar redes de cromo sobre vidrio como escalas, pero en ciertas circunstancias (con recorrido mayores que 3 metros o para anillos de gran tamaño) es necesario utilizar redes de difracción grabadas en acero. Estas últimas tienen un comportamiento óptico peor, disminuyendo las tolerancias mecánicas del sistema.

Apéndice B: Definiciones de funciones de coste

Los algoritmos de optimización utilizan funciones "de coste" (o "de mérito") que dan un valor numérico a la calidad de los resultados. Algunas de las funciones de coste más utilizadas en tareas de diseño de elementos micro-ópticos son la eficiencia de difracción, el error cuadrático medio, la relación señal/ruido y la uniformidad.

Conclusiones

Las principales aportaciones originales de esta Tesis Doctoral pueden resumirse en los siguientes puntos:

- Se ha puesto en marcha un sistema de ablación láser para micro-mecanizado. El equipo puede trabajar en configuración de grabación punto a punto (lo que resulta muy apropiado para la fabricación de elementos complejos) o en modo vectorial (que resulta idóneo para la grabación de redes de difracción). Se ha calibrado el equipo, obteniendo los parámetros adecuados de funcionamiento. Se ha probado el correcto funcionamiento sobre diferentes materiales, como metales (flejes de acero), dieléctricos (vidrio) y sólidos cristalinos (silicio cristalino). Al mismo tiempo, se ha adquirido una gran experiencia en el campo del micro-mecanizado por ablación láser.

- Se ha desarrollado un protocolo para el proceso de prototipado de elementos difractivos binarios, desde las tareas de diseño hasta su fabricación y caracterización.

- Para el caso de fabricación sobre flejes de acero, la rugosidad de los substratos afecta al efecto Talbot, haciendo disminuir el contraste de las autoimágenes. Hemos demostrado que controlando la calidad superficial de los substratos (así como el proceso de grabación), los flejes de acero pueden comportarse como un buen substrato para aplicaciones micro-ópticas. Además del estudio de la rugosidad, se han desarrollado expresiones analíticas que describen el proceso de las autoimágenes con redes de difracción definidas sobre superficies curvas.

- En cuanto a dieléctricos transparentes, se han analizado el efecto de los pulsos láser de nanosegundos en el interior de vidrio. En concreto, los pulsos laser de nanosegundo producen unas zonas con "micro-fracturas" alrededor de las áreas en las que el haz láser ha sido focalizado. No obstante, la relación calidad-precio de los elementos fabricados muestra que el método utilizado representa una buena alternativa para el prototipado rápido de elementos ópticos difractivos embebidos.

- Finalmente, se ha desarrollado una completa descripción del comportamiento de redes de difracción en campo cercano, teniendo en cuenta los parámetros de configuración de dichas redes: el carácter mixto amplitud/fase, el periodo de la red y el factor de relleno de

cada periodo. La distancia entre autoimágenes depende exclusivamente del periodo de la red y de la longitud de onda de la iluminación. Por el contrario, la posición y la forma de los máximos de contraste de las autoimágenes dependen del carácter amplitud/fase y del factor de relleno de las redes.

- Los resultados derivados de esta Tesis Doctoral (en concreto, la posibilidad de fabricar elementos sobre hacer así como embebidos en vidrio) han dado lugar a la aprobación de un proyecto para la grabación y lectura de encóderes anulares, liderado por Fagor Automation S. Coop en consorcio con el *Grupo Complutense de Óptica Aplicada* (AOCG; Applied Optics Complutense Group) y Rofin Baasel-España-S.L.U. Este proyecto supondrá la transferencia de los resultados de la investigación al ámbito industrial.

Table of contents

AGRADECIMIENTOS **I**

RESUMEN **III**

ABSTRACT **- 3 -**

1 INTRODUCTION **- 5 -**

1.1 DIFFRACTIVE OPTICAL ELEMENTS - 5 -

1.2 FABRICATION TECHNIQUES OF DOEs - 9 -

1.2.1 Direct machining - 10 -

1.2.2 Lithographic techniques - 11 -

1.3 OPTICAL ENCODERS AND HISTORICAL BACKGROUND - 13 -

1.4 AIMS AND OBJECTIVES OF THIS WORK - 15 -

1.5 OVERVIEW OF THE THESIS - 15 -

2 DESIGN AND SIMULATION OF DOES **- 17 -**

2.1 DIFFRACTION THEORY - 18 -

2.2 SCALAR DIFFRACTION THEORY - 20 -

2.2.1 Fresnel Diffraction Model - 21 -

2.2.2 Fraunhofer approach - 23 -

2.2.3 Thin Element Approximation - 24 -

2.3 NUMERICAL METHODS - 24 -

2.3.1 Fraunhofer Propagation though the FFT algorithm - 24 -

2.3.2 Rayleigh-Sommerfeld Propagator - 27 -

2.3.3 Beam Propagation Method - 28 -

2.4 ALGORITHMS FOR THE DESIGN OF DOEs - 31 -

2.4.1 Iterative Fourier Transform Algorithm (IFTA) - 32 -

2.4.2 Iterative Global Optimization Algorithms - 33 -

3 MICROMACHINING WITH NANOSECOND PULSED LASER **- 39 -**

3.1 INTRODUCTION - 41 -

3.2 Q-SWITCHED LASERS - 43 -

3.3 LASER ABLATION - 44 -

3.4 LASER ABLATION IN METALS - 46 -

3.4.1 Metal Optics - 47 -

3.4.2 Pulsed beams interaction - 48 -

3.5 LASER ABLATION SYSTEM - 49 -

3.5.1 Characterization of the Laser Ablation System - 55 -

3.6 DETERMINATION OF THE MANUFACTURING PARAMETERS: MICROMACHINING OF STEEL TAPES - 57 -

3.6.1 Estimation of the ablation threshold in steel - 57 -

3.6.2 Focusing tolerances - 61 -

3.7 MICROMACHINING OF TRANSPARENT DIELECTRICS - 61 -

3.8 SILICON PROCESSING BY NANOSECOND PULSED LASER ABLATION - 64 -

4 DIFFRACTIVE OPTICAL ELEMENTS OVER STEEL TAPES BY MEANS OF LASER ABLATION **- 69 -**

4.1 INTRODUCTION - 71 -

4.2 DIFFRACTION GRATINGS ON STEEL TAPES FOR OPTICAL ENCODERS - 71 -

4.2.1 Talbot effect with perfect gratings - 72 -

4.2.2 Talbot effect with a rough diffraction grating. - 74 -

4.2.3 Experimental approach - 77 -

4.3 SELF IMAGING WITH CURVED GRATINGS - 81 -

4.3.1 Theoretical analysis - 82 -

4.3.2 Experimental approach - 87 -

4.4 ROUGH DOEs OVER STEEL TAPES BY MEANS OF LASER ABLATION - 89 -

4.4.1 Rough Fresnel zone plates - 90 -

4.4.2 Numerical simulations of rough diffractive lenses - 93 -

4.4.3 Experimental results - *95* -
4.5 APPLICATION OF THE RESULTS: MICROMACHINING OF ANNULAR GRATINGS - 98 -

5 DOES EMBEDDED IN FUSED SILICA WITH NANOSECOND PULSED LASERS - 101 -
5.1 INTRODUCTION - 103 -
5.2 MICROMACHINING OF FUSED SILICA BY NANOSECOND PULSES ABLATION - 104 -
5.3 BINARY AMPLITUDE DIFFRACTIVE OPTICAL ELEMENTS - 107 -
5.3.1 Rough Fresnel Zone Plates - *108* -
5.3.2 Diffractive beam shaper in the far field - *109* -
5.4 DIFFRACTION GRATINGS IN FUSED SILICA - 113 -
5.5 APPLICATION OF EMBEDDED GRATINGS IN OPTICAL ENCODERS READING HEAD - 116 -

6 SELF-IMAGING PROCESS WITH BINARY NON-RONCHI GRATINGS - 117 -
6.1 INTRODUCTION - 119 -
6.2 SELF-IMAGES LOCATION OF AMPLITUDE/PHASE BINARY GRATINGS - 119 -
6.2.1 Theoretical model - *120* -
6.2.2 Phase-amplitude mixed gratings - *121* -
6.2.3 Numerical results - *124* -
6.2.4 Experimental approach - *127* -
6.3 EFFECT OF FILL-FACTOR ON THE SELF-IMAGES OF DIFFRACTION GRATINGS - 129 -
6.3.1 Simulations by means of Beam Propagation Method - *130* -
6.3.2 Analytical approach - *132* -

7 CONCLUSIONS - 139 -

APPENDIX A. OPTICAL ENCODERS - 141 -
A.1 POSITION ENCODERS - 141 -
A.2 ENCODER COMPONENTS - 143 -
A.3 READING SIGNALS - 144 -
A.4 ERRORS AFFECTING THE MEASUREMENT - 145 -

APPENDIX B. COST FUNCTION DEFINITIONS - 147 -
B.1 DIFFRACTION EFFICIENCY - 148 -
B.2 ROOT MEAN SQUARE ERROR - 148 -
B.3 THE SIGNAL-TO-NOISE RATIO - 149 -
B.4 UNIFORMITY - 149 -

REFERENCES - 151 -

PUBLICATIONS AND COMMUNICATIONS - 161 -
RELATED WITH THIS THESIS - 161 -
Publications - *161* -
Communications - *162* -
OTHER WORKS - 163 -
Publications - *163* -
OTHER WORKS - 164 -
Publications - *164* -

Abstract

Laser ablation micromachining represents a reliable fabrication method for diffractive optics with moderate costs. However, the process of laser ablation is far from a "clean process". In fact, during the interaction of focalized and high-energetic laser beams with matter involves many processes. The explosive character of this interaction makes very difficult to predict the result of the interaction. In this Doctorate Thesis, we have implemented a laser ablation system working with laser pulses with durations in the range of nanoseconds. A complete description of the system is developed, explaining the characteristics of the inscriptions depending on the variation of the fabrication parameters (the energy density and the pulses overlapping, fundamentally). The optical behavior of the fabricated devices is also analyzed. Particularly, the near field diffraction by rough diffractive elements over steel tapes is studied. A model taking into account the roughness of the surface and the roughness of the zones affected by laser interaction describes this optical behavior. In addition, we carry out a study of the effect of the curvature of the substrate over the Talbot effect of diffraction gratings. At the same time, we show the properties of diffractive elements michromachined by focalizing the laser pulses in bulk fused silica. The characteristics of the laser ablation system (concretely, the nanosecond duration of the laser pulses) make impossible to avoid thermal damages in the substrates. However, we prove that it is possible to fabricate binary diffractive devices. The quality/cost ratio of the fabricated elements shows that nanosecond laser ablation can be considered as a good alternative for rapid prototyping of embedded diffractive devices. Finally, a study of the diffraction produced by binary non-Ronchi gratings is developed, taking into account the effect of the amplitude/phase character, the period of the grating and the fill factor of each cycle over the Talbot self-imaging process.

1 Introduction

1.1 *Diffractive Optical Elements*

Diffraction effects appear when an aperture limits a wave, or when an obstacle intercepts the wave [1]. It is often described as the deviation of waves from a straight propagation line due to interaction with such the obstacles. The importance of the diffractive effects depends on the size of obstacles in comparison with the wavelength: smaller obstacles produce more considerable diffraction effects. Attending to the various phenomena that can affect to the propagation of light (such as refraction or reflection), diffraction and interference are directly related to the wave nature of light, in opposition to corpuscular nature of light. In this sense, the general electromagnetic fields theory is the basis of physical optics used to model diffractive optics [2]. The light is then considered as an electromagnetic wave.

Historically, diffraction effects are known from centuries ago [1], [2]. Probably the first reference to the diffraction phenomenon was made by Lenoardo da Vinci (1452-1519). However, the first accurate description was introduced by Francesco Maria Grimaldi (1618-1663) in a book published posthumously in 1665 [3]. He observed the shadow resulting from an aperture in an opaque screen illuminated by a light source, noticing that the transition from light to shadow was gradual rather than sharp. He called this effect as diffraction, from Latin "difringere" (disintegrate, to break into pieces). In those times, corpuscular theory of light was widely used to describe the optical phenomenology and it was not possible to explain correctly the diffraction phenomena under this theory. Christian Huygens (1629-1695) was the first proponent of a wave theory of light, describing diffraction as a source of secondary spherical disturbance [4]. Possibly, the strong support of corpuscular theory by Isaac Newton (1642-1727) and their influence over contemporary scientists had hold up the

development of diffraction theory until 19th century. In 1804, Thomas Young (1773-1829) introduced the concept of interference of the light, based in experimental evidences [5], helping to understand the wave nature of light. In 1816 appears the famous memoir of Augustin Jean Fresnel (1788-1827) in which the ideas of Huygens and Young were brought together for the first time, showing that diffraction can be explained by the application of Huygens' construction, together with the principle of interference [6]. In 1865 James Clerk Maxwell (1831-1879) identified light as an electromagnetic wave [7], and in 1883 Gustav Kirchhoff (1824-1887) written Fresnel's analysis on a more mathematical form [8]. In 1896 Arnold J.W. Sommerfeld (1868-1951) refined the theory deriving the so-called Rayleigh-Sommerfeld diffraction theory [9]. The rigorous solution of diffraction problems by means of these analytical tools can be found only for a limited number of cases, due mathematical difficulties. For this reason, approximate and numerical methods are used instead. Nowadays, the use of computers is unavoidable for the design of diffractive structures.

The use of refractive optics dominates the history of optics, whereas the use of diffractive devices (mainly gratings, and also Fresnel zone plates) has a relatively short history. Diffraction effects have been considered, historically, as parasitic phenomena that should be avoided whenever possible [10], because they reduce the imaging resolution limits of the optical systems. Only in the recent decades, such effects have been considered as being advantageous. Advances in microfabrication techniques and miniaturization, caused mainly by the electronic industry, stimulated the study of microstructured devices controlling the diffraction of light. In addition, the capability of computers to solve numerically complicated problems increases drastically the apparition of many ideas and concepts in this field.

Optical devices operating by diffraction are known as Diffractive Optical Elements (DOEs) [10], [11]. A DOE is a device that modifies an incident wavefront into a desired field or intensity by diffraction control [12]. Diffractive Optics has been developed in parallel to Holography and Fourier Optics [11], [13]. Holography was proved as a proper way to generate a specific distribution of light from an illuminating beam. Similarly, the purpose of DOEs is to generate a diffracted wave with the desired characteristics. The difference between them lies in the generation of the optical element. In Holography the desired field is recorded by interference between an Object beam and a Reference beam [14], whereas DOEs are usually designed by means of a computer, after calculating the proper diffractive figure that reproduces the desired field [15]. The modulation of light is based on controlling

some property of the light such as phase or amplitude, commonly. Nevertheless, other characteristics of the light such as the polarization or the coherence can also be modulated.

A common technique used to generate some DOEs is to replicate refractive interfaces at depths multiples of the depth needed to produce phase delays of 2π radians. The process is similar to the design of multi-part refractive devices, such as Fresnel lens used in lighthouses, but with depths approaching the wavelength of the working light (up to tens of microns). Thus, it acts by diffraction. Such a DOE consisting in a diffractive device whose phase-controlling surfaces are smoothly varying is called kinoform, [12]. The manufacturing of a microstructured continuous-relief surface can be complex and expensive.

In order to simplify the fabrication process, the continuous profile can be discretized in a certain number of levels. Thus, the surface obtained is an approach to the continuous-relief surface. The element generated in this way is called Multilevel Mask, with N levels of discretization. The best approach to the kinoform is obtained with a high number of levels, since the efficiency of the device decreases with the number of levels. Obviously, an increment in the number of levels involves an increase in the fabrication costs. The simplest diffractive device that can be designed by discretization is a 2-levels DOE, known as Binary DOE. When the device controls the phase of the light, each level of the DOE introduces either a 0 or π-phase delay. When the device controls the amplitude of the beam, each level has a value of 0 (opaque) or 1 (transparent). Although the loss of efficiency is high, when only two levels are used, they present some advantages and properties (in addition to the common properties of DOEs) that make them key components in some optical system. The first of them is the low costs of fabrication (in terms of time, and technical requirements) in comparison with other diffractive devices. Moreover, due the usual flat arrangement, it is very usual to combine binary diffractive elements with refractive components in order to refine their functionality, or to integrate several binary DOEs into micro-optical systems, implementing novel optical applications unattainable by means of refractive/reflective optics.

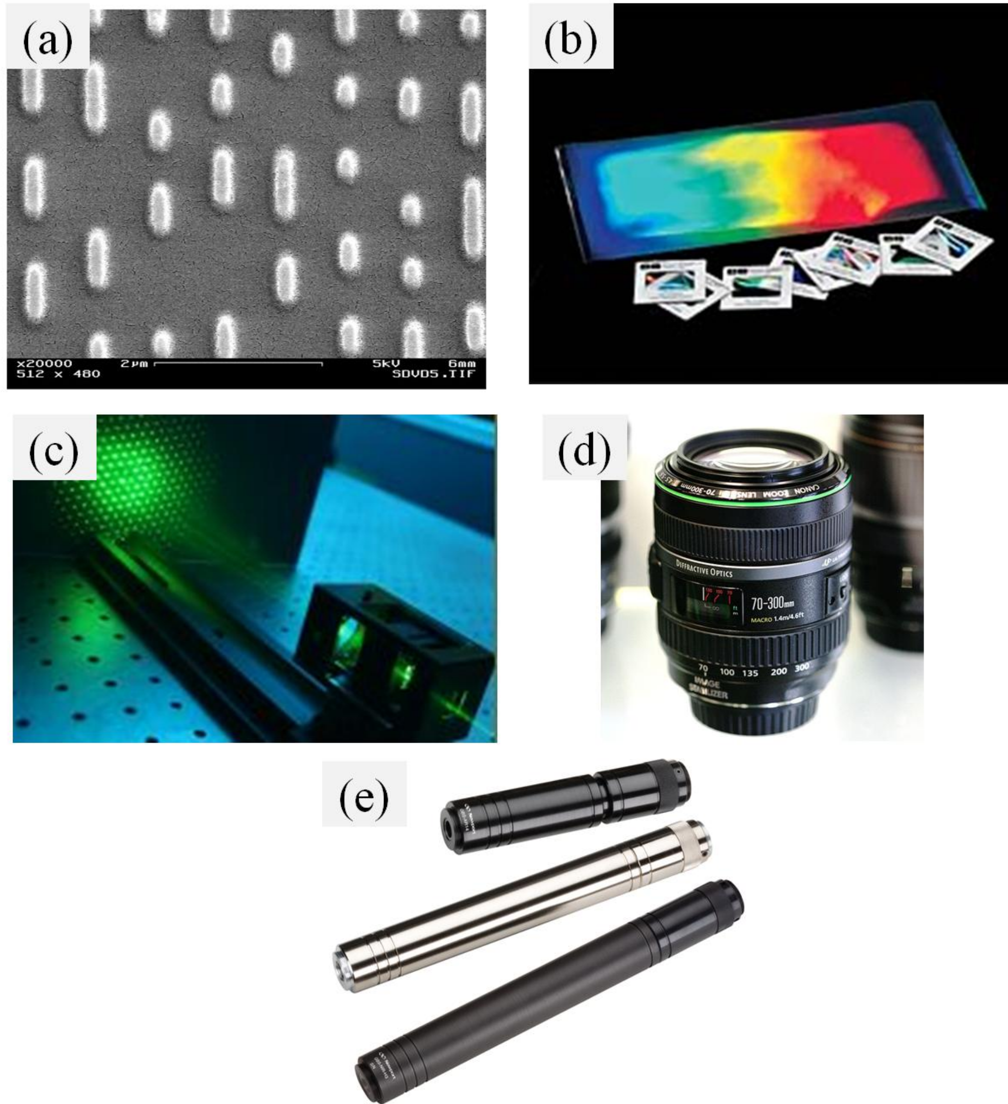

Figure 1.1: Examples of commercial micro-optical device a) a compact disc (SEM image); b) diffraction gratings, commercialized by Edmund Optics; c) diffractive spot array generator, by Suss MicroOptics; c) the Canon EF 70-300 mm zoom lens, using a diffractive lens correcting chromatic aberrations; e) diffractive beam shaping by Newport.

A refractive element has in some cases an equivalent diffractive device. In such a case, the use of diffractive devices can be advantageous, for example, when the low weight of DOEs is a matter. In addition, a wide set of novel applications that cannot be implemented by other methods demonstrates that diffraction is far from being detrimental. Specifically in fields such as spectroscopy or metrology, diffraction devices are key components with no equivalence with refractive devices. Among all diffractive elements, diffraction gratings are probably the most used diffractive devices. More complex examples are the so-called fan-out gratings, for optical fiber coupling purposes. There are actually several micro-optical and

diffractive devices commercialized in the market. Figure 1.1 shows some examples that can be easily found.

The commercial success of these devices depends strongly on the ability of manufacture DOEs of acceptable quality at a reasonable cost. In these sense, rapid-prototyping methods and low-cost manufacturing processes are research field of interest for the industry of micro-optics.

1.2 *Fabrication Techniques of DOEs*

We can found some examples of natural diffractive elements, as feathers acting as diffraction gratings (with features about $100\,\mu\text{m}$) able to diffract sunlight into a faint color spectrum, or even sub-wavelength structures, as butterfly wings. Nevertheless, the first diffractive devices assembled by man was probably gratings made out of hair run between sets of parallel screws (binary amplitude transmission gratings) [16]. In 1785 David Rittenhouse (1732-1796), an American astronomer, reported the first fabrication of a diffraction grating [17]. Fraunhofer ruled his own gratings by simply ruling gold films on glass or scratching shiny glass surfaces using a piece of diamond. By this time, an important commercial activity began, in order to supply the astronomers with precise instruments. After the progress by F.A. Nobert around 1850 and L.M. Rutherfurd in gratings ruling about 1870, Rowland constructed sophisticated ruling engines in the 1880's and invented the concave grating. In 1871 diffractive "zone plates" with focusing power were hand drawn as amplitude masks by Rayleigh and as phase structures in 1898 by Wood [18], who also ruled in 1910 blazed phase gratings in copper plates [19]. He was also the first in made up visual instruments using diffractive lenses.

The history of modern diffractive optics began with the development of Holography and the method proposed by Gabor in 1948 [13]. A hologram is able to reconstruct the image of an object, creating much more complicated diffraction patterns than can be achieved with mechanical ruling techniques. The next step was to create computer-generated holograms by imaging patterns plotted by computer on paper sheets or cathode ray tube screens [20]. With a control of the exposure [21], was also possible to engrave kinoforms with surface relief pattern [22], [23].

The development of microlithographic technologies for the manufacture of integrated circuits in the late 1950s was an important advance in the history of diffractive optics. The

convergence of principles of computer generated holography and lithographic fabrication methods form the basis for most modern diffractive optics.

The first examples of binary diffractive optics date back from early 1970s [24], while direct writing techniques were applied to DOEs fabrication at the end of 1970s and beginning of 1980 [25], [26]. Multilevel masks were also obtained by these years [27].

Current techniques are mostly based on these methods developed more than 30 years ago. The most usual techniques related to binary and multilevel optics fabrication are explained on next items.

1.2.1 Direct machining

High quality diffractive elements can be fabricated by mechanical ruling in a wide range of materials [1]. By means of computer control, a sharp stylus tip scrapes the substrate material [28] (see Figure 1.2).

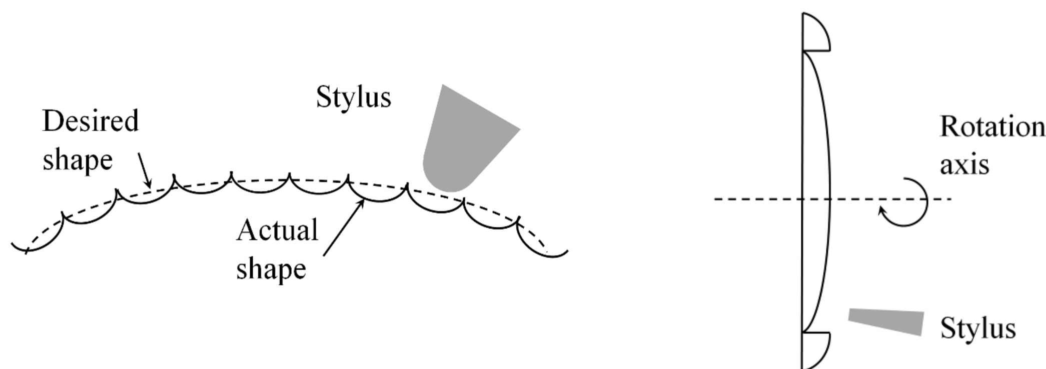

Figure 1.2: Mechanical ruling scheme.

This technique results specially indicated for radially symmetric patterns. The diffractive structure is then generated by rotating the substrate as it is brought into contact with the stylus, a technique known as diamond turning [29].

Direct machining techniques require precise mechanical control and are limited by the size of the stylus tip. The possible structures are either straight line or circularly symmetrical gratings. It would be extremely difficult to fabricate a generalized two-dimensional DOEs.

There exist other methods for direct machining, avoiding the use of mechanical stylus. For example, Ion Bean Milling (IBM) uses ions to extract atoms in the material from the surface [30]. The resolution is similar to that of electron-beam direct writing. Another method is Laser Ablation, based on focusing a high energetic laser beam to directly machining the

surface [31]. Unlike mechanical ruling, both processes are able to created arbitrary surfaces (and not only straight or circular). Laser Ablation method will be explained with more detail in Chapter 3.

1.2.2 Lithographic techniques

The lithographic methods used for DOEs manufacturing are based on the same techniques used to fabricate integrated circuits [32]. These methods require the use of photoresists, a kind of light-sensitive films, deposited on top of a substrate.

The process starts with the patterning of a photoresist layer. This is often performed exposing the resist to UV radiation using optical pattern generators or by light-beam scanning (also, electron-beam machines are used) [33], [34]. Development of a positive photoresist opens the substrate surface from the exposed regions; whereas with a negative resist the unexposed areas are dissolved in development. Substrate etching is the next step. Ion bombardment or chemical etching removes material from the metal layer. The remained resist layer areas protect the layer under. The final structure appears by chemical removing the resist film. The process is schematized in Figure 1.3.

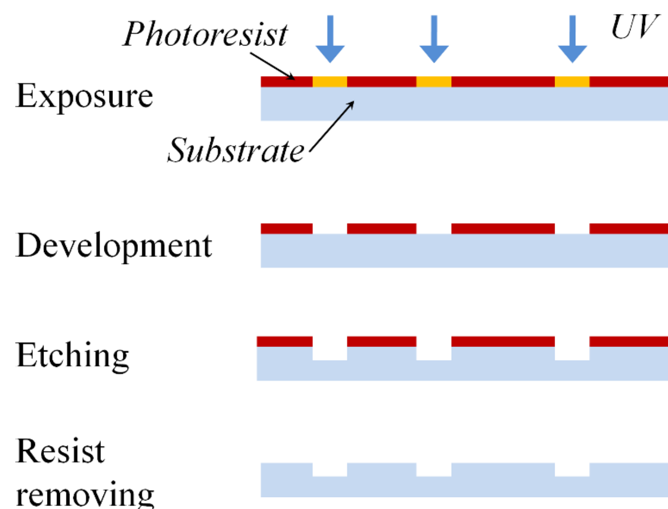

Figure 1.3: Scheme of photolithographic technique.

For multilevel masks, the etched substrate is recoated and re-exposed to a secondary pattern. After the development, the substrate is again etched, as it is shown in Figure 1.4. The process can be iterated as many times as desired, obtaining a multilevel mask.

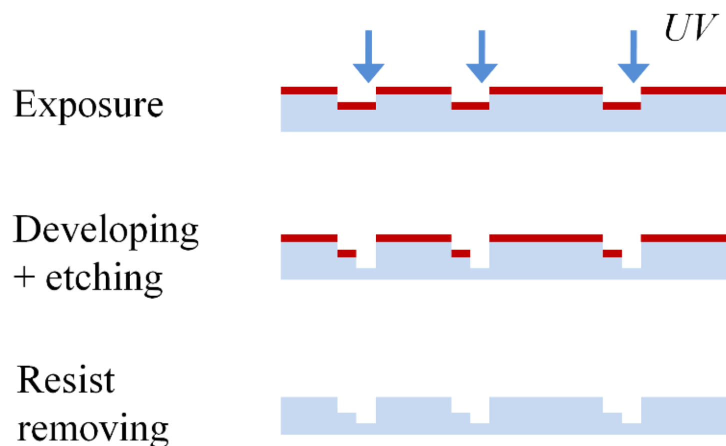

Figure 1.4: Multilevel mask fabrication by photolithography. The starting point is the result of the process depicted in Figure 1.3.

For each exposing process, there is a resist coating process, an alignment process and an etching process (and probably a surface cleaning process). In addition to the consequent generated costs, there are systematic fabrication errors that can lead to a severe drop in optical performance.

One of the most usual techniques is to use a chrome layer over a glass substrate (chrome-on glass masks). The diffractive devices obtained with this substrate act both in reflective or transmitive configuration. With only two levels (transparent and opaque), the amplitude of the illumination beam is locally modulated.

The lithographic process should be used under a high-controlled environment. Photoplotter need to be placed in clean rooms and isolated from external vibrations. As example, a photoplotter system at the Applied Optics Complutense Group (AOCG) installations for masters recording is shown in Figure 1.5. It works with a laser diode at $405\ \text{nm}$.

The critical feature size with optical lithography is limited by the optical wavelength around $0.5\ \mu\text{m}$. Electron beam lithography can reach up to true nanostructures, with details below to $50\ \text{nm}$ [34]. There also exist other technologies related to the lithographic techniques reaching smaller features than optical lithography, such as interferometric exposure or near-field holography.

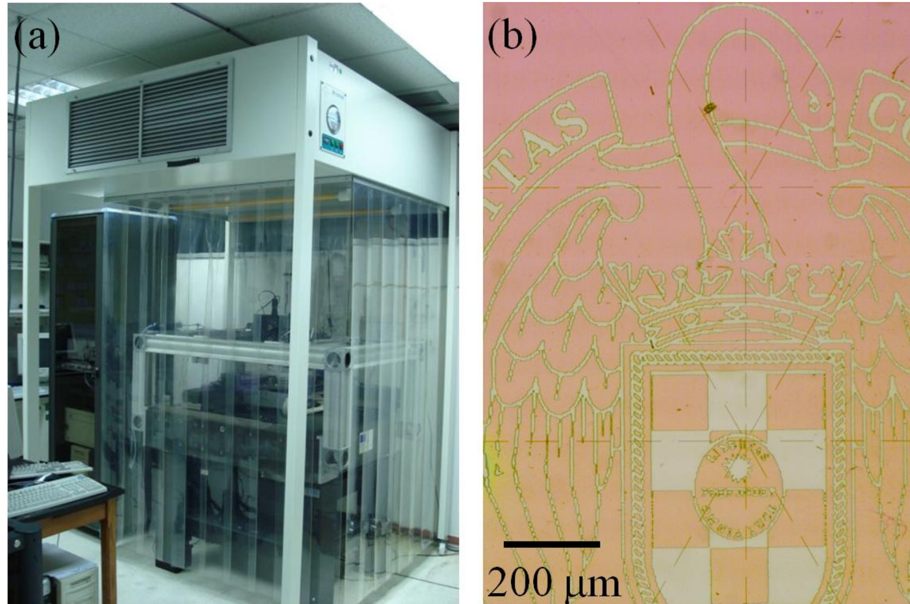

Figure 1.5: a) Laser Photoplotter for optical photolithography at the AOCG laboratories; b) example of recording: the logo of the Complutense University with pixel size of 5 μm *(confocal microscopy).*

1.3 *Optical encoders and historical background*

One of the field in which diffractive devices prove their capabilities is the measurement of displacements and positioning with high accuracy by means of optical encoders. These devices are optoelectronic elements of critical importance in those automatic systems with tight requirements on micro/nanopositioning over distances of meters/centimeters, such as machine-tools, robotic arms and high-quality scientific metrological instrumentation. An explanation of the operation principles can be found in Appendix A. Basically, they are compound of a scale (a diffraction grating) and a reading head with a second grating mounting together with a photodetector. The displacement of the reading head along the first grating produces an electrical signal giving the value of the displacement.

For the optical encoder scales, the most used substrates are fused silica (working both in transmission or reflection) and metallic tape (working only in reflection). The fused silica substrate present the best behavior attending to optical considerations, but it result very complex to handle when distances over tens of centimeters are required. On the contrary, the optical behavior of metallic substrates is not so good, but it is possible to manufacture scales up to 30 meters. On the other hand, the reading head is compound usually of a Silica-based photodetector and a chrome-on-glass mask.

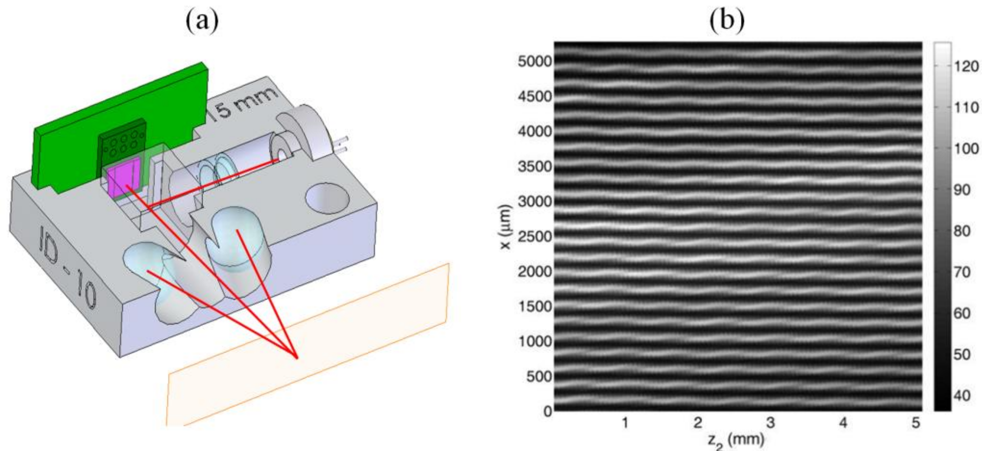

Figure 1.6: Some results of the AOCG - FAGOR AUTOMATION collaboration, a) prototype for interferodiffractive reading head for gratings with 4 μm of period; b) experimental verification of the Talbot effect cancelation using a double gratings system.

Although encoders present some interesting features like a high accuracy –with uncertainties below microns in distances of meters-, these devices show problems regarding mechanical tolerances in their positioning, therefore limiting their applicability in the fields aforementioned. For example, diffraction inherently linked to the propagation between the two gratings makes harder to enlarge the range of positioning of the second grating, thus reducing its mechanical tolerance. Moreover, these effects are more visible when the grating period is similar to the wavelength of the incoming light. For this reason, optical encoders represent an opportunity for research in the fields of engineering, electronics and optics. In this sense, a strong relationship between AOCG and FAGOR AUTOMATION S. COOP. has been established for a long time, in order to study the optical properties of the optical encoders taking advantage of them in several senses (improving the mechanical tolerances and the accuracy of the system). FAGOR AUTOMATION S. COOP. is a Spanish-based company, working in the manufacture of automation systems for machine-tool. The product of FAGOR AUTOMATION S. COOP is a complete suite for the control of machine-tool and other industrial processes, including numerical control and regulation systems. The development of this suite and the collaboration with AOCG has originated a wide number of scientific works involving patents [35]-[37] and PhD. Thesis [38]-[42] (see Figure 1.6). Particularly, the behavior of several systems working by means of diffraction gratings in the near field has been widely studied, developing several analytical models. The results of these researches indicate that optical encoders represent a good opportunity to prove the profits of micro-optics in industrial environments. In this sense, it is necessary to acquire the knowledge to design and fabricate generalized micro-optical devices.

1.4 *Aims and Objectives of this work*

The main aim of this work is to reach the capability to produce micro-optical devices, involving from the design tasks up to the manufacture and experimental evaluation of the designed elements. Optical encoding is one of the fields in which these devices can be used, but not the only one. Attending to the fabrication interest, the character of this work requires the use of a wide range of substrates. Moreover, a rapid and reliable prototyping is fundamental. In this sense, we consider the laser ablation process as the suitable method for these tasks.

We can summarize the objectives as follows:

- The development of tools for the design and evaluation of DOEs
- The implementation of a laser ablation system and the determination of the proper operation parameters. The capability of working with different substrates should be proved.
- The evaluation of the optical behavior of the manufactured devices.

1.5 *Overview of the Thesis*

This Thesis is compound of seven main chapters, organized as follows,

Chapter 1 is a general introduction, presenting the historical background in this field and the motivation of this work, as well as the goals to be fulfilled.

Chapter 2 summarizes the analytical and numerical tool used in this work for the description of the propagation of diffracted fields and for the design of diffractive devices.

Chapter 3 presents concepts relating to laser ablation process and micromachining by means of pulsed lasers. Moreover, the laser ablation system used in this work is presented and characterized.

Chapter 4 shows the capability of manufacturing diffractive structures on steel substrates. The optical behavior of these devices is discussed. Specifically, we focus on some concepts related to the roughness and the curvature of the samples in which the diffractive devices are engraved. Some methods for the simulation and emulation of rough diffractive elements are also shown.

Chapter 5 examines the feature of diffractive elements micromachined in bulk fused silica by means of nanosecond laser pulses. The results prove that this method is a good alternative for rapid prototyping and low cost processing of transparent materials.

Chapter 6 examines the effect of the configuration parameters of binary gratings (amplitude and phase character, period and fill factor) over the diffracted field in the near field.

Finally, Chapter 7 extracts the conclusions from this Thesis.

As well, Appendix A and Appendix B explain in detail some important concepts related with this Thesis.

2 Design and simulation of DOEs

This chapter collects several analytical and numerical tools used in this Thesis. Firstly, a mathematical description of the diffraction process is presented, starting with the Maxwell's equations. A scalar model for the diffraction is summarized, including the Fresnel diffraction model and the Fraunhofer approach. These models, combined with the Thin Element Approach, provide a proper scheme to explain the phenomenology presented in this Thesis. Next, some numerical implementations of this mathematical models are explained, as the Fraunhofer propagation, the Rayleigh-Sommerfeld propagator and the Beam Propagation Method. In the last section of this Chapter, we present some algorithms for the design of diffractive structures, such as the Iterative Fourier Transform Algorithm or the Global Optimization Algorithms.

2.1 *Diffraction Theory*

In this thesis we assume that light is an electromagnetic wave and, therefore, it is ruled by Maxwell's equations. It is usual to simplify the Maxwell's equations by a series of assumptions to a scalar form. This scalar approach is more convenient to our aims. However, when the wavelength of the incident radiation is comparable to or smaller than the size of the diffractive features, it is necessary to retain the vector forms.

Any electromagnetic field is defined by two vector quantities, the electric field $\vec{E}(\vec{r},t)$ and the magnetic field $\vec{B}(\vec{r},t)$. The Maxwell's equations for any electromagnetic fields (in the MKS system of units) are [43]

$$\begin{aligned} &\nabla\vec{E} = \frac{\rho}{\varepsilon}, \\ &\nabla\vec{B} = 0, \\ &\nabla\times\vec{E} = -\frac{\partial\vec{B}}{\partial t}, \\ &\nabla\times\vec{B} = \mu\vec{j} + \varepsilon\mu\frac{\partial\vec{E}}{\partial t}, \end{aligned} \tag{2.1}$$

where ρ is the charge density, ε is the electric permittivity, μ is the magnetic permeability, and $\vec{j}$ is the current density. Attending to the common characteristics of the optical media, we can make some assumptions. First, we assume that there are neither changes nor currents (although we assume an initial electric field $\vec{E}(\vec{r},t=0)$ that has been previously generated by changes on currents). Besides, we suppose at this point that the medium is homogenous, uniform and isotropic. Thus, ε and μ do not change with the position in the material, time or orientation, and they are not affected by the presence of electromagnetic fields. Under this circumstances Maxwell's equations result,

$$\begin{aligned} &\nabla\vec{E} = 0, \\ &\nabla\vec{B} = 0, \\ &\nabla\times\vec{E} = -\frac{\partial\vec{B}}{\partial t}, \\ &\nabla\times\vec{B} = \varepsilon\mu\frac{\partial\vec{E}}{\partial t}. \end{aligned} \tag{2.2}$$

Taking the second derivate of both $\vec{E}$ and $\vec{B}$, and making use of the triple vector product operator identity, it is possible to extract two differential wave equations for both components of the electromagnetic field,

$$\nabla^2 \vec{E} = \mu\varepsilon \frac{\partial^2 \vec{E}}{\partial t^2},$$
$$\nabla^2 \vec{B} = \mu\varepsilon \frac{\partial^2 \vec{B}}{\partial t^2}. \tag{2.3}$$

These vector expressions describe the propagation of an electromagnetic wave in a homogeneous and isotropic medium. The constant multiplying the right hand side in eq. (2.3) defines the propagation velocity of the wave in such a medium, as

$$\mathrm{v} = 1/\sqrt{\mu\varepsilon}, \tag{2.4}$$

and therefore the constant velocity of light in the vacuum is $c = 1/\sqrt{\mu_0\varepsilon_0}$. In turn, the index of refraction of the medium is the ratio

$$n = c/v. \tag{2.5}$$

The Laplacian ∇^2 operates on each orthogonal component of $\vec{E}$ and $\vec{B}$. Thus, eq. (2.3) can be treated as six separated scalar equations. The two equations for the x-axis

$$\frac{\partial^2 E_x}{\partial x^2} + \frac{\partial^2 E_y}{\partial y^2} + \frac{\partial^2 E_z}{\partial z^2} = \frac{n^2}{c^2}\frac{\partial^2 E_x}{\partial t^2},$$
$$\frac{\partial^2 B_x}{\partial x^2} + \frac{\partial^2 B_y}{\partial y^2} + \frac{\partial^2 B_z}{\partial z^2} = \frac{n^2}{c^2}\frac{\partial^2 B_x}{\partial t^2}. \tag{2.6}$$

The scalar equations for the other components (E_y, B_y, E_z, B_z) are obtained in a similar way. Assuming an harmonic wave, the spatial distribution of the electromagnetic field should satisfies the Helmholtz equation [1],

$$\nabla^2 U + k^2 U = 0. \tag{2.7}$$

where U represents either $\vec{E}$ or $\vec{B}$ (all components of the field have to satisfy the same equation), and the parameter k is known as wavenumber, defined as $k = 2\pi/\lambda$ and λ is the wavelength within the dielectric medium.

The assumption made over the medium nature is valid, for example, for free-space propagation with no boundary conditions. In such a case, eq. (2.3) is not an approach but the accurate expression for the wave propagation. For other cases, such as for light propagating

through step (abrupt) refractive index, the assumption of homogeneous and isotropic medium is not longer valid. For example, at the boundaries the $\vec{E}$ and $\vec{B}$ vectors are not independent, and coupling effects introduce some kind of correction over scalar diffraction theory. Rigorous diffraction theory takes into account the vector effects and the coupling between $\vec{E}$ and $\vec{B}$. Some deviations between scalar and real diffracted field appear, especially at the boundaries. After a few wavelengths away, scalar and rigorous theory lead to very similar predictions.

Rigorous vector analysis is needed when the smallest features comprising the diffractive device are less than three to four times the wavelength of light considered [44]. Nevertheless, divergences between the rigorous and scalar theories mainly affect the diffraction efficiency calculations, not those for the diffracted angles or the overall reconstruction geometry [45], [46]. As we will see, scalar diffraction theory is enough for the realization of this work.

2.2 *Scalar Diffraction Theory*

Due the superposition principle, a sum of solutions of the Maxwell's equations is also a solution of the equations system. In other words, we can propagate each plane wave separately and obtain the total propagation as the sum of each propagated plane wave.

Let us propose, firstly, a plane wave in vacuum as solution of Maxwell's equations,

$$U(\vec{r},t) = U_0 \exp\left[i\left(\vec{k}\cdot\vec{r} - \omega t\right)\right],, \tag{2.8}$$

where ω is the frequency, $\vec{k} = |k|\hat{u}_k$ with the wavenumber $k = \omega/c = 2\pi/\lambda$, and $\vec{k}\cdot\vec{r} = k_x x + k_y y + k_z z$.

A useful procedure to solve the propagation of a general harmonic wave is decomposing it as a sum of harmonic plane waves. Let us assume a wavefront U traveling in the positive z direction form $z = 0$ in Cartesian coordinates. This wavefront can be decomposed using the Fourier transform into an angular spectrum of plane waves,

$$U_0(\xi,\eta) = \left(\frac{1}{2\pi}\right)^2 \iint_\infty U_0(k_x,k_y)\cdot e^{i\left(k_x\xi + k_y\eta\right)} dk_x dk_y, \tag{2.9}$$

where k_x and k_y are the coordinates in the frequencies domain. Similarly, the spatial frequency spectrum is

$$U_0\left(k_x,k_y\right)=\int\int_{-\infty}^{\infty}U_0\left(\xi,\eta\right)\cdot e^{-i\left(k_x\xi+k_y\eta\right)}d\xi d\eta. \tag{2.10}$$

From eq. (2.8) and eq. (2.10), a plane wave propagates in vacuum as

$$U_{\left(k_x,k_y\right)}\left(x,y,z\right)=\left(\frac{1}{2\pi}\right)^2U_0\left(k_x,k_y\right)e^{i\left(k_xx+k_yy+k_zz\right)}e^{-i\omega t} \tag{2.11}$$

and the components of k must follow the relationship $k_x^2+k_y^2+k_z^2=k^2=\left(2\pi/\lambda\right)^2$. From here,

$$k_z^2=\sqrt{k^2-k_x^2-k_y^2}. \tag{2.12}$$

A set of plane waves will propagate according to

$$U\left(x,y,z\right)=\left(\frac{1}{2\pi}\right)^2\int\int_{-\infty}^{\infty}U_0\left(k_x,k_y\right)e^{i\left(k_xx+k_yy+k_zz\right)}e^{-i\omega t}dk_xdk_y \tag{2.13}$$

This expression can be rewritten as

$$U\left(x,y,z\right)=\int\int_{-\infty}^{\infty}U_0\left(\xi,\eta\right)h\left(x-\xi,y-\eta\right)d\xi d\eta \tag{2.14}$$

where $h\left(\xi,\eta\right)$ is the two-dimensional Green function, defined as

$$h\left(\xi,\eta\right)=\left(\frac{1}{2\pi}\right)^2\int\int_{-\infty}^{\infty}e^{i\left(k_x\xi+k_y\eta+\sqrt{k^2-k_x^2-k_y^2}\right)}dk_xdk_y. \tag{2.15}$$

Eq. (2.14) gives the exact solution for the scalar propagation of a harmonic wave. Nevertheless, it is very difficult to solve in the general case. For this reason, some approaches are usually made in order to obtain a more useful expression.

2.2.1 Fresnel Diffraction Model

Let us suppose an illumination field $U_i\left(\xi,\eta\right)$ propagating from a source, though a first plane called "aperture plane" with an arbitrarily shaped transparent structure, to a second plane, called "observation plane". The coordinates at the observation plane will be denoted by $\left(x,\ y,\ z\right)$, and the coordinates at the aperture plane at $\left(x,\ y,\ z=0\right)$ by $\left(\xi,\ \eta\right)$, as it is shown in Figure 2.1.

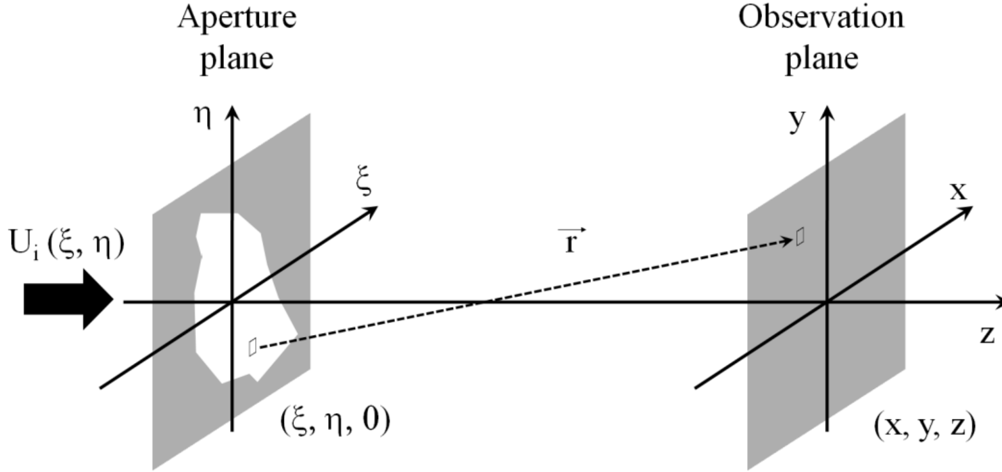

Figure 2.1: Diffraction due to illumination of an aperture generates a pattern on the observation plane. The distance $\vec{r}$ is that between any pair of points (ξ_i, η_i) at the aperture plane and (x_i, y_i) at the observation plane.

Let us now assume, moreover, that the distance from the aperture plane to the evaluation plane, and the beam size or aperture at the aperture plane, are large compared with the wavelength. We can then assume that $r \approx z$. Thus, $k_x, k_y << k$ and.

$$\sqrt{k^2 - k_x^2 - k_y^2} = k\sqrt{1 - \frac{k_x^2 + k_y^2}{k^2}} \approx k\left(1 - \frac{k_x^2 + k_y^2}{2k^2}\right) = k - \left(k_x^2 + k_y^2\right)/2k . \quad (2.16)$$

Thus, the Green function in eq. (2.15) is now

$$h(\xi,\eta) = \frac{e^{ikz}}{(2\pi)^2} \int \exp\left[i\left(-\frac{zk_x^2}{2k} + \xi k_x\right)\right] dk_x \int \exp\left[i\left(-\frac{zk_y^2}{2k} + \eta k_y\right)\right] dk_y . \quad (2.17)$$

Making use of the integral

$$\int e^{i\left(-\frac{zk_x^2}{2k} + \xi k_x\right)} dk_x = \frac{2\pi}{\sqrt{i\lambda z}} e^{i\frac{k}{2z}\xi^2} , \quad (2.18)$$

we can solve eq. (2.17) an obtain the next expression,

$$U_{Fresnel}(x, y, z) = \frac{1}{i\lambda z} e^{ikz} \iint U_0\left(k_x, k_y\right) \exp\left\{ i\frac{k}{2z}\left[(x-\xi)^2 - (y-\eta)^2\right]\right\} d\xi d\eta , \quad (2.19)$$

which is known as the Fresnel approach. The field calculated by this expression is known as "near field", and it is a very useful tool for analyzing the scalar propagation of light for a wide range of optics problems. In the near field, the diffraction pattern varies strongly with distance, as the observation plane is moved from the aperture. From eq. (2.19) we see that

the total field at any position in the observation plane may be determined form the integral of all the effective point emitters in the aperture.

The range of validity of this approach depends on the relationship between the characteristic size of the aperture L, the distance of the observation plane from the aperture z and the wavelength λ. It is common to use the number n_F, defined as

$$n_F = \frac{L^2}{\lambda z}. \tag{2.20}$$

Commonly, Fresnel approach is used when $n_F \gg 1$ and, consequently, $z << L^2/\lambda$. On the other hand, when $n_F \ll 1$ the so-called Fraunhofer approach rules the propagation of light. This approach is explained in next section.

2.2.2 Fraunhofer approach

Let us now assume that the distance from the aperture plane to the evaluation plane is very large compared with the aperture size, $n_F \ll 1$. Then, we can write

$$z >> \frac{k}{2}\left(\xi^2 + \eta^2\right). \tag{2.21}$$

In this case, it can be demonstrated [2] that the field at the evaluation plane is the Fourier transform of the input plane,

$$U_{Fraunhofer}\left(x, y, z\right) = \frac{e^{ik\left(z + \frac{x^2+y^2}{2z}\right)}}{i\lambda z} \int_{aperture} U\left(\xi, \eta\right) e^{-i\frac{k}{z}\left(x\xi + y\eta\right)} d\xi d\eta. \tag{2.22}$$

This integral in eq. (2.22) is in the form of a two-dimensional Fourier transform and the factor out of the integral is a scale factor. Eq. (2.22) is usually written in a compact notation as $U_{Fraunhofer}\left(x, y, z\right) = K \cdot FT\left\lfloor U\left(\xi, \eta\right)\right\rfloor$ where $K = \exp(z + \frac{x^2 + y^2}{2z}) / (i\lambda z)$ is the scale factor. It shows that the optical disturbance in a plane far from the diffracting aperture can easily be determined by taking the Fourier transform of the complex transmittance of the diffracting aperture. This is the basis of the entire Fourier Optics theory, and is also known as far field approximation. In contrast with the near field, the far field diffraction pattern has a stable form as the image plane moves, and only changes in size.

For an aperture of $1\,\text{mm}$ illuminated with visible light the Fourier approach is valid for distances longer than $10\ \text{m}$. Equivalently, it is possible to transform to the far field by using a convergent lens and observing the focusing plane of the lens.

2.2.3 Thin Element Approximation

For scalar treatment of the diffraction effects, the thin Element Approximation (TEA) is used. This approach consists of the assumption that the diffractive element can be modeled using a transmittance function [47]. It results useful to simplify the calculations, but it is not valid in almost cases. The approach is valid as long as the feature size is large compared with the wavelength, and the element thickness is comparable with the wavelength.

2.3 *Numerical methods*

The analytical resolution of eq. (2.19) and eq. (2.22) is only possible for some cases, even using a computer. For complex structures, it is necessary to use alternative tools. A wide variety of numerical methods has been proposed, as the Local Grating Approximation Method (LGA) or Finite-difference time-domain methods (FDTD). In this section, we will focus on two methods developed and used for the realization of the present work. Both lead to scalar analysis of diffracted field propagation.

2.3.1 Fraunhofer Propagation though the FFT algorithm

Due eq. (2.22), the far-field diffraction pattern can be expressed as the two-dimensional Complex Fourier Transform avoiding the scaling factor,

$$U'(x,y) = FT\lfloor U(\xi,\eta)\rfloor, \tag{2.23}$$

where FT denotes the numerical performance of the Fourier transform $U(\xi,\eta) = A(\xi,\eta)\cdot e^{-i\varphi(\xi,\eta)}$ and $U'(x,y) = A'(x,y)\cdot e^{-i\varphi'(x,y)}$. Thus, the incoming complex amplitude is the complex diffractive element plane (phase, amplitude, or both) modulated by the complex amplitude of the incoming wavefront.

In eq. (2.23), $U'(x,y)$ is the angular spectrum of the incoming complex wavefront $U(\xi,\eta)$. Both functions are sampled with the same number of pixels. The sampling size in the aperture plane will be limited, usually, by the fabrications capabilities. The Fourier

reconstruction window size is scaled so that it includes the largest frequency present in the original element. Let us suppose a Fourier-type diffractive element, sampled with squared pixels with size $c_\xi \times c_\eta$. Therefore, the output window size will be $N \cdot c_\xi \times M \cdot c_\eta$ where N and M are the number of pixels in each direction. The pixel size (in angular terms) at the observation plane will be [1]

$$\begin{cases} c_x = \dfrac{2}{N} \arcsin\left(\dfrac{\lambda}{2c_\xi}\right) \\ c_y = \dfrac{2}{M} \arcsin\left(\dfrac{\lambda}{2c_\eta}\right) \end{cases}. \tag{2.24}$$

And, therefore, the window size at the observation plane will be $N \cdot c_x \times M \cdot c_y$. The scaling properties of the FFT algorithm are collected in Figure 2.2 and Figure 2.3.

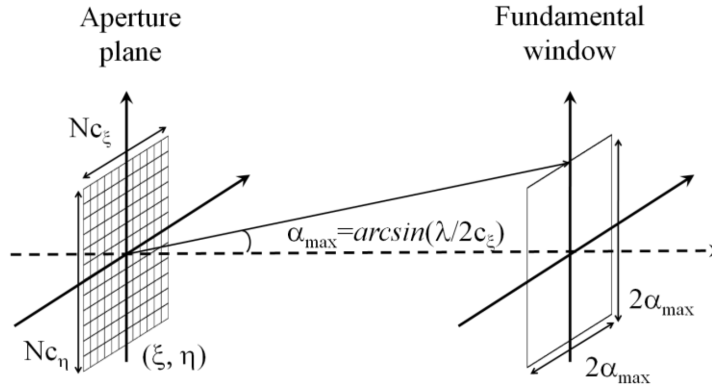

Figure 2.2: Angular scaling properties in the far field.

Each pixel at the observation plane corresponds, therefore, to an angular direction from the origin at the aperture plane. The pixel size dictates the size of the fundamental reconstruction window for each direction.

A central maximum peak will appear in the observation plane corresponding to the 0th order, in particular for amplitude CGHs. For numerical calculation, it is usual to remove the central point of the reconstructed CGH. Moreover, many orders will appear in the reconstruction plane. Each order defines a cell in which the objective will be replicated. The cell in the 0th order is called "fundamental window".

	Aperture plane	Far field
Pixel size	c_ξ, c_η	c_x, c_y
Window size	Nc_ξ, Mc_η	Nc_x, Mc_y

Figure 2.3: Pixel scaling properties of the FFT algorithm.

The position of the object that will be reconstructed within the fundamental window is also important, especially for binary masks. With binary CHGs, the fundamental negative and positive orders have the same efficiency (no higher orders appear in the fundamental window). When the objective pattern is not symmetric and is placed on-axis in the aperture plane, negative and positive order will be mixed at the reconstruction plane. This effect can be avoided by using multilevel mask with $N > 2$, as it is shown in Figure 2.4.

A usual performance is to place the pattern objective off-axis. Thus, a binary CGH reconstructs the pattern and its symmetrical image. With more than two levels, the symmetrical image vanishes and the efficiency increases, as it is shown in Figure 2.5.

Nevertheless, it should be remember here that the use of a high number of levels in the design of a DOE implies an increment in the fabrication costs, as have been explained in Section 1.2. For this reason, it could be advantageous the use of binary masks, if the application of the DOE allow it.

When the illumination wavefront is not a plane wave, rather an arbitrary field (like a Gaussian beam, an aberrated beam, or any shaped beam) the diffracted field is obtained performing the Fourier transform of the aperture multiplied by the complex field of illumination,

$$U'(x,y) = FT\left\lfloor U_I(\xi,\eta)\cdot U(\xi,\eta)\right\rfloor, \tag{2.25}$$

where $U_I(\xi,\eta)$ is the illumination field at the aperture plane. The wavelength of the illumination field only affect to the angular size, as (2.24).

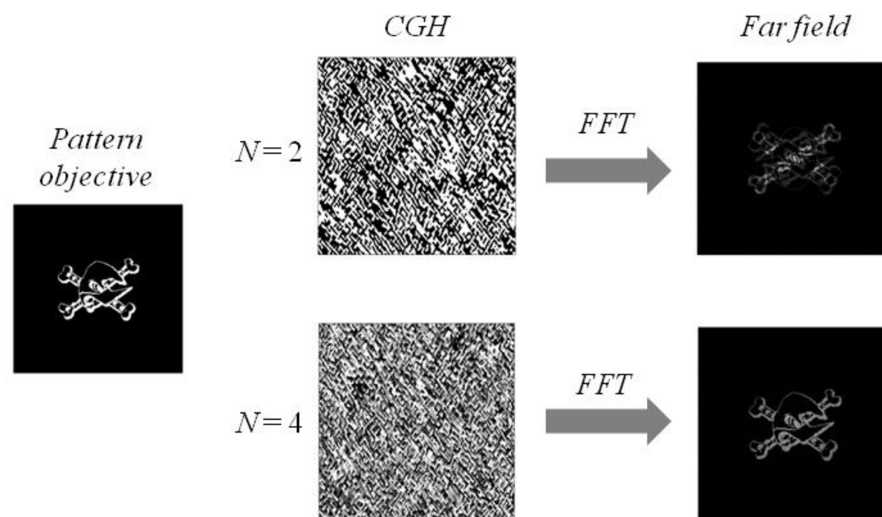

Figure 2.4: Reconstruction of on-axis multilevel CGHs.

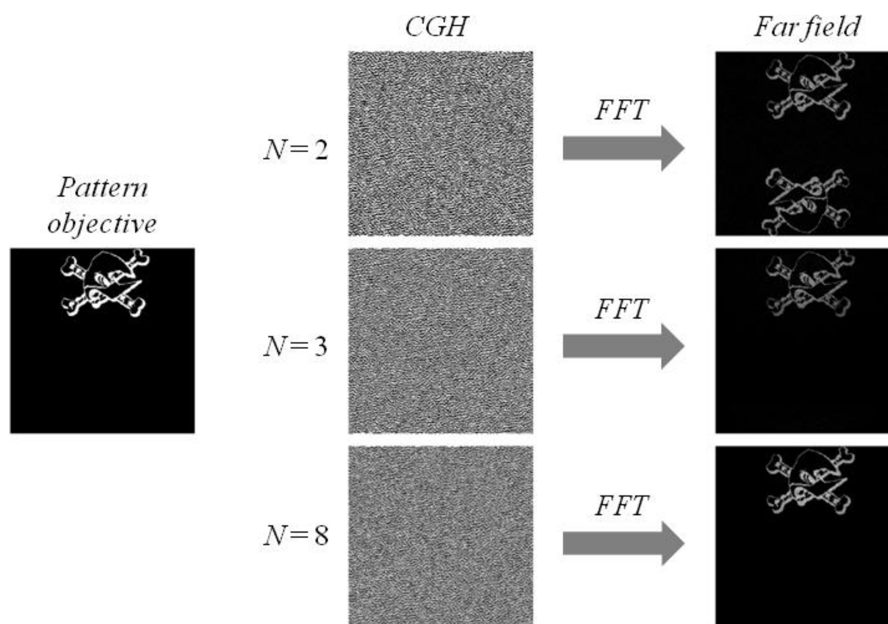

Figure 2.5: CHG reconstruction with an off-axis objective pattern.

2.3.2 Rayleigh-Sommerfeld Propagator

Helmholtz's wave equation, eq. (2.7), is the major foundation of scalar theory, and gives the Helmholtz-Kirchhoff integral theorem. The Rayleigh-Sommerfeld diffraction formulation for monochromatic waves follows, and it is very useful for scalar propagation analysis. The expression leads to more exact solutions than Fresnel and Fraunhofer approach, but usually it is very difficult to solve analytically.

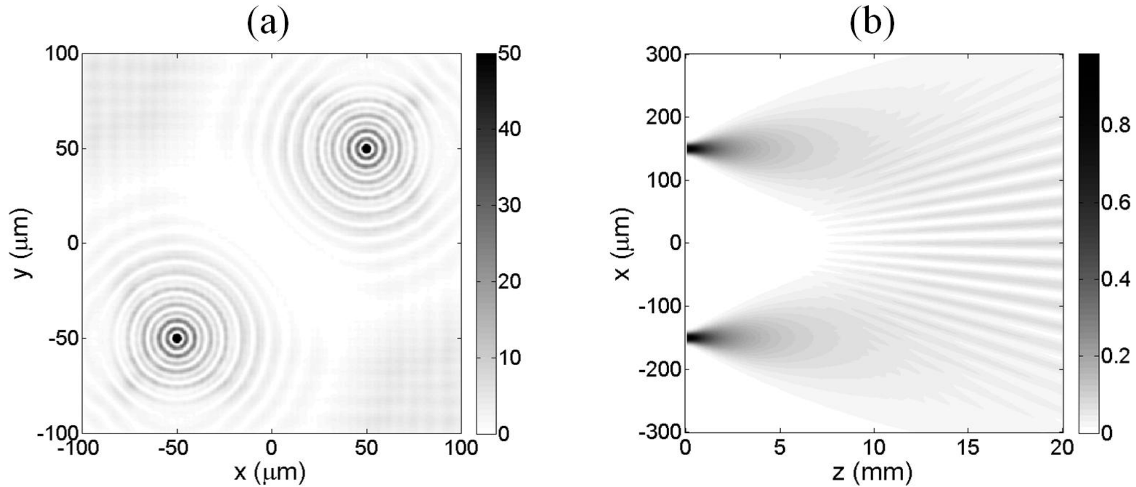

Figure 2.6: examples of propagation by means of RS approach; a) two refractive axicons illuminated by a plane wave with , $\lambda = 500\ nm$, at 750 μm from the aperture plane; b) propagation of a plane wave, $\lambda = 500\ nm$ diffracted by two gratings with a width of 15 μm and separated 300 μm .

The numerical solution of the Rayleigh-Sommerfeld formula using a Fast-Fourier transform based direct integration algorithm has been performed [48]. In Figure 2.6 it is shown an example of propagation using this Rayleigh-Sommerfeld numerical approach (RS), where the aperture plane has the form of two axicons width $200\ \mu m$ of diameter, refractive index $n = 1.5$ and $12\ \mu m$ of height. The field diffracted by this mask has been propagated at a distance of $750\ \mu m$ from the mask in vacuum.

The process can be iterated in steps along z -axis. Thus, a three-dimensional propagation in vacuum can be calculated by means of RS. For example, in Figure 2.6b a propagation of a diffracted field by a double gratings system is shown. Some boundary effects due the computational window appear along the propagation. Besides, the number of points in which is pixelated the field is critical and it can give a wrong result. The algorithm, gives a quality factor expressing the accuracy of the calculus.

2.3.3 Beam Propagation Method

The Beam Propagation Method (BPM) is a split-step method in which an input field is propagated under scalar approach in alternating steps through a defined map of refractive index [49]. Originally, it was proposed for the simulation of waveguides with variable refractive index [50], but it is also successfully used for the simulation of gratings [51], liquid crystal devices [52] and, in general, photonics devices with complex analytical description [53]. Thus, the algorithm transports the optical field within one propagation step from a

transverse plane at the longitudinal coordinate z to a transverse plane at $z+\Delta z$, taking into account the variation in the refractive index between both planes.

The method is summarized in Figure 2.7. Firstly, the input field is transformed into its angular spectrum. A propagation of the angular spectrum is performed using the Fourier transform up to $z+\Delta z$. Using the inverse Fourier transform the field returns to the position space, and the phase portrait is corrected according to the refractive index step. This output field works as input field for the next step iteration. It is necessary to assume that the diffraction effects and the inhomogeneities effects can be treated independent of each other.

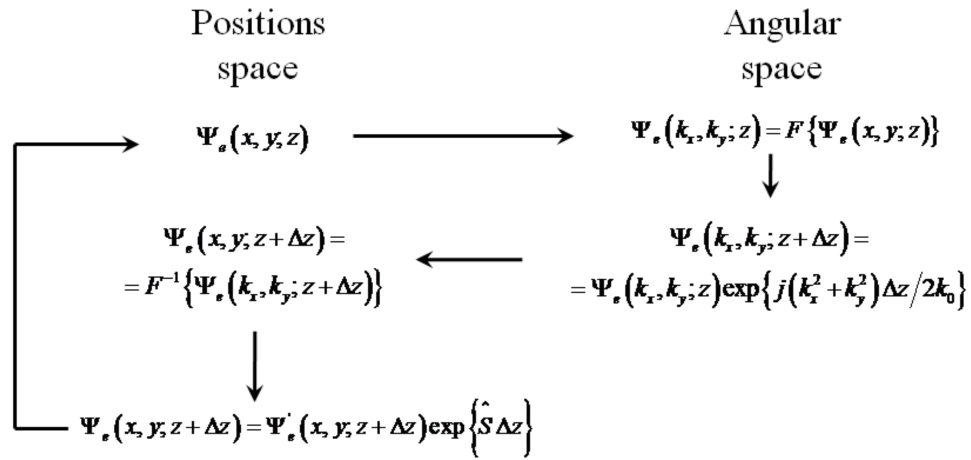

Figure 2.7: Propagation scheme of BPM, with $\hat{S}=i\Delta nk_0$ *and* FT *and* FT^{-1} *are the direct and inverse Fourier transform.*

Thus, the propagation of an optical beam in an inhomogeneous medium is replaced by a sequence of free space propagation steps and phase corrections. For a good resolution, the step size in the z direction should be smaller when the refractive index is abrupt.

In the numerical performance of this method, Berenguer's Perfectly Matched Layers (PML) are normally used to avoid reflections at the border of the computation window [53]-[56]. This method consists of adding additional layers to the computation window, with a refractive index calculated in order to result locally transparent to the electric field in this region. Then, the field at the boundary leaves the computational window. Instead, we prefer to use a super-Gaussian absorbing profile avoiding the amplitude at the borders and, consequently, avoiding the spurious boundaries reflections, as is schematized in Figure 2.8.

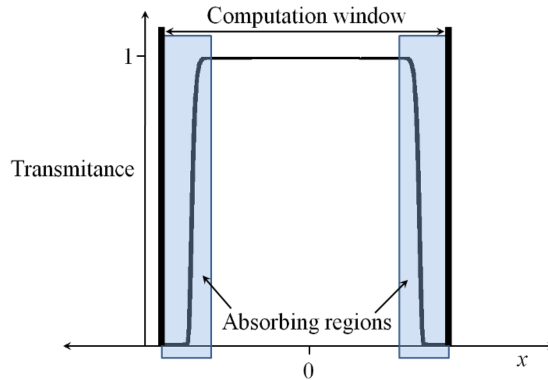

Figure 2.8: Supergaussian filter profile.

When the last iteration of the algorithm ends, we obtain the field and the phase (and consequently the intensity of the field) of the propagation for each plane along z -axis. In Figure 2.9 we show an example of the BPM working. A Gaussian beam with $\omega_0 = 80\,\mu\text{m}$ impinges on a micro-refractive sphere with $n = 1.5$ and a radius of $r = 40\,\mu\text{m}$ placed at $75\,\mu\text{m}$ of the origin in the z -axis. The field is the absolute value of the complex field, and the phase is the argument of the complex field. The intensity has been calculated performing the square of the complex field for each position.

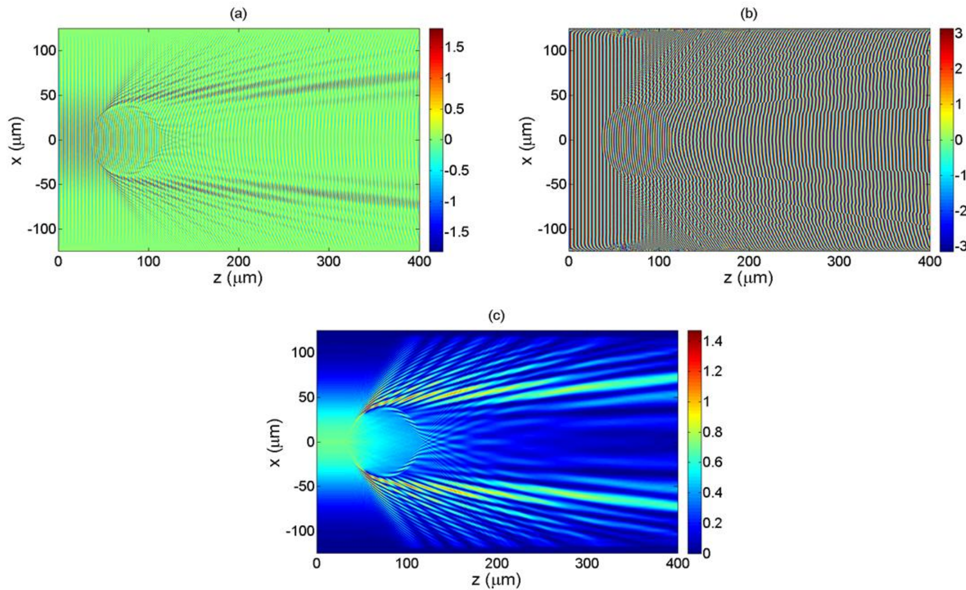

Figure 2.9: Example of BPM simulation. A Gaussian beam impinges on a micro-refractive sphere; a) amplitude, b) phase, and c) intensity of the propagation.

BPM is specially indicated for the simulation of volumetric devices. In this sense, the algorithm is developed to work in 2D or 3D configuration. In Figure 2.10 it is shown an example of 3D-BPM propagation with a double grating system.

This algorithm has been entirely developed during the realization of this work, due the capability to propagate light through complex structures. It is remarkable to notice that the BPM needs to generate the whole map of propagation before the beginning of the iteration. Therefore, when a high number of pixels is needed, (depending on the resolution and the extension of the computation window) the memory of the computer can overflow. For this reason, in the cases of propagation through vacuum, it is possible to combine BPM with RS minimizing the number of pixels needed.

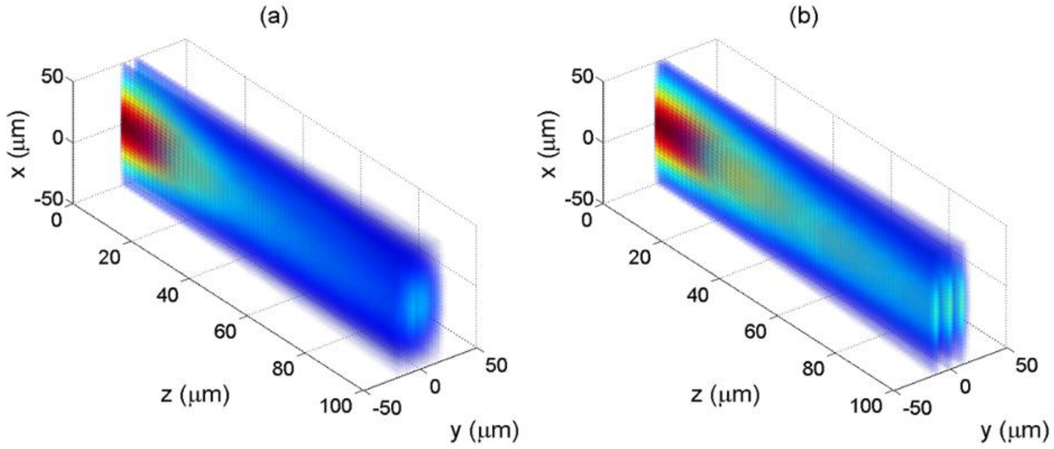

Figure 2.10: 3D-BPM simulation of a double slit system illuminated by a Gaussian beam with w_0 *=50* μm *and* $\lambda = 0.5$ μm *impinging on two slits (width=* 2 μm *) a)separated* 10 μm *and b) separated* 5 μm *.*

2.4 *Algorithms for the design of DOEs*

In microoptics design, the basic problem is to find a microstructured relief that produces a determined intensity pattern at a determined distance from the device. There exist several methods for the design of diffractive elements [1], [15], [57]. When possible, it is preferably to find an analytical solution. Nevertheless, the resolution of eq. (2.19) or eq. (2.22) is not always possible.

We centre here in Iterative Optimization Algorithms. The goal of these methods is to look for the best possible solution to a complex problem, according to a set of criteria. These criteria are expressed as mathematical functions, the so-called objective functions. The optimal solution is expressed as the minimum of a cost function. Iterative optimization algorithms evaluate different solutions to a problem during iteration, looking for a minimum in the cost function. Usually, iterative algorithms get stuck in a local minimum (that is not

necessarily a global minimum). Therefore, it is important to allow the algorithm to get out from the local minima that are not acceptable solutions.

We summarize here some optimization algorithms developed during the realization of this work. One of them is specifically designed for the optimization of DOEs (Iterative Fourier Transform Algorithm). The rest of them are Global Optimization Algorithms, used extensively used in engineering and applied mathematics.

2.4.1 Iterative Fourier Transform Algorithm (IFTA)

The classical Iterative Fourier Transform Algorithm was first proposed in the 70s [58], [59] based in the Gerchberg-Saxton Algorithm (GSA) [60] for e-beam microscopy phase retrieval in the far field. Figure 2.11 shows the working scheme of this algorithm.

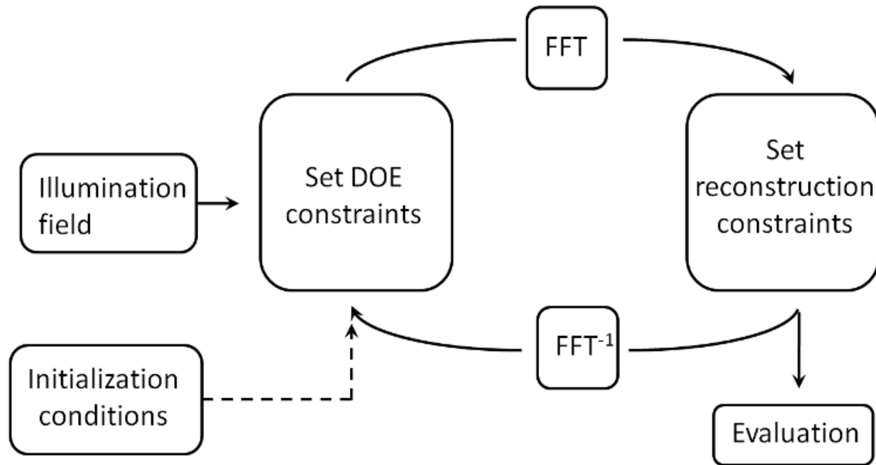

Figure 2.11: The classical Gerchberg-Saxton iterative optimization algorithm scheme.

IFTA evaluates a DOE distribution in the far field. Then, it changes the obtained field by the desired field, and turn back to the DOE plane by means of an inverse propagation. The obtained DOE is again propagated, and the algorithm iterates until it reaches the stop criterion.

Actually, IFTA can be evaluated in the far field or in the near field, substituting the Fraunhofer propagator in the scheme of Figure 2.11 by the Fresnel propagator. Several improvements have been proposed. The most known improvements were proposed by Wyroswki attending to the quantization process and band-width limitations [61]-[63]. Another improvement is the use of a secondary parameter, adjusting the amplitude or the phase of the desired pattern during the iteration [64]-[66].

As it can be appreciated in Figure 2.12, the optimum solution is reached with less than 20 iterations (requiring about a minute of computation). Then, the algorithm do not improves the result. This behavior (the stagnation of the fitness value during the algorithm) is common for the optimization algorithms.

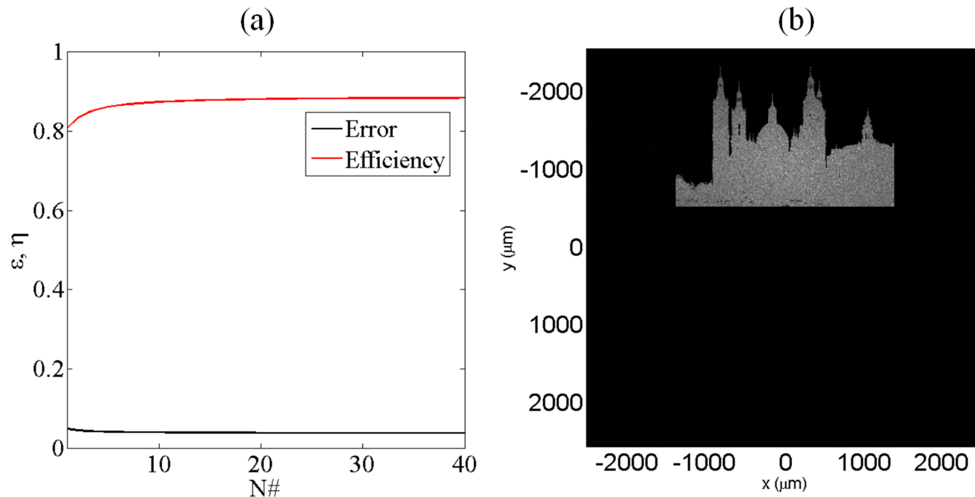

Figure 2.12: Example of IFTA, a) error and efficiency reached for each iteration; b) optimized propagation.

2.4.2 Iterative Global Optimization Algorithms

Besides IFTA, that has been developed for micro-optical purposes only, there exist several Global Optimization Algorithm (GOA), used in various fields of engineering for the search and optimization of complex functions with a high amount of variables. The function minimized is called cost or merit function. Some interesting cost functions used in micro-optical devices design are defined in Appendix B. All the algorithms explained here have been performed using the Optimization Toolbox from Matlab, by MathWorks [67].

When the cost function is a monotonous function, finding the global minimum is trivial. On the contrary, when the function has several local minima, it results difficult to determine when an optimal value is in fact the global minimum. Therefore, it is important to allow the algorithm, to get out from local minimum.

Moreover, when the number of variables is high, the problem becomes still more complicated. When these algorithms are applied to the design of DOEs, it is usual to consider each pixel of the aperture plane as variable. Then, the design of a 64×64 CGH has a 4096-dimension solution space.

The first GSA that we will treat here, Genetic Algorithms (GA), are part of a set of optimization techniques inspired by evolutionary strategies known as evolutionary algorithms. GA uses a certain number of variables (for example, the amplitude and phase of

each pixel of a diffracting mask) concatenated forming a “chromosome”. A set of chromosomes define the “population”, equivalent to individuals in a species competing for the minimum value of the evaluation function. The optimization is performed on a population of estimates in parallel, in an “environment” that favors better merit functions. The chromosomes are then arranged depending on their cost function evaluation. The individuals with low cost function values, in general, are rejected. On the contrary, better-performed individuals have a higher probability of passing their attributes. The next generation is formed with the best individuals, and also recombining some of the best individuals. Random mutations on the chromosomes produce new attributes that can improve the performing of the population and maintaining some degree of diversity in the population. After some iteration, the algorithm converges to an optimum.

Another performed algorithm is the Pattern Search Algorithm (PS). This algorithm is linear, in the sense that, when it evaluates a change in one variable of the original population, when the change decreases the evaluation function the change is accepted, otherwise is rejected. When all the variables have been changed and evaluated, another loop is performed. The magnitude of the variation in each variable changes for each iteration, avoiding to prevent local minimum.

The metal cooling processes inspire Simulated Annealing (SA). Slow cooling processes ensure a highly ordered crystal structure, resulting in a stronger material. On the contrary, rapid cooling produces irregular and fragile structures. The ground stems on the melting processes nature: when the metal is fluid, the molecules are randomly oriented. If the metal freezes slowly, the molecules orient themselves as crystal structures. On the contrary, if the metal freezes quickly, a degree of disorder remains. In the optimization algorithm, the variables define the “orientation” of the molecules. The degree of “order” between the molecules defines the merit function. The algorithm changes the variables during iteration. The changes improving the merit function value are accepted. Some of the changes that increase the merit function value are also accepted, with the intention of prevent local minima. As the algorithm iterates, the probability of accepting non-improving changes decreases (corresponding to a cooling process). At the end of the algorithm, a minimum should be reached.

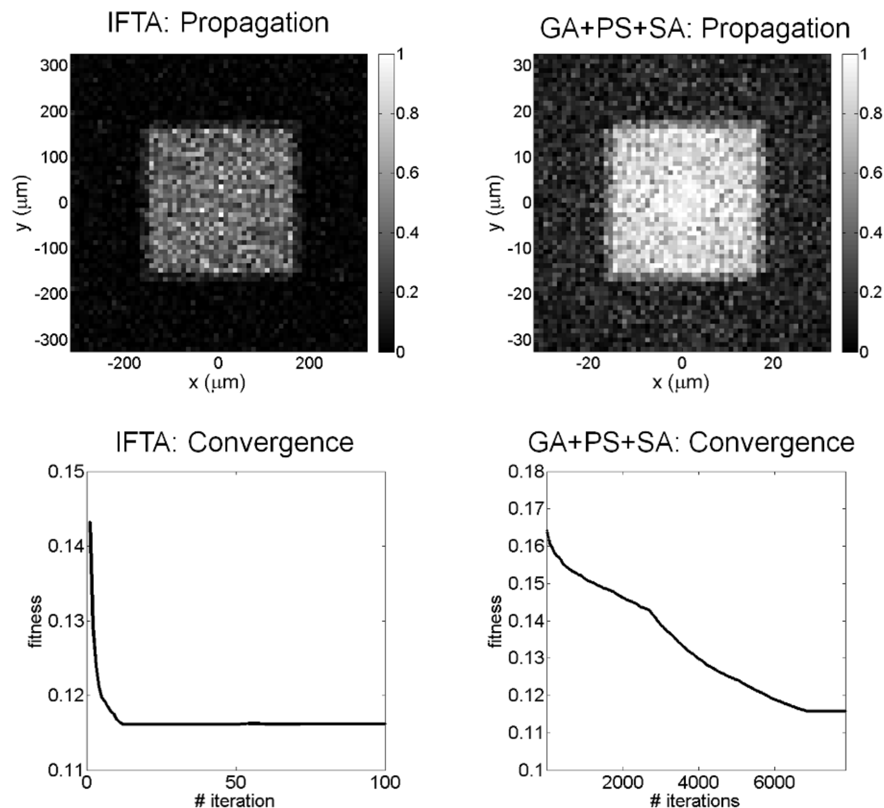

Figure 2.13: DOE optimization by means of IFTA and Global Optimization Algorithm. The target is a square with 64x64 pixels.

In Figure 2.13 it is shown a comparison between an optimization carried out by IFTA and a DOE generated using the Global Search Algorithms. The order used was first a GA optimization, the final result was used to seed a PS optimization, and, finally, a SA optimization ends the process. It is remarkable that IFTA needed less than 20 iterations to reach the best fitness value. It takes only about one minute to develop 100 iterations. On the contrary, the Global Search Algorithms needed more than 6000 iterations to reach a similar value, consuming more than 4 hours in the process. Moreover, the Global Optimization Algorithms are more sensitive to an increment in the number of pixels of the target mask. In this sense, IFTA is considered as better algorithm for the design of DOEs.

Nevertheless, Global Optimization Algorithms can be used for other tasks regarding to microoptical design. For example, we propose the design of a volumetric device, consisting on stacked gratings embedded in bulk fused silica. This kind of device, as it will be shown in the next sections, can be manufactured at our laboratory. We try to shape the far field intensity produced by this device. The design of such a volumetric device is quite complicated with the common tools. As variables for the optimization, we consider the

relative location of each grating, and their periods. Thus, using N gratings, the problem has $2N$ design variables.

We divide the propagation in two steps: firstly, the illumination field is propagated through the bulk device (containing the stacked gratings) by means of BPM. Finally, the last plane of the propagation is carried up to the far field by means of FFT. The scheme of the problem is shown in Figure 2.14.

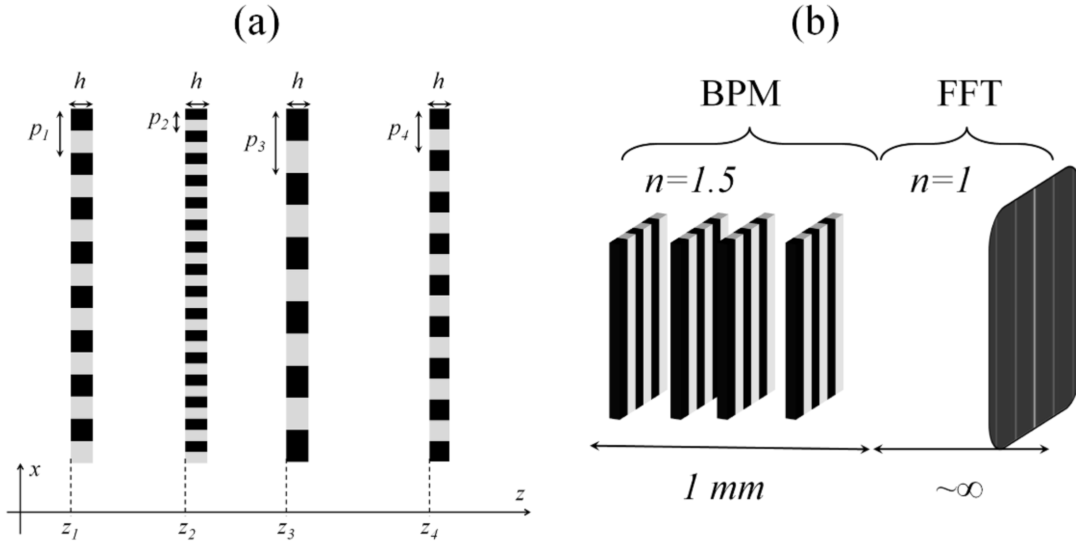

Figure 2.14: Scheme of the problem, with 4 gratings in stack embedded in bulk fused silica, a) variables for the optimization, b) scheme of propagation.

As target, we look for the configuration that maximize the intensity of the I_{-3}, I_{-2}, I_{-1}, I_1, I_2 and I_3, where I_n are the intensity of the n-th diffraction order. Using GOA, we can perform an optimization in the same order as previously: first GA, then PS and lastly SA. The period of each grating can take any value between $20\ \mu\text{m}$ and $80\ \mu\text{m}$. The distance between gratings can be $20\ \mu\text{m}$ as minimum and $500\ \mu\text{m}$ as maximum value. All the gratings have a height of $h = 20\ \mu\text{m}$ and a fill factor of 50%.

The result of the optimization is shown in Figure 2.15. The period of the gratings are $p_1 = 78\ \mu\text{m}$, $p_2 = 48\ \mu\text{m}$, $p_3 = 20\ \mu\text{m}$ and $p_4 = 47\ \mu\text{m}$, and they are located at $z_1 = 50\ \mu\text{m}$, $z_2 = 507\ \mu\text{m}$, $z_3 = 954\ \mu\text{m}$ and $z_4 = 974\ \mu\text{m}$.

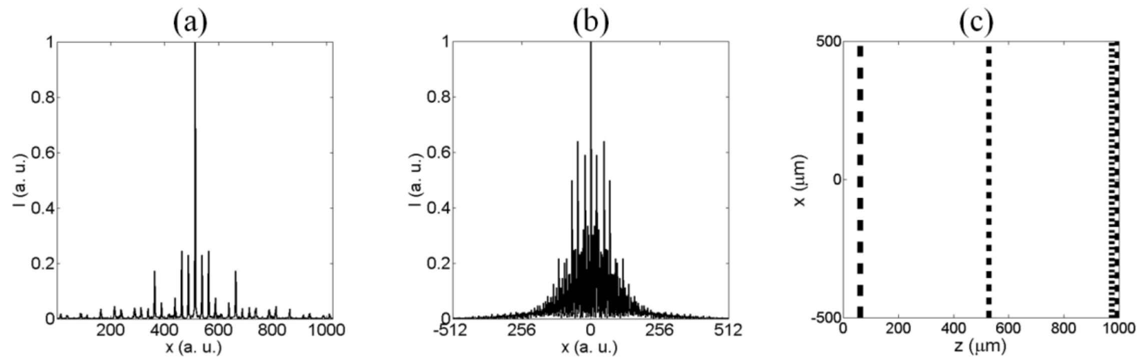

Figure 2.15:a) Diffracted field in the far field of an embedded grating with $p = 40\ \mu m$*; b) diffracted field in the far field of the optimized system with 4 gratings embedded in fused silica, and c) optimized system configuration. Red areas correspond to fused silica (*$n = 1.5$*) and blue areas correspond to absorbing zones.*

3 Micromachining with nanosecond pulsed laser

In this chapter some important facts related to laser ablation processes are presented. The main operation principles of pulsed lasers and the effect of focalized light pulses over the matter are also introduced. Following, a laser ablation system is shown, explained all the components and configurations. A complete characterization is developed, showing the proper operation parameter. Some examples of sample manufacturing are presented. In concrete, we show the effects of ablation with steel (a metal), fused silica (a transparent dielectric) and silica (a crystalline solid).

3.1 *Introduction*

A laser (Light Amplification by Stimulated Emission of Radiation) is a light source with very singular properties, as for example,

- Light is usually emitted with a well-defined propagation direction, without much divergence. The electric field at different locations across a beam profile oscillates coherently, remaining the relationship between phase planes over a relatively large distance (spatial coherence). This coherence is, in fact, the reason because of that the beam can propagates with low divergence, and allows a highly collimated laser beam.
- Besides the spatial coherence, laser light usually presents an elevated temporal coherence. Phase relationship between consecutive wavefronts remains during relatively large time intervals, in terms of light oscillations periods.
- The large temporal coherence causes a very narrow spectral bandwidth (in the special cases of ultra-short pulses, a large optical bandwidth is possible although a high degree of coherence). Laser can be considered as monochromatic light source.
- The emitted light is, in most cases, linearly polarized.

Light is not always emitted in continuous mode, but it may be delivered in the form of pulses. In such a case, it is possible to confine the output intensity in a sharp temporal interval, reaching extremely high peak powers when the pulse duration is far below the temporal distance of the pulses.

Since its versatility and the wide range of working configurations, lasers are key components in industrial environments. They are firmly entrenched, for example, in fields as manufacturing (in a variety of applications such as drilling, cutting, marking, micromachining, lithography, or surfaces treatments), medical applications (eye and dentistry treatments, bloodless surgery, skin treatments), scientific research (spectroscopy, interferometry, fluorescence microscopy, optical trapping), metrology (non-contact measurements), data storage (reading and writing optical disks) or communications [68].

In the particular case of fabrication, lasers normally presents high optical intensities, confined in a small area (in other words, strongly focalized) in order to reach a very high heating in a

very short time interval, allowing the material vaporization and the generation of plasma. Pulsed lasers are the best choice for these requirements.

The characterization of the optical pulses and regular optical pulse trains is based on various respects: the pulses repetition rate, the pulse duration or pulse length, the pulse energy, the peak power, the length pulse and the spatial and spectral shape of the pulse. There are methods for the complete characterization of the pulses, both in the temporal domain [69], [70], [71] as in the spatial domain [72].

Currently, and depending on the circumstances, different lasers can be used for manufacturing. In most of cases, they shall satisfy the following requirements:

- It is necessary to reach the intensity threshold for the desired process (ablation, marking, engraving...). The intensity is related to peak power and beam width.
- Repetition rate is important to optimize the process duration. Sometimes this repetition rate dramatically affects to peak power.

Although there are actually different definitions of a pulse length (τ), the most frequently used is based on the full width at half maximum (FWHM) of the optical power versus time. Usually these pulse length fall between 10^{-3} s and 10^{-15} s. It is common to use the prefixes of the International System of Units collected in Table 3.1.

Prefix	*Equivalence*
1 ms *(milisecond)*	10^{-3} s
1 μs *(microsecond)*	10^{-6} s
1 ns *(nanosecond)*	10^{-9} s
1 ps *(picosecond)*	10^{-12} s
1 fs *(femtosecond)*	10^{-15} s
1 as *(attosecond)*	10^{-18} s

Table 3.1: International System prefixes for time measurement.

The different pulses generation techniques produce pulses in a wide range. By modulating directly a light source it is possible to obtain pulses length from tens of picoseconds to arbitrary high values. By gain switching in diode lasers, pulses lengths can reach up to few nanoseconds. By Q factor switching (Q-switching) pulse lengths fare typically in the nanosecond range (corresponding to several cavity round trips). With Mode-Locked lasers,

pulses with typical durations between 30 fs and 100 ps can be achieved. The shortest pulses (around 100 attoseconds) have been obtained using High Harmonic Generation [68].

As a general rule, when the pulse length is bellow tens of picoseconds, the pulses are called "ultra-short pulses". The threshold of this definition is based, usually, in the threshold of thermal processes that take place during light-matter interactions.

For some applications, CO_2 lasers are suitable when their high working wavelength and high averaged intensity are needed. On the other hand, fiber lasers present a high flexibility in terms of repetition rate but, usually the power is not too elevated and the pulse duration is quiet long for material processing. Vanadate lasers combine a good repetition rate with relatively short pulses (in comparison with fiber lasers), producing high peak power.

3.2 *Q-switched lasers*

A laser comprises, basically, an optical resonator (laser cavity) and within this resonator a gain medium, which serves to amplify the light. The gain medium, by means of some external supply of energy -"pumping"-, amplifies the circulating light. However, the circulating light also experiences some losses (e.g., upon reflection at mirrors). A laser cannot operate when the gain is smaller than the resonator losses (laser threshold). A very important factor for the characterization of a laser is the Q-factor (quality factor), which is a measure of the power losses per round trip. For a determined frequency ν_0, Q-factor is defined as [73],

$$Q = \frac{2\pi\nu_0 E_{stored}}{E_{loss}}, \tag{3.1}$$

where E_{stored} is the mean energy stored by the cavity, and E_{loss} represents the losses of the cavity.

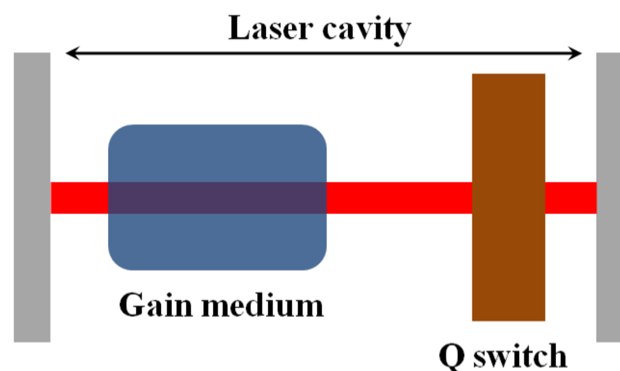

Figure 3.1: Sketch of a Q-switched laser.

The modulation of the Q-factor [74], is a useful method to obtain pulsed beams. In general terms, the process can be summarized as follows [68]. Initially, the cavity losses are kept at a high level, preventing the laser emission. The energy fed into the gain medium by pumping accumulates there. The amount of stored energy is limited by spontaneous emission. At a determined time, the losses are suddenly reduced to a small value, so that the power of the laser radiation builds up very quickly in the laser resonator. Once the intracavity power has reached the order of the saturation energy of the gain medium, the gains reach the saturation level. The maximum peak of the emitted pulse takes place when the gain equals the remain (low) resonator losses. Further depletion of the stored energy during the time where the power decays is due to the large intracavity power present at that time. Usually the energy extracted after the pulse maximum is similar to that before the pulse maximum.

The pulse duration achieved with Q-switching is typically in the nanosecond range (corresponding to several cavity round trips), and the peak power can be orders of magnitude higher than the power which is achievable in continuous-wave operation. Usually Q-switching is repeated regularly, obtaining trains of pulses. Typically the pulse repetition rate is in the range from 1 to 100 KHz.

The modulation of the cavity losses can be active or passive. For the first case, acousto-optic or electro-optic modulators (but also mechanical devices) are commonly used. For passive modulation, the losses are automatically modulated with a saturable absorber. The pulse is formed when the stored energy reach the saturation level of the saturable absorber. Repetition rate results then difficult to modulate. In general, the duration of the pulses increases with the repetition rate.

3.3 *Laser Ablation*

One of the best-known examples of the interaction between light and matter is the photoelectric effect, predicted by Einstein in 1905 [75] and experimentally demonstrated by Millikan [76]. According to this effect, an electron is ejected from an atom when a photon with energy $\hbar\omega$ (where $\hbar = 1.05\times10^{-34}\ \mathrm{J\cdot s}$ is the reduced Planck's constant, and ω is the light frequency) reaches the potential barrier I_p level in the vicinity of an ion, $\hbar\omega = I_p$. Usually this energy is in the range of KeV, corresponding to X-ray radiation. For electrons

in outer shells of most atoms, I_p is around few electron-volts, corresponding to UV photons.

The most common lasers work between $0.25\ \mu m$ and $13.4\ \mu m$. The energy of the photons in this region is much lower than I_p and one cannot observe the photoelectric effect. However, when the laser is able to produce a high quantity of energy it becomes possible to consider multiphoton ionization [77], when the expression $n\hbar\omega = I_p$ is satisfied. Thus, instead of absorbing just one photon (but a very energetic photon), an electron absorbs n photons of moderate energy (typically in the range of eV), making possible its ejection. Therefore, when a high energetic laser beam is focalized on a material (or in bulk, if possible), it generates free electrons moving through an intense radiation. A wide phenomenology appears during the process. The kinetics and dynamics of this conversion depend critically on several aspects such as the mechanism of light absorption, electron-lattice interaction characteristic of the sample and surface defects.

The term "laser ablation" is used generically to describe the explosive laser-material interaction [31], involving several processes, such as coupling of optical energy into a solid resulting in vaporization; ejection of atoms, ions, molecular species and fragments; shock waves; plasma initiation and expansion; and a hybrid of these and other processes. Many models have been developed to describe these processes [78], but each pertains only to a separate component of the interaction and is applicable only under limited conditions. There are no models that completely describe explosive laser ablation processes. Laser irradiance (power density) and the thermo-optical properties of the material are critical processes. Two general descriptions for the laser-material interaction are described on the basis of irradiance: vaporization and ablation.

When the laser pulse duration is microseconds or longer and the irradiance is high, vaporization is the dominant process during light-material interaction. Phonon relaxation rates are on the order of 0.1 ps, and absorbed optical energy is rapidly converted into heat. Heat dissipation and vaporization are fast in comparison to the laser pulse duration. The thermal and optical properties of the sample influence the amount of material removed during the laser pulse. The absorption and reflection determine both the fraction of the incident power that is absorbed and the depth of optical absorption within the sample. Different heating and cooling rates are expected when the depth of absorption is approximately the thermal diffusion length in the material. Although this interaction is

defined as vaporization, the energy is delivered in a very short time and localized in a small area. Thermodynamic models do not completely describe the interaction. Moreover, the optical and thermal properties of the material vary during the laser pulse, which makes it difficult to predict accurately the amount of energy coupled to the target and the quantity of mass removed. However, the interaction is predominantly thermal. Melting is common and fractional vaporization is possible.

At a high irradiance, and with nanosecond and shorter laser pulses focused onto any material, an explosion occurs. The term "laser ablation" has been adopted to describe this interaction. From a physical point of view, the surface temperature is instantaneously heated reaching its vaporization temperature by means of one-photon absorption, multi-photon absorption and additional undefined mechanisms [79].

The vaporization temperature of the surface is exceeded within a fraction of the laser pulse duration. Before the surface layer vaporizes, underlying material will reach its vaporization temperature. Temperature and pressure of the underlying material are raised beyond their critical values, causing the surface to explode. This explosive interaction has been described as "non-thermal", and melting is often not observed around the crater. Energy developed in vaporization of the material grows with the duration of the interaction (in other words, with de pulse duration). When the pulse duration is short enough, it is possible to avoid vaporization (and thermal) effects. However, during an ablative interaction, a plasma is initiated at the sample. Plasma temperatures are in excess of 10^4 K, and radiative heat transport can establish a plasma-material interaction. The plasma duration is microseconds, which is long in comparison to the short laser pulse. Fractional vaporization may occur during this plasma-material interaction, over a greater region than in the case of the direct laser vaporization interaction.

3.4 *Laser Ablation in metals*

In order to obtain a more detailed description of the process of Laser Ablation, we study in this section the interaction of high energetic beams with metallic surfaces. This case will allow us to describe later our laser ablation system.

3.4.1 Metal Optics

We make use of Drude's model of electron conduction [80] in order to understand the interaction between laser radiation and metallic solids. This model is based on the assumption that the atoms in a metal, in some way, share a limited number of valence electrons, appearing a conduction band. The electrons forming this band can move away from their parents carrying current and heat during the process.

For an atomic element with mass density ρ and atomic weight A, the free electron density is given by [79]

$$n_e = \frac{N_A Z^* \rho}{A}, \tag{3.2}$$

being N_A is Avogadro's number and Z^* the number of valence electrons per atom.

On the other hand, the conductivity of a metal depends on the probability of the electrons to collide with the ions and, therefore, decrease their velocity. This idea can be expressed as

$$\sigma_e = \frac{n_e e^2 \tau}{m_e}, \tag{3.3}$$

where e and m_e are the charge and the mass of the electron, respectively, and τ is known as the collision or relaxation time, which depends on several aspects as the atomic structure and electronic configuration. This conductivity can be experimentally obtained using Ohm's law, $j = \sigma_e E$. For optical purposes, this expression can be expressed as

$$\sigma(\omega) = \frac{\sigma_e}{1 - i\omega\tau}. \tag{3.4}$$

where ω is, again, the light frequency. Combining with Maxwell's equations, it is possible to define a complex dielectric constant as

$$\varepsilon = 1 - \frac{\omega_p^2}{\omega(\omega + i\nu)}, \tag{3.5}$$

where $\nu = \tau^{-1}$ is the collision or relaxation time of the valence electrons, and

$$\omega_p^2 = \frac{4\pi n_e e^2}{m_e} \tag{3.6}$$

is the plasma frequency of the valence electrons. This expression predicts that a metal will be transparent only for wavelengths $\lambda < \lambda_p = 2\pi c/\omega_p$, that use to be in the UV range

($200-400$ nm). Radiation with longer wavelength (like standard lasers) will be absorbed or reflected depending on τ.

Therefore, when a laser beam with $\lambda < \lambda_p$ impinges a metallic object, will be initially reflected, acting the metallic object like a mirror. The kind of predominating interaction between radiation, plasma and metallic surface will depend mainly on the laser intensity and the interaction time duration.

3.4.2 Pulsed beams interaction

It is now clear that when a laser beam impinges a metallic sample, a fraction of the light will be absorbed and the rest of the light will be reflected. Due to ionization, plasma will appear surrounding the impact zone. This plasma, moreover, will affect to the radiation over the sample. We will assume, at a first stage, that absorption of laser energy will involve, inevitably, a heating in the sample. On the other hand, the ratio at which the radiation energy is transformed into thermal energy depends on the temperature of the plasma. Thus, heating and absorption are strongly related each other and should be treated accordingly in a self-consistent way.

Let us suppose a light pulse impinging on a metal. A calorific wave will propagate into the sample. When the duration of the pulse is large in comparison with the thermal conductivity of the material, we can assume a continuous heat source. The equation that rules the energy transport under these circumstances is

$$\frac{\partial \varepsilon}{\partial t} + \nabla \cdot \left(q + \Phi_a \right) = 0, \tag{3.7}$$

where ε is the energy density, q us the heat flow and $\Phi_a = \eta_a \Phi_L$ is the amount of absorbed laser flux (with an absorption coefficient η_a). After some femtoseconds a heat transport will appear, from the light incidence zone (heat source) to the cool zones [79]. If the pulse duration is in the range of femtosecond, the excess of heat will be evacuated. Under this circumstances, there will be material ejected by ionization (ablation processes) but thermal effects (melting material) will be minimized. On the contrary, for longer pulses, thermal effects become more important in comparison with pure ablative effects.

From a heuristic point of view, we can summarize the process as follows. On a first stage, when a “long pulse” (a long-duration pulse, in comparison with the typical heat evacuation times) impinges over a solid surface (we will suppose, at the moment, a metallic surface), a

plasma will appear, consisting on high energized electrons ejected by multiphoton ionization. The amount of light absorbed by the material will cause a fast heating in the self material. Some ions will be able to change its phase end be ejected from the sample (ablation or vaporization). If the energy contribution remains, there will be areas surrounding the volatilized zones where the material has been changed to a liquid phase (melting). When the contribution of light ends, the temperature decrease quickly, propagating along the sample. Some part of the ejected material can fall down to the sample, appearing droplets and zones with debris in the area. At the same time, the zones under thermal processes in a liquid state, when cool down returning to a solid state, will take the form due the pressure equilibrium between thermal waves and radiative pressure. Summarizing, there will appear three different zones, schematized in Figure 3.2: the central zone, coinciding with the illumination point, where the material have been volatilized; the nearest surrounding zones, with melted material, and the rest of the surfaces where no changes can be appreciate, but maybe droplets and debris.

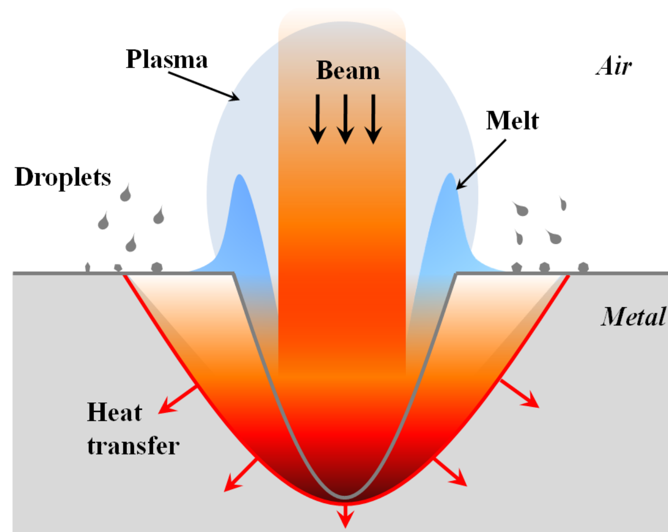

Figure 3.2: Scheme of the processes involved during Laser Ablation over a metallic surface.

3.5 *Laser Ablation System*

For the experimental work of this thesis we have used a Laser Ablation System. The main component of this system is a NAVIGATOR I solid-state laser head from Spectra-Physics, model J40-X15SC [81], with a $Nd{:}YVO_4$ (Vanadate) based amplifier medium. The cavity is pumped by a laser diode module with 808 nm infrared pump power. This output power of the pumping laser diode module is delivered to the laser head via fiber coupling. The power supply contains a RS232C interface for the control of the Q-switch cavity.

The Q-switching system allows pulses with duration around tens of nanosecond, and an adjustable repetition rate from 1 KHz to 100 KHz. The Vanadate based head provides laser emission in 1064 nm, with a maximum peak power around 10 W. Figure 3.3 shows the external view and physical dimensions of the system.

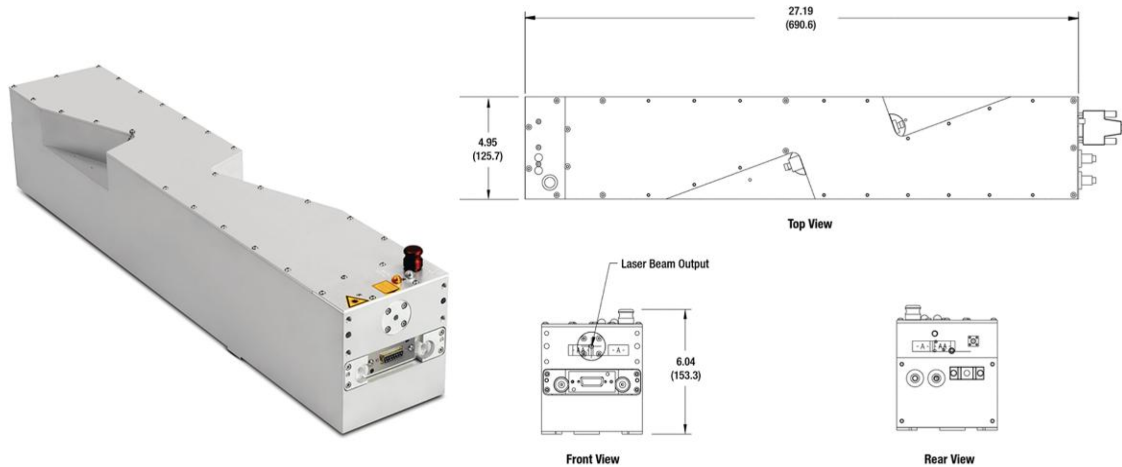

Figure 3.3: Navigator I Laser Head external aspect and dimensions given by the manufacturer.

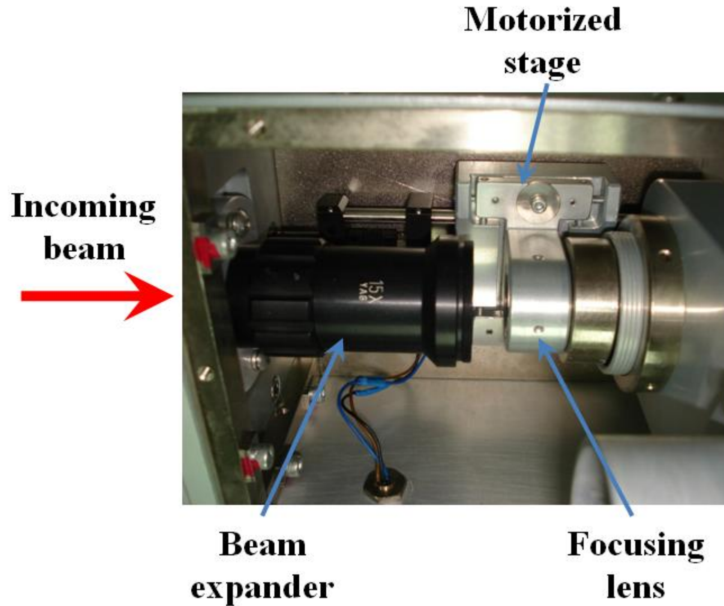

Figure 3.4: View of the optical focusing system.

We make also use of an optical focalization module designed for 1064 nm, shown in Figure 3.4. It consists of a 15× beam expander and a focusing lens with focal $f = 46$ mm mounted over a motorized stage. The beam expander enlarges and collimates the incoming beam, in order to obtain a bigger beam waist before the final focusing lens. Moving the focusing lens it is possible to change the location of the laser focus, which results very useful to engrave

over different samples. The optical focalization module has also an air-suction system, in order to remove the volatilized material from the ablation zone.

In order to work with a lower wavelength, it is possible to attach a Third Harmonic Gerenator (THG) providing $355\ \text{nm}$ pulses with maximum peak power of $2\ \text{W}$. The THG consist of a crystal able to absorb light at $1064\ \text{nm}$ and re-emit it at $355\ \text{nm}$ by non-linear processes. Another optical focusing module is available, with the optics adapted to work in $355\ \text{nm}$. A view of the system operating with the THG is shown in Figure 3.5.

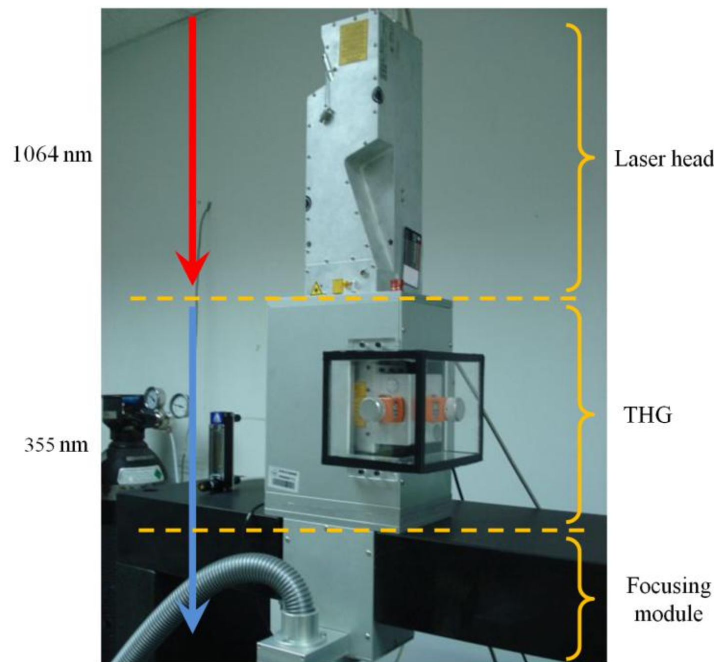

Figure 3.5: View of the laser system operating with the THG.

Finally, the laser system is mounted on an optical table isolated from external vibration. The mechanical stability is very important, since our aim is to engrave elements with features in the order of microns. The optical table is made of granite, in order to avoid the possibility of vibrations reaching a high inertial mass.

The samples are placed over a two-axis linear stages (model M-IMS300CCHA from Newport), able to travel along $300\ \text{mm}$ in each axis with a resolution of $0.1\ \mu\text{m}$. This motorized stage is also calibrated in order to avoid as much as possible the vibrations over the table. Figure 3.6 shows a global view of the complete Laser Ablation System.

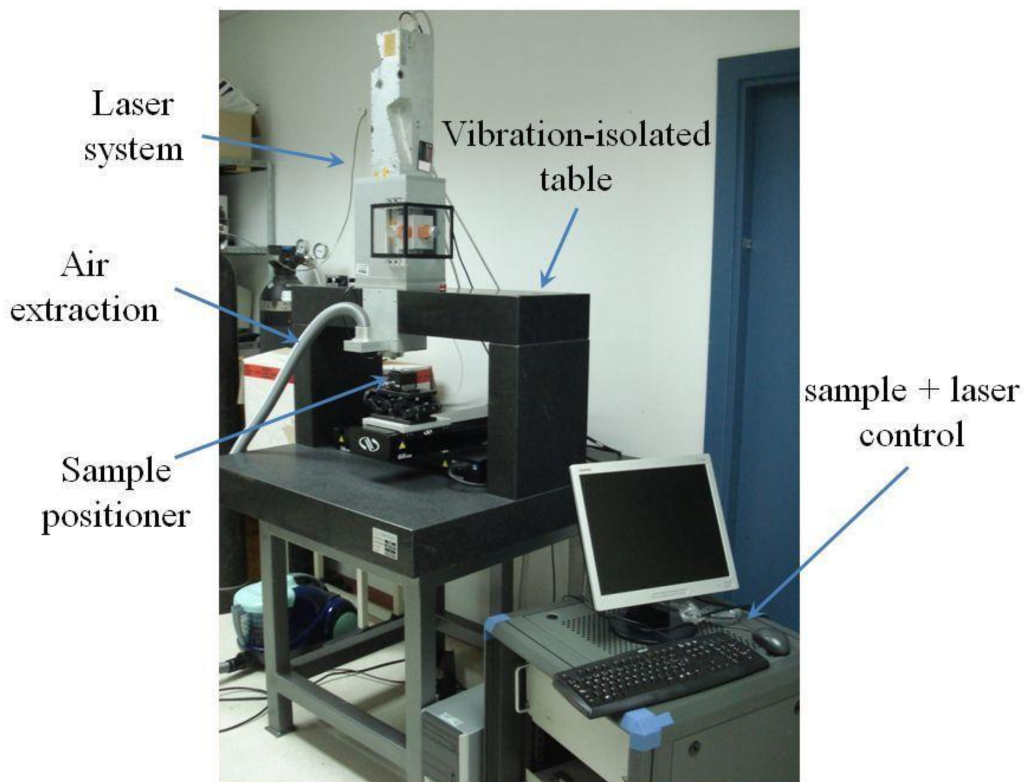

Figure 3.6: The Laser Ablation System, working with the THG.

When the laser is focalized on the sample, an amount of material is ejected depending on the energy of the laser beam and the duration of the interaction. If the sample moves, a trace of ablationed zones is engraved on the sample. In Figure 3.7 some example of the first attempts are shown. The target was to engrave parallel lines over a steel sample. As it is clear, some problems appear during the process. For example, some mechanical instabilities are present. To solve these problems, a new stage with a more robust design was implemented. Some other problems, related to the control method, are present. For example, if the velocity of the motors is not constant, the light dose on the sample varies along the path. Then, the width of the engraved lines is not constant.

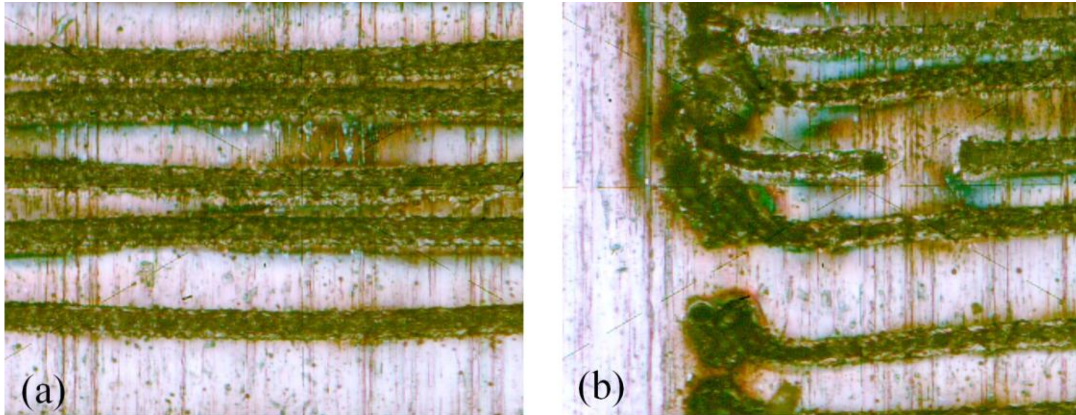

Figure 3.7: Example of the effect of the Laser Ablation System over steel samples ($20\times$ microscope images). Dark zones have been exposed to laser irradiation. We realize some significant defects: in (a) the lines are not parallel (due to mechanical instabilities), whereas in (b), besides mechanical instabilities, the effect of the acceleration of the motor is appreciable, in the form of a thick spot. Moreover, some control problems produces the switch-off of the laser during the process.

At the beginning of this work, the control of the system, combining the control of the linear motors and the laser head, was performed by means of a RS-232 port. The typical delays of this kind of ports produce an elevated incertitude of this method, making impossible to synchronize properly the location of the sample and the emission of light by the laser head. Moreover, it is necessary to perform a control method that allows engraving at constant velocity. We solved these problems by relegating the direct control of the laser to an external hardware (a Digital Signal Processor, DSP). It consist of a double-sided printed circuit board and some surface mount components (SMC), shown in Figure 3.8.

Figure 3.8: DSP board with surface mount components for the control of the laser system.

The design of the board was made by members of our research group, and was manufactured by Gold Phoenix Printed Circuit Board Co. Ltd. in China. This hardware also controls the motor of the focusing lens. The DSP is controlled from a computer by means of an USB port. The maximum velocity of this port is 3 Mb/s (mega-bits per second), enough for the control/monitoring of the system. Figure 3.9 shows a diagram of the control system.

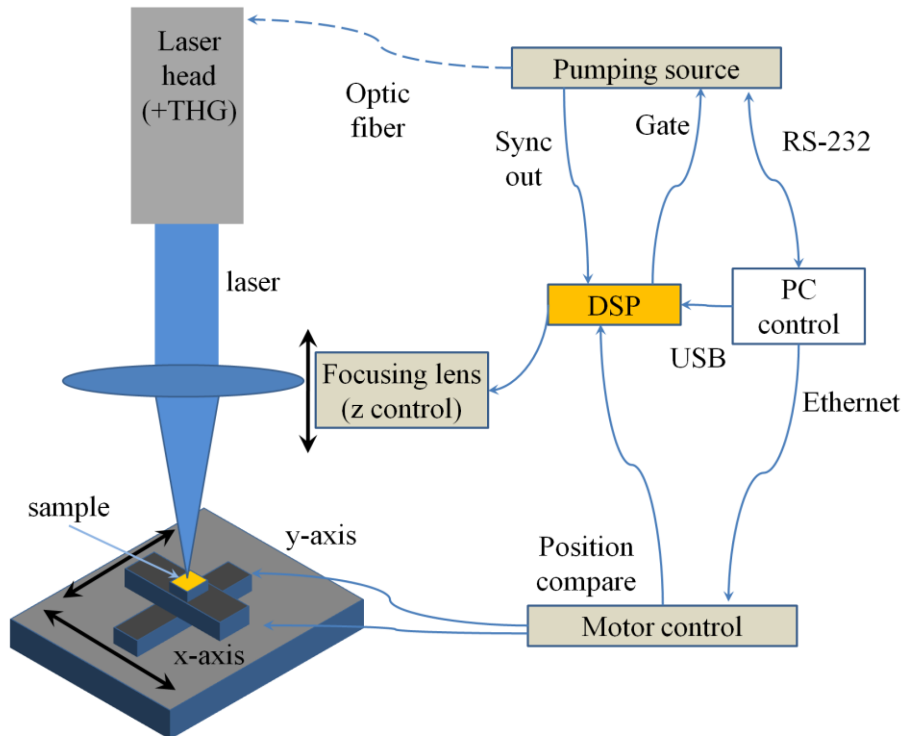

Figure 3.9: Laser Ablation System control diagram.

The DSP allows two operating modes: the "window" mode and the "point-to-point" mode.

In the "window" mode, we define a region in which the laser can emit light, otherwise the laser do not emit. The motor driver sends a signal to the DSP when the motors (with the sample) are inside this region. The DSP switches on the laser with a delay shorter than 100 ns. For example, in order to engrave a diffraction grating, a window with the size of the grating is previously defined. The motors begin their displacement out of this window, reaching a constant velocity before entering in the window. Then, the energy of the laser on the sample will be constant along the window.

In the "point-to-point" mode, the sample is firstly located at a determined position, and when the motorized stage is stopped at this point, a certain number of laser pulses (between 1 and 65535 pulses) are emitted. For each emitted laser pulse, the pumping source sends a signal to the DSP. This number of pulses is counted by the DSP, until the desired number of pulses is reached. After that, the emission of laser light is stopped and the sample is positioned at another position, and the process is iterated. The locations of the points are introduced in the form of a digital image file. With this mode, more complicated masks than with the "window" can be engraved. On the contrary, it results slower. The time developed in the process grows with the number of pixels of the mask.

For the control of the motor stage the API (application Programming Interface) provided by the manufacture have been used. For the control and configuration of the laser a new API has been created, consisting of a set of strings instructions sent by the RS-232 port. Also a specific API for the configuration and control of the DSP has been created. For the complete control of the system, we use a set of instructions running under Matlab. With this set of functions, the operation mode can be chosen and control all the system.

3.5.1 Characterization of the Laser Ablation System

In order to determine completely the behavior of the system, in this section we characterize its dependence with some operation parameters as repetition rate or pumping intensity.

Firstly, we show the output power of the laser at different repetition rates using the maximum pumping power in Figure 3.10a. The output power has been obtained with a calibrated photodiode placed at the output of the laser head. It is clear the dependence with the repetition rate, due the change in the gain condition for both configurations induced by the Q-switcher. Operating at $1064\,\mathrm{nm}$, the maximum peak power rounding $12\,\mathrm{W}$ is obtained for higher repetition rates, whereas for repetition rates lower than $20\,\mathrm{KHz}$ the output power falls down quickly. Operating at $355\,\mathrm{nm}$, the maximum peak power is $2\,\mathrm{W}$ at $20\,\mathrm{KHz}$.

Similarly, the pulse duration for different repetition rates is shown in Figure 3.10b. Data have been provided by the manufacturer. The pulse width grows, for both configurations, with the repetition rate, as have been indicated in Section 3.2, rounding tens of nanosecond.

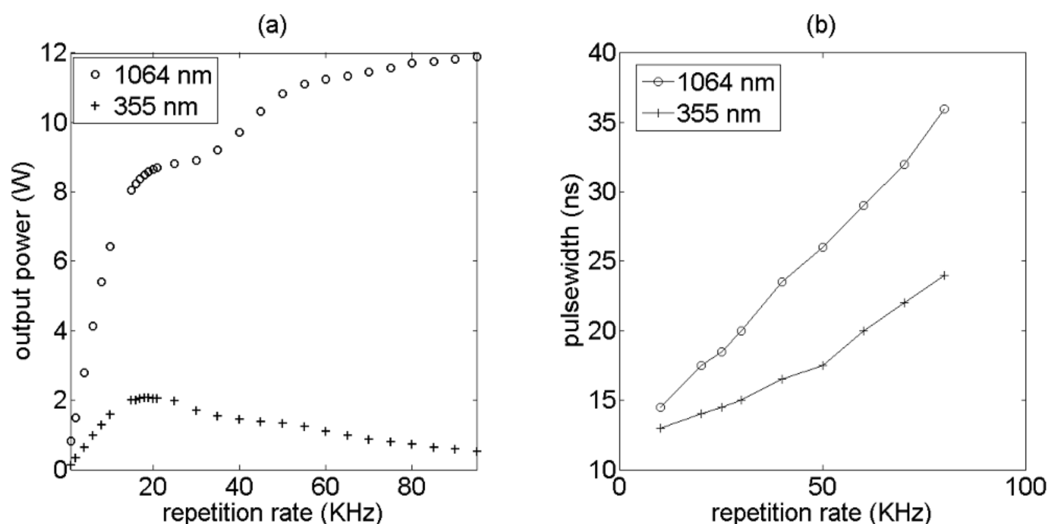

Figure 3.10: Dependence of the output power with the repetition rate, working in $1064\ nm$ and $355\ nm$; (a) output power against repetition rate; (b) pulsewidth against repetition rate.

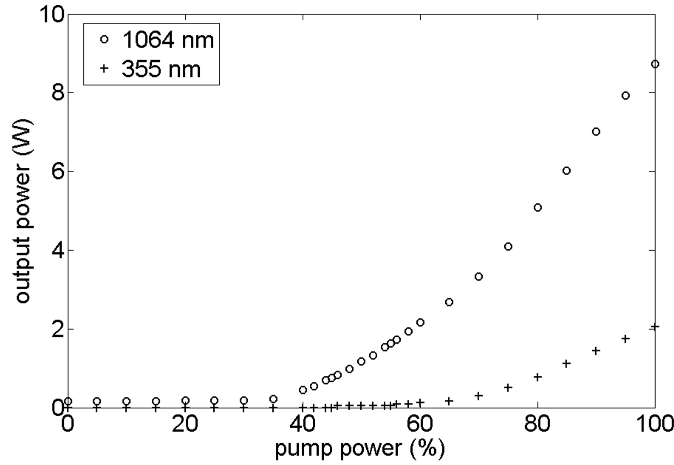

Figure 3.11: Output power versus pumping power (in percentage of the maximum) of the Laser Ablation System using a repetition rate of 21 KHz for different wavelengths. The threshold pump power for both configurations is around 40% of the maximum pump power.

Next, we show the output power for different pumping powers and a fixed repetition rate (we have chosen 21 KHz) in Figure 3.11**¡Error! No se encuentra el origen de la referencia.**. The behavior follows the typical behavior of the laser, with a threshold pump power around 40 % of the maximum pump power. Varying the repetition rate similar curves are obtained, but with different maxima values depending on the plot in Figure 3.10a.

Finally, we calculate the dimensional characteristics of the beam at the focus of the system. The beam waist of the focal spot produced by a lens with focal f from a collimated Gaussian beam with radius r just after the lens is [82]

$$\omega_0^G = \frac{\lambda}{\pi}\left(\frac{f}{r}\right)M^2, \tag{3.8}$$

where M^2 is the beam quality factor, a parameter for quantifying the beam quality of laser beams [83]. Obviously, the spot area at the focus is

$$\mathrm{A}_{focus} = \pi\left(\frac{\omega_0^G}{2}\right)^2. \tag{3.9}$$

Another useful parameter is the depth of focus DOF, defined as two times the Rayleigh distance z_R (the distance from the beam waist where the beam radius is increased by a factor of the square root of 2) [84],

$$DOF = 2z_R = 2\frac{\lambda f^2}{\pi r^2}, \tag{3.10}$$

and the Numerical Aperture NA defined as

$$NA = \frac{f}{2r}. \quad (3.11)$$

We summarize in Table 3.2 the data provided by the manufacturer and the calculated values.

	$f\,(\text{mm})$	M^2	$r\,(\mu\text{m})$	$\omega_0^G\,(\mu\text{m})$	$DOF\,(\mu\text{m})$	NA	$\text{A}_{focus}\,(\mu\text{m}^2)$
$\lambda = 1064$ nm	*46*	*1.15*	*4.5*	*7.94*	*70.8*	*5.1*	*49.55*
$\lambda = 355$ nm	*46*	*1.3*	*4.5*	*2.99*	*23.6*	*5.1*	*7.05*

Table 3.2: Dimensional characteristics of the beam at the focus.

As it can be observed in Table 3.2, the use of the THG allows us to reach a smaller spot area at the focus.

3.6 *Determination of the manufacturing parameters: micromachining of steel tapes*

Once we have characterized the Laser Ablation System, it is necessary to find the suitable parameters for the manufacturing process. These parameters depend strongly on the nature of the samples. In order to exemplify the manufacturing calibration process, we will center at the moment on the study of the micromachining of steel tapes. This material result of high interest due the application in optical encoders (see Appendix A).

3.6.1 Estimation of the ablation threshold in steel

In order to minimize de spot size and maximize the output power, we will work at $\lambda = 355\text{ nm}$ with a repetition rate of 20 KHz. Under these circumstances, and depending on the pumping power, the maximum attainable peak power is $P_{Max} = 2\text{ W}$ and the pulse energy is, therefore,

$$E_{pulse}^{Max} = \frac{2\text{ W}}{20\text{ KHz}} = 0.1\text{ mJ}. \quad (3.12)$$

Consequently, the maximum energy density, "fluence", attainable at the focus will be

$$F_{focus}^{Max} = \frac{E_{pulse}^{Max}}{A_{focus}} = 1.4 \times 10^3\ \text{J/cm}^2. \quad (3.13)$$

The sample stage can travel at a maximum velocity of $\text{v}_{scan}^{Max} = 300\text{ mm/s}$. Depending on the scan velocity and the repetition rate, the pulses over the surface can overlap according to [85]

$$S = \left(1 - \frac{v_{scan} / f}{\omega_0^G}\right) \cdot 100, \qquad (3.14)$$

where S is the overlapping ratio and f is the repetition rate, and we have assumed that the pulse duration is short in comparison with the temporal separation between pulses. A positive value of S in eq. (3.14) will mean overlapping, whereas a negative value of S will mean absence of overlapping. It should be noticed that the spot size is not necessary equal to the size of the affected zone on the steel surface. In fact, each laser pulse re-melts a portion of the previous spot. For this reason, there can be superposed affected areas even with negative overlapping. In Figure 3.12 it is shown an example of the ablation effect over a steel sample, obtained by means of Scanning Electron Microscope (SEM). It is possible to appreciate the volatilized zones by ablation and the melted material. It is also significant, due the overlapping effect, the alternation in the scanning direction for each line.

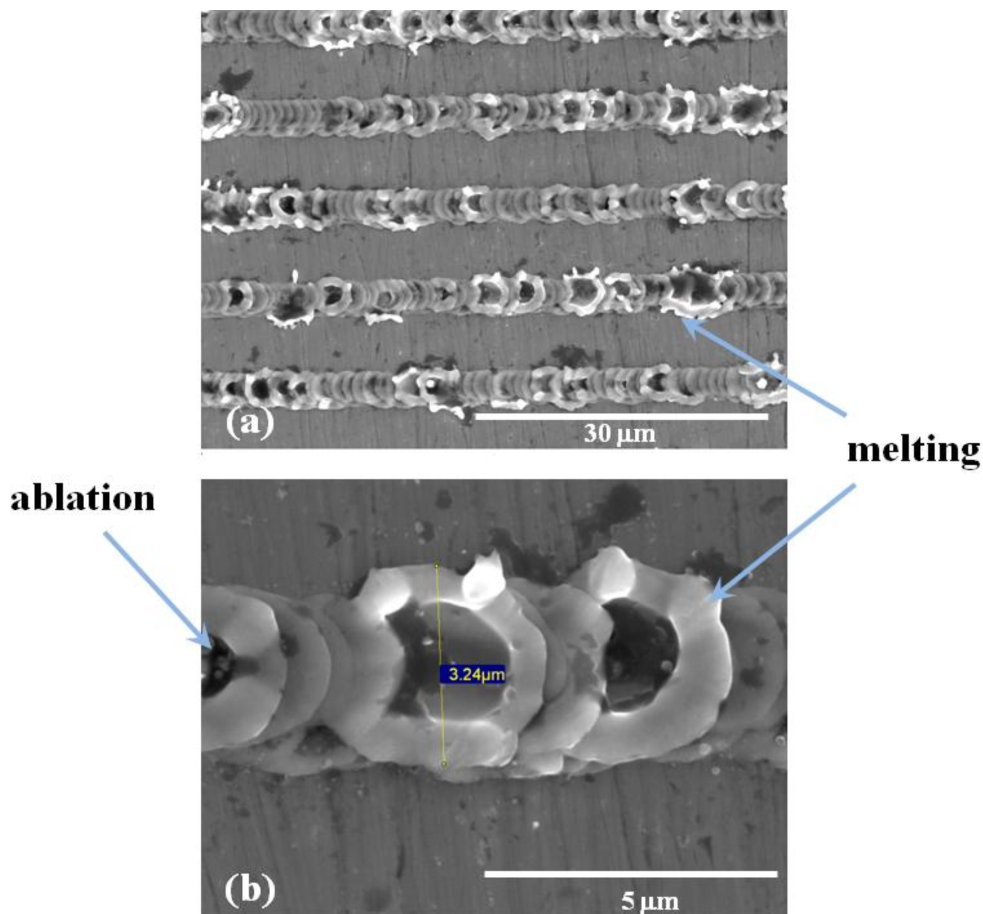

Figure 3.12: a) SEM (Scanning Electron Microscopy) image of an ablation example over steel surface; b) detail of the damaged zones.

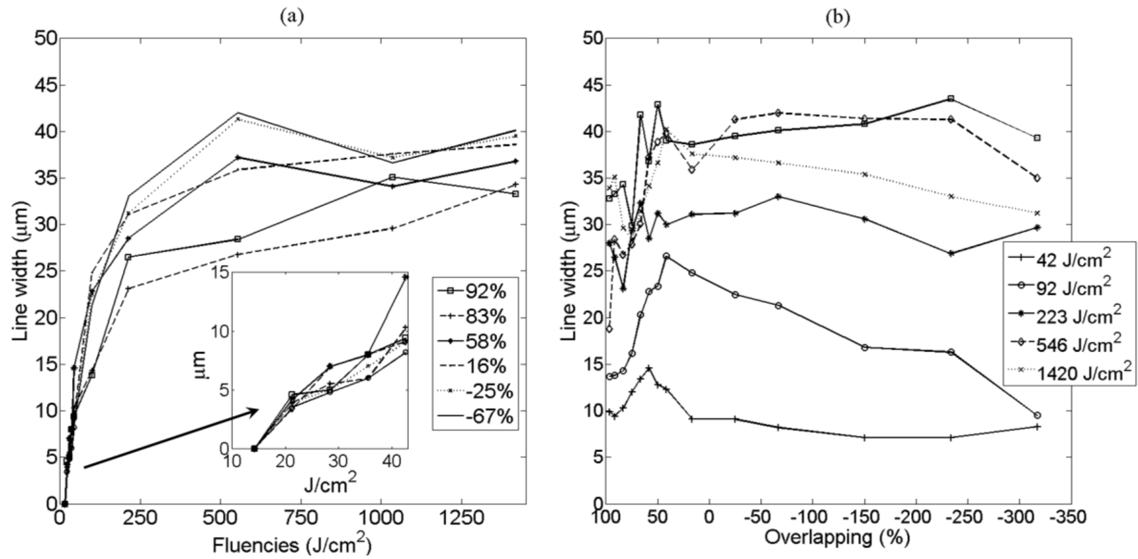

Figure 3.13: Line width against the fluence for different values of S *, working with* $\lambda = 355$ *nm and a repetition rate of* 20 *KHz* .

We define the threshold fluence as the minimum fluence at which the 100% of the emitted pulses can damage the material. In Figure 3.13a there are plotted the line widths obtained for different values of F and S . These values have been obtained averaging over several trials.

The threshold fluence falls around $20\ \mathrm{J/cm^2}$. In general terms, the line width grows with F. But this growth depends also with S . Figure 3.13b shows another point of view, the dependence of the line width with S for different fluencies. Whereas the dependence with the fluence appears clearly, the effect of the overlapping is more complex.

We can understand the effect of the overlapping studying the shape of the lines and its dependence with the overlapping value. In Figure 3.14, several lines engraved with different values of fluence and overlapping are compared. For high overlapping (between 100% and 50%) the laser pulses falls close together. The effect of the overheating is then concentrated over the same area. When the overlapping decreases (until 50%), laser pulses falls more separately. Since the metal is overheated, the next pulses impinge over heated zones: it is easier to reach the melting temperature. For this reason, the thermal damage (and also line width) is higher for $S = 60\%$ than for $S = 80\%$. On the contrary, when the overlapping is less than 50%, the substrate is able to evacuate the overheating before the impact of the next pulse. Therefore, this next pulse needs to warm up again the substrate, and the amount of energy inverted in the warming up increases when the pulses are more separate. Consequently, the line width falls down for values of overlapping lesser than 50%.

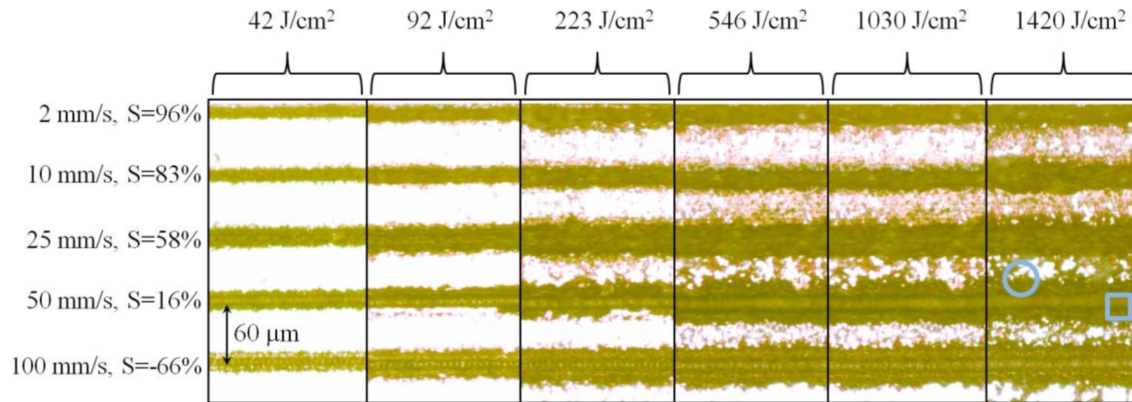

Figure 3.14: Engraved lines for different fluences, with overlapping from 96% to -66%. Thermal damages are surrounding with a circle, ablation damages are surrounding with a square.

For a same value of fluence, melting zones appear more clearly when the overlapping is lower (more negative), as it is shown in Figure 3.14. Since the thermal nature prevails over pure ablative processes, the damage loss homogeneity. Moreover, for low overlapping, it is possible to appreciate the effect of the pulses over the melting zones (as occurs in Figure 3.12). On the contrary, with high values of overlapping (more positive), the features are more uniforms and thermal effects appear not so clearly with common optical microscopy. It is more difficult to distinguish each pulse.

When a pulse impinges too far from the last pulse, the melting zones surrounding each impact can appear separated. The overlapping, consequently, is not effective. Figure 3.15 shows this effect. We have used pulses of $546\ \mathrm{J/cm^2}$ at $1\ \mathrm{KHz}$ to ensure the separation between pulses. It is clear that when the overlapping is too elevated, the effect of the pulses and the melting zones does not overlap.

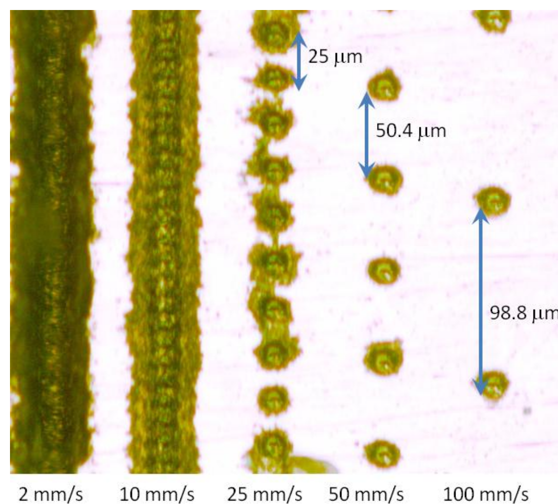

Figure 3.15: Effect of laser pulses at $355\ nm$ operating at $1\ KHz$ with $F = 1135\ J/cm^2$ fir different velocities of movement (and therefore, for different overlapping values).

3.6.2 Focusing tolerances

In order to determine the tolerance of the system versus miss focusing of the sample, we perform a set of engravings with $F = 14\ \mathrm{J/cm^2}$ and $S = 16\,\%$. The process is iterated a certain number of times. After each iteration, the focusing lens is displaced $\Delta z = 20\ \mu\mathrm{m}$. The line widths are collected in Figure 3.16.

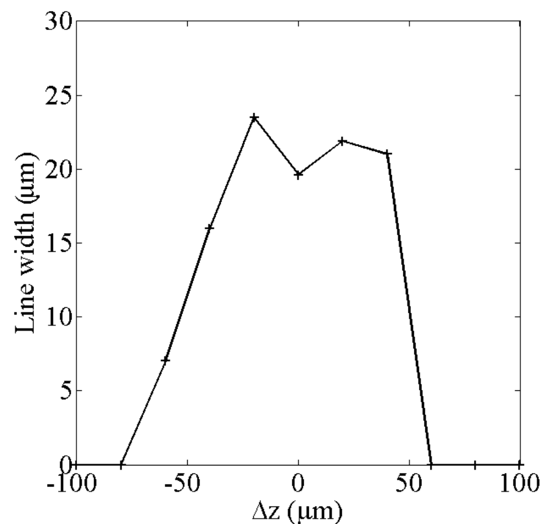

Figure 3.16: Line widths obtained for different positions of the focusing lens.

After Figure 3.16, we can consider that the ablation process is stable along $100\ \mu\mathrm{m}$ rounding the focus location.

3.7 *Micromachining of transparent dielectrics*

In dielectric materials, unlike metals, there are not free charge carriers, and the absorption, that is mostly due to inter-bands transitions and inner defects, is lower than in metals. For these reasons, the threshold damage fluences use to be higher than in metals. We centre our efforts in transparent dielectrics, since they present a high potential for industrial applications.

Specifically, we work with fused silica, consisting essentially of silicon dioxide with some amount of impurities. This material is usually considered as linear, homogenous, isotropic, inert and reasonably robust. Moreover, standard glasses (as BK7 from Schott [86]) result relatively inexpensive. Nevertheless, we will see in this work that the micromachining of fused silica by laser ablation presents some problems.

There are, at least, three possible methods for coupling laser energy into a non-absorbing material [87]. One possibility is to use an auxiliary material that use to be a liquid [88] or a metal [89], in contact with the sample. The heat absorbed by the auxiliary material will be transferred to the surface of the transparent sample. The second possibility is to use a laser with a wavelength that is absorbed by the sample [90]. Fused silica, for example, has a bandgap energy of $9.3\ \text{eV}$, equivalent to $133\ \text{nm}$ wavelength. Lastly, the third possibility is to achieve multi-photon ionization in the material by means of laser peaks with high fluencies [91]. This last method can be performed with our Laser Ablation System.

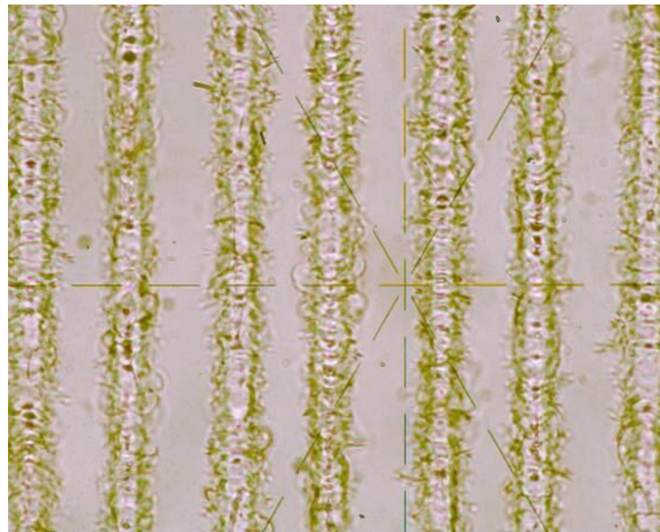

Figure 3.17: Detail of a diffraction grating in inner fused silica by nanosecond laser ablation. Common optical microscopy ($20\times$*).*

Under this circumstances (high fluencies peaks in the visible range), the most important parameter is the pulse duration. Pulses in the nanosecond range will involve, inevitably, micro-carks in the transparent material [79]. An example of the effects of nanosecond pulses trains with high energy in a transparent material is shown in Figure 3.17.

The feature of the damages is far from a “clean” process. A more detailed analysis of this kind of structures will be shown in Chapter 5. Nevertheless, the possibility of micromachining 3-dimensional structures [92], integrated devices [93] and, in general, embedded diffractive devices [94] makes this technology quite promising.

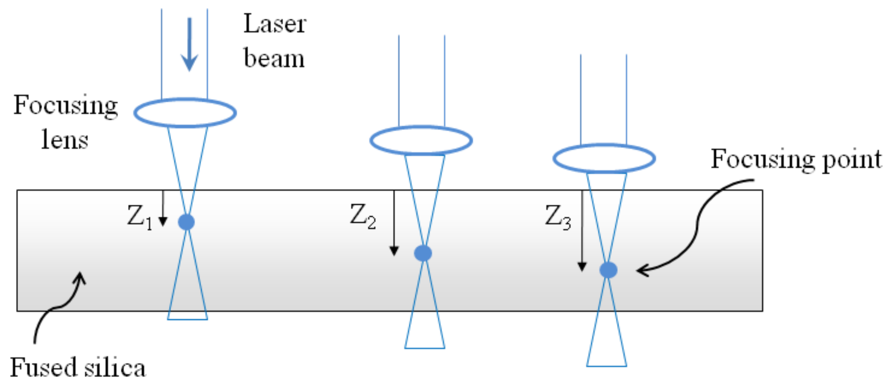

Figure 3.18: Schematic view of the engraving at three different depths controlling the focus location of the Laser Ablation System.

The process of three-dimensional engraving consists of moving the focusing lens in the laser ablation system, allowing engraving at different depths in the sample. Figure 3.18 shows a scheme of this method of controlling the location of the focus.

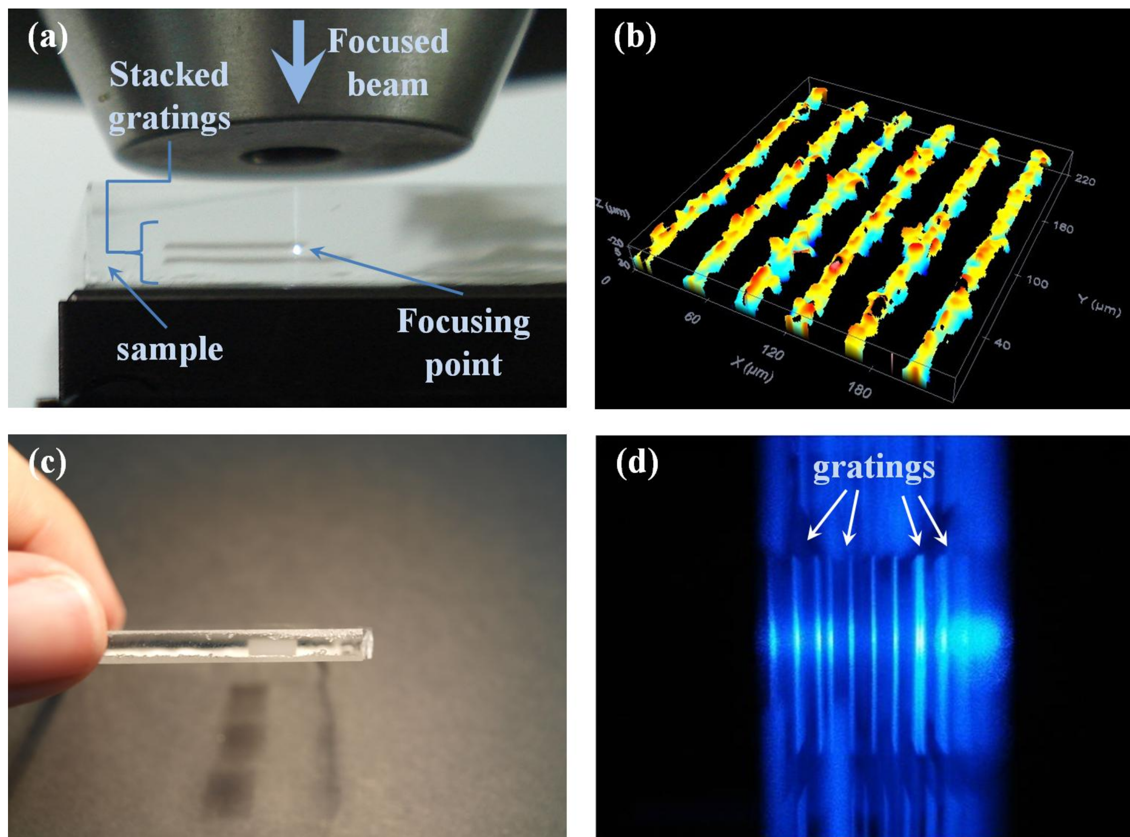

Figure 3.19: Example of stacked gratings in bulk fused silica engraving; a) image of the focusing spot in a fused silica sample. A grating has been engraved, the image is acquired during the process of engraving a second grating at a different depth; b) confocal image of a diffraction grating in bulk fused silica; c) lateral view of several stacked gratings in a glass sample; d) lateral view of the stacked gratings illuminated (from the left to the right) with a blue laser.

In addition, Figure 3.19 shows an example of this kind of processing. A grating is engraved in a sample of fused silica. The shape of one of these gratings is shown in a confocal microscopy image in Figure 3.19b. Next, the focusing lens has been moving upward, and another grating is engraved. The amount of displacement should take into account the refractive index of the sample, in order to locate the gratings at the proper positions. The process is iterated until all the stacked elements have been engraved. At the end of the process, we obtain a three-dimensional diffractive device, shown in Figure 3.19c and Figure 3.19d. With this method, the devices designed in Section 2.4.2 can be manufactured.

For the simulation and analysis of embedded DOEs the Beam Propagation Method (BPM) explained in Section 2.3.3 is the best choice, due the ability of propagating light through an inhomogeneous medium. As we have mentioned, Chapter 5 will tackle this subject in detail.

3.8 *Silicon processing by nanosecond pulsed laser ablation*

Silicon cutting and wafer dicing are key activities for microelectronic and photovoltaic applications, that can be performed by means of pulsed lasers [95], [96].

Besides the microelectronics and photovoltaic applications, silicon crystal has many applications as substrate for infrared optics, since it is transparent between $1.1\ \mu\text{m}$ and $6.5\ \mu\text{m}$ [97]. A brief description of the possibilities in silicon processing (and DOEs fabrication for infrared range) is shown in this section.

Some lines engraved on a silicon wafer, working at $355\ \text{nm}$ are shown in Figure 3.20. As it is observed, thermal effects are minimized in comparison with fused silica and metal processing, due the lattice properties of the crystalline silicon.

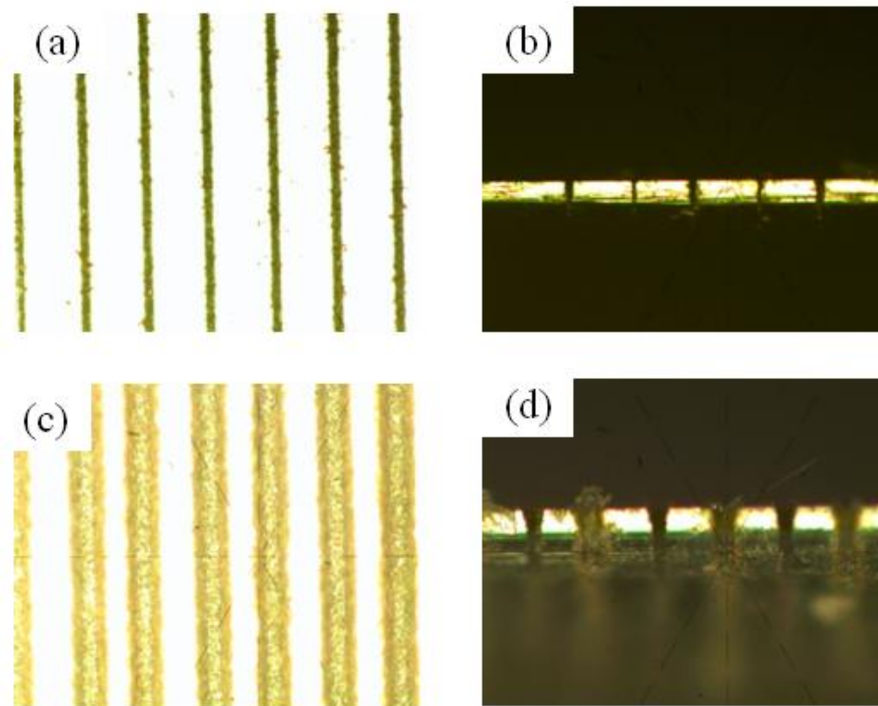

Figure 3.20: Lines engraved on silicon wafer with nanosecond laser pulses at 355 nm (optical microscope); a) 8 μm width, zenithal view, b) 8 μm width, lateral view; c) 25 μm width, zenithal view; d) 25 μm width, lateral view.

A more detailed view, obtained by confocal microscopy, is shown in Figure 3.21.

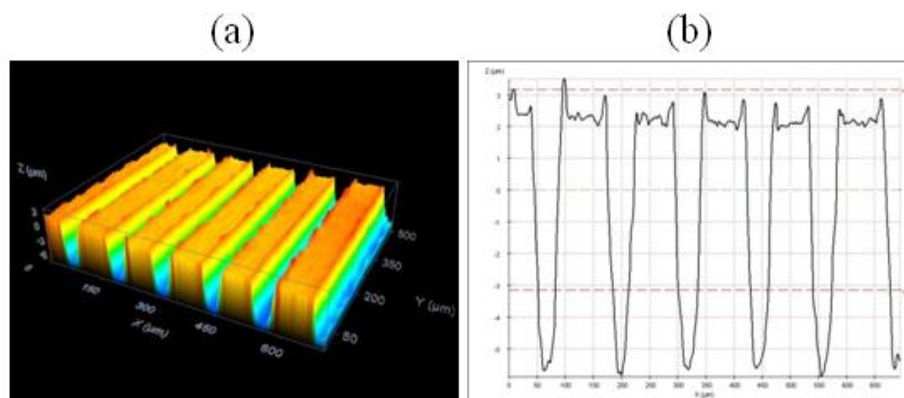

Figure 3.21: Lines with 50 μm of width engraved on silicon wafer. Data obtained by confocal microscopy; a) 3-dimensional view; b) profile.

Laser ablation can also be performed directly over a photodiode, in order to manufacture structured photodiodes. Usually, this kind of devices is fabricated by photolithographic methods, requiring several processes [98]. The most common approach is to place a chrome-on-glass mask over the photodiode in optoelectronic systems [99]. This method presents some disadvantages: multiple interfaces reflections, misalignments or poor mechanical

tolerances. A possible alternative is to use laser ablation, in order to fabricate structured photodiodes. Ablationed zones cannot detect light so that we can define different areas over the photodetector surface. With this technique, we can integrate complex structures in a single device. This method, in comparison with traditional methods, is fast and simple, and represents a rapid prototyping technique. Moreover, pre- or post-treatment are not required.

As is explained in Appendix A, an optical encoder consists of a scale (in the form of a diffraction grating), a photodiode, and a second grating placed before the photodetector. This second grating is usually a chrome-on-glass mask engraved by means of photolithography. The use of this element can introduce several problems: misalignments or internal reflections.

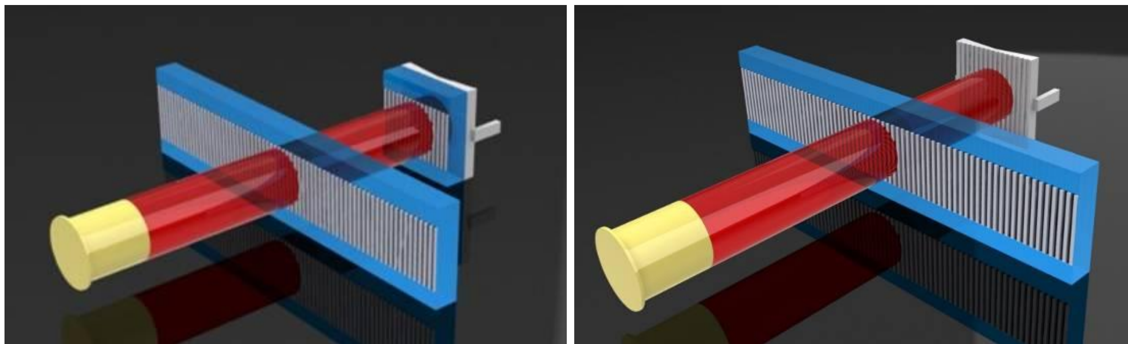

Figure 3.22: Schematic view of an optical encoder, a) with a photolithographic mask over the photodetector; b) optical encoder with structured photodiode.

By means of laser ablation we can engrave the second grating directly on the surface of the detector. Then, we obtain an integrated system, avoiding the problems caused by external elements. The encoder is schematized in Figure 3.22.

The structured photodetectors have been manufactured using the Laser Ablation System working at 355 nm, and a planar photodiode (SLCD-61N2 by Silonex.) We first calibrate the response with and without illumination. Next, two areas are isolated on the photodiode surface, cutting the metallic contact and demonstrating that both zones are isolated each other, as it is shown in Figure 3.23.

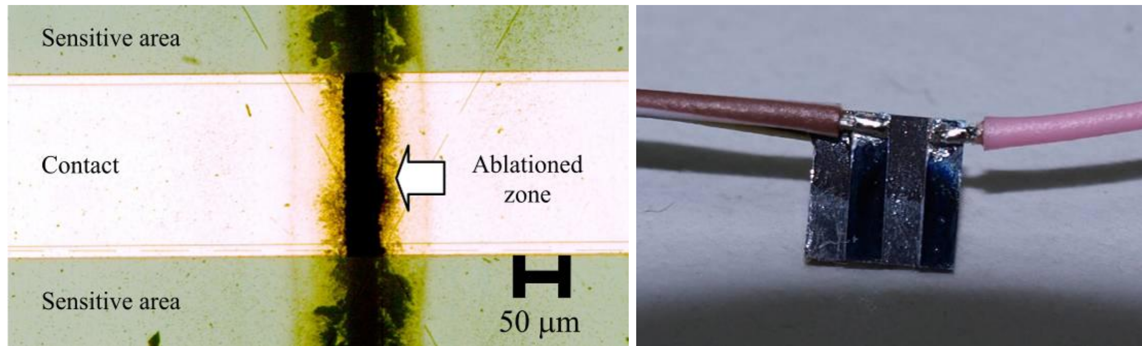

Figure 3.23: Isolated areas on the photodetector surface by laser ablation.

We connect each zone to a multimeter, and focusing a laser on one of the zones we confirm that the isolation was properly performed.

Next, we engrave a grating over another photodetector. We shown in Figure 3.24 a topographical view of the structured photodiode obtained by means of confocal microscopy.

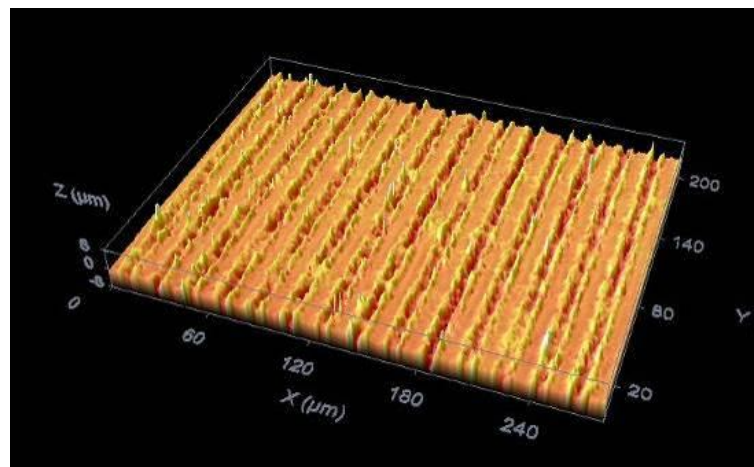

Figure 3.24: Confocal microscopy measurement of the photodetector surface with an engraved grating with 20 μm of period.

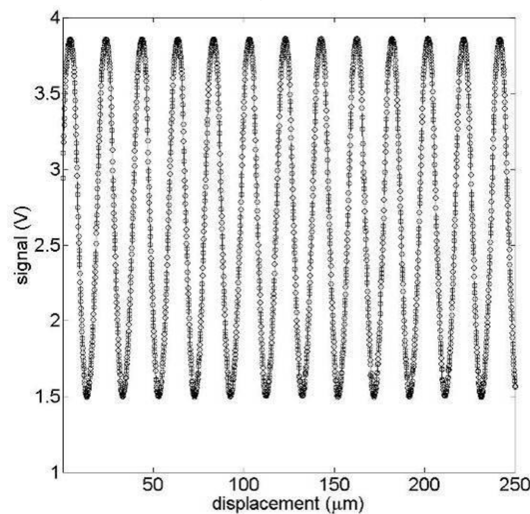

Figure 3.25: Experimental optical signal obtained with the structured photodiode for different positions of the grating.

Using the set-up of Figure 3.22 and displacing the grating, a sinusoidal signal is obtained, plotted in Figure 3.25.

This plot shows that the Laser Ablation System can be also used for photodetector processing. More complex designs can be also engraved.

4 Diffractive Optical Elements over steel tapes by means of laser ablation

---

Steel tape is used in optical applications due to its mechanical properties. However, it presents some special characteristics, in comparison with the common substrates used in micro-optics. One of these characteristics is the roughness of steel surfaces, which affects to wave propagation. The effect can be observed using diffraction gratings with low periods. In such a case, self-images of the grating appear at certain periodic distances from the grating (Talbot planes). When standard steel is used, the contrast of Talbot self-images strongly decreases with the distance from the grating. In this work, we prove that controlling the surface quality of steel, it is possible to improve its optical behaviour and, as a consequence, high quality surface steel represents a good choice for diffractive optics when the use of chrome-on-glass masks is not indicated. As an example, we have manufactured diffraction gratings over high quality steel surfaces by means of an ablation process with a nanosecond pulsed laser. The contrast of the self-images for these gratings decreases very slowly with the distance, in comparison with the self-images obtained with standard steel tape gratings. This formalism is extended to more complex devices, such as Fresnel zone plates. In addition, we analyze the near field behaviour of binary amplitude gratings that present a curved profile. This configuration has an important application in rotary optical encoders. This kind of encoders is used to measure the angular displacement between two different parts of the devices. To our knowledge, its behaviour in the near field has not been analyzed yet. We have found that Talbot effect is produced but the period of the self-images and Talbot distance change as we separate from the grating. We have fabricated a curved grating and perform an experiment in order to corroborate this behaviour This fact could be useful in systems that use Talbot effect to measure displacements, since the mechanical tolerances grow.

4.1 *Introduction*

Diffractive optical elements are commonly manufactured using chrome-on-glass masks, dielectric materials (glass, plastics and organic components) or semiconductors (silica) as substrates. Nevertheless, there exist applications where the environmental conditions are extreme due to vibrations, impacts, or thermal variations. In such a case, it is necessary to fabricate micro-optical elements over more robust substrates as for example steel tapes.

Photolithographic techniques are extendedly used for the manufacture of binary diffractive elements, with a very high accuracy after decades of developing for the semiconductor industry, especially with chrome-over-glass masks. However, pulsed laser micromachining represents a good alternative, reducing costs and time. We perform here a study of the optical behavior of steel tapes micromachined by means of laser ablation with the system explained in Chapter 3. This study will be very helpful in order to consider the introduction of pulsed laser micromachining in the manufacturing processes of diffractive devices on steel.

4.2 *Diffraction gratings on steel tapes for optical encoders*

As have been mentioned in Chapter 1, diffraction gratings are one of the most used optical elements, since they can be applied in a high number of different branches of science (chemistry, photonics, astrophysics, engineering, biology, etc.) and also in several applications, such as telescopes, machine-tool, spectroscopy, precision optical metrology, etc [100]. Chrome on glass gratings are commonly used for precision optical metrology purposes [101]. These gratings are formed by chrome strips on a glass substrate and their optical behavior is near to the ideal. However, there exist applications that require using gratings with a long length (more than 3 meters). In such a case, glass gratings are not appropriate since they result hard to manufacture and handle. Therefore, steel tape gratings are preferred [102]. Unfortunately, they present a worse optical behavior due to surface roughness. This roughness affects to the optical properties of the gratings. For example, the effect over Talbot self-images is notorious and it has been analyzed in previous works [103], [104]. Talbot effect consists of the replication of the intensity pattern at some certain distances from the grating when it is illuminated by a collimated beam [105]. When the grating is engraved over a rough surface, the contrast of Talbot self-images decreases with the distance

between the grating and the observation plane. Therefore, the behavior of the devices that use steel tape gratings gets worse. This decreasing depends strongly on the roughness parameters.

In this section we show the conditions in which steel tapes can be used in diffractive optics applications. In particular we have focused on the self-imaging process. We experimentally investigate the effect of the roughness parameters on the contrast of the self-images. Steel tape gratings have been manufactured using the laser ablation station described in Section 3.5. As substrates, we have used two different steel tapes with different levels of roughness. We will show that controlling the surface quality of the steel tape it is possible to achieve a high-quality grating, acting close to the ideal behavior of a grating (like a chrome-on-glass grating).

4.2.1 Talbot effect with perfect gratings

Let us assume a perfect and one-dimensional diffraction grating with period p. We also assume that the transparent area is equal to the opaque area for each period. Since diffraction gratings are periodical elements, they can be described as a series expansion. According to TEA (Section 2.2.3), the transmittance of the grating is given by

$$t(\xi) = \sum_l c_l \exp(iql\xi), \tag{4.1}$$

where $q = 2\pi/p$, ξ is the position along the grating and c_l are the Fourier coefficients of the grating,

$$c_l = \frac{1}{p}\int_{-p/2}^{p/2} t(\xi)\exp(-ilq\xi)\,d\xi. \tag{4.2}$$

A scalar treatment of the diffraction is possible when the period of the grating is much longer than the wavelength of the incident beam. When a monochromatic wavefront U_0 impinges on the grating, the diffracted field at a distance z from the grating can be described using the Fresnel approach, eq. (2.19). Thus, the field just after the grating is

$$U(x,z) = \frac{\exp(ikz)}{\sqrt{i\lambda z}}\int U_0(\xi)t(\xi)\exp\left[i\frac{k}{2z}(x-\xi)^2\right]d\xi, \tag{4.3}$$

where $U_0(\xi)$ is the illumination wave. When a monochromatic plane wave $U_0(\xi) = A_0$ illuminates the diffraction grating, the diffracted field at a distance z from the grating results

$$U(x,z) = A_0 \sum_l c_l \exp(iqxl) \exp(i\pi l^2 z / z_T) \tag{4.4}$$

where $z_T = p^2 / \lambda$ is the Talbot distance. The normalized intensity of the diffracted field, $\hat{I}(x,z) = U(x,z)U^*(x,z) / |A_0|^2$, results in

$$\hat{I}(z,x) = \sum_l \sum_{l'} c_l c_{l'}^* \exp[iqx(l - l')] \exp[\pi i(l^2 - l'^2)\hat{z}], \tag{4.5}$$

where $\hat{z} = z / z_T$ and $*$ denotes complex conjugated. Eq. (4.5) shows the light diffracted by a perfect grating has two modulations. The first modulation is produced along x -axis, and it is ruled by the firs exponential term in eq. (4.5). It follows the grating with the same period p. The second exponential term in eq. (4.5) rules the other modulation, taking place along z -axis. This second modulation consist of a replication of the grating along z -axis at certain distances after the grating separated by z_T. In other words, self-images of the grating appear at distances multiple of z_T. This effect is known as Talbot self-imaging or Talbot effect after its discover [105]. For odd multiples of z_T, these self-images are the negatives of the grating [106]. This effect affects not only to diffraction gratings, but also to any periodical diffractive element in the near field. In the specific case of optical encoders, it results very important since it limits the location of the reading head and decreases the mechanical tolerances of the system. An example is shown in Figure 4.1a, where the value of eq. (4.5) has been plotted for different values of x and z. Only the orders c_{-1}, c_0 and c_1 have been taken into account, since they carry the 90% of the total energy. The illumination field is a plane wavefront with $\lambda = 632$ nm. The grating plotted has a period of $p = 40$ μm, Thus, $z_T = 2.53$ mm.

A useful parameter for the study of gratings in the near field is the contrast along z -axis, defined as

$$Contrast(z) = \left| \frac{I_{\max} - I_{\min}}{I_{\max} + I_{\min}} \right|, \tag{4.6}$$

where $I_{\max}$ is the intensity at $x = 0$ for every value of z, $I_{\max} = I(x = 0, z)$, and $I_{\min}$ is the intensity at $x = p/2$ for every value of z, $I_{\min} = I(x = p/2, z)$. Therefore, the contrast depends on the distance z from the grating. Due this definition, odd and even self-images are equivalent attending to the contrast value, and we do not consider the inversion of contrast.

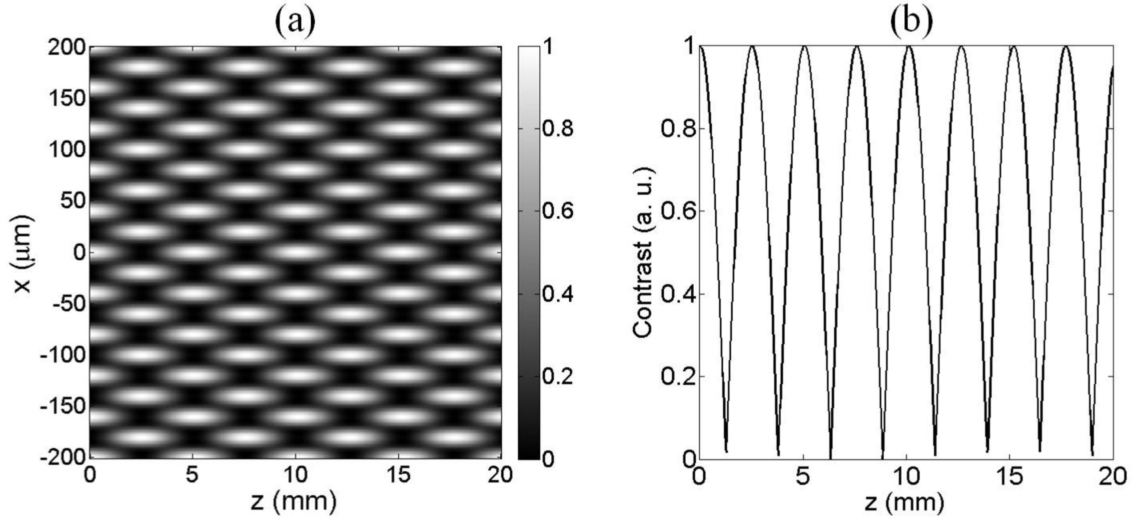

Figure 4.1: Talbot effect by an amplitude diffraction with $p = 40\ \mu m$ illuminated with a plane and monochromatic wavefront traveling from the left to the right; a) intensity of the field after the grating. The grating is placed in the vertical axis at z =0; b) contrast along z -axis calculated using eq. (4.6).

In Figure 4.1b the contrast obtained using eq. (4.6) and the data from Figure 4.1a is plotted. As it can be observed, the contrast reach de maximum value for even multiples of z_T , and the minimum value for odd multiples of z_T . This maximum value remains the same along z -axis. It should be mentioned that the experimental evaluation of eq. (4.6) can result complex and difficult. For this reason, it is usual to substitute $I_{\max}$ and $I_{\min}$ by a spatial average in intervals of $p/2$ around $x = 0$ and $x = p/2$ along z -axis.

4.2.2 Talbot effect with a rough diffraction grating.

Steel tape gratings have be modeled in the near field by means of a formalism taking into account the roughness of the substrate. [103], [104]. One of the effects of roughness is the decreasing of the contrast of the self-images with the distance from the grating to the observation plane. Since the roughness follows a random distribution, it must be described in terms of statistical parameters such as the correlation length, T , and the standard deviation of heights, σ. A Gaussian distribution on heights and a decreasing exponential autocorrelation function are assumed to describe the roughness over the surface [107], [108]. We have selected these functions based on an experimental analysis, as will be shown in Section 4.2.3.

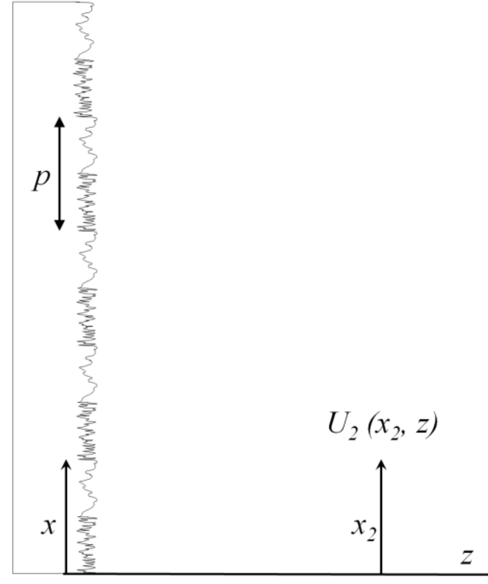

Figure 4.2: Scheme of a rough grating and the coordinates used in this work.

Let us assume the scheme shown in Figure 4.2. The grating is binary and characterized by two levels of roughness. Considering monochromatic plane wave, the field after the grating can be calculated by solving

$$U(x_2, z) = A_0 \sum_l c_l \int_{-\infty}^{\infty} \exp\left(iqxn\right) \exp\left[\frac{ik}{2z}(x_2 - x)^2\right] r\left(x\right) dx, \tag{4.7}$$

where $r(x)$ is the reflectivity of the surface and it is obviously unknown due to the random nature of the surface. Therefore, it is not possible to determine analytically the field after the grating. Although, it is possible to obtain the mean intensity as follows. Considering that the roughness has a Gaussian distribution in heights, a decreasing exponential correlation function and that higher order surface properties do not affect, let us take the characteristic function of the roughness given in Section 5.3 of [107],

$$\chi_2 = \exp\left[-g(1-C)\right], \tag{4.8}$$

where $g = \left(2k\sigma\right)^2$, $k = 2\pi/\lambda$, and C is the correlation function. Now, choosing as correlation function, (Section 2.1.2 in [108]), a decreasing exponential function, $C = \exp(-|\tau|/T)$ with $\tau = x - x'$, which can be approximated for high roughness limit to $C \approx 1 - |\tau|/T$, [107]. Substituting this expression in eq. (4.8) we obtain the characteristic function of the roughness for high roughness limit, $\left\langle r\left(x\right) r^*\left(x'\right)\right\rangle = \exp\left(-|x - x'|/T_0\right)$, being T_0 the optical correlation length of the field after the grating [107]. This parameter for

a decreasing exponential function is related to the roughness by means of $T_0 = T/(2k\sigma)^2$, [109]. The statistical parameters T and σ correspond to the surface before the engraving process. After the ablation process, the surface topology changes in the zones where ablation occurred. This new roughness is much higher than the original one and it acts like a scatterer, redirecting light into all directions, [104], [110], contributing to the diffracted intensity like a background factor. The rough grating acts, consequently, as an amplitude grating in reflective configuration.

The mean intensity in the near field can be calculated solving [103]

$$\begin{gathered}\langle I(x_2,z)\rangle = |A_0|^2 \sum_{l,l'} c_l c_{l'}^* \iint_\infty \exp\left[iq\left(xl - x'l'\right)\right] \\ \exp\left\{\frac{ik}{2z}\left[(x_2-x)^2-(x_2-x')^2\right]\right\}\exp\left(\frac{-|x-x'|}{T_0}\right)dxdx'.\end{gathered} \tag{4.9}$$

where A_0 is the amplitude of the wave, c_l, $c_{l'}^*$ are the Fourier coefficients of the grating with l, l' entire, $q = 2\pi/p$ and resulting in [103]

$$\begin{gathered}\langle I(x_2,z)\rangle = |A_0|^2 \sum_{l}\sum_{l'} c_l c_{l'}^* \exp\left[iqx_2(l'-l)\right] \\ \exp\left[-i\frac{q^2}{2k}(l'^2-l^2)z\right]\exp\left(-\frac{z}{w}|l-l'|\right),\end{gathered} \tag{4.10}$$

with $w = pT_0/\lambda = p\lambda T/(4\pi\sigma)^2$. The first exponential factor indicates the period of the self-images, the second exponential factor indicates the location of the self-images along the z-axis and the third exponential factor describes the decreasing of the global intensity along propagation axis owing to the surface roughness. The parameter w describes the distance at which the intensity reduces a ratio $1/e$. This fact is hugely detrimental since the gratings usually need to be separated from the detector for an appropriate design of the devices that use steel tape gratings.

The 90% of the total energy is with the orders -1, 0, 1. Then, we can truncate the summations in eq. (4.10) up to first order. Then the intensity simplifies to

$$\begin{gathered}\langle I(x_2,z)\rangle/|A_0|^2 \approx c_0{}^2 + 2c_1^2 + 4c_0c_1\cos(qx_2)\cos\left[q^2z/(2k)\right]\exp(-z/w) \\ +2c_1{}^2\cos(2qx_2)\exp\left[-z/(w/2)\right],\end{gathered} \tag{4.11}$$

where we have assumed an amplitude binary grating and $c_1 = c_{-1}$

For the experimental measurement of eq. (4.6), we define $I_{\max}(z)=\max\left(\langle I(x,z)\rangle\right)_x$ and $I_{\min}(z)=\min\left(\langle I(x,z)\rangle\right)_x$ as the maximum and minimum intensity for each observation plane, where $\max(\ )_x$ and $\min(\ )_x$ stand for the maximum and the minimum along x-axis at a certain plane at z respectively. Therefore, the dependence of the contrast on the distance z from the grating is ruled by the roughness of the surface through w. The general functional equation to give the contrast results very difficult to handle, but we can give an approximate expression from eq. (4.11) and eq. (4.6) resulting in

$$\langle C(z)\rangle=\frac{8c_0c_1\exp\left(-z/w\right)}{2\left|c_0\right|^2+4\left|c_1\right|^2\left\{1+\exp\left[-z/(w/2)\right]\right\}}. \tag{4.12}$$

4.2.3 Experimental approach

According to Eq. (4.10) and (4.12), the contrast of the self- images decreases slower when the roughness of the steel tape surface is lower. In order to verify this theoretical assumption, we have fabricated diffraction gratings over two different steel samples with different surface quality. We have obtained the value of w from topological measurements. The resulting decreasing exponential is then compared with the experimental decaying of the Talbot self-images. Following we show the experimental approach used and the obtained results.

Fabrication and characterization of steel tapes gratings

Topological images of both steel substrates, obtained using a confocal microscope ($Pl\mu$ by Sensofar, Barcelona, Spain), are shown in Figure 4.3a and Figure 4.3b. This kind of microscope is indicated for three-dimensional measurements of surfaces since it allows us to calculate the roughness parameters from the surface topologies. We have computed the correlation lengths T taking the semi-width of the autocorrelation peak at $1/e$ of its height. Similarly, we obtain σ from the heights histogram, as the semi-width at $1/\sqrt{e}$. Examples of this measurements are shown in Figure 4.4a (the correlation function) and in Figure 4.4b (heights histogram). The shape of an exponential function for the correlation function and a Gaussian function for the heights histogram appears here clearly. For a more realistic measure, we have computed both parameters over an ensemble of 488 linear measurements.

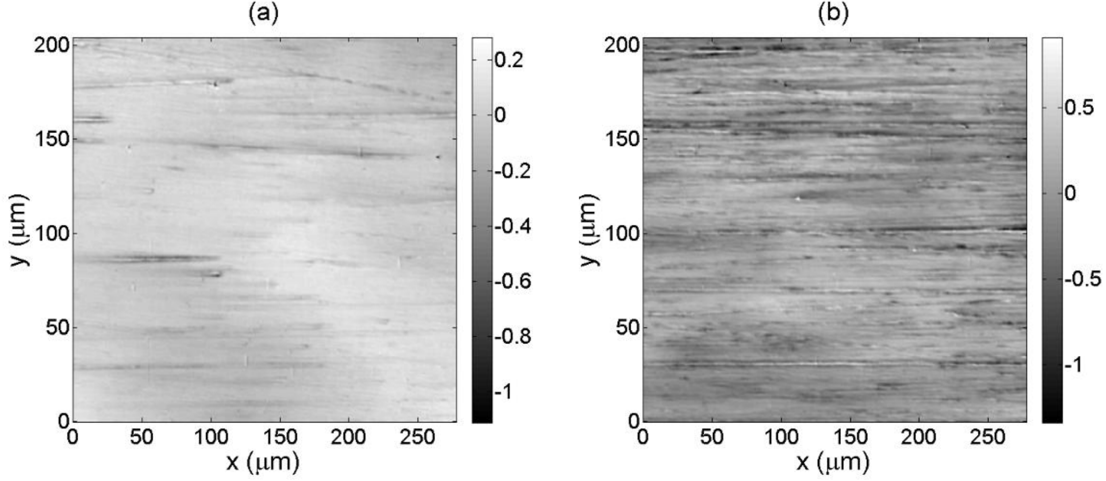

Figure 4.3: Rough surfaces, obtained by means of confocal microscopy: a) low roughness steel, b) high roughness steel, height in microns.

The results are collected in Table 4.1, where we show the mean values of the roughness parameters over the ensemble linear measurements. Steel tapes present a strong anisotropy due to the manufacturing processes. For this reason, we require two different correlation lengths, one for each orthogonal direction (T_x and T_y), in order to describe the statistical properties of the surface. We perform an integration of the intensity along the axis parallel to the strips. We carry out this integration because it is the usual operating system of an optical linear encoder and with this integration we can obtain an average in our measurements. Then, effects due to roughness along y-axis are avoided, and we only need T_x for our calculations since it is the roughness that affects to the decreasing of the Talbot self-images contrast [110].

Once we have the roughness description of each surface, we can calculate w as

$$w = w_x = \frac{p\lambda T_x}{(4\pi\sigma)^2} \quad (4.13)$$

which appears in the last exponential term of eq. (4.10). Then, we only need one parameter to know the optical behavior of the grating in the near field. We will make use of this parameter to compare our results. The values of w are also shown in Table 4.1.

	T_x	T_y	σ	w
High roughness substrate	505.86 μm	44.86 μm	0.182 μm	2.97 μm
Low roughness substrate	407.24 μm	118.71 μm	0.062 μm	22.20 μm

Table 4.1: Roughness data obtained with a confocal microscope, for the two steel samples.

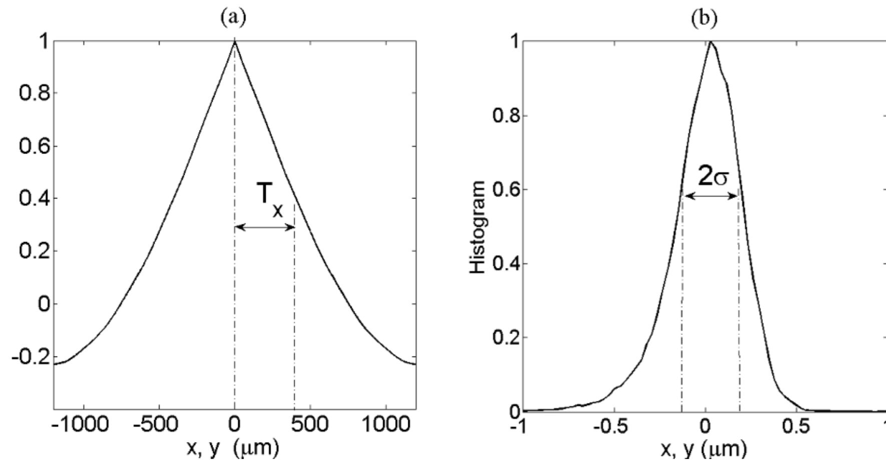

Figure 4.4: Example of topographical measurements of steel tape surface; a) correlation function of a rough surface; b) heights histogram.

The gratings were engraved using the nano-second pulsed laser ablation system described in Section 3.5. The effect of the ablation laser is to remove material and modify the surface topology, obtaining zones with different roughness. The parameters of the laser system (that is, the intensity over the samples) were chosen in order to minimize the removal of material, modifying only the surface roughness. Then, the mean height remains the same. With this requirement, we ensure that the grating acts like an amplitude binary grating. Images of the diffraction gratings are shown in Figure 4.5 .

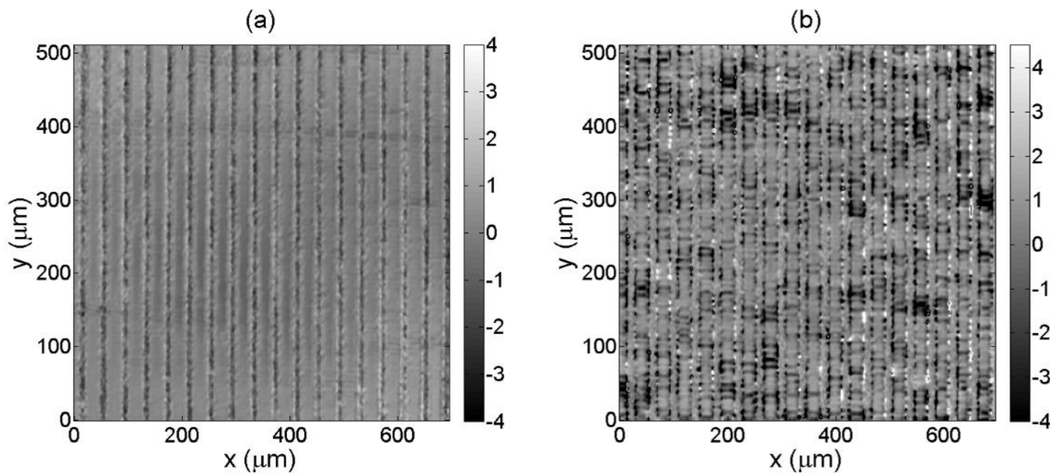

Figure 4.5 Rough reflection grating, over a steel tape, a) low roughness steel; b) high roughness steel.

Experimental measurements of self-images

In order to corroborate our approach, we have measured the field diffracted by this kind of gratings using the experimental set-up shown in Figure 4.6. A monochromatic collimated laser beam of wavelength $\lambda = 675\ \mu\text{m}$ (MC6707O model by Monocrom) impinges on a steel tape grating ($p = 40\ \mu\text{m}$) with normal incidence with respect to its surface. The diffracted

light crosses a beam splitter and is collected by a CCD camera (DFK 31BF03 model by Imagine Source, pixel size 4.65×4.65 μm) with a $10\times$ microscope objective. The camera is placed on a motorized linear stage travelling along the z direction, so it can collect images at any desirable distance.

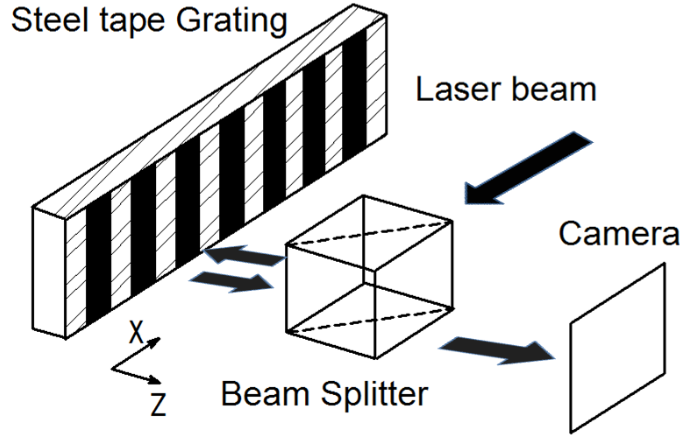

Figure 4.6: Scheme of the experimental set-up.

As we have mentioned, we perform a vertical average (in the direction of the grating strips) for each plane, to obtain the evolution of the intensity diffracted by the grating (Figure 4.7). Using these averaged images, we calculate the contrast for different distances z between the grating and the observation plane.

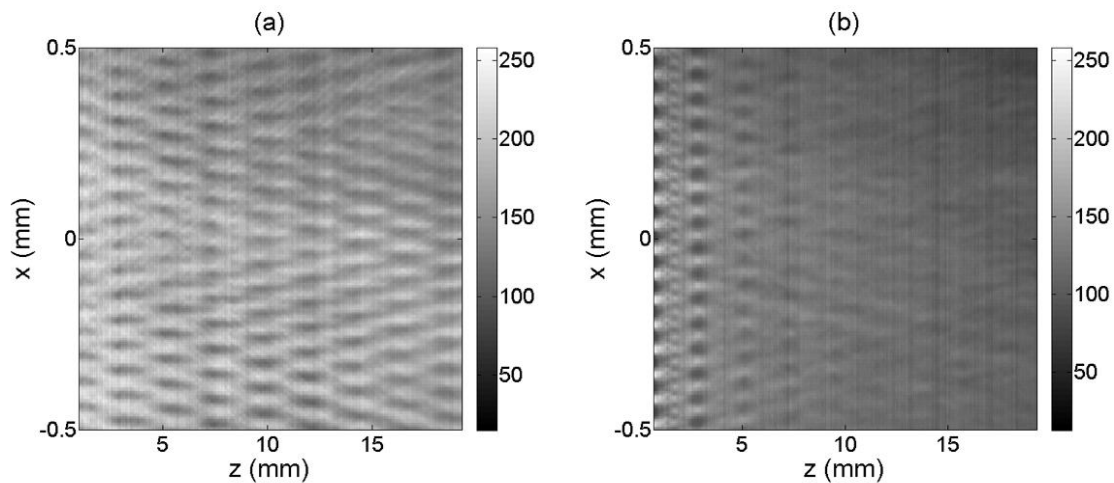

Figure 4.7: Evolution of Talbot self-images along z -axis, a) low level roughness steel; b) high level roughness steel.

The contrast evolution along z -axis for both kinds of steel is shown in Figure 4.8. The dependence on roughness appears clearly, in the form of a decreasing of the contrast. We plot two theoretical fittings to the experimental self-images, one using almost the complete

sums and the other one using eq. (4.12). To measure the contrast, we have used a variogram-based technique, since it provides an accurate measurement of contrast for experimental noisy measurements [111].

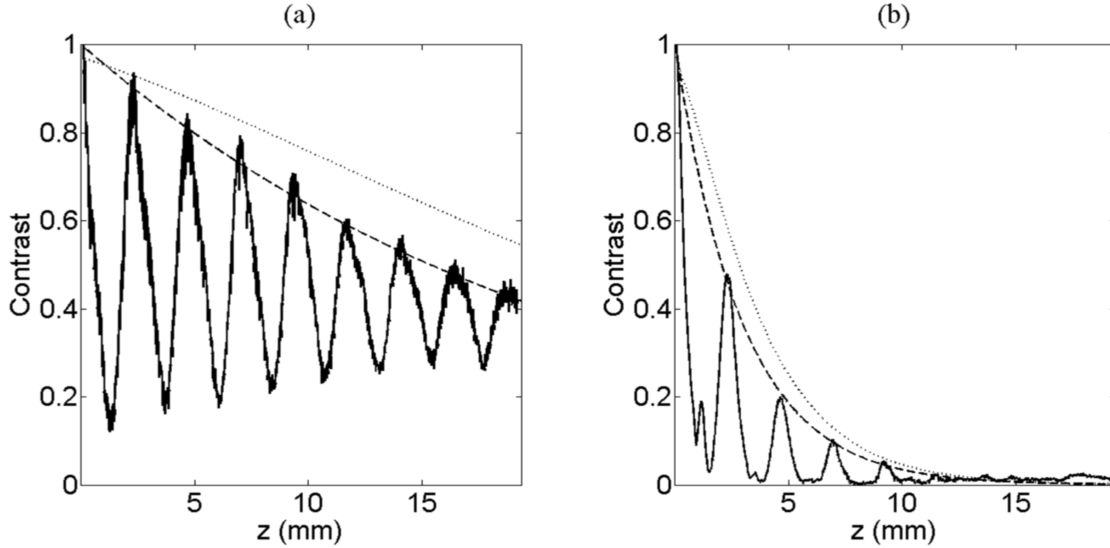

Figure 4.8: Experimental contrast in terms of the distance from the grating (solid line), and theoretical decreasing of the Talbot self-imaging contrast, using eq. (4.6) (dashed line) and using eq. (4.12) (dotted line), for a) low level roughness steel; and b) high level roughness steel.

To validate the theoretical predictions, we have also plotted the exponential functions ruled by $F(z) = a \cdot \exp(-z / w)$, where w was obtained from roughness data using eq. (4.13) -this parameter is also shown in Table 4.1-. It can be observed that the contrast of the self-images and the exponential decreasing ruled by the topographical measurements lead to very close results. As it can be expected, the fitting theory-experiment is more accurate for the high roughness steel tape grating, since the model was developed for high roughness limit. However, for the low roughness steel tape grating, the adjustment is also quite good. Therefore, we have demonstrated that controlling the topographical surface quality of the steel tapes where the grating is engraved, it is possible to improve its optical behavior.

4.3 *Self Imaging with curved gratings*

For the ideal case described in 4.2.1, gratings have been considered as flat or non-curved surfaces, illuminated by a plane and monochromatic wavefront [112]. This model has been progressively improved introducing new concepts: finite spectral width [113], Gaussian illumination [102], total incoherence [114] or partially coherent light [115]-[119]. Also non-

ideal gratings have been studied [120], [121], as for example, the effect of surface roughness developed in last section. These works took into account only flat surfaces. From the point of view of optical encoders, it results interesting to analyze the effects that the curvature of the gratings can induce in the diffracted field.

Effects of curvature over gratings have been also studied [122]-[125], but focused to other applications or points of view. Concave or cylindrical gratings have been successfully used in spectrometry, in order to avoid the use of focusing lenses [2], [126]. Nevertheless, up to our knowledge, there is not a study centered on near-field diffraction of cylindrical gratings. Cylindrical gratings can be used in annular encoders to measure angular displacements, see Figure 4.9. Our objective is to reach analytical expressions, which lead us to analyze the effect of the grating curvature over the diffraction pattern in near field.

In the present work, we consider a diffraction grating working in reflective mode. The grating is defined over a cylindrical surface, with the strips periodically located along surface. Assuming that Fresnel approach is valid, the near field propagation of light reflected by cylindrical grating is analyzed and theoretically predicted. Finally, experimental results using cylindrical diffraction gratings engraved by laser ablation are shown, being clear the accordance with theoretical analysis.

4.3.1 Theoretical analysis

Let us consider the scheme shown in Figure 4.9, where a monochromatic plane wave with amplitude A_0 is propagating from right along z-axis direction and impinges a diffraction grating. The grating presents a cylindrical shape. In Figure 4.9, (ξ, z) are the coordinates centered at the point in which the grating crosses the z-axis, P is a plane perpendicular to the propagation direction placed at the origin of coordinates, L is the projection of the grating length over the ξ-axis, $\delta(\theta)$ is the distance between every point of grating and the plane P, taking it perpendicular to the z-axis, and R is the curvature radius of the grating. The radius is defined positive when the center of curvature is placed at the left side of the grating.

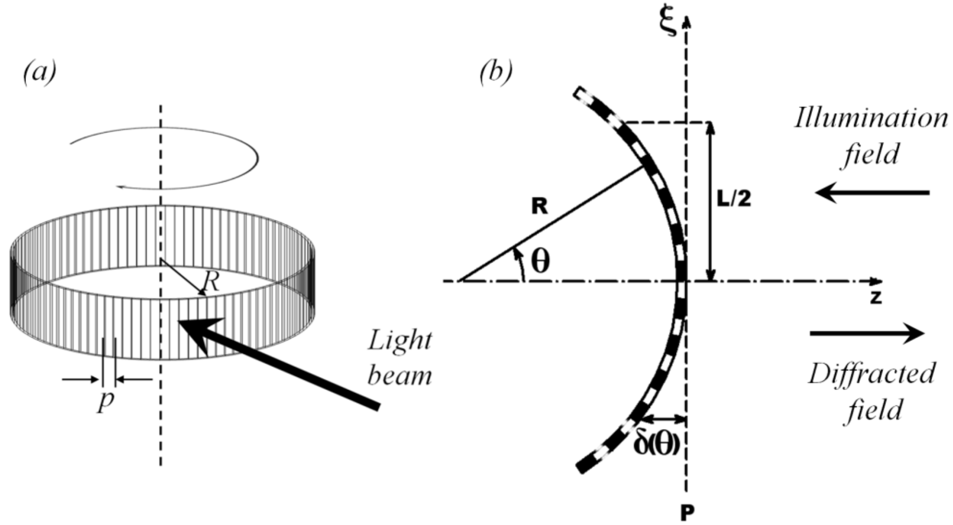

Figure 4.9: a) Scheme of an annular encoder; b) Curved grating, showing the parameters involved. Light comes from the right to the left, and it is reflected in the opposite direction.

We consider an amplitude grating working in reflection configuration, since they are normally engraved over steel tape gratings, [103]. To calculate the diffraction pattern produced by the grating, we use a partially geometrical approach. At plane P, the wave remains as a plane wave, but from this plane to the grating, every point along the ξ-axis covers different distance to the curved surface, so it is affected by different optical path. From Figure 4.9, we calculate the optical path for every ray at ξ, resulting $\delta(\theta)=\mathrm{R}(1-\cos\theta)$. Then the phase change for every point $\xi(\theta)=\mathrm{R}\sin\theta$ corresponds to

$$\Delta(\theta)=\exp\left\lfloor ik\mathrm{R}(1-\cos\theta)\right\rfloor. \tag{4.14}$$

Performing a change of variables to Cartesian coordinates, eq. (4.14) results

$$\Delta(\xi)=\exp\left\{ik\mathrm{R}\left[1-\sqrt{1-\left(\frac{\xi}{\mathrm{R}}\right)^2}\right]\right\}. \tag{4.15}$$

On the other hand, the periodicity of the diffraction grating is not longer linear but angular. Then, its reflectance can be expressed as a Fourier series expansion depending on θ,

$$t(\theta)=\sum_n a_n \exp\left(iq_\theta n\theta\right), \tag{4.16}$$

being a_n the Fourier coefficients with n integer, $q_\theta=2\pi/p_\theta$ and p_θ the angular period whose relation with the linear period is $p_\theta=p/\mathrm{R}$. Performing the change of variables to Cartesian coordinates, eq. (4.16) results

$$t(\xi)=\sum_n a_n \exp\left[iq_\theta n \arcsin\left(\frac{\xi}{R}\right)\right]. \tag{4.17}$$

Considering equations (4.15) and (4.17), the field at the plane P, after being diffracted by the grating is

$$U_1(\xi,z=0)=A_0\sum_n a_n \exp\left\{2ikR\left[1-\sqrt{1-\left(\frac{\xi}{R}\right)^2}\right]\right\}\exp\left[iq_\theta n \arcsin\left(\frac{\xi}{R}\right)\right], \tag{4.18}$$

that is given by the product of the incident field, the reflectance of the grating and the phase difference corresponding to every ray. Since light covers twice the distance from the plane P to the grating due the reflective configuration, $\delta(\theta)$, the optical path doubles its value.

To calculate the field propagation from the plane P forward, we use the Fresnel approach, eq. (2.19), taking into account only the coordinates that define the propagation plane, x and z,

$$U_2(x,z)=\frac{\exp(ikz)}{\sqrt{ikz}}\int_{-L/2}^{L/2} U_1(\xi,z=0)\exp\left[\frac{ik(x-\xi)^2}{2z}\right]d\xi, \tag{4.19}$$

where x is coordinate perpendicular to the propagation axis at the observation planes, λ the illumination wavelength and $k=2\pi/\lambda$. To solve eq. (4.19) we consider that the radius is much larger than the illuminated length of the grating, $R>>L$, and we perform Taylor expansions in the exponents of eq. (4.18). Taking into account only up to second power in both Taylor expansions, the integral to solve is

$$U_2(x,z)=A_0\frac{\exp(ikz)}{\sqrt{ikz}}\sum_n a_n\int_{-L/2}^{L/2}\exp\left[ikR\left(\frac{\xi}{R}\right)^2\right]\exp\left(iq_\theta n\frac{\xi}{R}\right)\exp\left[\frac{ik(x-\xi)^2}{2z}\right]d\xi. \tag{4.20}$$

Then the field amplitude at near distances results,

$$U_2(x,z)=\frac{A_0}{2}\sqrt{\frac{R}{R+2z}}\exp\left(ikz+\frac{ikx^2}{R+2z}\right)\sum_n a_n\exp\left(\frac{inq_\theta x}{R+2z}\right)\exp\left(-\frac{in^2q_\theta^{\,2}z}{2kR(R+2z)}\right)$$
$$\times\left(\begin{array}{l} erf\left\{\dfrac{(1-i)\left[kR(L+2x)+2z(kL-nq_\theta)\right]}{4\sqrt{kzR(R+2z)}}\right\} \\ +erf\left\{\dfrac{(1-i)\left[kR(L-2x)+2z(kL+nq_\theta)\right]}{4\sqrt{kzR(R+2z)}}\right\}\end{array}\right), \tag{4.21}$$

where $erf(\gamma)$ is the error function, defined by $erf(\gamma)=\left(2/\sqrt{\pi}\right)\int_0^{\gamma}\exp(-\kappa^2)d\kappa$.

To understand better the behavior of the grating, we calculate the intensity just performing $I_2(x,z) = U_2(x,z)U_2^*(x,z)$. Thus, it results,

$$I_2(x,z) = \frac{I_0}{4}\frac{R}{R+2z}\sum_{n,n'} a_n a_{n'}^* \exp\left(\frac{i(n-n')q_\theta x}{R+2z}\right)\exp\left(-\frac{i(n^2-n'^2)q_\theta^2 z}{2kR(R+2z)}\right)$$
$$\times\left(\begin{array}{l} erf\left\{\dfrac{(1-i)\left[kR(L+2x)+2z(kL-nq_\theta)\right]}{4\sqrt{kzR(R+2z)}}\right\} \\ +erf\left\{\dfrac{(1-i)\left[kR(L-2x)+2z(kL+nq_\theta)\right]}{4\sqrt{kzR(R+2z)}}\right\}\end{array}\right)$$
$$\times\left(\begin{array}{l} erf\left\{\dfrac{(1+i)\left[kR(L+2x)+2z(kL-n'q_\theta)\right]}{4\sqrt{kzR(R+2z)}}\right\} \\ +erf\left\{\dfrac{(1+i)\left[kR(L-2x)+2z(kL+n'q_\theta)\right]}{4\sqrt{kzR(R+2z)}}\right\}\end{array}\right). \tag{4.22}$$

Basically, the effect of curvature is present into the exponential factors producing a variation on the longitudinal and transversal periods of the self-images. The other factors are due to finite length of the grating. In Figure 4.10a we show the amplitude for a grating with $R = 50\,\text{mm}$, $p = 20\,\mu\text{m}$, $L = 1\,\text{mm}$, $\lambda = 632.8\,\text{nm}$ and $n, n' = -3,-2,...,2,3$. The Fourier coefficients of the grating correspond to the plane grating and are given by $a_n = sinc(n\pi/2)$. The Talbot self-images x-periodicity varies, increasing in terms of the distance between grating and observation plane. For visual comparison, the near field diffraction pattern produced by a grating with the same characteristics but without curvature (which occurs when $R \to \infty$) is shown in Figure 4.10b.

From the first exponential factor of eq.(4.22), the transversal period of the self-images, $\hat{p}$, depends on the radius and the distance from the grating in the following way

$$\hat{p} = p\left(1+\frac{2z}{R}\right). \tag{4.23}$$

This transversal period increases linearly along distance from the grating for a fixed radius. As it was expected, $\hat{p} = p$ for $R \to \infty$.

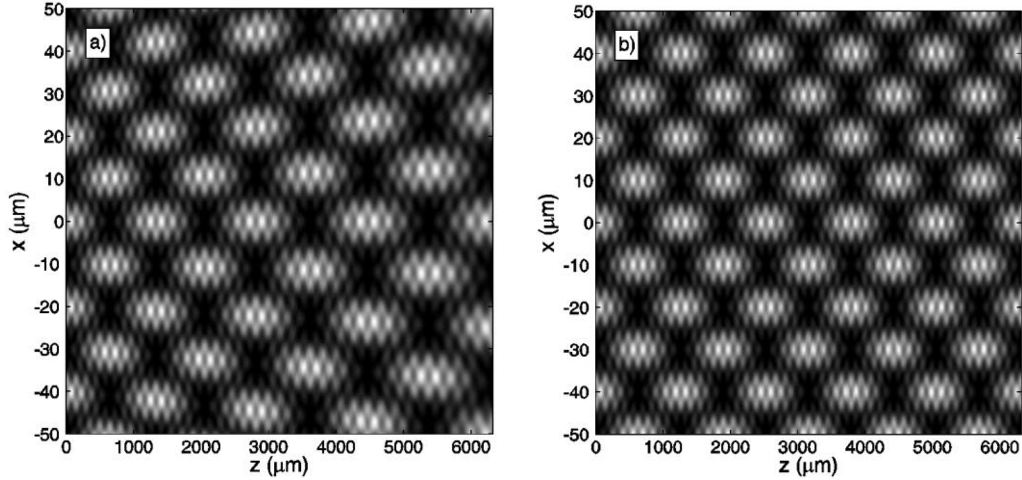

Figure 4.10: Analytical self-images for a grating with period $p = 20\ \mu m$, *illuminated projection of the grating* $L = 1\ mm$, *illumination wavelength* $\lambda = 632.8\ nm$ *and taking diffraction orders* $n, n' = -3, -2, \ldots, 2, 3$, *a)* $R = 50\ mm$, *b)* $R \to \infty$.

In Figure 4.11 we show the profiles corresponding to the first seven self-images of Figure 4.10a. To observe more clearly the effect, we have separated between even (Figure 4.11a) and odd (Figure 4.11b) self-images. As it can be observed, the period of the self-image increases with the order.

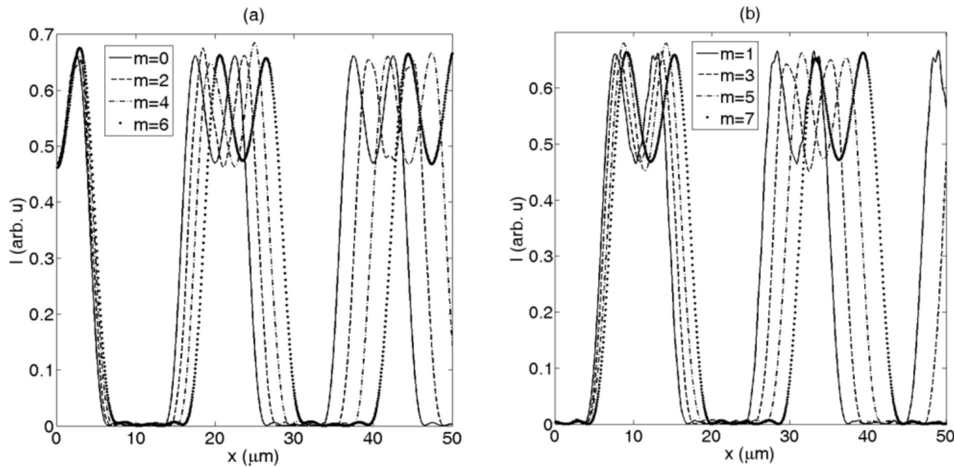

Figure 4.11: Profile of the first seven self-images corresponding to Figure 4.10a, a) even self-images, b) odd self-images.

In addition, the Talbot distance also varies linearly, following

$$\hat{z}_T = z_T \left(1 + \frac{2z}{R}\right)^2. \tag{4.24}$$

We show in Figure 4.12a the profile along the z-axis for $x = 0$, corresponding with Figure 4.10, the dashed line corresponds to a plane grating and the solid line to a curved grating

with $R = 50$ mm. In addition, in Figure 4.12b we show the location of the self-images in terms of the order of self-image for the same cases of Figure 4.12b. We can observe that the position of the self-image separates from a straight line following a quadratic dependence.

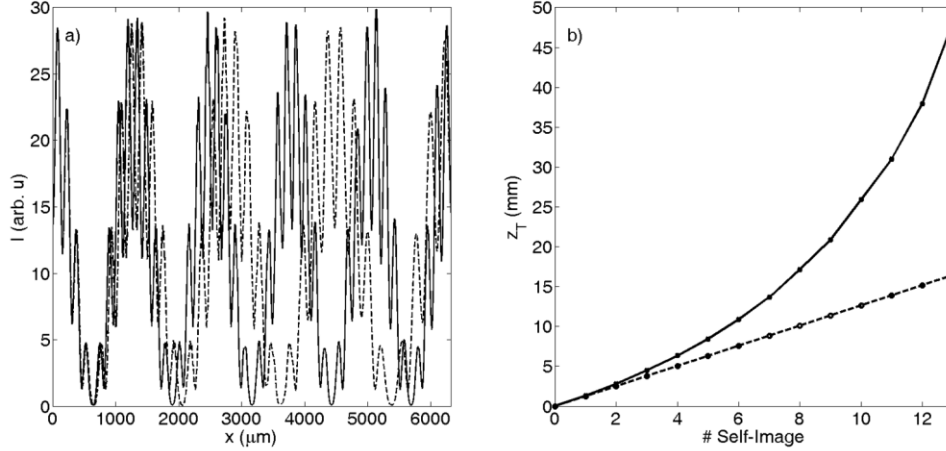

Figure 4.12: a) Profile of the self-imaging process (Figure 4.10) for $x = 0$ along the z-axis, plane grating (dashed line), curved grating (solid line), b) Behavior of the Talbot distance, z_T, in terms of the order of self-image, curved grating ($R = 50$ mm) (solid line), plane grating (dashed line).

To finally corroborate the consistence of eq. (4.22) with previous results, we carry out the limit for $R \to \infty$, which corresponds to plane grating, resulting

$$\begin{aligned} I_2(x,z) = \frac{I_0}{4}\sum_{n,n'} a_n a_{n'}^* \exp\left[\frac{i(n-n')2\pi x}{p}\right]\exp\left[-\frac{i(n^2-n'^2)(2\pi)^2 z}{2kp^2}\right] \\ \times\left(erf\left[\frac{(1-i)k(L+2x)}{4\sqrt{kz}}\right]+erf\left[\frac{(1-i)k(L-2x)}{4\sqrt{kz}}\right]\right) \\ \times\left(erf\left[\frac{(1+i)k(L-2x)}{4\sqrt{kz}}\right]+erf\left[\frac{(1+i)k(L-2x)}{4\sqrt{kz}}\right]\right). \end{aligned} \tag{4.25}$$

Finally, considering $L \to \infty$, the classical expression for Talbot effect is recovered [105],

$$I_2(x,z) = I_0\sum_{n,n'} a_n a_{n'}^* \exp\left[\frac{i(n-n')2\pi x}{p}\right]\exp\left[-\frac{i(n^2-n'^2)(2\pi)^2 z}{2kp^2}\right], \tag{4.26}$$

since $erf(\gamma \to \infty) \to 1$.

4.3.2 Experimental approach

We have manufactured a diffraction grating over a flexible steel substrate using the laser ablation system. The period of the engraved grating is $p = 20\,\mu\text{m}$. The nature of the

substrate allows to curve the grating, giving a cylindrical shape. The radius given to the grating is $R = 50\,\text{mm}$. The set-up is shown in Figure 4.13 and it is similar to the set-up used in Figure 4.6 but with a curved grating instead of a flat one. Since the grating acts in reflection configuration, a beam-splitter becomes necessary. Afterwards, light is captured by a CMOS camera ($\mu -$eye, pixel size $6\times 6\,\mu\text{m}$) coupled to a microscope objective, which is used to magnify the fringes. The camera is free to travel along the propagation axis. The experiment consists of displacing the camera along the propagation axis, acquiring images of the diffracted intensity at different planes. The use of a beam-splitter makes impossible to measure the firsts Talbot planes but the self-images behavior are still observed.

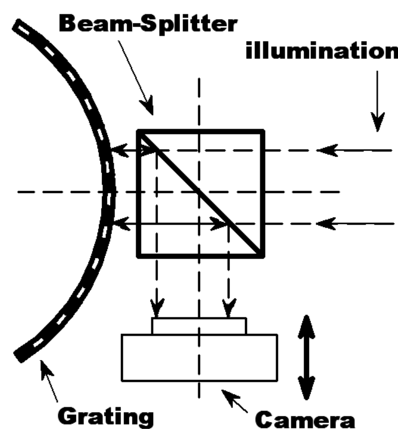

Figure 4.13: Scheme of the experimental set-up.

In Figure 4.14 the experimental measurements for a curved and a plane grating are shown. We have included into the images two straight lines to observe the increasing of the period. As it can be observed in (Figure 4.14a), the curvature of the grating produces changes into the period of the self-images and the Talbot distance, as it was found theoretically. On the other hand, in Figure 4.14b both lines are parallel, which reveals that the period of the fringes does not change for a plane grating. Due to experimental adjustments, the self-images are not exactly parallel to the x -axis, but the results corroborate the theoretical analysis.

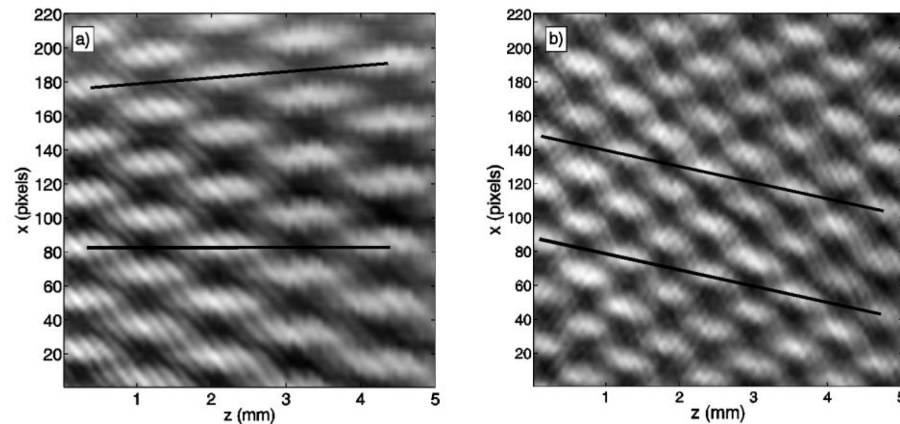

Figure 4.14: Experimental intensity distribution after the gratings, $p = 20\ \mu m$, $\lambda = 632.8\ nm$, *a)* $R = 50\ mm$, *b)* $R \to \infty$.

4.4 *Rough DOEs over steel tapes by means of laser ablation*

For simple structures, such as diffraction gratings, it is possible to develop theoretical models that allow us to predict their optical behavior as it has been shown in previous sections. For more complex devices, it is not always possible to carry out an analytical treatment. Thus, other design methods are required, such as numerical simulations and experimental analysis. In contrast to rough diffraction gratings, where the one-dimensional character of these devices allows us to dispense with the anisotropy of the substrate, in the case of bi-dimensional elements it is necessary to consider the anisotropy of the surface roughness. For example, Figure 4.15a shows an example of a binary DOE engraved over a steel sample. The analytical description of the diffraction field of this kind of devices is much more complex that in the case of rough diffraction gratings.

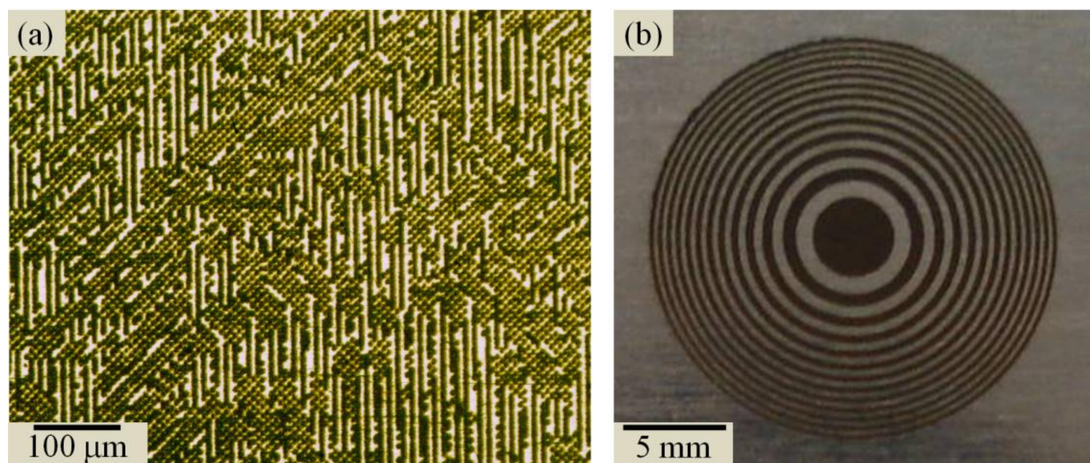

Figure 4.15: a) Example of binary DOE engraved on a steel sample with our laser ablation system. Microscope image (5×). Distance between pixels is 5 μm. *b) FZP engraved over steel sample. Focal length 450* mm.

We propose then the study of more complicated micro-optical designs. Concretely, Fresnel Zones Plates (FZP) are one of the most used micro-optical elements since they allow the focalization of a light beam with advantages over conventional lenses: there can be used, for example, over spectral regions where refractive lenses are useless (as UV), or in applications where their lower weight (in comparison with refractive lenses) suggest their use. The typical flat arrangement is well suited for the integration of diffractive lenses within a micro-optics set-up [102], [103]. On the contrary, FZP presents some disadvantage such as their worse optical behavior. For example, a FZP presents a principal focus, and a collection of higher order foci. The appearance of multifoci implies the reduction of optical efficiency, and a worse concentration capability in the principal focus. With regard to binary-amplitude FZP, a modulation in amplitude implies lost of irradiance at the observation plane.

We center our analysis in FZP engraved over rough steel tapes (rough FZP, or RFZP) with two different levels of roughness (on one hand the roughness of the steel substrate, and on the other hand the roughness produced by the laser ablation process) working in reflection configuration. Moreover, anisotropy due steel fabrication processes has been also included in the theoretical model. We will analyze the focusing properties of RFZPs in terms of the statistical properties of roughness. A generalized analytical method, including two different roughness levels and anisotropy seems to be unattainable. The results obtained for the RFZPs can be extended to any binary diffractive element engraved on a steel tape. For the roughness description, we assume a Gaussian distribution of surface heights (based on experimental data). Roughness should also be higher than wavelength. Referring to the numerical analysis, we have used the scalar theory for the light propagation, in particular Rayleigh-Sommerfeld approach, shown in Section 2.3.2.

4.4.1 Rough Fresnel zone plates

A Fresnel Zone Plate (FZP) is one of the most used micro-optical elements since they concentrate light at the focal point placed at a distance f from the FZP. These diffractive lenses present some advantages over conventional lenses. They can be used, for example, over spectral regions where refractive lenses are useless (as UV), or in applications where low weight is required. A FZP consists of alternately opaque and transparent rings (in the transmission case) or reflective and non-reflective rings (in the reflective case). These elements have been known for more than 100 years [18], [127]-[129], and they can be manufactured by laser ablation. The transmitivity function $L(x, y)$ results in [130]

$$L(x,y)=\begin{cases}1 & if\ \sqrt{m\lambda f}\le x^2+y^2<\sqrt{(m+1)\lambda f}\\ 0 & if\ \sqrt{(m-1)\lambda f}\le x^2+y^2<\sqrt{m\lambda f}\end{cases} \tag{4.27}$$

where λ is the wavelength, f is the focal of the FZP, and m is an integer $m=1,2,3\ldots$ With this definition, the central ring is opaque, and FZP is called then "even" or "negative" FZP. In Figure 4.16a we show an example of a negative FZP designed following eq.(4.27), for a focal length $f=450$ mm.

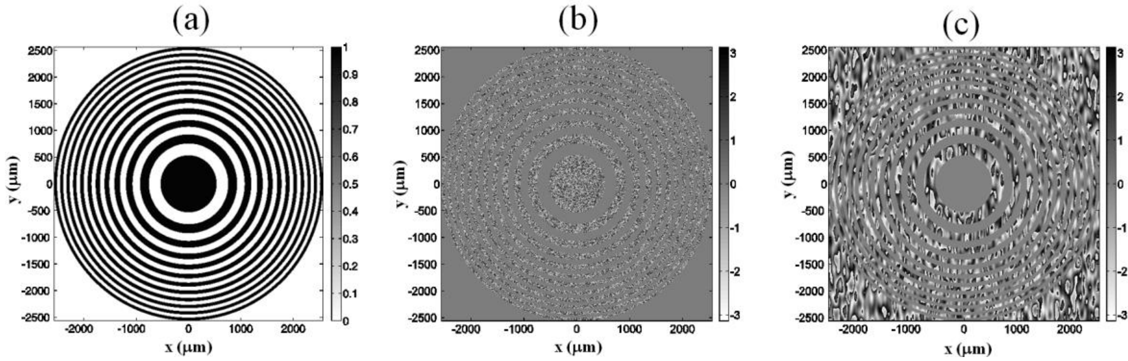

Figure 4.16: Images of the Fresnel zone plate used in the simulations. The FZP presents a focal length of $f=450$ *mm, a) Ideal FZP; b) phase map of a RFZP engraved by laser ablation (data from Table 4.2:* $\sigma_2=0.27\ \mu m$*,* $T_{2x}=4.2\ \mu m$*,* $T_{2y}=4.8\ \mu m$*) over a flat surface,* $\sigma_1=0\ \mu m$*; c) phase map of a RFZP engraved by laser ablation over a real surface with low roughness level (data from Table 4.2* $\sigma_1=0.05\ \mu m$*,* $T_{1x}=50.23\ \mu m$*,* $T_{1y}=164.38\ \mu m$*) but with* $\sigma_2=0\ \mu m$*.*

	T_x	T_y	σ
Substrate with low roughness level	50.23 μm	164.38 μm	0.06 μm
Substrate with high roughness level	11.60 μm	119.20 μm	0.16 μm
Substrate after ablation process	4.20 μm	4.80 μm	0.26 μm

Table 4.2: Roughness values obtained by confocal microscopy from the two manufactured RFZPs.

Let us follow the same formalism used to describe the rough gratings in Section 4.2. Since the RFZP is engraved on a steel tape, we need to know the topographical properties of roughness. Let us assume again that steel samples present stochastical topography $h_1(x,y)$ [108]. Let us assume that the statistical height distribution of the topography, $p(h)$, presents a Gaussian distribution. Considering that the mean height of the topography is null, $\langle h\rangle_s=\int_{-\infty}^{\infty}hp(h)dh=0$, where $\langle\ \rangle_s$ denotes spatial averaging, the standard deviation of

heights is given by $\sigma = \sqrt{\left\langle h^2 \right\rangle_s}$. The important parameter to characterize the surface roughness is the correlation distance, which can be determined from the autocorrelation function of $h(x,y)$, defined by $C(\mathrm{R}) = \left\langle h(r)h(r+\mathrm{R}) \right\rangle_s / \sigma^2$, where r is the spatial coordinate. The surface correlation function is normally assumed as Gaussian,

$$C(R) = \exp\left(-\frac{\mathrm{R}^2}{T^2} \right), \tag{4.28}$$

where T is the correlation length, being the distance over which the correlation function falls by $1/e$, and indicates the rate of change of surface height along the surface. Due to the fabrication process the surface is not normally isotropic. Therefore we need to define the correlation length for each direction, T_x and T_y.

The ablation process produces a local change in the topography. Moreover, a superficial ablation of the material produces a change in roughness, and a slight variation in the mean depth, as we will see in Section 4.4.3. Under this condition, the ablation process modifies the original topography $h_1(x,y)$ to a new topography $h_2(x,y)$ with different statistical properties. Then, we will describe the statistical properties of the steel surface by T_{1x}, T_{1y} and σ_1. and those of the ablationed zone by T_{2x}, T_{2y} and σ_2. It should be noted that, in contrast to Section 4.2.2, we need to take into account the roughness along both directions.

Finally, the reflectance of the RFZP is

$$r(x,y) = L(x,y)\exp[-2ikh_1(x,y)] + [1 - L(x,y)]\exp[-2ikh_2(x,y)]. \tag{4.29}$$

Eq. (4.29) allows us to generalize the description of any binary diffractive element over a steel tape, not only to FZPs. In this general case, $L(x,y)$ is the expression for the shape of the diffractive element, that is, the non-ablationed zone.

In order to determine the field after the RFZP, let us consider a plane wave $U_0(\xi,\eta) = A_0$ illuminating the diffractive element $L(x,y)$. The near field can be determined using the Fresnel integral,

$$U(x,y,z) = \frac{A_0\, \mathrm{e}^{ikz}}{i\lambda z} \iint r(\xi,\eta)\, \mathrm{e}^{i\frac{k}{2z}\left[(x-\xi)^2 + (y-\eta)^2\right]}\, d\xi d\eta, \tag{4.30}$$

where z is the distance between the diffractive element and the observation plane, λ is the wavelength, and $k = 2\pi/\lambda$.

An analytical development of eq. (4.30), taking into account a rough and anisotropic topology, results hard and tedious. On the contrary, numerical methods lead us to analyze the optical behavior of any rough binary diffractive element, regardless of its forms. In Section 4.4.2 we explain how to determine the optical field diffracted by a RZFP.

4.4.2 Numerical simulations of rough diffractive lenses

To solve the Rayleigh-Sommerfeld diffraction integral, we have used the Fast-Fourier-Transform-based Direct Integration (FFT-DI) method explained in Section 2.3.2. The approach is accurate whereas the features of the mask (the FZP) are larger than the wavelength. In addition, we need to simulate surfaces with stochastical topology. We make use of software based on ref. [107] to generate virtual topologies which present a selected correlation length and a standard deviation, assuming that the spatial distribution follows a Gaussian distribution. Rough topology is included as phase variations over the RFZP.

For the simulations, we consider the experimental conditions detailed in Section 4.4.3. The light source is a plane wave with wavelength $\lambda = 632.8\ \text{nm}$, which illuminates the RFZP in normal incidence. Here we have used the FZP from Figure 4.16a ($f = 450\ \text{mm}$, 512×512 pixel number) as a guide for our simulations. The roughness values are suggested by experimental results, collected in Table 4.2 and explained in detail in Section 4.4.3. When the FZP is engraved on a flat surface (without roughness) the result is similar to that shown in Figure 4.16b, where the rough surface simulates the ablation process. On the other hand, a flat FZP engraved over a rough surfaces is shown in Figure 4.16c. Additionally two examples of RFZPs with σ_2 from Table 4.2 and two different values for σ_1 (that means, with different value of roughness in over the sampling without ablation process) are shown in Figure 4.17a and Figure 4.17b, emulating the real RFZP manufactured. These masks will be used in our simulations.

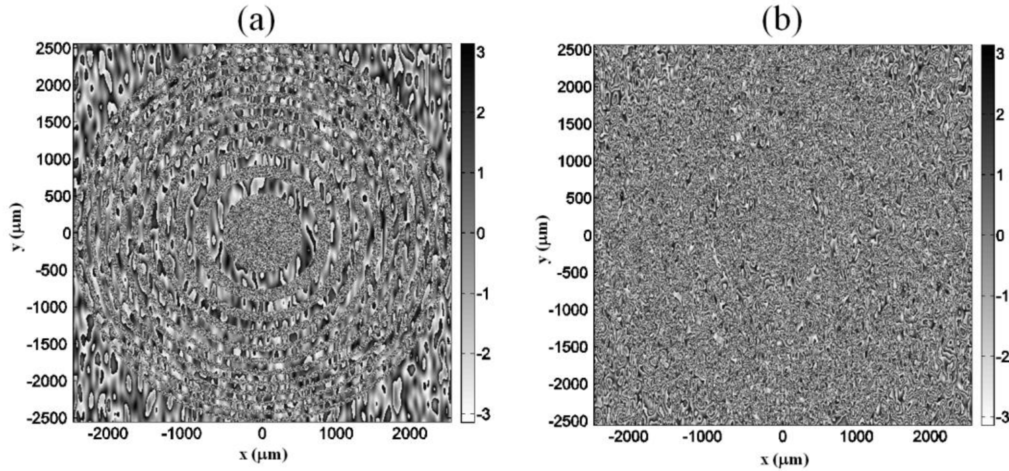

Figure 4.17: a) Simulation of a RFZP engraved by laser ablation over a real surface with low roughness level (data from Table 4.2: $\sigma_1 = 0.05\ \mu m$, $T_{1x} = 50.23\ \mu m$, $T_{1y} = 164.38\ \mu m$; *b) Simulation of a RFZP engraved by laser ablation over a real surface with high roughness level (data from Table 4.2:* $\sigma_1 = 0.15\ \mu m$, $T_{1x} = 11.60\ \mu m$, $T_{1y} = 119.20\ \mu m$.

To understand the importance of the substrate roughness, we first analyze the dependence of the focusing capability of the RFZP in terms of the standard deviation of the substrate, σ_1. In Figure 4.18a the maximum intensity at the focal plane is shown for FZPs with a lens similar to the lenses shown in Figure 4.16, but for different values of σ_1, normalized to the maximum (obtained with $\sigma_1 = 0$). The intensity at the focus decays strongly as σ_1 increases. The intensity profile along z-axis (propagation axis) for five different values of σ_1 is shown in Figure 4.18b, normalized again to the maximum. We can appreciate how the focusing capability decreases as σ_1 increases. It is also notorious that the depth of focus remains unchanged, despite the variation in σ_1. In Figure 4.18c and Figure 4.18d we show the same results, but varying σ_2 (corresponding to Figure 4.16c). Also, the depth of focus is independent on σ_2. For this case, there exists a superior limit for the focusing capability. By means of laser ablation it is possible to reach this limit, but not to go beyond it. This fact lead us to center our discussion in the effect of σ_1, as the appropriate parameter to controls the optical behavior of the RFZP.

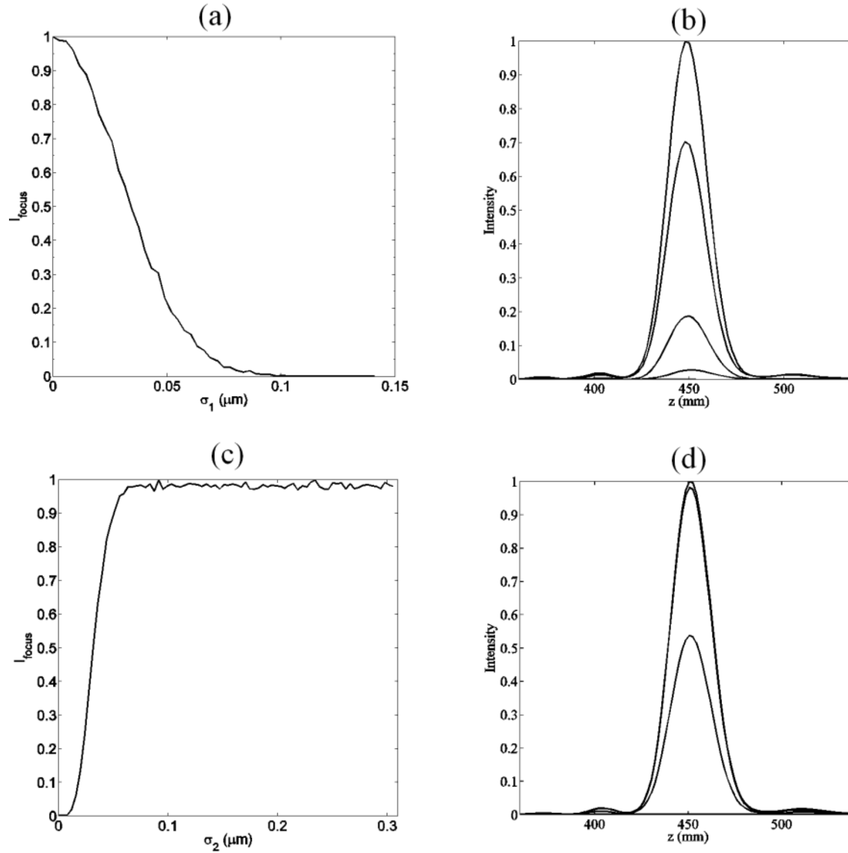

Figure 4.18: Dependence of the focusing capability with roughness. a) Maximum of intensity at the focal plane for different values of σ_1*, , with* $\sigma_2 = 4.5\ \mu m$*; b) irradiance profiles along z -axis for different values of* σ_1*:* $0\ \mu m$ *(highest),* $0.01\ \mu m$*,* $0.03\ \mu m$*,* $0.05\ \mu m$ *and* $0.07\ \mu m$ *and the same value for* $\sigma_2 = 4.5\ \mu m$*, normalized to the maximum; c) Maximum of intensity at the focal plane for different values of* σ_2*, with* $\sigma_2 = 0.05\ \mu m$*; and d) irradiance profiles along z-axis for different values of* σ_2*: (*$0\ \mu m$ *- the lowest one-,* $0.03\ \mu m$*,* $0.06\ \mu m$*, and* $0.1\ \mu m$*) and the same value for* $\sigma_1 = 0.05\ \mu m$*, normalized to the maximum.*

4.4.3 Experimental results

The FZP of Figure 4.16 has been engraved over two different samples of steel using the laser ablation system described in Section 3.5. In order to minimize the spot size, we operate at $355\ \text{nm}$. The system is arranged to work as a plotter, so we can manufacture a mask pixel by pixel. The manufactured RFZP are shown in Figure 4.19a (with a low roughness level steel sample) and Figure 4.19b (with a high roughness level steel sample).

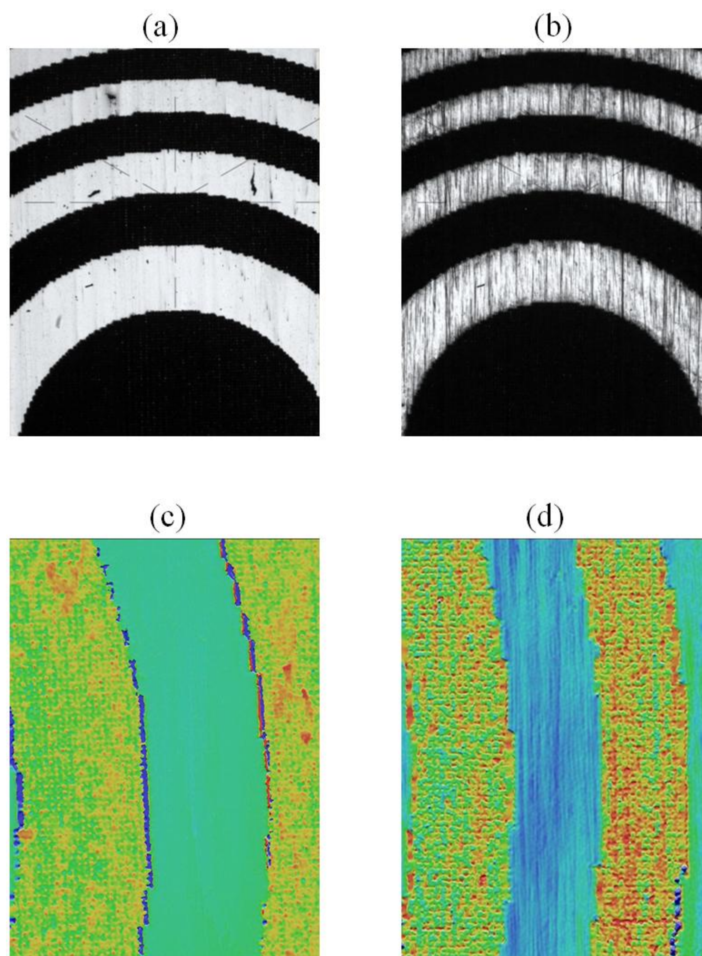

Figure 4.19: a) and b) Optical microscopy image of a RFZP for low and high roughness steel substrates respectively; c) and d) confocal microscopy image of a RFZP for low and high roughness steel substrates, respectively.

We have measured the surface topography of the samples (Figure 4.19c and Figure 4.19d) from images obtained using a confocal microscope (Plμ by Sensofar, Spain). The roughness parameters of the RFZP measured from the images have been collected in Table 4.2. The correlation length depends on the direction, due the fabrication process of the steel tapes. Therefore we have used T_x and T_y to simulate the correlation length in the x and y directions.

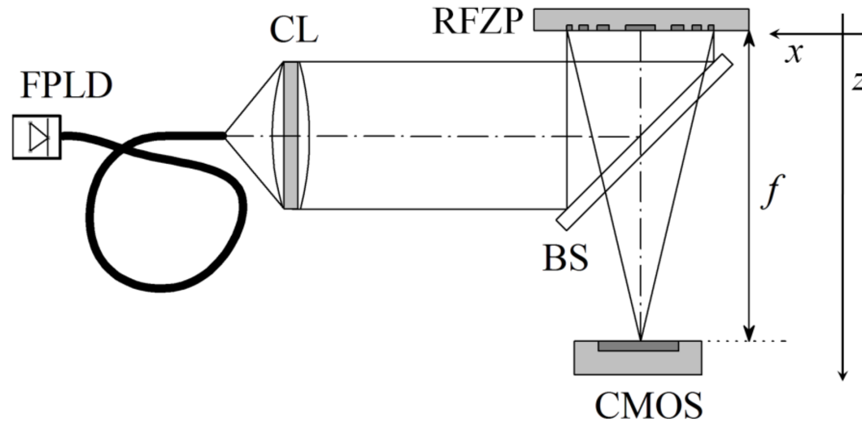

Figure 4.20: Experimental set-up. FPLD is a Fiber Pigtailed Laser Diode, CL is a Collimation Lens, BS is a Beam Splitter and f is the focal length of the RFZP.

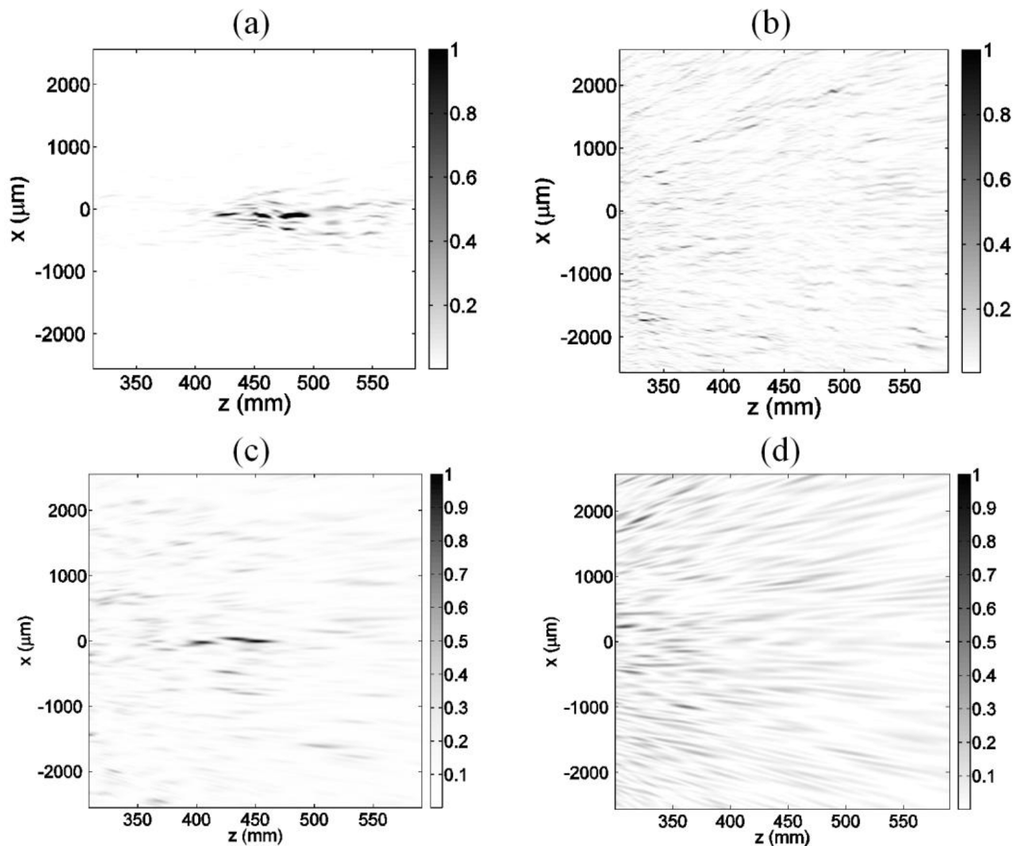

Figure 4.21: a) and b) Transversal view of the propagation of light with RFZP from Figure 4.19a and Figure 4.19b, respectively (experimental data); c) and d) simulations with Rayleigh-Sommerfeld approach of propagation of light from Figure 4.19a and Figure 4.19b respectively.

In order to perform the experimental verification of the results obtained from the simulations, we have used the set-up shown in Figure 4.20. The beam produced by a Fiber Pigtailed Laser Diode (FPLD, with $\lambda = 632.8\,\text{nm}$) impinges over the RFZP in normal incidence. The use of a fiber pigtailed diode ensures a filtered and Gaussian-like beam, and with a Collimation Lens (CL) we obtain a quasi-plane wavefront to illuminate the RFZP. In

order to obtain a perpendicular illumination, we use a 50/50 Beam Splitter (BS) placed at 45º with the beam propagation direction. The light reflected by the RFPZ is redirected trough the BS to a CMOS (UI-1220-M by U-Eye, Germany), with a pixel pitch of $6\,\mu\text{m}$. The camera is mounted over a motorized linear stage, so it can travel along propagation axis and images can be acquired at any desired plane. Under these conditions, we have obtained the intensity distribution along the propagation axis around the focus of the RFZPs. In Figure 4.21, we show a transversal view of the propagation of the light using a RFZP with low roughness level (Figure 4.21a) and with high roughness level (Figure 4.21b), obtained experimentally with the described set-up. The substrates in which lenses were engraved can induce optical aberrations, due the overall lack of flatness of the surface. For comparison, we show the Rayleigh-Sommerfeld simulations for the same cases in Figure 4.21c and Figure 4.21d respectively. The simulated lenses are not exactly equal to the fabricated lenses, but they have the same statistical parameters. Light concentration clearly appears for low roughness of the steel substrate, whereas for high roughness the RFZP does not present focusing capability, corroborating the predictions shown in Figure 4.18. The simulations shown in Figure 4.21c and Figure 4.21d also show a concentration of light around the focus for the low roughness level FZP, and the absence of light concentration for a high roughness level. A completely coincidence between experimental and simulated results is not expected, since we do not use exactly the same topography for the simulation and the experiment but they have the same statistical properties.

4.5 *Application of the results: micromachining of annular gratings*

Along this Chapter, we have seen that steel tapes can be a good substrate for micro-.optical applications, and pulsed laser micromachining of steel surfaces is an advantageous method for DOEs manufacturing. We have characterized the manufactured devices, and we have found analytical expressions ruling the propagation under real conditions. In this sense, we have studied the diffraction after rough devices, and the effect of the curvature of the grating on the self-imaging phenomenon.

However, this work would be not completed if we do not considerate the application of our results in industrial environments. The collaboration with FAGOR AUTOMATION S. COOP. in this point results indispensable. In this sense, and after the results shown in this Chapter, we have started a project (INNPACTO Fore 2010) in partnership within ROFIN-BAASEL

ESPAÑA S.L.U. (a company centered in industrial laser systems for cutting, welding, marking and other laser applications) and the leadership of FAGOR AUTOMATION S. COOP. in order to implement new technologies for annular gratings production.

The main aim is the implementation of an industrial system with the capability of engraving gratings over non-flat metallic surfaces (typically, steel cylinders, but also other kind of substrates). The intention is to engrave by means of pulsed laser micromachining, due the results of this Thesis. The annular gratings manufactured will be commercialized within the annular encoders by FAGOR AUTOMATION S. COOP.

The task of the AOCG in this project involves the parameterization of the system and the evaluation and characterization of the gratings. It is expected that the fulfillment of the objectives of the project will lead to the production of scientific works. It is also expected the generation of an industrial patent in the field of annular gratings manufacturing.

The project began in 2010 with a duration of 3 years, and a budget of 2.700.00€. It will imply the consolidation of this research line, the stabilization of the current research staff and the acquisition of new equipment for laser micromachining tasks.

5 DOEs embedded in fused silica with nanosecond pulsed lasers

Micro-optical devices embedded in transparent materials are usually manufactured focusing a pulsed laser in-bulk fused silica. Under this condition, pulse width becomes the most important parameter that rules the size of the inscriptions. Ultrafast pulses (pico- and femtosecond pulses) avoid thermal effects and the results present a high efficiency. Nevertheless, nanosecond lasers are more available, due the reduced costs. Therefore, a study of the optical behavior of embedded elements micromachined by nanosecond pulses is required. In this work, we show that this regime of pulses can still be used for engraving Diffractive Optical Elements in transparent materials, regardless of the thermal damage. A Fresnel zone plate and a far-field beam shaper have been manufactured as an example of the functionality of these devices.

5.1 *Introduction*

We have seen in the previous section the possibility of steel micromachining by means of laser ablation for micro-optical purposes. Now, we show the possibility of micromachining transparent dielectrics by means highly focused lasers [131]-[133]. This technique represents a good alternative for fabrication of waveguides [134], optical memories [135] or photonic crystals [136]. Although it is possible to engrave on the surface of the transparent sample [89], advantages of engrave in bulk transparent materials are clear. For example, it allows isolating the optical element from external agents [94], and it is also possible to fabricate three-dimensional elements [137], [138], [139]. There is always a clear interest on the minimization of the production costs of this kind of devices [140]. In this sense, laser ablation with pulsed lasers has become an important alternative in the manufacturing of micro-optical devices in transparent substrates.

Ultra fast laser inscription is used in a wide variety of glasses to manufacture embedded DOEs [141]. This technology requires a relative complex system. Several processes during the interaction light-matter with pulsed lasers are involved [142]. Thermal effects produced during the interaction between light and matter can produce undesired effects, which can be minimized using short- and ultrashort-pulses lasers (picosecond and femtosecond pulses laser) [79]. In the range of long pulse widths (nanosecond pulses), micro-cracks appear surrounding the damaged zones, even at fluencies near the Laser Induced Damage (LID) threshold of the material [143]. For that reason, the efforts in the micromachining of transparent materials are focused in the short- and ultra-short pulses laser. In the present work, we use a simple nanosecond laser to engrave DOEs in bulk fused silica. Although this technique produces elements with lower efficiency than photolithography or femtosecond laser inscription, it can be performed in just one single step. Then, it can be useful for rapid prototyping of DOEs. Actually, most of the works in this field are centered in femtosecond laser micromachining. On the contrary, in this chapter the optical behavior of DOEs in transparent materials micromachined by means of nanosecond pulses trains is shown. The low number of works in this field using nanosecond pulse lasers is usually centered in the study of the light-matter interaction. In fact, the phenomenology involved in this kind of interaction is not yet well known due the amount of effects implicated during the process. The use of diffractive optical elements micromachined by this kind of lasers is not well

studied. In this sense, the present work pretends to illustrate the possibilities of nanosecond pulse lasers in the field of bulk fused silica micromachining.

5.2 *Micromachining of fused silica by nanosecond pulses ablation*

For the fabrication of DOEs in bulk fused silica we have used again the laser ablation system described in Section 3.5 working at $\lambda = 355\,\text{nm}$. The transparent sample is located over the two-axis linear stage. The laser beam is focused in bulk glass, similarly to the image shown in Figure 3.19a. The system is arranged to work as a plotter, so we manufacture the masks pixel by pixel.

We use fused silica microscope slides as substrate, since they are inexpensive and easy to find. The thickness of the samples is $1\,\text{mm}$ and they present a high quality surface. We have used a repetition frequency of $20\,\text{KHz}$, with a pulse width of $\tau = 12\,\text{ns}$. As we have mentioned, thermal effects become important in the long-pulses regime working with fused silica, due the strong dependency between thermal and mechanical properties of the sample. With this configuration, we analyze the behavior of the glass for multi-pulse damage. In order to minimize the thermal damage and energy propagation, we use pulses with low energy. Figure 5.1 shows the shape of the damages produced by the laser pulses. The evolution of the damages with the number of pulses and the fluence can be appreciated in Figure 5.1a, and a more detailed image is shown in Figure 5.1b. As it can be observed, there are two different regions of damage. One of them consists of dark zones, appearing due the accumulation of pulses. The nature of these zones is usually assumed as process of heating/melting in the glass with a transition dielectric/metal [143]. After a certain number of pulses appear highly-absorbing zones with a metal-like state inside the dielectric. Our purpose is to use these highly-absorbing zones as dark zones for binary amplitude masks. The other kind of damage consists of breaks in the glass, due the high temperatures reached with the focalized laser that can induce some kind of aberrations in the wavefront.

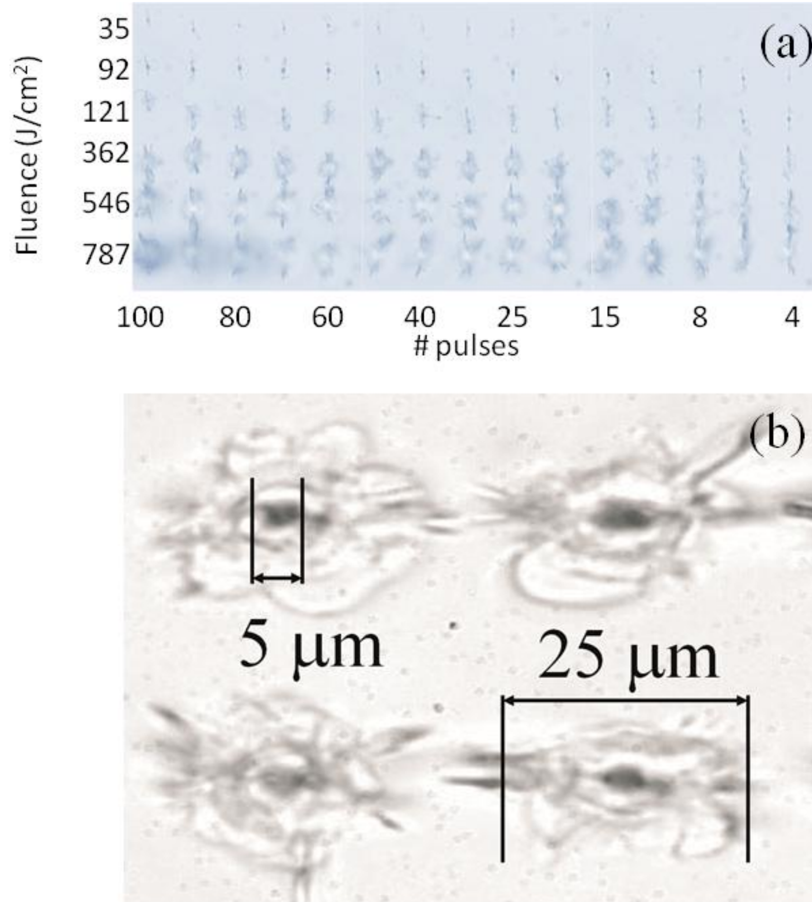

Figure 5.1: Calibration process; a) calibration of damages for different values of fluence and different number of pulses; b) shape of the damages obtained with $\tau = 12\ ns$ and $F = 546\ J/cm^2$. (20× optical microscopy). Dark zones are surrounded by thermal break zones.

The widths of the damages, along x-and y-axis, obtained for different number of pulses and different fluences, are collected in Figure 5.2a and Figure 5.2b. These data were obtained after averaging over 256 measurements for each value of fluence and for each number of pixels. We can appreciate that there exist a clear dependence between the width of the dark zone and the fluence at focus. The dependence with the number of pulses, however, is not so clear. Moreover, there exist a strong asymmetry between x-axis and y-axis. In order to reach a good accuracy it is important to obtain a circular-like pixel shape. In Figure 5.2c the difference between dark zones width along x-axis and y-axis is plotted. The minimum difference (and, consequently, the more circular-like shape) is obtained for low fluencies.

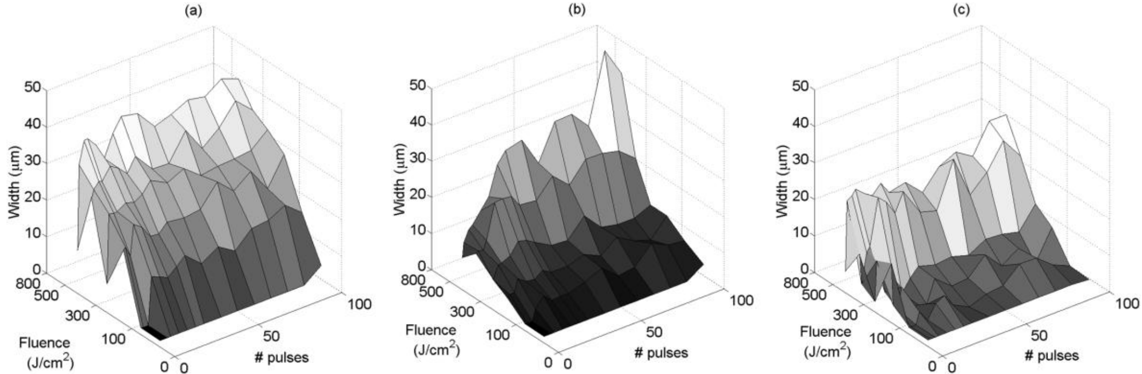

Figure 5.2: Dark zones widths at 20 KHz *and* $\tau = 12$ *ns for different number of pulses and different values of fluence, a) along* x *-axis and b) along* y *-axis; c) differences between width along* x *-axis and width along* y *-axis.*

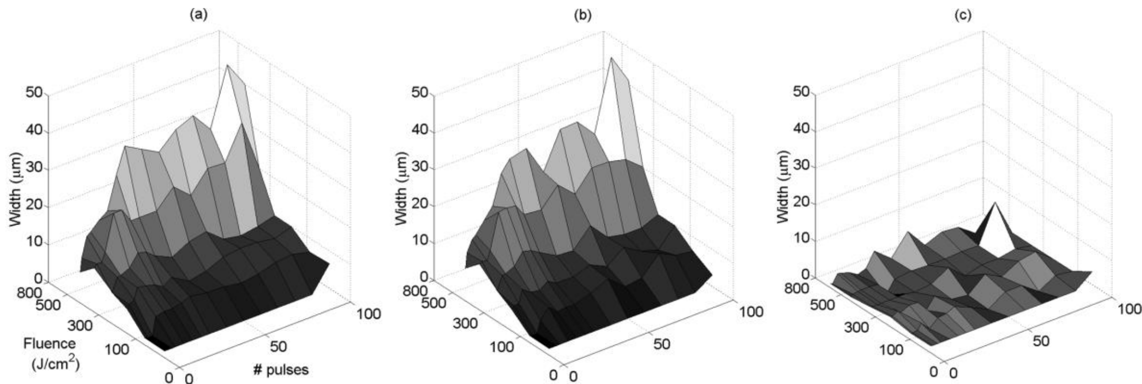

Figure 5.3: Thermal breaks widths at 20 KHz *and* $\tau = 12$ *ns for different number of pulses and different values of fluence, a) along* x *-axis and b) along* y *-axis; c) differences between width along* x *-axis and width along* y *-axis.*

Moreover, we have experimentally found that when the thermal damages around two dark zones are too close, thermal breaks can propagate along the glass, destroying it. The evolution of the width of the thermal damages is shown in Figure 5.3. In addition to the effect of the fluence, a dependence with the number of pulses can be observed. Moreover, for a low number of pulses, the shape and width of this thermal damage is not constant. Repeatability is an important factor in diffractive elements fabrication. For these reasons, our interest is to find an optimal solution where a number of pulses produce the smaller thermal damage width and with a constant shape of the dark zones. We have performed a calibration with different power, number of pulses and separation of dark zones, finding that the optimal solution without breaking the glass results for 20 pulses with $7\ \mu\text{J}$, with a fluence in focus of $92\ \text{J}/\text{cm}^2$ and a separation of $10\ \mu\text{m}$ between pixels. The lack of works with DOEs micromachined by nanosecond pulse lasers is probably due to the impossibility to avoid the micro-cracks due the thermal effects, as it is shown in the calibration data of Figure

5.2 and Figure 5.3. The chosen parameters minimize thermal damage and anisotropy of the dark zones, allowing also a good repeatability ratio.

With this technique, we can engrave any desire pattern embedded in fused silica, as shows Figure 5.4. The optical behavior of this kind of structures is described in the next Sections.

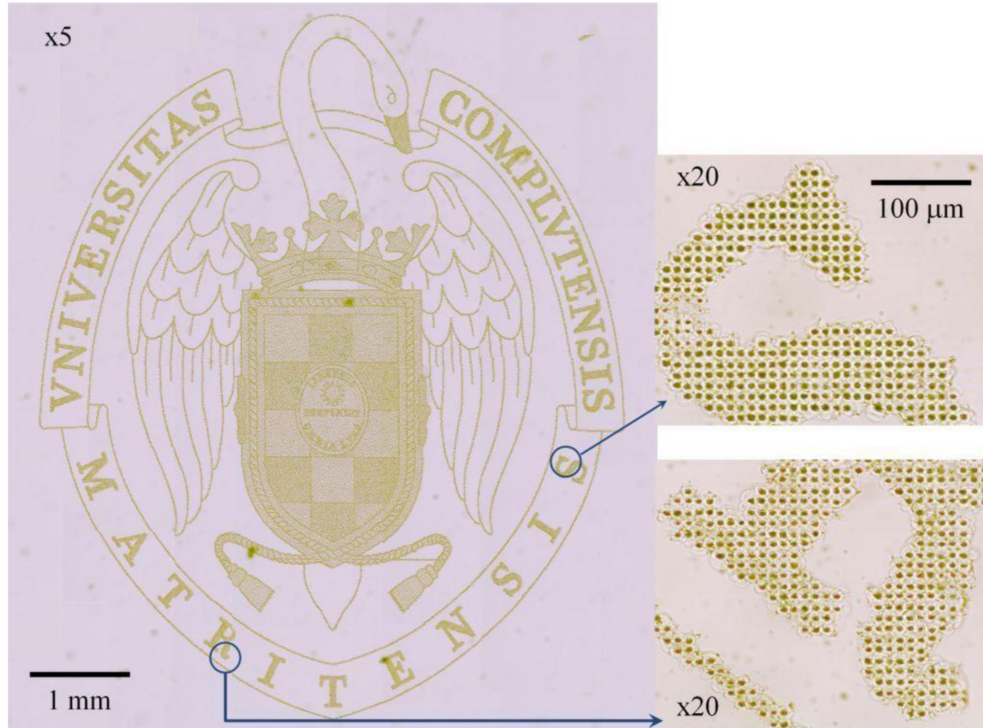

Figure 5.4: Complutense University emblem embedded in bulk fused silica by nanosecond laser pulses (microscopy image). Distance between pixels is $10\ \mu m$*. The image with* $5\times$ *objective is compound of 64 images.*

5.3 *Binary Amplitude Diffractive Optical Elements*

Once we have analyzed how laser engraving affects to pixels generation in bulk glass, now we can fabricate DOEs. Due to the characteristics of the laser damage in bulk fused silica, we can engrave binary DOEs that modify the amplitude of the incident field. The engraved DOE consists of a pixelated mask with two levels of transmitivity: opaque and transparent pixels. In Figure 5.5 a schematic view of the system is shown. In order to study the optical behavior, we have engraved two DOEs with different characteristics: a Fresnel zone plate and a DOE for beam shaping, generating a certain intensity distribution in the far field.

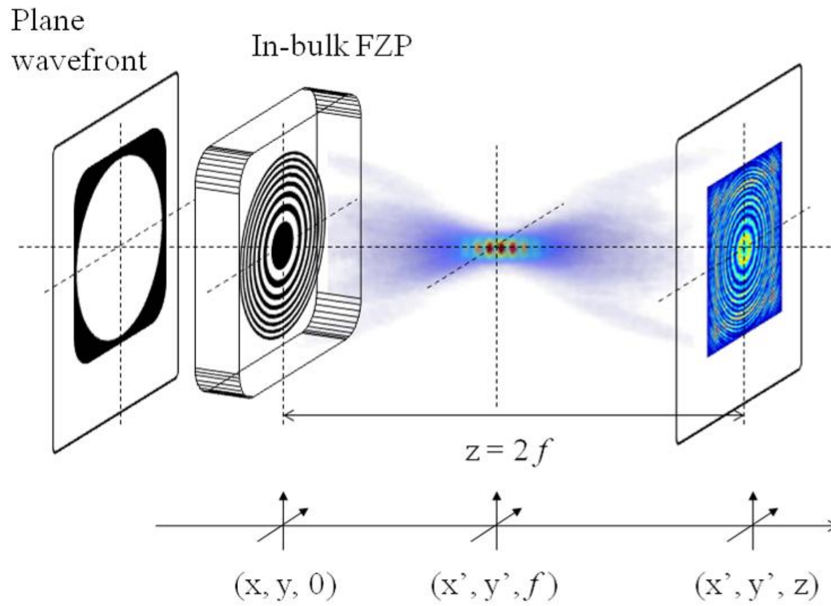

Figure 5.5: Schematic view of the system working with an embedded FZP.

5.3.1 Rough Fresnel Zone Plates

The Fresnel Zone Plate (FZP) has been defined in Section 4.4.1. In Figure 5.6a we show an example of a FZP for a focal length $f = 450$ mm. Also, a microscope view of a FZP engraved into a bulk fused silica sample is shown in Figure 5.6b.

FZP has been designed to work in transmission at $\lambda = 632.8$ nm . Following the schemes of Figure 5.5, and illuminating with a Laser Diode emitting at the working wavelength, modulated light after the DOEs is collected with a CMOS (UI-1220-M by U-Eye, Germany), with a pixel pitch of $6\ \mu\text{m}$. The camera is mounted over a motorized linear stage, so it can travel along propagation axis and images are acquired at any desired plane, as usual. Under these conditions, we have obtained the intensity distribution along the propagation axis (Figure 5.6c). This propagation is compared with a numerical simulation. We have used the scalar theory for the light propagation, in particular the Rayleigh-Sommerfeld approach described in 2.3.2. With this algorithm, we have computed the propagation around the focus of the binary Fresnel lens, assuming Thin Element Approximation (TEA, explained in Section 2.2.3). This simulation is plotted in Figure 5.6d The results are very similar in both cases except for a slight asymmetry in the experimental intensity distribution.

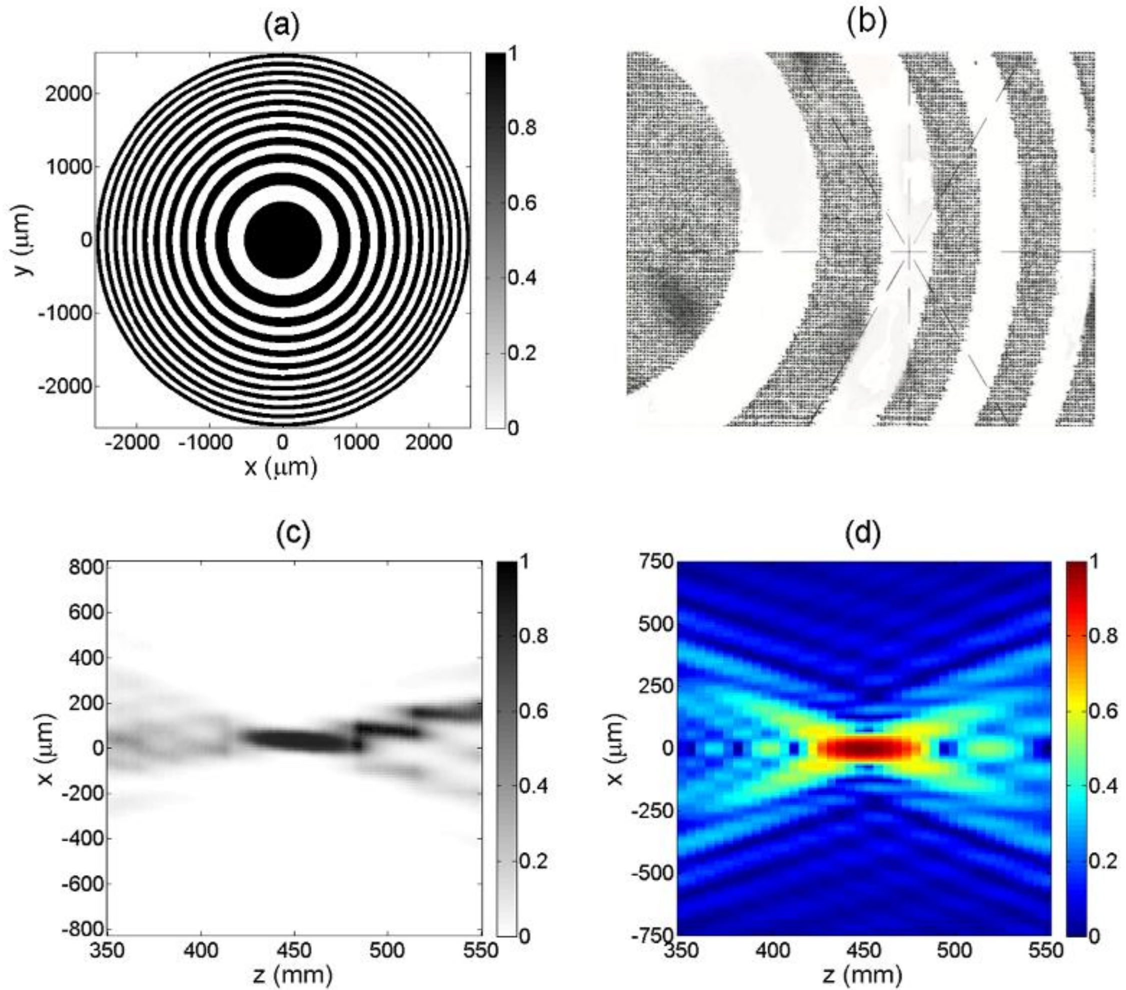

Figure 5.6: a) Binary amplitude FZP with $f = 450\ \text{mm}$ *; b) Microscopy image of the FZP in bulk fused silica (5× optical microscopy). Separation between pixels is* $10\ \mu\text{m}$ *; c) experimental propagation after the embedded FZP around the principal focus; d) simulation obtained with Rayleigh-Sommerfeld approach for the same parameters.*

5.3.2 Diffractive beam shaper in the far field

Another kind of diffractive element that can be engraved in bulk fused silica is a beam shaper, which is an optical element that transforms an incoming wavefront $U(x, y, 0)$ into a desired intensity distribution at an observation plane z, as it is shown in Figure 5.7. When the wavefront is modulated by means of diffraction, it is called Diffractive Beam Shaper (DBS) [10].

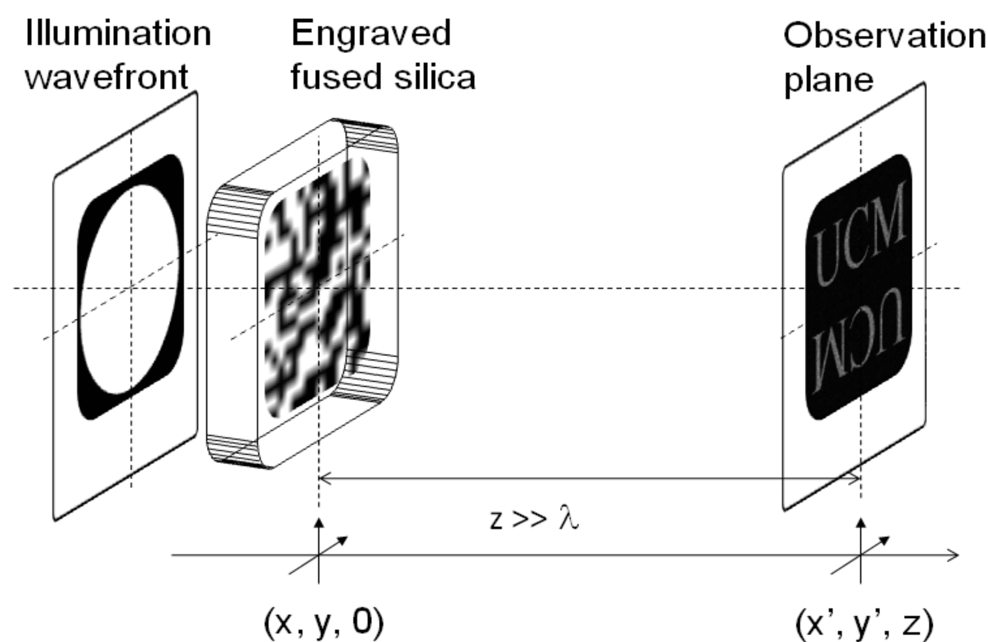

Figure 5.7: View of the system working with an embedded DBS.

In order to design the diffractive beam shaper, we have considered Fraunhofer approach. We have used the iterative Fourier Transform Algorithm (IFTA, see Section 2.4.1), adding the restriction of binary and amplitude elements [144]. The BS has been designed to work in transmission at $\lambda = 632.8$ nm.

As an example, in Figure 5.8a and Figure 5.8b we can find the desired far field intensity distribution and the binary DBS designed with the IFTA algorithm. Since the DBS is binary we always obtain at the observation plane the desired intensity distribution and also the symmetrical image of this field, according to the mathematical properties of the Fourier transform (see Section 2.3.1). The Fourier Transform of the mask in Figure 5.8b is shown in Figure 5.8c where we can observe the double image.

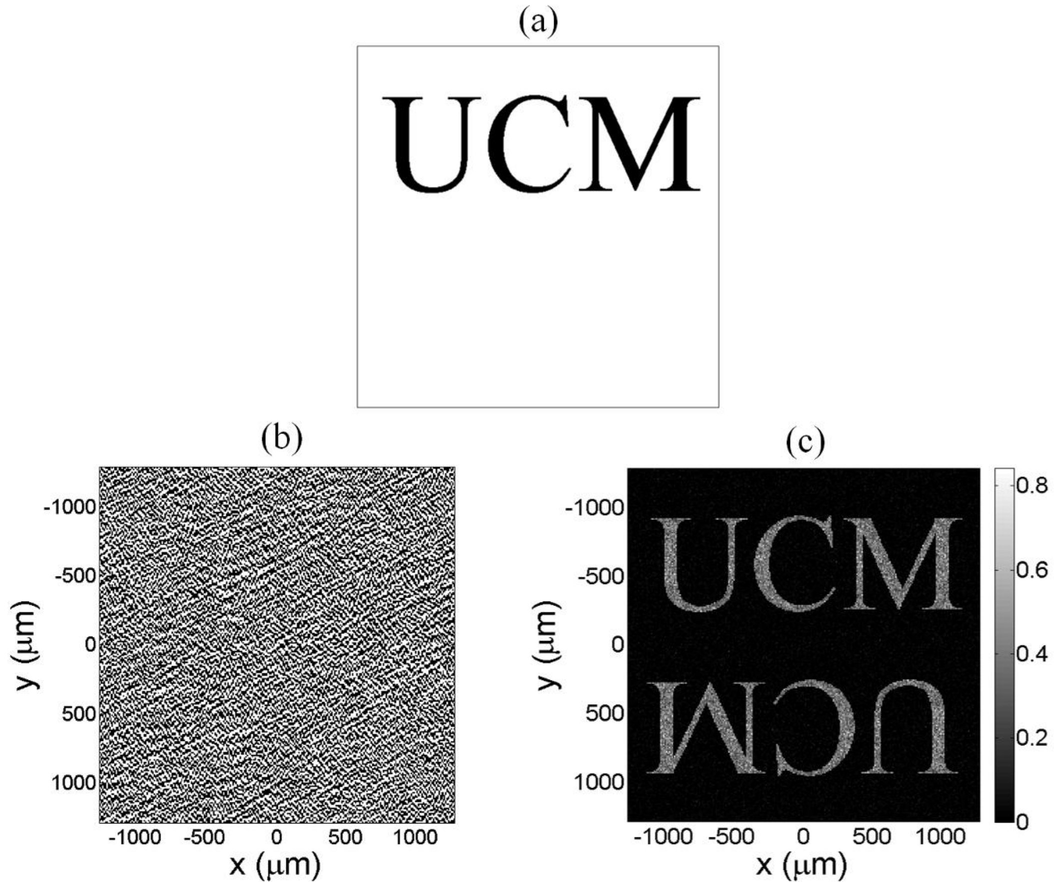

Figure 5.8: a) Desired intensity distribution at the far field; b) Binary amplitude DBS obtained with IFTA designed to obtained the intensity distribution given in a); c) Fourier Transform of the DBS (central maximum peak was removed).

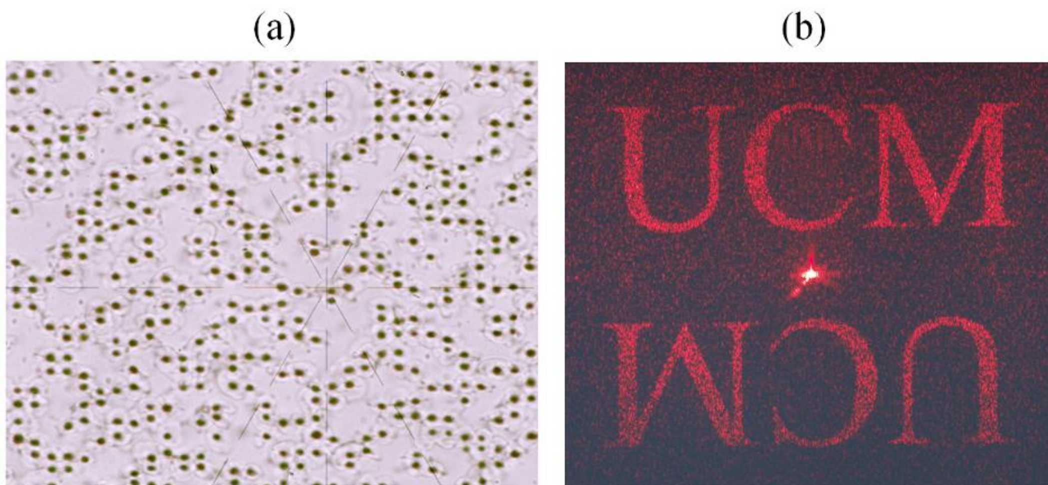

Figure 5.9: a) Microscopy image of the DBS in bulk fused silica (20× optical microscopy). Separation between pixels is 10 μm ; b) experimental propagation after the embedded DBS in the far field. The results are very similar to the expected in Figure 5.8c.

In Figure 5.9a we can see an optical microscopy image of the manufactured DBS (designed in Figure 5.8b) and also the intensity distribution in the far field obtained with this DOE in

Figure 5.9b. As we can see, the experimental results are very similar to the expected (Figure 5.8c).

In order to numerically evaluate the behavior of the DBS, we can follow the method explained in [140]. We choose a region in the objective field in which we define a window surrounding the signal area (the pixel in which the intensity should be a maximum). We consider this window as signal intensity, i_{signal}. The rest of the region is considered as noise intensity. i_{noise}. We also measure the standard deviation σ in both areas. This process is applied to the experimental propagation and also to a simulated propagation of the designed element in Figure 5.8a.

In Figure 5.10 we show the windows used for the numerical evaluation. We collected all the values in Table 5.1. The values of the intensity are normalized to the area of the signal window.

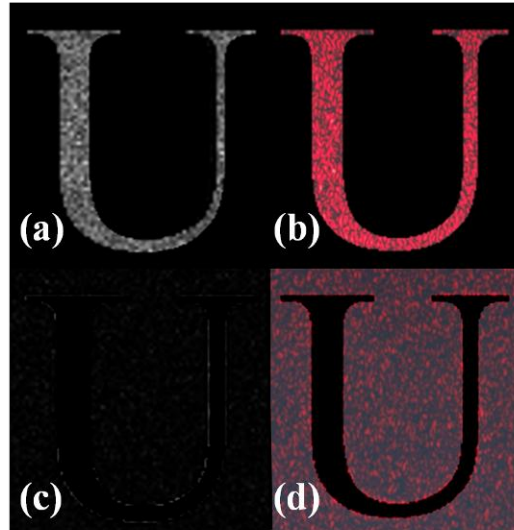

Figure 5.10: a) Signal window for the simulated propagation; b) signal window for the experimental propagation; c) noise window for the simulated propagation, and d) noise window for the experimental propagation.

	i_{signal}/i_{noise}	σ_{signal}	σ_{noise}
Designed	*21.15*	*0.136*	*0.018*
Experimental	*7.37*	*0.262*	*0.153*

Table 5.1: Numerical evaluation of the simulated propagation and the experimental propagation.

As we can appreciate, the signal to noise ratio (SNR) for the experimental propagation is 3 times higher than the SNR of the designed DOE. The loss of SNR is due the high level of noise, attached to the imperfections in the DBS. The standard deviations of both signals are comparable, but the standard deviation of the noise is much higher for the experimental propagation. In this sense, the embedded DOEs fabricated are useful for applications in which the loss of energy by fabrication errors is not so important as to obtain a desirable distribution field with a low cost, with the value added of the protection of the diffractive element by the substrate.

5.4 *Diffraction gratings in fused silica*

Taking into account the calibration developed in Section 5.2, we manufacture different kinds of gratings. A brief analysis of these devices is here summarized. An example of diffraction grating, with $p = 40\,\mu\text{m}$ has been shown in Figure 3.17. The propagation through this grating along z-axis is shown in Figure 5.11, using a laser ($\lambda = 632.8\,\text{nm}$) and a LED ($\lambda = 850\,\text{nm}$) as illumination source. The measurement has been obtained, as usual, performing a vertical average in the CCD. Since the grating is embedded in a bulk glass, part of the diffracted light is propagated in glass, until the surface of the substrate. The location of this surface is marked with a white line in Figure 5.11.

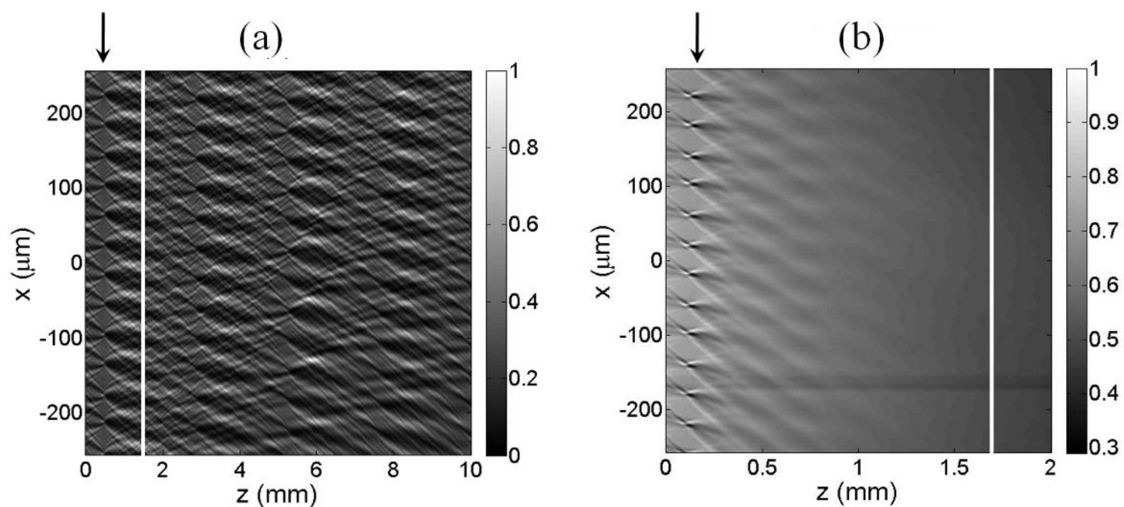

Figure 5.11: Propagation of the diffracted field by an embedded grating micromachined by nanosecond laser, with $p = 40\ \mu m$. The black arrow marks the position of the grating, the white line indicates the glass-air interface; a) illuminated with a laser at $\lambda = 633\ nm$, and b) illuminated with a LED at $\lambda = 850\ nm$.

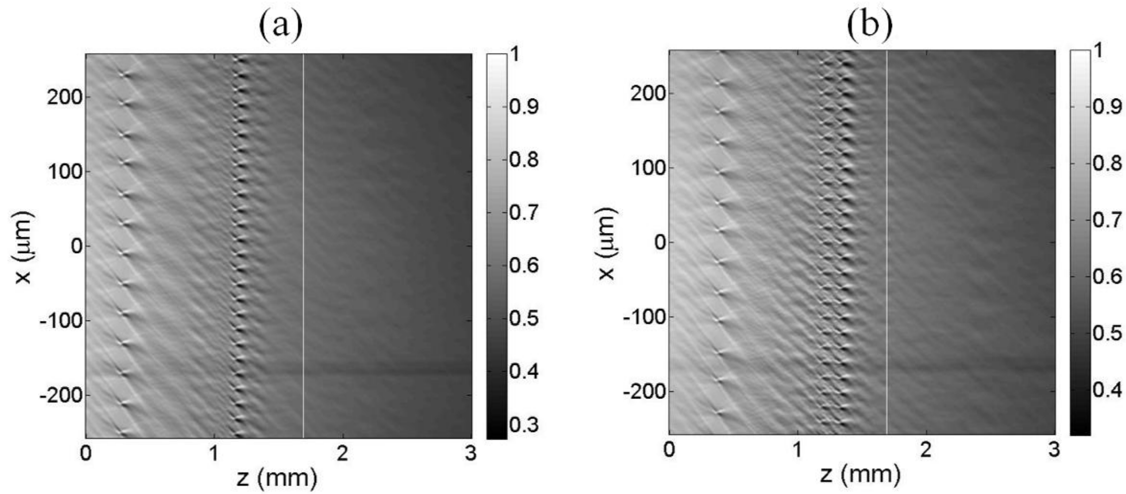

Figure 5.12: Diffracted field by stacked gratings in bulk fused silica, a) two-gratings system with $p_1 = 40$ μm and $p_2 = 20$ μm; b) three-gratings system with $p_1 = 40$ μm and $p_2 = p_3 = 20$ μm. Light source is a LED ($\lambda = 850$ nm). White line denotes the glass-air interface.

The possibility of engraving a stack of several diffraction gratings in-bulk material results a promising technique with a wide range of applications [145]-[147]. Specifically, it is a good alternative to substitute the second grating in an optical encoder by a three-dimensional element such as volume grating. For example, in Figure 5.12a it is shown a two-gratings system with $p_1 = 40\ \mu\text{m}$ and $p_2 = 20\ \mu\text{m}$, and in Figure 5.12b it is shown a three-gratings system with $p_1 = 40\ \mu\text{m}$ and $p_2 = p_3 = 20\ \mu\text{m}$, both illuminated with a LED working at $\lambda = 850\ \text{nm}$. With this technology, we are able to fabricate, for example, three-dimensional masks for optical encoders reading heads.

However, before continue, we have to characterize the parameters of the grating. Comparing Figure 5.11a with Figure 4.1 (the propagation of the light diffracted by a perfect amplitude grating) we realize that the self-imaging phenomenon occurs, but the shape of the self-images is not the expected shape. As hypothesis, we can attribute this discrepancy to the non-clean feature of the engraved lines.

Thus, we need first to characterize the diffraction gratings for the study of this kind of devices. Figure 5.13 shows two examples of lines obtained with different parameters of manufacturing. The lines are compound of absorbing zones (dark zones) and thermal break zones, as occur with the pixel-to-pixel fabrication As it can be shown, it is clear the line-width obtained (around $25\ \mu\text{m}$), but it results very difficult to define the duty cycle when this lines form a grating. Moreover, it results complicated to evaluate the level of amplitude

modulation produced by each line, due the effect of the dark zones and the thermal break zones.

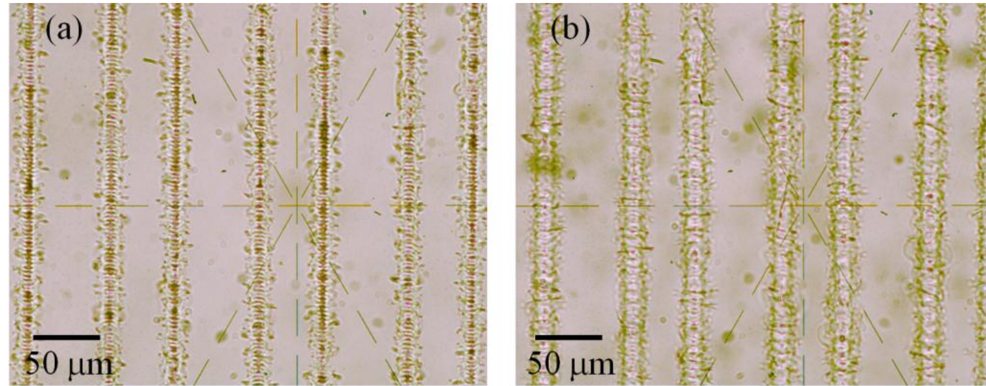

Figure 5.13: Examples of lines engraved in bulk fused silica by means of nanosecond laser pulses at $355\ nm$, *overlapping of -200%, (*$20\times$ *microscopy images); a) with a fluence of* $63.8\ J/cm^2$ *, and b) with a fluence of* $213\ J/cm^2$ *.*

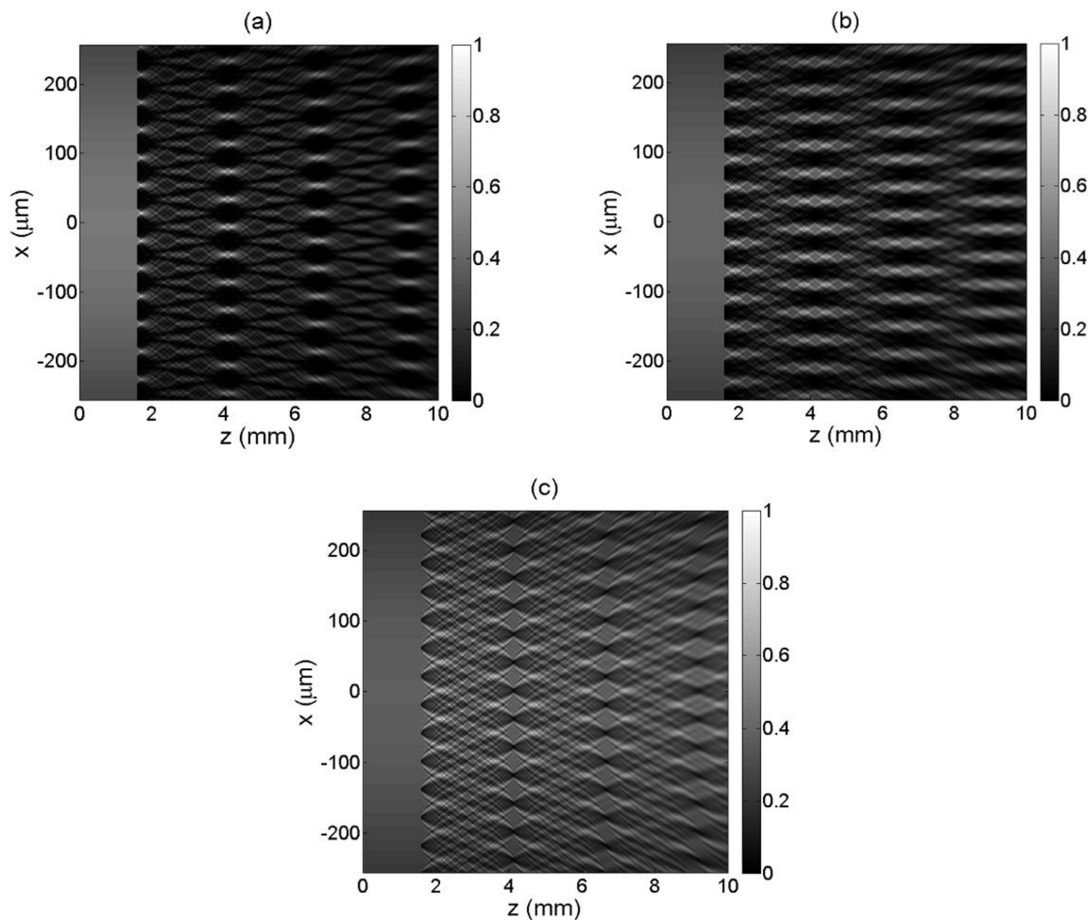

Figure 5.14: BPM simulation of the intensity of the filed diffracted by an embedded grating $p = 40\ \mu m$ *illuminated with a Gaussian beam with* $\lambda = 633\ nm$ *; a) fill-factor of 30%, b fill-factor of 50%; c) fill-factor of 10%. All values normalized to its maximum. The grating is placed at* $1.6\ mm$ *form the origin.*

The grating considered until now are Ronchi gratings, with two levels of amplitude: 1 transparent zones) and 0 (opaque zones), and with a fill factor of 50%. We consider necessary a study in depth of the effect of the variation of the grating characteristics on the near field propagation. This study is developed in Chapter 6.

5.5 *Application of embedded gratings in optical encoders reading head*

The project INNPACTO Fore 2010, described in Section 4.5, also contemplate the developing of reading heads for annular encoders. As it has been explained in Appendix A, the reading head consists of a photodetector and a chrome-on-glass grating. Nevertheless, this scheme refers to encoders with scales defined over flat surfaces (regardless the linear or angular character of the measurement). On the contrary, as it has been studied in Section 4.3 (self-imaging with curved gratings), the curvature of the scale affects to the self-imaging process, changing the periodicity of the self-images along the scale direction.

The reading of optical signals in encoders with curved scales represents a novel field of research for the group. The behavior observed with the embedded DOEs indicates that it is possible to integrate them in a reading head. It could be possible to engrave diffractive structures with cylindrical distribution, allowing the reading of the optical system. This kind of device will increase the tolerances of the head (since the alignment of the components will be easier) and will simplify the mechanical design of the encoder. It is expected that the development of a reading head for annular encoders based on the use of embedded devices will involve a patent, due the novelty and industrial interest of the system.

.

6 Self-imaging process with binary non-Ronchi gratings

We analyze in this chapter the behavior in the the near field of binary gratings in terms of the grating configuration parameters: the amplitude or phase character, the period, and the fill factor. A formalism concerning mixed amplitude/phase grating has been developed. As it is expected, the distance between two consecutive maxima of contrast of the grating self-images depends only on the period of the grating and the wavelength of the illumination. On the contrary, the location of these maxima of contrast depends on the specific properties of the grating: the amplitude/phase character and the fill factor. This last parameter, the fill factor, also modifies the shape of the contrast along the propagation axis. In this work, we analyze the location of the contrast maxima in terms of the Fourier coefficients of the grating obtaining analytical expressions. This analysis can be useful in applications in which the position of the maxima of contrast must be placed at certain fixed distances from the grating, or in order to improve the shape of the contrast attending to certain restrictions (as for example, maximize the signal). Moreover, form the point of view of grating fabrication, it is important to know the effect of these parameters in order to set the tolerances of the devices.

6.1 *Introduction*

The behavior of diffraction gratings in the far field has been well studied under a wide range of conditions [12], [148], [149]. A model based on the Fourier approach gives the description of the diffracted field, finding directions in the space where light is preferably diffracted according to grating equation, known as diffraction orders [2], [148]. The angular separation of the orders depends on the period of the grating and the wavelength. These characteristics make them especially relevant in spectroscopy, due to its ability to separate a polychromatic light into a spectrum in the far field [149]. This kind of studies result more complex in near field, where a Fresnel propagation based model is normally used to describe the behavior of gratings when the period is longer than the wavelength [100], as it is explained in Section 4.2.1. Self imaging effect rules the propagation of light. The location of the maximum of contrast of the self-images depends on the characteristics of the grating. For amplitude gratings with a fill factor of 50% of the grating period, the maxima of contrast are placed at distances $z = l\, p^2 / \lambda$, where p is the period of the grating, λ is the wavelength and l is an integer. On the other hand, for phase gratings with a fill factor of 50% of the grating period, the maxima of contrast are placed at distances $z = (l + 1/2)\, p^2 / \lambda$.

We develop here a formalism assuming a binary grating working in transmission with a mixed amplitude-phase character [150], giving a description of the effects of the amplitude/phase parameters over the propagation. In addition, we will analyze the effect of fill factor on the contrast of the self-images produced by amplitude and phase diffraction gratings.

6.2 *Self-images location of amplitude/phase binary gratings*

As we have seen in Section 4.2.1, the distance between two consecutive maxima of contrast of the self-images (or Talbot planes) is given by the well-known Talbot distance, $z_T = p^2 / \lambda$. However, the location of the maxima of contrast self-images depends on the character of the diffraction grating. For an amplitude diffraction gratings, the first maximum of contrast is placed at $z = z_T$, whereas for a phase diffraction grating the first maximum of contrast appears at $z = z_T / 2$.

An analysis of the dependence between self-images formation and the modulation character (in terms of amplitude/phase) of binary gratings is required. The use of partial amplitude/phase gratings may be interesting to control the location of the maximum of contrast planes, in applications where they must be located at a specific distance from the grating, but the period of the grating cannot be modified. This position can be controlled by means of the transmittance of the chrome strips, which is related with the thickness of the chrome layer.

6.2.1 Theoretical model

In Section 4.2.1 we have described the behavior of diffraction gratings in the near field. Let us develop a formalism describing both amplitude and phase gratings. The involved parameters are described in Figure 6.1. A plane wave with wavelength λ illuminates a binary grating with period p. The fill factor of the grating, α, is the ratio between the width of the strips of the grating and the period p. The parameters a and b represent the maximum and minimum value of the amplitude modulation, and the phase retardation produced by phase gratings is $\delta = 2\pi h(n-1)/\lambda$, where n is the refractive index of the grating and h is the height of the strips. Thus, for the case of ideal amplitude gratings $a=1$, $b=0$, and $\delta=0$, and for phase gratings $a=1$, $a=1$ and δ with the proper value. The grating is defined along x -axis, and the beam light propagates along z -axis.

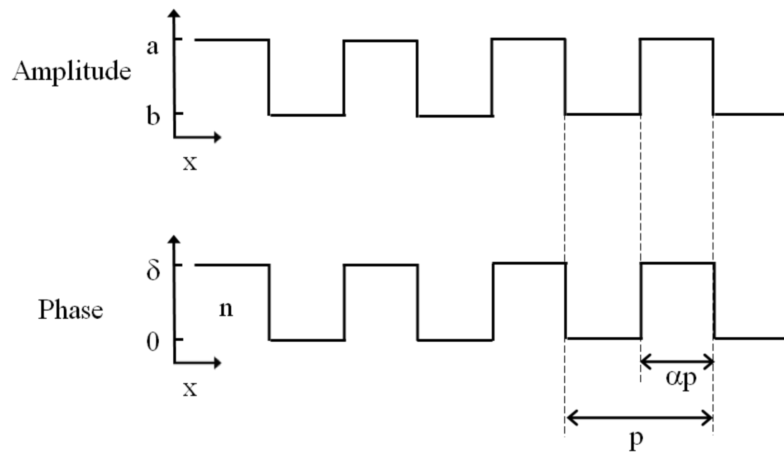

Figure 6.1: Mixed amplitude-phase grating scheme with the involved parameters.

Eq. (4.5) describes the diffracted field by a grating. The Fourier coefficients of a Ronchi grating will be defined by [150]

$$c_0 = \alpha\left(ae^{-i\delta} - b\right) + b,$$
$$c_0 = \alpha\left(ae^{-i\delta} - b\right)\mathrm{sinc}\left(\pi l \alpha\right). \qquad (6.1)$$

In general, the Fourier coefficients are complex variables, and they are written as $c_l = C_l \exp\left(i\beta_l\right)$, being C_l their modulus and β_l their phase. Then eq. (4.5) can be rewritten as

$$\hat{I}(z,x) = \sum_l \sum_{l'} C_l C_{l'} \exp[iqx(l-l')]\exp[i\pi(l^2 - l'^2)\hat{z} + i\left(\beta_l - \beta_{l'}\right)]. \qquad (6.2)$$

The accuracy of this analytical development depends on the number of orders taken into account. On the other hand, a high number of orders implies a high complexity in the final expressions. The factor $\left(\beta_n - \beta_{n'}\right)$ in eq. (6.2) produces a displacement of the maxima of the intensity along z. The amount of this factor (and consequently, the magnitude of the displacement) depends on the configuration of the grating.

6.2.2 Phase-amplitude mixed gratings

For a rough estimation of the intensity distribution at the self-images, we can use only the -1st, 0th and 1st orders. This approximation is valid enough to extract some conclusions from the results. Figure 6.2 shows the cumulative efficiency of the grating, taking into account different number of orders, for different values of the fill factor for an amplitude grating and for a phase grating. In the case of an amplitude grating with $a = 1$ and $b = 0$ the total efficiency should be linear with α (since the total energy that can pass through the grating depends linearly with α). On the other hand, for a phase grating the total efficiency should be always equal to unity. It can be observed that the -1st, 0th and 1st orders carry more than 80 % of the theoretical energy for both kind of gratings. Considering only these three orders simple equations are obtained. This approach has been successfully used to determine the behavior of diffraction gratings in the near field under a wide range of circumstances [150] [151]. For example, for the intensity distribution, taking into account that for Ronchi gratings $c_n = c_{-n}$, eq. (6.2) simplifies to

$$\hat{I}\left(z,x\right) \approx C_0^2 + 2C_1^2 + 4C_1^2\cos\left(qx\right)^2 + 4C_0C_1\cos\left(qx\right)\cos\left(\pi\hat{z} + \beta_0 - \beta_1\right). \qquad (6.3)$$

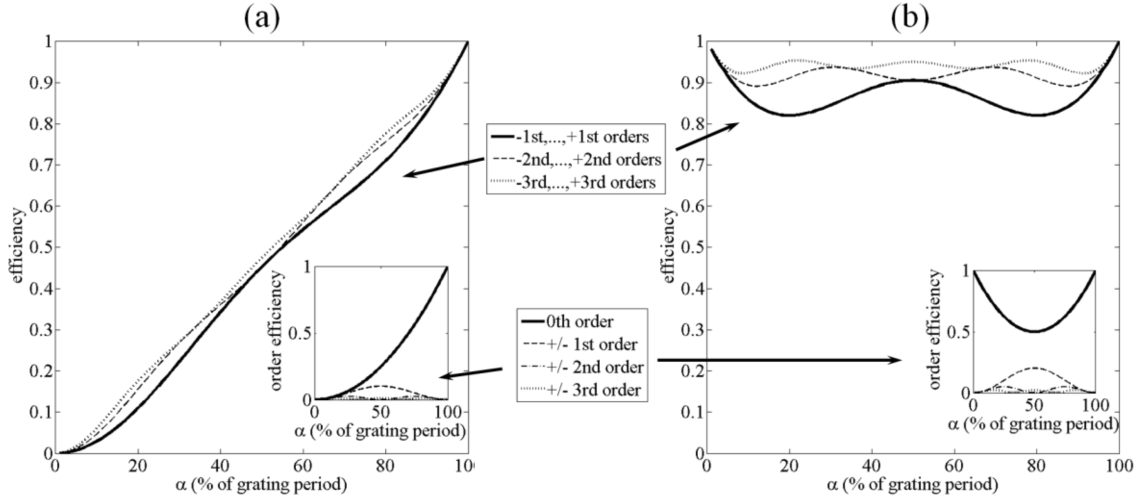

Figure 6.2: Cumulative efficiency of the grating against fill factor, taking into account up to the $\pm 1^{st}$ *(continuous line),* $\pm 2^{nd}$ *(dashed line) and* $\pm 3^{rd}$ *(plotted line) diffracting orders (subplot: efficiency of each order for different values of* α *), a) pure amplitude grating with* $a=1,\ b=0$ *and* $\delta=0$*; and b) phase grating with* $a=1,\ b=1,\ \delta=\pi/2$.

The two first terms of eq. (6.3) represent the background intensity, the third one is an independent term on z that produces constant fringes along x, and the last one presents a dependence on z and x, which corresponds with Talbot effect.

In a first stage, let us consider that $a=1$ (maximum of transmitivity) and $\alpha=1/2$. From eq. (6.1), the complex form of the zero and first coefficients are

$$
\begin{aligned}
c_0 &= \frac{1}{2}\sqrt{1+b^2+2b\cos\delta}\,\exp\left[i\,\mathrm{atan}\left(\frac{\sin\delta}{b+\cos\delta}\right)\right],\\
c_1 &= \frac{1}{\pi}\sqrt{1+b^2-2b\cos\delta}\,\exp\left[i\,\mathrm{atan}\left(\frac{\sin\delta}{-b+\cos\delta}\right)\right].
\end{aligned}
\tag{6.4}
$$

Introducing eq. (6.4) into eq. (6.3) and simplifying, the intensity results

$$
\begin{aligned}
\hat{I}(z,x) \approx{} & \frac{1}{4}(1+b^2+2b\cos\delta)+\\
& +\frac{2}{\pi}\sqrt{1+b^4-2b^2\cos(2\delta)}\cos(qx)\cos\left[\frac{\pi}{z_T}\left(z+z_S\right)\right]\\
& +\frac{2}{\pi^2}(1+b^2-2b\cos\delta)\left[1+\cos(2qx)\right],
\end{aligned}
\tag{6.5}
$$

where the parameter

$$
z_S=\frac{z_T}{\pi}\left(\beta_n-\beta_{n'}\right)=\frac{z_T}{\pi}\left\{\mathrm{acot}\left[\left(b+\cos\delta\right)\csc\delta\right]-\mathrm{acot}\left(\cot\delta-b\csc\delta\right)\right\}
\tag{6.6}
$$

gives the displacement of the self-images along the z -axis. As it can be observed in eq. (6.6) the displacement depends on the Fourier coefficients that describe the grating by means of b and δ. Thus, for a given value of the phase retardation, δ, we can control the position of the maximum of intensity just controlling the value of b. To understand in a better way the functional form of this displacement effect, we perform a Taylor series expansion in b on $(\beta_n - \beta_{n'})$ around $b_0 = 0$ (purely amplitude) and around $b_0 = 1$ (purely phase) resulting,

$$z_S = \begin{cases} -2b\sin\delta - \dfrac{2}{3}b^3\sin(3\delta) & \text{for } b_0 = 0, \\ \chi - (b-1)\csc\delta + \dfrac{(b-1)^2}{2}\csc\delta & \text{for } b_0 = 1, \end{cases} \tag{6.7}$$

where $\chi = \pi$ for $\delta \in \lfloor 2N\pi, (2N+1)\pi \rfloor$ and $\chi = -\pi$ for $\delta \in \lfloor (2N-1)\pi, 2N\pi \rfloor$. Although eq. (6.7) is an approximation, we can assume it is correct for the cases in which b is close to 0 (quasi-amplitude grating) or 1 (quasi-phase grating).

An important parameter to analyze is the contrast of the self-images. We can obtain it from eq.(6.5). Instead of using the standard definition of contrast, we assume that the contrast is measured using a periodic mask with the period of the grating. This definition of contrast is better than the standard definition in sense of applications, since usually the contrast is measured using another diffraction grating which acts like a mask. This definition is also better to compare analytical results with experimental results, since experimental fluctuations are avoided. In this way, we obtain an analytical expression for the contrast taking as maximum intensity ($I_{\max}$) the integration of eq. (6.5) between $x = -p/4$ and $x = p/4$ and the minimum intensity ($I_{\min}$), as the integration of same equation between $x = p/4$ and $x = 3p/4$. Now, we define the contrast as $Contrast(z) = (I_{\max} - I_{\min})/(I_{\max} + I_{\min})$, resulting in

$$Contrast(z) = \frac{16\sqrt{1 + b^4 - 2b^2\cos(2\delta)}}{(1+b^2)(8+\pi^2) + 2b(-8+\pi^2)\cos(\delta)} \cos\left[\frac{\pi}{z_T}(z + z_S)\right]. \tag{6.8}$$

The contrast depends on δ and b, since the period of the grating and the wavelength are fixed values. However, eq. (6.8) is only valid when δ is not around $(2N+1)\pi$ with N entire, since for these situations the frequency of the fringes doubles and the period of the mask is not right to analyze the fringes.

6.2.3 Numerical results

As it has been explained in the previous section, the values of a, b and δ determine the behavior of the diffraction grating. Although eq. (6.3) has an easy and functional shape, it presents an interesting phenomenology depending on the values that we apply to the parameters of the Fourier coefficients.

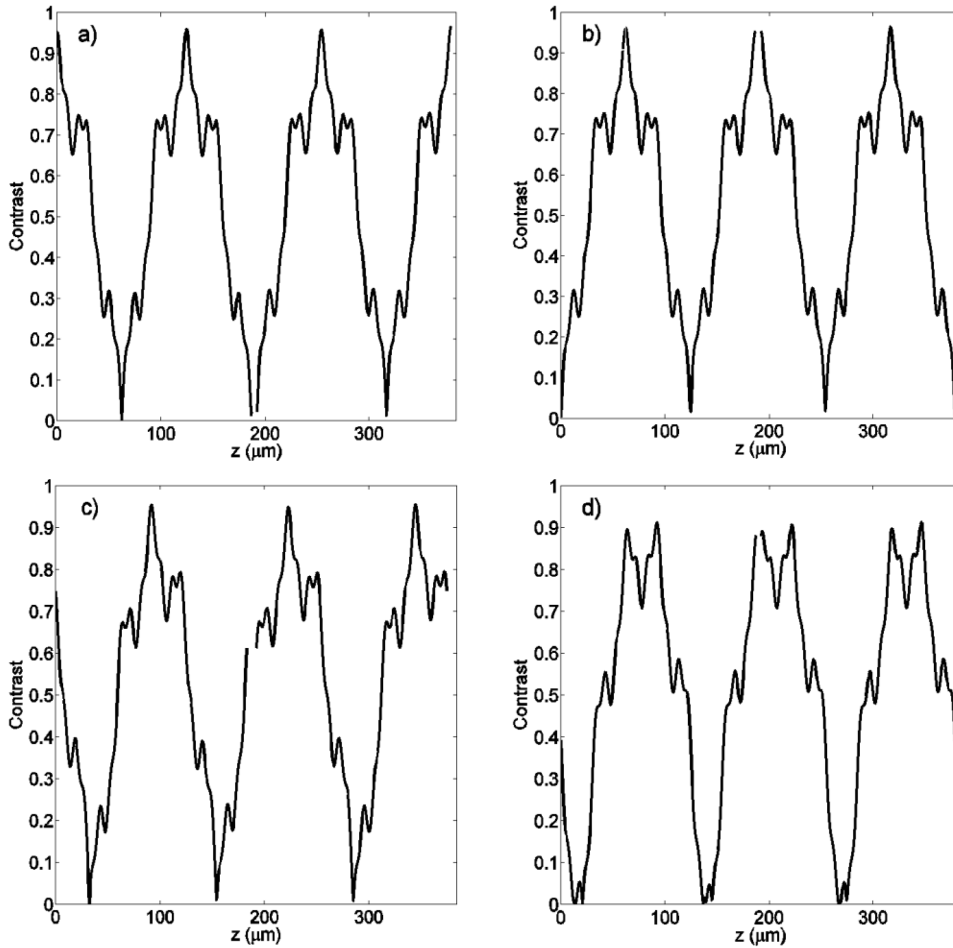

Figure 6.3: Contrast along z of the self-images produced by a diffraction grating with period $p = 5\ \mu m$, fill-factor $\alpha = 1/2$ and phase retardation $\delta = \pi/2$, where we consider $a = 1$, a) $b = 0$, b) $b = 1$, c) $b = 0.35$ and d) $b = 0.65$.

Using eq. (6.3), we have performed numerical simulations of the near field diffraction pattern produced by the proposed grating. Thus, we obtain the position of the maxima of the Talbot self-images contrast along the z-axis. In Figure 6.3 it is shown this contrast along the z-axis produced by a pure phase grating, a pure amplitude grating and two intermediate cases calculated using eq. (6.2) up to the ninth order of diffraction.

We can observe that the position of the maximum contrast varies along z-axis, depending on the amplitude-phase character of the grating. Since Fresnel approach is only valid for

distances longer than 2λ [152], we have also calculated the contrast along z for three particular cases, pure amplitude grating, pure phase grating and partial amplitude/phase grating, Figure 6.4, by using the Rigorous Coupled Wave Analysis method (RCWA) [153]-[155]. We have simulated the variations in the transmittance b by changing the thickness of a layer of chromium.

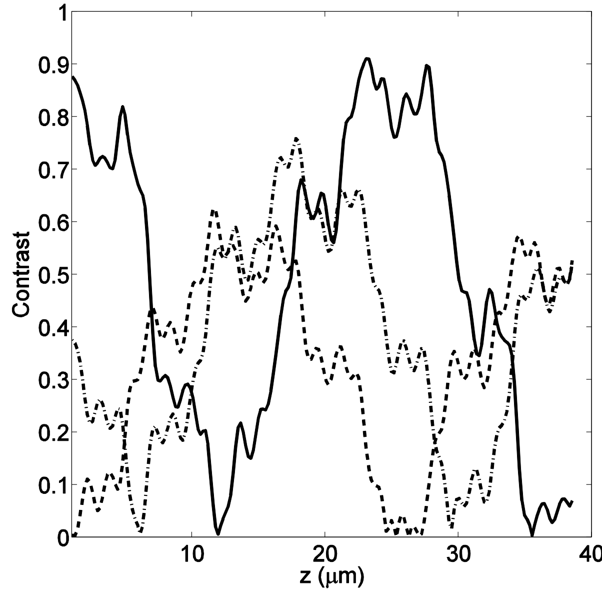

Figure 6.4: Contrast along z of the self-images obtained using Rigorous Coupled Wave Analysis (RCWA). The period of the grating is $p = 5\ \mu m$, the fill-factor is $\alpha = 1/2$, and phase retardation is $\delta = \pi/2$, where we consider $a = 1$. We have simulated the change of b by means of the thickness of the chromium layer (h), solid line $(h = 100\ nm)$, dash-dot line $(h = 10\ nm)$ and dash line $(h = 1\ nm)$.

For more detail, in Figure 6.5 we calculate the position along z of the maximum contrast in terms of b for four particular cases ($\delta = 0, \pi/2, 3\pi/2, \pi$). The parameter b takes values between 0 (pure amplitude grating) and 1 (pure phase grating). Then, in all cases the grating behaves as an amplitude grating just for b =0 and its behavior changes gradually to phase grating (b =0). For this calculation we use eq.(6.8). As it can be observed in Figure 6.5a, the grating disappears when b is equal to 1 for $\delta = 0$. In Figure 6.5b and Figure 6.5c we can observe that the grating changes gradually from a pure amplitude grating to a pure phase grating, whereas the position of the self-images displaces along z. It is also plotted the value of z_S (solid lines), which is in total agreement with the total results. Finally, in Figure 6.5d it is shown a special case in which the modulation in contrast disappears when the grating is a pure phase grating, but with a phase retardation of $\delta = \pi$. The contrast remains as the maximum along z. This fact means that Talbot effect is cancelled.

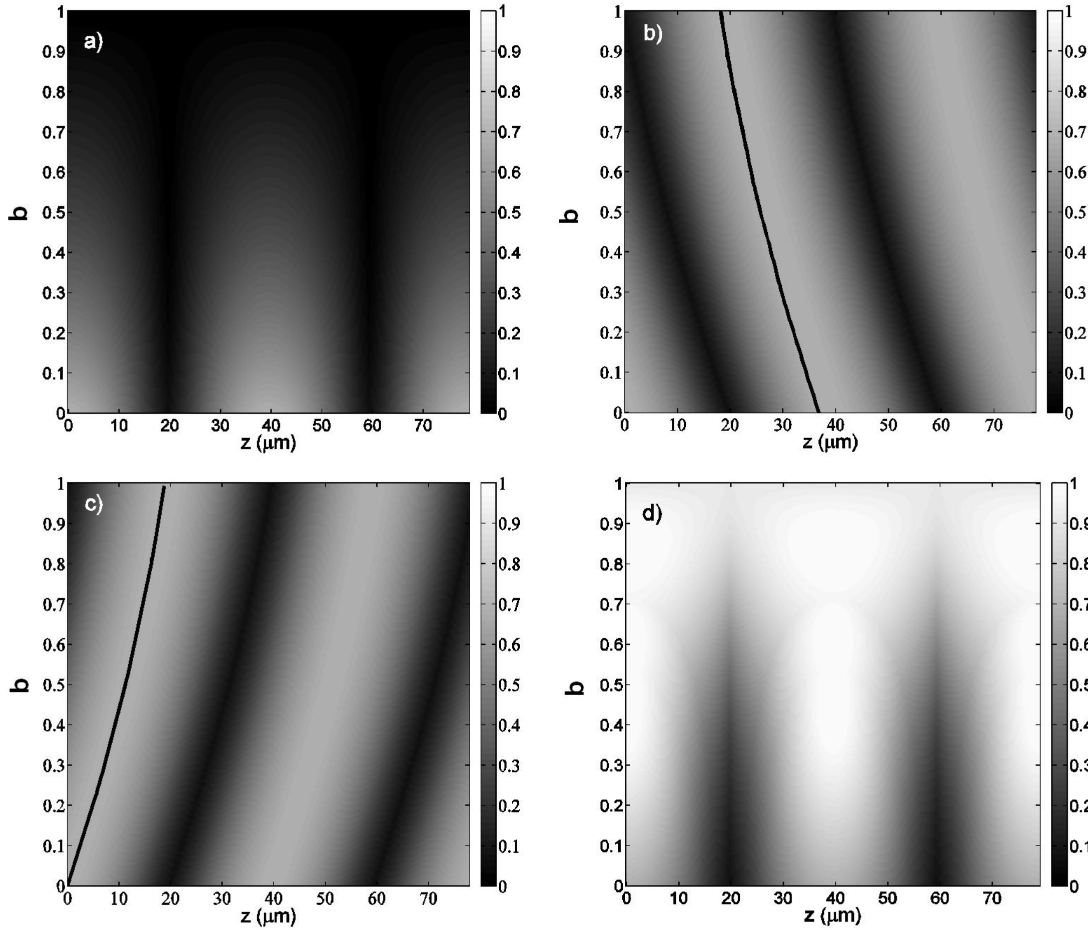

Figure 6.5: Contrast of the fringes produced by a diffraction grating with period $p = 5\ \mu m$*, fill-factor* $\alpha = 1/2$ *and* $a = 1$ *in terms of* z *and* b *for, a)* $\delta = 0$*, b)* $\delta = \pi/2$*, c)* $\delta = 3\pi/2$*, d)* $\delta = \pi$*.. The solid lines in b) and c) are plotted using equation (6.8).*

The behavior of the grating from a more general point of view is shown in Figure 6.6. We show the position of the first maximum of contrast along z-axis in terms of b and δ (Figure 6.6a) and the value of this maximum (Figure 6.6b). These two images have been calculated using eq.(6.8). We can see that there exists a relationship between the position of the maximum of the contrast and the value of parameter b. The position of the maximum of contrast along z presents discontinuities when $b = \cos(\delta)$, but this fact does not affect to the self-images, since the discontinuities are very narrow. On the other hand, taking into account the behavior of this maximum value, in Figure 6.6b it is shown that the maximum contrast is obtained for $\delta = N\pi / 2$, with N entire.

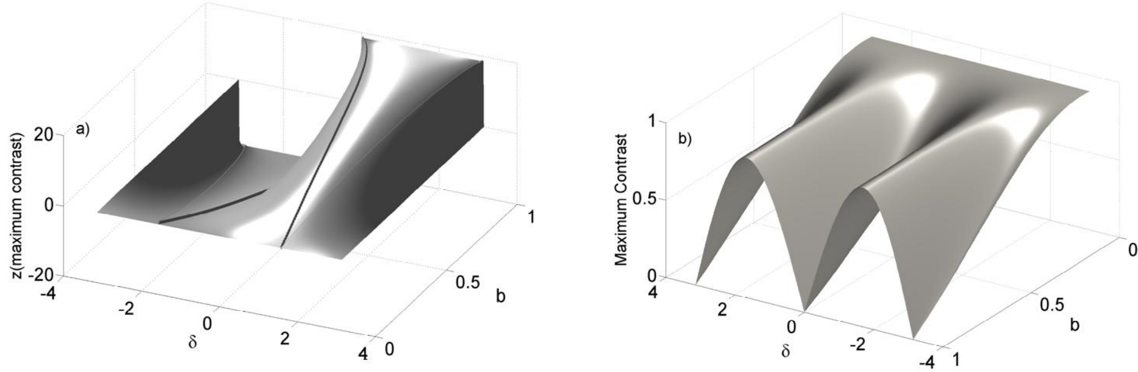

Figure 6.6: a) Maximum contrast position along z in terms of b and δ, b) Maximum contrast value in terms of b and δ.

6.2.4 Experimental approach

We have manufactured a grating behaving as amplitude and phase grating at the same time. By etching a chrome on glass grating (that means, a pure-amplitude grating) using acid fluorhidric (HF) we are able to etch only the glass strips. Thus, we obtain an amplitude grating but with a phase retardation. It corresponds to $a=1$, $b=0$ and $\delta \neq 0$. We measure the Talbot effect using this grating. Following, we immerse the grating into a chrome etching to remove part of the chrome. Thus, the transmittance of the chrome fringes varies. This step corresponds to $a=1$, $0<b<1$ and $\delta \neq 0$. Finally, we introduce the grating again into the chrome etching to remove all the chrome. In this way, we obtain a pure phase grating, which correspond to $a=1$, $b=1$ and $\delta \neq 0$. In Figure 6.7 it is shown the self-imaging process corresponding to the three steps. The maxima of the Talbot self-images are placed between $z=0$ and $z=z_T=p^2/\lambda$, that for our case is $z_T=632.1\ \mu\text{m}$ $(p=20\ \mu\text{m}, \lambda=632.8\ \text{nm})$. In addition, the chrome thickness of the grating used in Figure 6.7b is around $10\ \text{nm}$, that corresponds to $b=0.4$ and the phase retardation is around $\pi/2$. Then the theoretical value (eq.(6.6)) for z_S results around $445\ \mu\text{m}$ which is quite close to the experimental result.

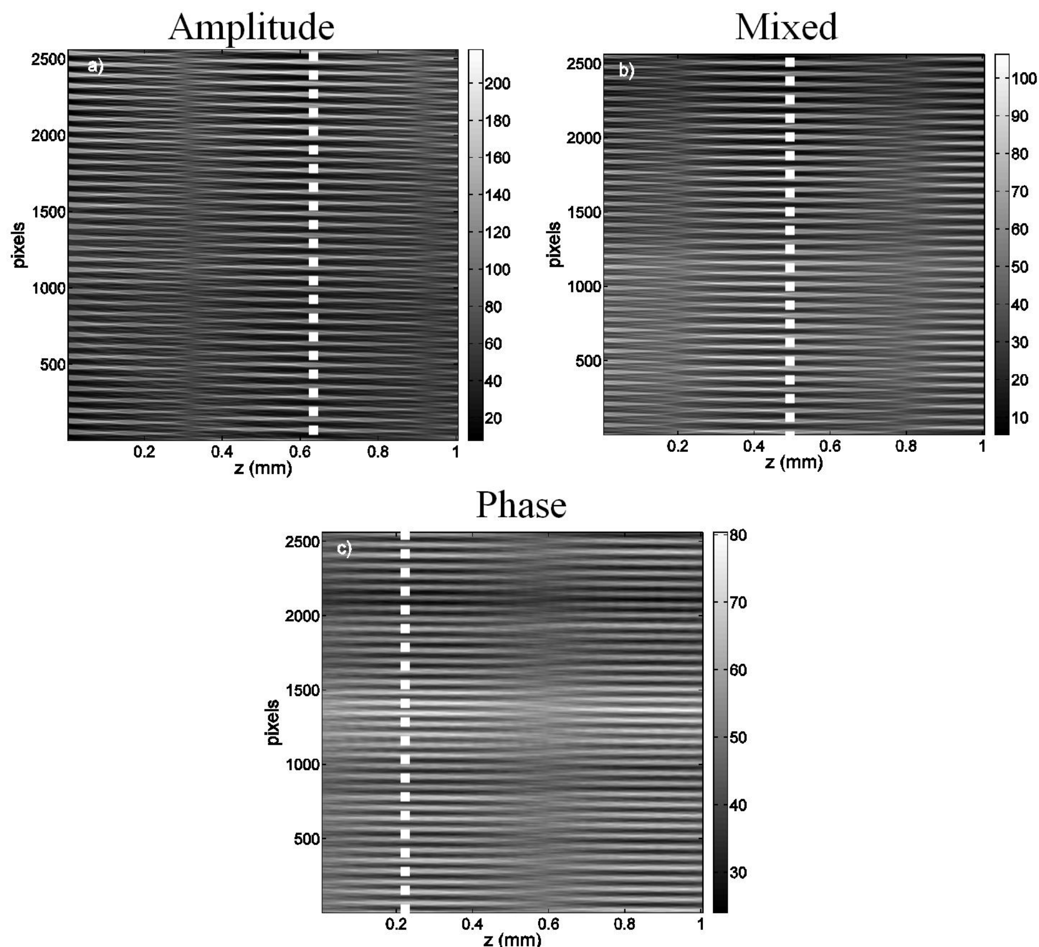

Figure 6.7: Experimental Talbot effect for several ratios of amplitude-phase in the diffraction grating, a) pure amplitude grating, b) amplitude/phase grating and c) pure phase grating.($p = 20\ \mu m$, $\alpha = 0.5$, $\delta = \pi / 2$ *). White dotted lines show the position of the maximum of contrast.*

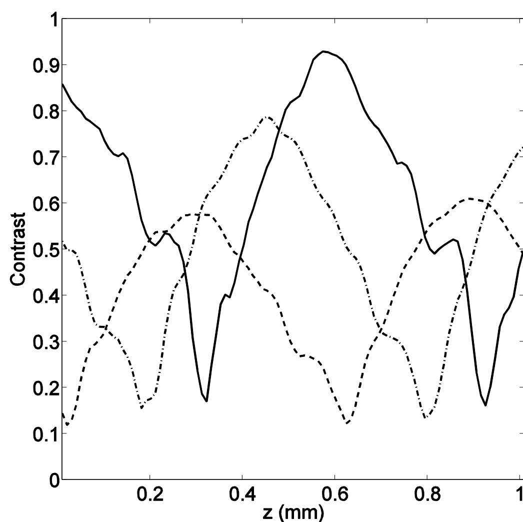

Figure 6.8: Experimental contrasts corresponding to situations depicted in Figure 6.7, solid line (Figure 6.7a), dashed-dot line (Figure 6.7b) and dashed line (Figure 6.7c).

On the other hand, in Figure 6.8 we show the contrasts calculated from Figure 6.7, where the shifting of the contrast in terms of the ratio amplitude-phase can be observed. The decreasing of the contrast, when the grating turns into phase grating, is due to the phase retardation. As it can be observed in Figure 6.6b, the maximum contrast for pure phase gratings $(a=1, b=1)$ depends on the phase retardation.

The ratio amplitude-phase is easily obtained controlling the thickness of the chrome strips. In Figure 6.9 we show the transmittance of a layer of chrome in terms of its thickness, calculated using Rigorous Coupled Wave Analysis (RCWA). This fact allows manufacturing a diffraction grating by controlling the location of the maxima of the self-images contrast, making it to appear at a certain fixed distance from the grating.

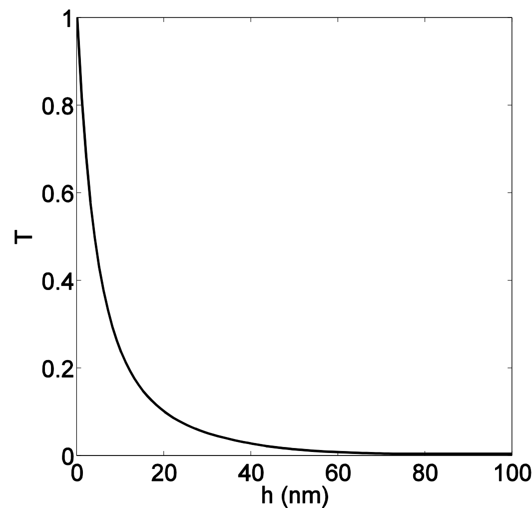

Figure 6.9: Dependence of the transmittance of chrome in terms of the thickness of the layer.

6.3 *Effect of fill-factor on the self-images of diffraction gratings*

The process of manufacturing of diffraction gratings requires of a good calibration of the fabrication system. Nevertheless, it is very difficult to achieve the desirable line widths with a good accuracy. Moreover, under some circumstances (as for example, the micromachining of fused silica by means of nanosecond pulses lasers shown in Chapter 5) it is very difficult to reach the proper line with conforming a fill factor of 50%. In Section 5.4 some problems related with diffraction gratings were commented. We perform here an analysis of the effect of the fill factor over the diffraction in the near field. We consider gratings with periods much greater than the wavelength, so we make use of the scalar approach..

6.3.1 Simulations by means of Beam Propagation Method

We have developed numerical simulations of the field propagated after a diffraction grating in the near field, for amplitude and phase gratings with different fill factor based on the Beam Propagation Method (BPM), explained in Section 2.3.3.

For the simulation of the system, we use two steps. First, we propagate the illumination field (a plane wave with normalized amplitude) through a diffracting grating defined by the configuration parameters: amplitude, phase, period, and fill factor. The resulting field, at the end of the grating, is taken as illumination field for the last propagation, along vacuum space. Then, the origin at the z-axis is located at the end of the grating. This performance is motivated by the need of a good resolution inside the grating. In this way, we obtain different resolution for the propagation through the grating and for the propagation through free space.

In Figure 6.10 we have plotted the diffracted intensity in the near field, and also the contrast obtained with eq. (4.6), for an amplitude grating ($a = 1$, $b = 0$, $\delta = 0$) for the cases of $\alpha = 30\,\%$, $\alpha = 50\,\%$, and $\alpha = 70\,\%$. As it can be observed, the shape and the width of the self-images change for each value of α, but the maximum of contrast (and consequently, self-images location) are placed at the same positions. It is clear that fill factor has an effect over the self-imaging process.

It is remarkable that a grating with narrow transparent strips along x-axis (low fill factor) produces a contrast profile with narrow maxima along z-axis. On the contrary, the contrast of a grating with wide transparent strips (high fill factor) has wide maxima along z-axis, improving the visibility. In this case, the minimum of contrast are narrow peaks, whereas the maximum tends to a stable value, but a rippled function.

A stable high value over a wide region along z-axis results interesting for applications in which self-images are used, increasing the tolerances. For $\alpha = 50\,\%$ the contrast of the self-images tends to a cosine function.

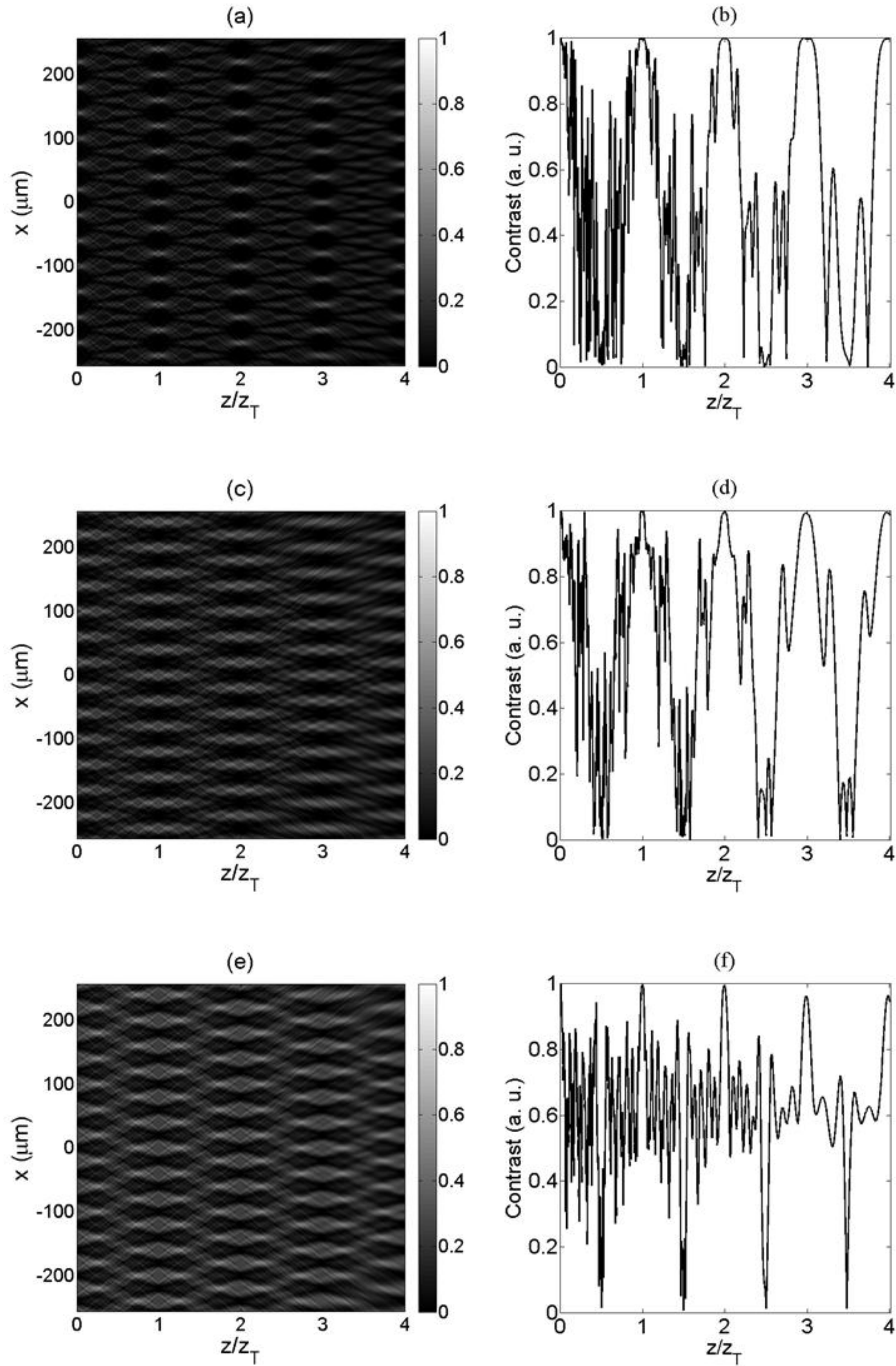

Figure 6.10: Intensity (logarithmic scale) and contrast obtained by means of BPM simulations for a grating with $a=1$, $b=0$ *and* $\delta=0$, *for different values of* α; *a) and b)* $\alpha=30\,\%$ *of the grating period; c) and d)* $\alpha=50\,\%$ *of the grating period; e) and f)* $\alpha=70\,\%$ *of the grating period.*

In order to reach a more generalized point of view, we perform a simulation of an amplitude grating ($a=1$, $b=0$, $\delta=0$ and $p=40\ \mu m$) and also for a phase grating ($a=1$, $b=1$, $\delta=\pi/2$ and $p=40\ \mu m$) over a wide range of values of α. The values of the contrast are

now collected at the same figure for each kind of grating, where the vertical axis represent the value of α. These plots are normalized to its maximum value. The results are shown in Figure 6.11a and Figure 6.11b.

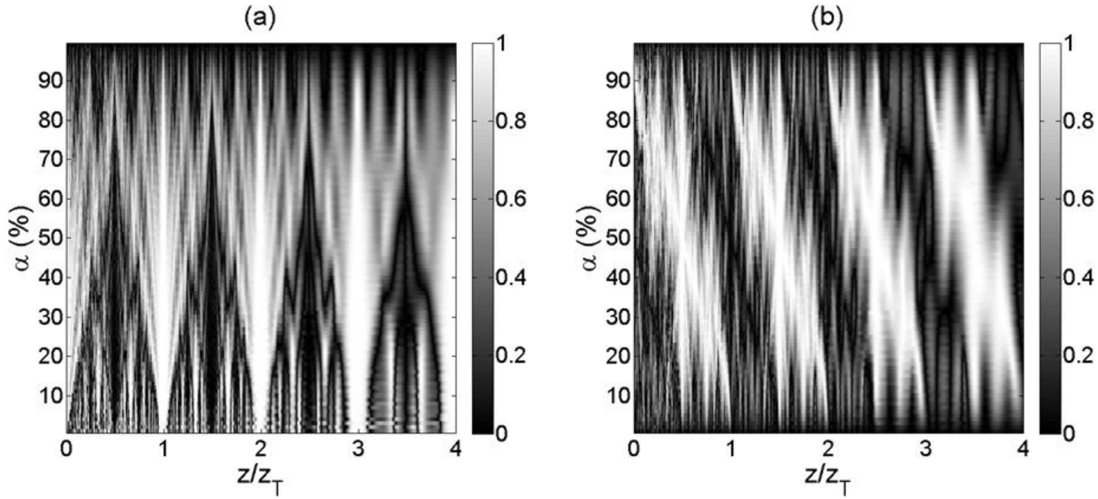

Figure 6.11: Dependence of contrast obtained using BPM with α (in % of the grating period) for a grating with $p = 40\ \mu m$, and a) $a = 1,\ b = 0$ and $\delta = 0$; and b) $a = 1,\ b = 1,\ \delta = \pi/2$.

The dependence with α is notorious. Moreover, this dependence is not the same for amplitude gratings that for phase gratings. For an amplitude grating the width of the maxima of the self-images contrast tends to increase with α. The location of the maximum values, as we have seen, remains the same for every value of α. On the contrary, the location of this maxima for a phase grating moves along a Talbot period when α changes, whereas the shape of the self-images contrast remains almost constant. Up to our knowledge, this behavior (specially, the change of the location of the self-images) was not still explained. We find necessary an analytical study of this phenomenology.

6.3.2 Analytical approach

We make use of eq. (4.6) in order to describe the effect of the fill factor over the self-image phenomenon. Using eq. (6.3), the contrast results in

$$Contrast_{\pm 1}(z) = \frac{4C_0 C_1}{C_0^2 + 4C_1^2} \left| \cos\left(\pi \hat{z} + \beta_0 - \beta_1\right) \right|. \qquad (6.9)$$

where the subindex ± 1 indicates that only the -1st, 0th and 1st order have been taken into account. For the case of an amplitude grating, the Fourier coefficients are $c_0 = \alpha$, $c_1 = c_{-1} = \alpha \operatorname{sinc}(\pi\alpha)$, then the coefficients $\beta_0 = \beta_1 = 0$ are null. However, this is not the

case for phase gratings. For example, the Fourier coefficients for a $\pi/2$ phase grating are $c_0 = \sqrt{2\alpha^2 - 2\alpha + 1}\exp\left[-i\alpha/(1-\alpha)\right]$, and $c_1 = \alpha\sqrt{2}\text{sinc}(\pi\alpha)\exp(3\pi i/4)$. Then there is a shift in the location of the maxima of the self-images contrast which depends on the fill factor according to

$$\beta_0 - \beta_1 = \frac{-\alpha}{1-\alpha} - \frac{3\pi}{4}. \tag{6.10}$$

The intensity distribution in the near field for these two particular cases (the amplitude grating and the $\pi/2$ phase grating) is shown in Figure 6.12. Attending to these figures, we notice that eq. (6.9) explains the location of the maximum contrast: a change in the location of these maxima is appreciable for the phase grating, but not for the amplitude grating. Up to our knowledge, the dependence of the location of the contrast maxima with the fill-factor of the grating has not been reported yet.

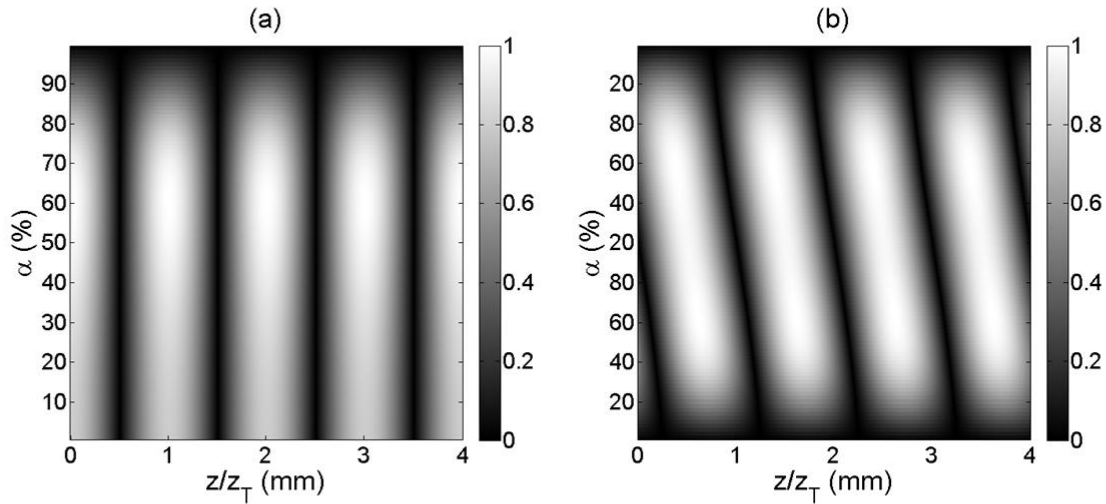

Figure 6.12: Dependence of contrast (absolute value) with α using up to the -1st, 0th and 1st orders for a) a pure amplitude grating with $a=1$, $b=0$ and $\delta=0$; and b) a phase grating with $a=1$, $b=1$, $\delta=\pi/2$.

Nevertheless, a visual comparison between Figure 6.11 and Figure 6.12 shows that eq. (6.9) does not predict completely the behavior of the grating in the near field, especially in terms of self-images contrast shape. Then, it is necessary to consider a higher number of orders to explain the effect of the fill factor over self-images contrast of amplitude grating, in particular the change of the contrast shape. These effects can be attributed to the energy carried by upper orders, shown in Figure 6.10. When the fill factor is higher or lower than 50% of the

grating period, the upper orders ($\pm$2nd, $\pm$3rd…) reach a higher percentage in the energetic distribution of Figure 6.2.

In order to evaluate the number of orders needed, we solve numerically eq. (6.2) for amplitude gratings, since the effect is visually more obvious for this case, taking into account different number of orders. The results are shown in Figure 6.13. It is clear that the inclusion of the $\pm$2nd orders is enough to predict a dependence between the fill factor and the width of the self-images contrast. For a higher number of orders, rippled signals with spatial periodicity lower than z_T appear over the fundamental signal with periodicity z_T. These higher frequencies are more visible for high fill factors (over 80%) and low fill factors (under 20%). Therefore, very narrow peaks on the contrast profiles can be obtained using high or low fill factors. This fact can be used to manufacture Talbot array illuminators, or to determine the distance from the grating with high resolution.

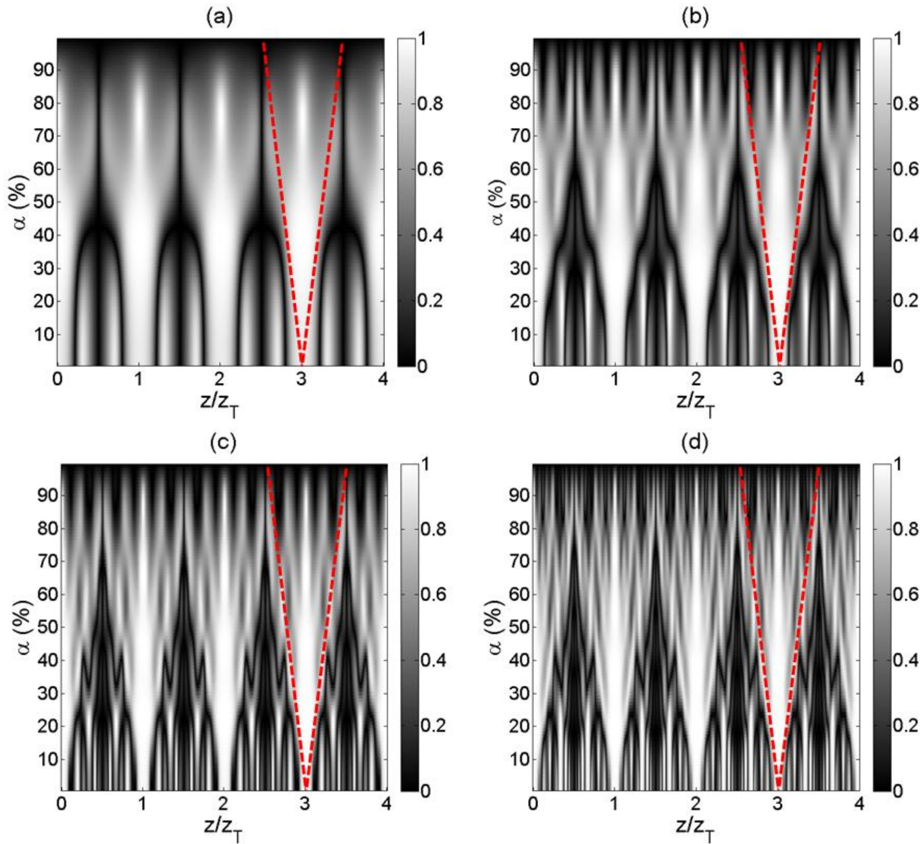

Figure 6.13: Dependence of the contrast with α *for pure amplitude gratings with* $a=1$, $b=0$, $\delta=0$ *and* $p=40\ \mu m$ *taking into account different number of orders; a) using up to the* $\pm 2^{nd}$ *orders; b) using up to the* $\pm 3^{rd}$ *orders;. c) using up to the* $\pm 4^{th}$ *orders;. and d) using up to the* $\pm$ *5th orders.*

Moreover, the width of the self-images contrast tends, when the number of orders involved increases, to a linear dependence with α. This dependence is shown with dashed lines over

plots of Figure 6.13. Assuming that width of the self-images contrast, W_s, is the distance between points at z-axis where the contrast fall down to half-height, we can write

$$W_s \approx \alpha, \tag{6.11}$$

which can be a useful expression for diffraction grating design. For applications using self-imaging effects, it is important to obtain wide self-images, as in optical encoders.

Attending to the plots in Figure 6.13, we notice that using up to $\pm$ 3rd orders we can obtain a description of both effects: the secondary peaks in the contrast from extreme fill factors, and the almost-linearly dependence between W_s and α. Expanding eq. (6.2) up to $\pm$ 3rd orders, and taking into account that $C_l = C_{-l}$ (since *sinc* is an even function), then the intensity results

$$\begin{aligned}
&\hat{I}(z,x) \approx C_0^2 + 4C_1^2\cos(qx)^2 + 4C_2^2\cos(2qx)^2 + 4C_3^2\cos(3qx)^2 \\
&+4C_0C_1\cos(qx)\cos(\pi\hat{z} - \beta_0 + \beta_1) + 4C_0C_2\cos(2qx)\cos(4\pi\hat{z} - \beta_0 + \beta_2) + \\
&+4C_0C_3\cos(3qx)\cos(9\pi\hat{z} - \beta_0 + \beta_3) + 8C_1C_2\cos(qx)\cos(2qx)\cos(3\pi\hat{z} - \beta_1 + \beta_2) + \\
&+8C_1C_3\cos(2qx)^2\left[2\cos(2qx) - 1\right]\cos(8\pi\hat{z} - \beta_1 + \beta_3) + \\
&+4C_2C_3\left[\cos(qx) + \cos(5qx)\right]\cos(5\pi\hat{z} - \beta_2 + \beta_3).
\end{aligned} \tag{6.12}$$

and the contrast results in

$$Contrast_{\pm 3}(z) = \frac{\begin{pmatrix} 4C_0C_1\cos(\pi\hat{z} - \beta_0 + \beta_1) + 8C_1C_2\cos(3\pi\hat{z} - \beta_1 + \beta_2) \\ +8C_2C_3\cos(5\pi\hat{z} - \beta_2 + \beta_3) + 4C_0C_3\cos(9\pi\hat{z} - \beta_0 + \beta_1) \end{pmatrix}}{\begin{pmatrix} C_0^2 + 4C_1^2 + 4C_2^2 + 4C_3^2 + 4C_0C_2\cos(4\pi\hat{z} - \beta_0 + \beta_2) \\ +4C_1C_3\cos(8\pi\hat{z} - \beta_1 + \beta_3) \end{pmatrix}}. \tag{6.13}$$

The numerical solutions of eq. (6.13) for a pure amplitude grating and for a $\pi/2$ phase grating (with the proper Fourier coefficients) has been plotted in Figure 6.14 for different values of z and α. The concordance with the BPM simulations is clear.

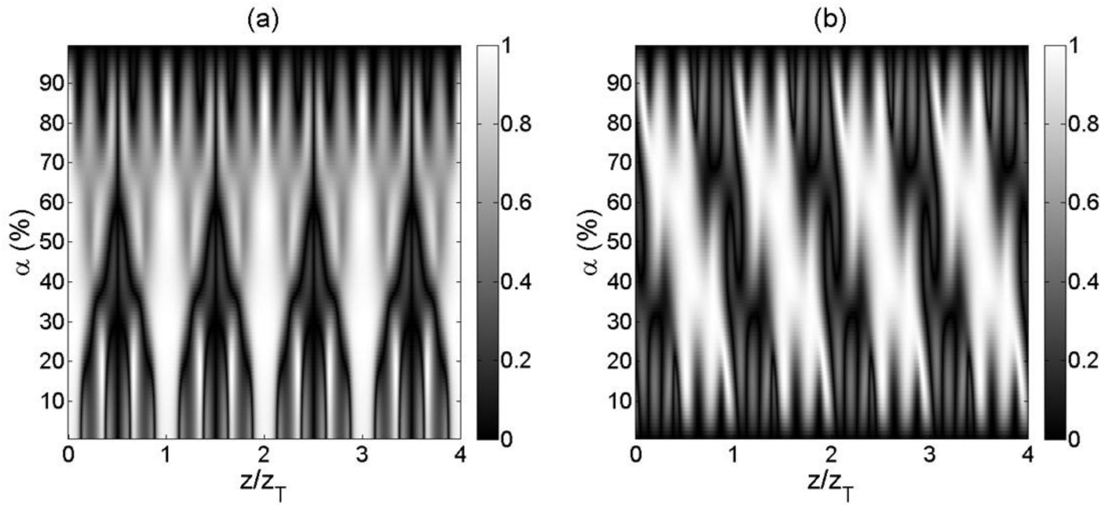

Figure 6.14: Analytical contrast obtained taking into account up to the ± 3rd orders for different values of α*, for a grating with* $p = 40\ \mu m$*, and a) a pure amplitude grating with* $a = 1,\ b = 0$ *and* $\delta = 0$*; and b) a phase grating with* $a = 1,\ b = 1,$ *and* $\delta = \pi/2$.

This expression is quite complicated to handle. Nevertheless, we can take some heuristic considerations. In eq. (6.13) some cosine functions with different frequencies, z_T, $z_T/3$, $z_T/5$, and $z_T/9$ appear. The arguments of the grating Fourier coefficients, β_l, introduce a displacement in the maxima of each cosine function. For the case of an amplitude grating, the Fourier coefficients are $c_0 = \alpha$, $c_1 = \alpha \mathrm{sinc}(\pi\alpha)$, $c_2 = \alpha \mathrm{sinc}(2\pi\alpha)$, and $c_3 = \alpha \mathrm{sinc}(3\pi\alpha)$, and consequently the arguments β_l are null. Therefore there is not displacement of the maxima of contrast with α.

Disregarding the displacement introduced by each β_l, the numerator in eq. (6.13) is a sum of cosine functions with frequencies z_T, $z_T/3$, $z_T/5$, and $z_T/9$. The absence of even spatial frequencies in the numerator ensures a minimum of contrast at multiplies of $z_T/2$ and a maximum at multiplies of z_T. The final contrast can be understood as a sum of cosines with different weights. Depending on the factors multiplying each cosine function, the smaller frequencies can be more visible than the frequency z_T, as occurs for high and low α. Under some circumstances, the sum of cosine functions produces an enlarging of W_s with α.

For a $\pi/2$ phase grating the 0th Fourier coefficients is $c_0 = \sqrt{2\alpha^2 - 2\alpha + 1}\exp\left[-\alpha i/(1-\alpha)\right]$ and therefore β_0 introduces a displacement in the maxima which is linear with α. The upper coefficients are $c_1 = \alpha\sqrt{2}\mathrm{sinc}(\pi\alpha)\exp(3\pi i/4)$,

$c_2 = \alpha\sqrt{2}\mathrm{sinc}(2\pi\alpha)\exp(3\pi i/4)$, and $c_3 = \alpha\sqrt{2}\mathrm{sinc}(3\pi\alpha)\exp(3\pi i/4)$. Thus, these upper coefficients are not necessary to explain the linear dependence of the location of the contrast maxima with α, but they introduce some higher spatial frequencies in the self-imaging contrast.

We can extract some conclusions. First, for the amplitude grating, it is notorious the strong dependence of the width of the self-images contrast maxima with the fill factor. For lower values of α, self images contrast maxima are almost a peak center on the position of the Talbot planes. Secondary maxima appear for the low and high values of α. The dependence of the shape can be understood as a sum of cosine functions with odd spatial frequencies. Nevertheless, the location of the Talbot planes does not change. On the contrary, for the $\pi/2$ phase grating case shown in Figure 6.11b we can appreciate the strong dependence of the location of the maximum contrast with the fill factor, whereas the width of this maxima do not change considerably.

The proper election of the parameters involved in eq. (6.13) can be used for the optimization of the self-images contrast shape. For example, it could be possible to maximize the self-images visibility along a deeper interval in the propagation axis, which result really interesting for optical encoders, or on the contrary, to minimize the spatial visibility of the self-images along the propagation axis, obtaining a Talbot array illuminator.

.

7 Conclusions

The main and original contribution of this PhD Thesis can be summarized in the following items,

- A laser ablation system for micromachining has been implemented. The system is arranged to work in a raster scan mode (suitable for the fabrication of complex elements) or in a vector scan mode (indicated for gratings manufacturing). A complete characterization and calibration provides us the proper operation parameters. It has been proved to work with different substrates: metals (steel tapes), dielectrics (fused silica) and crystalline solids (silica crystal). Besides, a background in laser micromachining processes has been acquired.

- At this moment, we control the complete process of binary diffractive devices rapid prototyping, from the design tasks to the manufacturing and characterization.

- In the case of steel micromachining, the roughness of the surface affects to the Talbot effect, decreasing the contrast of the self-images. We have shown that controlling the roughness of the substrate (and under the proper manufacturing process), steel tapes can be a good substrate for micro-optical applications. Besides the study of the roughness effects, we also have developed analytical expressions describing the effect of curvature of the substrate over the self-imaging process.

- Attending to transparent dielectrics, we have analyzed the effects of pulsed laser in bulk fused silica. Concretely, nanosecond laser pulses produce micro-cracks in the sample surrounding the areas where the laser has been focused. Nevertheless, the

quality/cost ratio shows that our method represents a good alternative for rapid prototyping of embedded DOEs.

- Finally, a complete description of the near field behavior of diffraction gratings has been developed, attending to the configuration parameters: the mixed amplitude/phase character, the period and fill factor of the grating. The distance between two consecutive maxima of the self-images contrast only depends on the period and the illumination wavelength. On the contrary, the location and shape of the maxima of the self-images contrast depends on the amplitude/phase character and the fill factor of the grating.

- The results derived from this Doctorate Thesis (in concrete, the manufacturing over steel substrates and in-bulk fused silica) have originated a project for the recording and reading of annular encoders, under the leadership of Fagor Automation S. Coop. in partnership with AOCG and Rofin Baasel-España-S.L.U. This project will suppose the transferring of this research results to the industrial environment.

.

Appendix A. Optical encoders

A.1 Position encoders

A position encoder (usually known as "encoder", see Figure A.1) is a device used to obtain the amount of displacement of a mobile object with respect to an origin point. When the displacement is angular, the encoder is called "rotary encoder", whereas if the displacement is longitudinal, the encoder is called "linear encoder". The basic parts of the most typical encoders are the scale and the reading head. The displacement of the reading head along the scale gives the position. However, there exist also encoders that avoid the use of scales. Regarding to the physical working principle, there exist wide variety of encoders, such as optical or magnetic encoders. In these cases, the reading head produces an electric signal based on a variation in the optical field or the magnetic field, respectively.

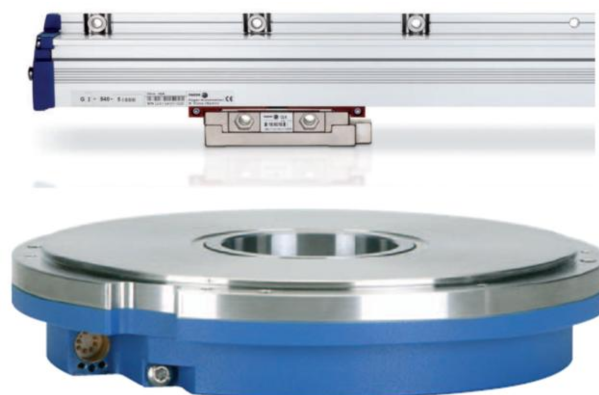

Figure A.1: Linear optical encoder (Up) and rotary optical encoder (Down) by Fagor Automation.

For the case of the optical encoders, there exist diffractive encoders, interferometric, and interfero-diffractive encoders. Due the nature of this work, we center here in diffractive linear optical encoders. In this case, the scale is a diffraction grating, and the reading head is,

basically, a photodetector. An external light source produces the desired illumination. Figure A.2 shows a schematic view of this kind of device. The measurement consists of an exploration of the optical field diffracted by the grating, as a function of the displacement.

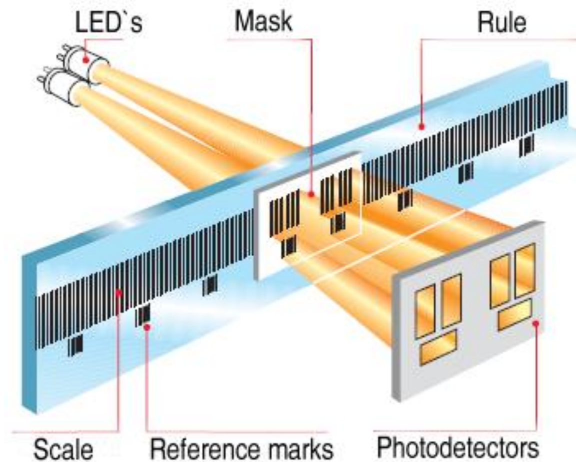

Figure A.2: Scheme of a diffractive linear encoder considered in this thesis. The mask and the photodetector move together.

The reading head produces an electric signal when it moves along the scale. The variations in the intensity are usually sinusoidal oscillations with the same period than the grating. The accuracy of the system depends, consequently, on the quality of the diffracted pattern and the mechanical tolerances. The fabrication of high quality gratings represents a field of improvement for the optical encoders. In order to obtain the absolute position (and not only the relative displacement) some reference masks are engraved in the scale.

For optical encoders based on the image formation, a second grating is used (double grating configuration) in order to form the proper optical signal over the photodetector. Whereas the first grating, acting as a scale, is fixed, the second grating moves jointly with the reading head. This second grating (usually known as "mask") has a period equal or close to the period of the first grating. Sometimes, a shaped mask substitutes the second grating, in order to improve the tolerances of the system. When the mask moves along the first grating (an also the rest of the reading head), periodical variations of the intensity are collected by the photodetector. These variations correspond to optical effects as moiré shadow, Lau effect or generalized self-imaging. The periodical variations are translated to voltage or current variations, expressing the amount of displacement. In this sense, the measurement is relative, since it corresponds to a displacement from the origin. In order to obtain an absolute measurement, the scale disposes of some reference marks at determined locations. The

absolute measurement is obtained as a relative displacement from one of these reference marks.

A.2 Encoder components

We try here to generalize the basic configuration of a diffractive optical encoder shown in Figure A.2. The main components of this system are the scale (a diffraction grating) and a mobile part, the reading head.

In general terms, there exit two configurations, transmitive or reflective, attending to the diffraction grating nature. In transmitive configuration, the grating is placed between the light source and the reading head, whereas in the reflective configuration the light source and the reading head are placed at the same side form the grating. The transmitive grating are, usually, chrome-on-glass masks or phase gratings. In the reflection configuration, both chrome-on-glass masks and metallic gratings are used. The reflective configuration allows more compact and stable reading heads. Some examples of scales used by Fagor Automation are shown in Figure A.3.

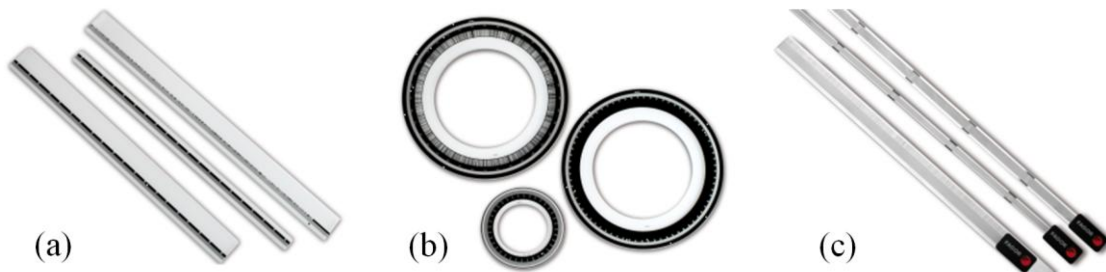

Figure A.3: Scales for optical encoders (from Fagor Automation); a) for transmitive linear encoder (chrome-on-glass), b) for transmitive rotary encoder (chrome-on-glass), and c) for reflective linear encoder (steel tape).

The chrome-on-glass gratings can be considered as nearly perfect grating, with a behavior close to the behavior predict by the theory. On the contrary, metallic gratings present some problems, since the reflective surfaces present some amount of roughness, decreasing the quality of the diffracted field.

Regarding to the moving part, it is composed of the photodetectors, the mask and the illumination source. Some other components can be included, such as polarizers or electronical devices. The complete device is free to move along the scale, giving the position at each point. The design should combine a compact packaging (in terms of size and weight) with a good mechanical behavior. An example of design is shown in Figure A.4.

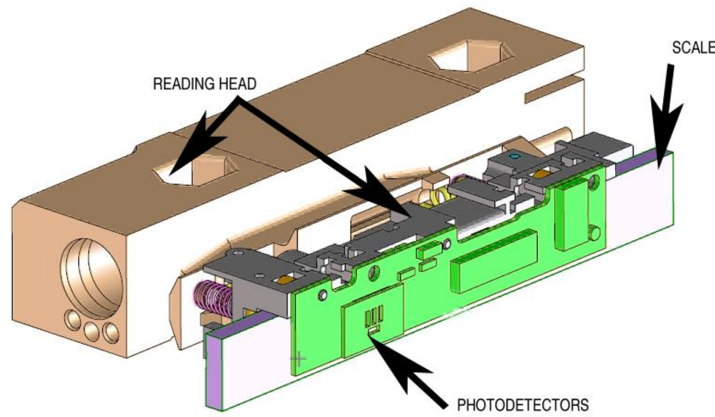

Figure A.4: Reading head of a transmission optical encoder form Fagor Automation, mounted with the scale.

A.3 Reading signals

The displacement of the mask along the grating produces a sinusoidal signal on the photodetector, known as signal A. By means of this signal, it is possible to determine the amount of displacement, but not the direction (the displacement can be positive or negative). The use of the mask in the form of a second grating produces a secondary sinusoidal signal, B with a relative shift of $\pi/4$ with A, as it is shown in Fig. A.5a. The combination of both signals allows us to know the direction of the displacement. An additional reference signal, I_0, coming from the reference marks, is used to obtain the absolute position.

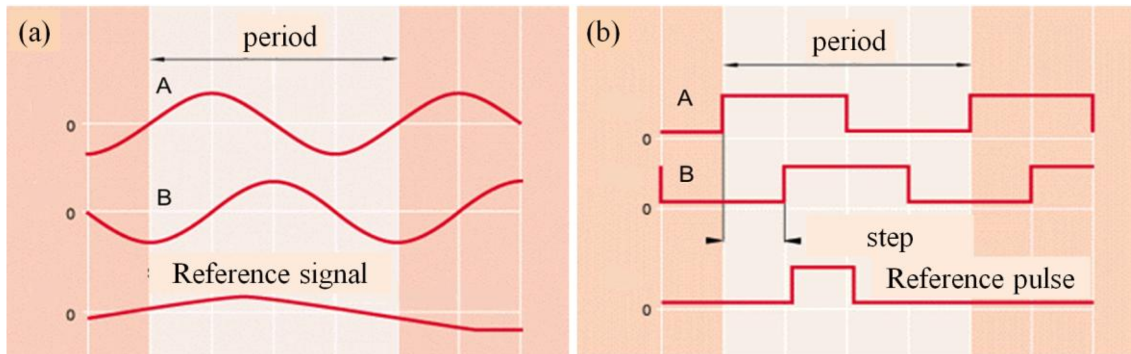

Fig. A.5: Incremental signals A and B and reference signal I_0; a) optical signals on the photodetector, and b) electronic squared signals obtained from the optical signals.

These optical signals are electronically converted into squared signals, with the same period than the original signals, shown in Fig. A.5b. It is also possible to reach lower periods by means of interpolation. The measurement is made detecting the borders of the squared signals: when a border is detected, an increment of $1/4$ of the period is accounted. The resolution is, consequently, $1/4$ of the period of the signal. When the signals are interpolated,

this period can be lower than the period of the grating. The sense of the displacement is determined by the value of signal B when a change in signal A is detected, and vice versa.

When the optical signals over the photodetector are not pure sinusoidal signals, the measurement can be erroneous. Moreover, it is very important that A and B have the same maximum and minimum value. For this reason it is usual to produce 4 signals, rather than 2, termed as A_0, A_0^-, B_0 and B_0^-. There exist a relative delay of π between A_0 and A_0^-, and also between B_0 and B_0^-. On the other hand, there exist a relative delay of $\pi/4$ between A_0 and, B_0, and between A_0^- and B_0^-. The final signal are obtained as

$$\begin{aligned} A &= A_0 - A_0^- \\ B &= B_0 - B_0^- \end{aligned} \tag{A.1}$$

When the reading head is correctly designed, the four signals have the same amount of ground intensity, and the calculated signals A and B are center around 0, regardless the ground intensity. When the shift between the four signals is not correct, some problems can appear during the measurement.

A.4 Errors affecting the measurement

Optical encoders are commonly designed to work in industrial environments. Under these circumstances, is not always possible to ensure the proper operation of the system. The most usual problems come from contamination in the system (as dust over the scale or the photodetector) introducing spurious signals.

In addition, variations in the temperature can produce thermal expansions or contractions in the scale or the mask. Then, the period of the signals changes, or the relative delays can be affected. Therefore, it is desirable to manufacture the scale and the mask with the same material, if possible.

Attending to mechanical problems, the most usual is a miss-alignment between the scale and the reading head (and, consequently, between the scale and the mask). In this situation, it cannot be ensured that A and B are center around 0. Another typical problem is any kind of curvature on the scale, changing the period locally along the grating. The reading head should be carefully designed in order to obtain a robust system, incrementing the tolerances.

.

Appendix B. Cost Function Definitions

Any optimization algorithm requires of criteria which define the goodness of result obtained by the optimization. These criteria are expressed as a mathematical function Ψ , called merit, cost or fitness function. The objective of the optimization algorithm is to look for a global minimum in the merit function value. In this sense, the merit function has to be carefully defined. For example, if we want to maximize some parameter, the merit function should be minimum whenever the optimized parameter is maximum.

In other words, let us suppose a merit function defined over a n-dimensional space $\mathrm{X} = (X_1, \ldots X_n)$, $\Psi(X_1, \ldots X_n)$. The objective of the optimization is to find, at least, a set of coordinates in the space $(x_1, \ldots x_n)$ defining a minimum,

$$\Psi(x_1, \ldots x_n) \leq \Psi(X_1, \ldots X_n), \quad \forall x_n \exists \mathrm{X} \tag{B.1}$$

Usually an optimization process falls down in a local minimum, avoiding the possibility to reach a global minimum.

A characteristic of the Global Optimization Algorithm is that they can be used to find, simultaneously, optimum values for several merit functions. In such a case, the cost function is usually defined as a linear combination of each criterion weighted by a coefficient related to the importance of that particular criterion,

$$\Psi = \sum_{l=1}^{N} c_l \cdot \psi_l \tag{B.2}$$

where c_l are the normalized weights of each normalized cost function ψ_l.

Attending to DOEs design, the most used cost functions make reference to the maximum efficiency reached or a high fidelity with a desired pattern. Another interesting function are the contrast along a profile (indicated for optimization of systems with diffraction gratings), or the intensity at a point. Some other cost functions widely used for the optimization of generalized DOEs are defined bellow.

B.1 Diffraction Efficiency

The Diffraction Efficiency η is the capability of a DOE to concentrate an input field in a desired region (plane or volumetric region), usually known as Region Of Interest,

$$\eta = \frac{I_{ROI}}{I_0} \tag{B.3}$$

where I_{ROI} and I_0 are the intensity of light in the Region Of Interest and the input illumination intensity respectively.

This criterion can be used not only for optimization task, but also for evaluation concepts, as the evaluation of losses due the DOE. It is a very useful parameter for devices working in the far field as fan-out grating, where the intensity of each diffraction order is the most important parameter. It is also in the near field for CGH as for example Fresnel zone plates, where a high amount of light is diffracted in diverging negative orders.

It results very easy to calculate the efficiency of periodical elements in the far field, where the efficiency of each order is the square of the Fourier coefficients of its series expansion.

B.2 Root Mean Square Error

The Root Mean Square quantifies the similarity between the target intensity distribution I_T and the intensity distribution I_p produced by the optimized CGH. Is defined as

$$\varepsilon = \sqrt{\frac{\sum_{x,y,z} \left| \sqrt{I_p} - \sqrt{I_T} \right|}{\sum_{x,y,z} I_T}} \tag{B.4}$$

It is the best parameter to the evaluation of the quality of the reconstruction and its fidelity to the target objective. Usually is defined at the reconstruction plane (and the only x and y coordinates should be taken into account), but it is also possible to define a reconstruction

volume. This is the parameter used by IFTA in order to obtain the desired diffraction pattern at a determined distance from the DOE.

B.3 The Signal-to-Noise Ratio

The Signal-to-Noise Ratio (SNR) express the amount of spurious diffracted light induced by quantization or fabrication errors. In patterns formed by two levels of luminosity (1 and 0), the signal I_{Signal} is defined as the light diffracted into the bright areas and the noise I_{Noise} is defined as the light diffracted into the dark areas. Thus, the SNR is defined as

$$SNR = \frac{I_{Signal}}{I_{Noise}} \tag{B.5}$$

B.4 Uniformity

Uniformity is defined as the standard deviation

$$\sigma = std(I_{Signal}) \tag{B.6}$$

σ of the intensity diffracted by a DOE in some region. Usually the Uniformity is defined in the Signal and Noise regions defined in Section B.3.

References

[1] B.C. Kress, P. Meyueis, *Applied Digital Optics: From Micro-optics to Nanophotonics*. John Wiley & Sons Ltd, Chippenham, Wiltshire (UK), 2009.

[2] M. Born, E. Wolf, *Principles of Optics*. Pergamon Press, Oxford, 1980.

[3] F.M. Grimaldi, *Physico mathesis de lumine, cloribus, et iride, aliisque annexis libri duo*. Bologna ("Bonomia"), Italy, pages 1-11. Available on-line (in Latin) at http://fermi.imss.fi.it/rd/bdv?/bdviewer/bid=300682#.

[4] C. Huygens, *Traité de la lumiere*. Leiden, Netherlands, 1690.

[5] T. Young, "The Bakerian Lecture: Experiments and calculations relative to physical optics," Philosophical Transactions of the Royal Society of London 94, 1-16, 1804.

[6] A.J. Fresnel, "Premiere mémoire sur la diffraction de la lumière," Ann. Chem. Phys. 1, 239-281 (1816).

[7] J.C. Maxwell, "A dynamical theory of the electromagnetic field," Philosophical Transactions of the Royal Society of London 155, 459-512 (1865).

[8] G. Kirchhoff, "Zur Theorie der Lichtstrahlen," Ann. Phys. 254(4), 663-695 (1883).

[9] A. Sommerfeld, "Mathematische Theorie der Diffraction," Math. Ann. 47, 317374 (1896).

[10] J. Turunen, F. Wyrowski, *Diffractive Optics for Industrial and Commercial Applications*. J. Turunen, and F. Wyrowski Ed. Berlin, Germany: Akademie-Verlag, 1997.

[11] F. Wyrowski, O. Bryngdahl, "Digital holography as part of diffractive optics", Rep. Prog. Phys., 54, 1484-1571, (1991).

[12] D.C. O'Shea, T.J. Suleski, A.D. Kathman, D.W. Prather, *Diffractive optics: design, fabrication and test*. SPIE Press, Bellingham, Whashington, USA, 2004.

[13] D. Gabor, "A new microscopi principle," Nature, 161(4098), 777-778, (1948).

[14] H. Kogelnik, "Coupled wave theory for thick hologram gratings," Bell Syst. Tech. J., 48(9), 2909-2947,(1969)

[15] H.P. Herzig, *Micro-optics. Elements, systems and applications*, H.P. Herzig Ed., London, United Kingdom, Taylor & Francis, 1997.

[16] T.J. Suleski, R.D. Te Kolste, "Fabrication Trends for Free-Space Microoptics," J. Lightwave Technol., 23(2), (2005).

[17] C. Palmer, "Diffraction Grating Handbook", Richardson Grating Laboratory, New York, 2000.

[18] R. W. Wood, "Phase-reversal zone plates, and diffraction-telescopes," Philos. Mag. **45**, 511-522, (1898).

[19] A. Trowbridge, R. W. Wood, "Groove-form and energy distribution of diffraction gratings," Phil. Mag., 20, 886–898 (1910).

[20] A.W. Lohmann, D.P. Paris, "Binary Fraunhofer holograms, generated by computer," Appl. Opt., 6(10), 1739-1748 , (1967).

[21] J. Mait, "From ink bottles to E-beams: A historical perspective of diffractive optics," in *Proc. SPIE Optical Processing and Computing: A Tribute to Adolf Lohmann*, PM117, 201-226, 2001.

[22] L. Lesem, P. Hirsch, J. Jordan, "The kinoform: A new wavefront reconstruction device," IBM J. Res. Dev., 13(2), 150-155, (1969).

[23] J.A. Jordan Jr., P.M. Hirsch, L.B. Lesem, D.L. Van Rooy, "Kinoform Lenses," Appl. Opt., 9(8), 1883-1887, (1970).

[24] L. d'Auria, J.P. Huignard, A.M. Roy, E. Spitz, "Photolithographic fabrication of thin film lenses," Opt. Comm., 5(4), 232-235, 1972.

[25] O.K. Ersoy, "Construction of point images with the scanning electron microscope: A simple algorithm," Optik, 46(1), 61-66, (1976).

[26] T. Fujita, H. Nishihara, J. Koyama, "Fabrication of micro-lenses using electron beam lithography," Opt. Lett., 6(12), 613-615, (1981).

[27] G.J. Swanson, W.B. Veldkamp, "Binary lenses for use at 10.6 micrometers," Opt. Eng., 24(5), 791-795, 1985.

[28] M.B. Fleming, M.C. Hutley, "Blazed diffractive optics," Appl. Opt., 36(20), 4635-4643, (1997).

[29] B.A. Fuchs, C. Syn, S.P. Velsko, "Diamond turning of lithium niobate for optical applications", Appl. Opt., 31(27), 5788-5793, (1992).

[30] F. Lacour, N. Courjal, M.-P. Bernal, A. Sabac, C. Bainier, M. Spajer, "Nanostructuring lithium niobate substrates by focused ion beam milling", Opt. Mater., 27, 1421-1425, (2005).

[31] E. Russo, "Laser Ablation," Focal Point 46(9), 14A, (1995).

[32] H.J. Levinson, *Principles of Lithography*, SPIE Press, Bellingham, WA (2001).

[33] M. Haruna, M. Takahashi, K. Wakahayashi, H. Nishihara, "Laser beam lithographed micro-Fresnel lenses," Appl. Opt. 29(34), 5120-5126, 1990.

[34] P.B. Fischer, S.Y. Chou, "Sub-50 nm high aspect-ratio silicon pillars, ridges, and trenches fabricated using ultrahigh resolution electron beam lithography and reactive ion etching," Appl. Phys. Lett. 62(12), 1414-1417, (1993).

[35] T. Morlanes, D. Crespo, J. Alonso. Spanish patent 200001496, "Disposición Optoelectrónica de Fotodetectores para la Medición de Longitud" (2000).

[36] T. Morlanes, J. Alonso, E. Bernabeu, Spanish patent 05380095, "Dispositivo optoeléctrico de medida" (2005).

[37] J. Alonso, E. Bernabeu, U.E patent G01B11/14, "Optisches Kodificiergerat zum Messesvon Verschiegbungen" (1992).

[38] J. Alonso Fernández, *Aportaciones a las técnicas de codificación óptica*, PhD thesis, Universidad Complutense de Madrid (1992).

[39] T. Morlanes Calvo, *Dispositivos optoelectrónicos interferométricos con láseres de semiconductor estabilizados en longitud de onda aplicados a la medida de desplazamientos*. PhD thesis, Universidad Complutense de Madrid (1999).

[40] D. Crespo Vázquez, *Nuevas herramientas aplicadas a la codificación óptica*, PhD thesis, Universidad Complutense de Madrid (2001).

[41] J.B. Sáez Landete, *Generación de señales ópticas de referencia para posicionamiento de alta resolución*, PhD thesis, Universidad Complutense de Madrid (2006).

[42] F.J. Torcal Milla, *Rough diffraction gratings: applications to linear optical encoders*, PhD thesis, Universidad Complutense de Madrid (2009).

[43] J.R. Reitz, F.J. Milford, R.W. Christy, *Fundamentos de la teoría electromagnética*, 4rd edition, Addison-Wesley Iberoamericana, (1991).

[44] P.G. Rudolf, J.J. Tollet, R.R. MacGowan, "Computer modeling wave propagation with a variation of the Helmholtz–Kirchhoff relation," Appl. Opt., 29(7), 998–1003, 1990.

[45] J.C. Hurtley, "Scalar Rayleigh–Sommerfeld and Kirchhoff diffraction integrals: a comparison of exact evaluations for axial points," J. Opt. Soc. Am., 63(8), 1003-1008, 1973.

[46] E. Wolf, E.W. Marchand, "Comparison of the Kirchhoff and Rayleigh–Sommerfeld theories of diffraction at an Aperture," J. Opt. Soc. Am. 54(5), 587-594, 1964.

[47] U. Levy, E. Marom, D. Mendlovic, "Thin element approximation for the analysis of blazed gratings: simplified model and validity limits," Opt. Comm. 229, 11–21 (2004).

[48] F. Shen, A. Wang, "Fast-Fourier-transform based numerical integration method for the Rayleigh–Sommerfeld diffraction formula," Appl. Opt. 45 1102-1110, (2006).

[49] M. D. Feit and J. A. Fleck Jr., "Light propagation in graded-index optical fibers," App. Opt., 17, 3990-3998 (1978).

[50] M. Koshiba, Y. Tsuji and M. Hikari, "Finite Element Beam Propagation Method with Perfectly Matched Layer Boundary Conditions," IEEE Trans. on Magnetics, 35, 1482-1485 (1999).

[51] D. Yevick and L. Thylén, "Analysis of gratings by the beam-propagation method," J. Opt. Soc. Am., 72, 1084-1089 (1982).

[52] P.J.M. Vanbrabant, J. Beeckman, K. Nayts, R. James and F.A. Fernandez, "A finite element beam propagation method for simulation of liquid crystal devices," Opt. Express, 17, 10895-10909 (2009).

[53] J.P. Berenguer, "A perfectly matched layer for the absorption of electromagnetic waves," J. Comput. Phys., 114, 185-200 (1994).

[54] P. Srisungsitthisunti, O.K. Ersoy, X. Xu, "Beam propagation method modeling of modified volume Fresnel zone plates fabricated by femtosecond laser direct writing," J. Opt. Soc. Am. A, 26, 188-194 (2009).

[55] W.P. Huang, C.L. Xu, W. Lui, K. Yokoyama, "The perfectly matched layer (PML) boundary condition for the beam propagation method," IEEE Photon. Technol. Lett., 8, 649-651 (1996).

[56] M. Koshiba, Y. Tsuji, M. Hikari, "Finite Element Beam Propagation Method with Perfectly Matched Layer Boundary Conditions", IEEE Trans. on Magnetics 35(3), 1482-1485 (1999).

[57] J.R. Fienup, "Phase retrieval algorithms: a comparison," Appl. Opt. 21(15), 2758-2769 (1982).

[58] N.C. Gallagher, B. Liu, "Method for computing kinoforms that reduces image reconstruction err,' Appl. Opt. 12(10), 2328-2335 (1973).

[59] J.R. Fienup, "Reconstruction of an object from the modulus its Fourier transform," Opt. Lett. 3(1), 27-29 (1978).

[60] R.W. Gerchberg, W.O. Saxton, "A practical algorithm for the determination of phase from image and diffraction plane pictures," Optik 34(8), 237-246 (1972).

[61] F. Wyrowski, O. Bryngdahl, "Iterative Fourier-transform algorithm applied to computer holography," J. Opt. Soc. Am. A 5(7), 1058-1065 (1988).

[62] F. Wyrowski, "Diffractive optical elements: iterative calculation of quantized, blazed phase structures," J. Opt. Soc. Am. A 7(6), 961-969 (1990).

[63] F. Wyrowski, "Design theory of diffractived elements in the paraxial domain," J. Opt. Soc. Am. A 10(7), 1553-1561 (1993).

[64] H. Zhai, F. Liu, X. Yang, G. Mu, P. Chavel, "Improving binary images reconstructed from kinoforms by amplitude adjustment," Opt. Comm. 219, 81-85 (2003).

[65] J.S. Liu, M.R. Taghizadeh, "Iterative algorithm for the design of diffractive phase elements for laser beam shaping," Opt. Lett. 27(16), 1463-1465 (2002).

[66] S. Liu, A.J. Caley, M.R. Taghizadeh, "Symmetrical iterative Fourier-transform algorithm using both phase and amplitude freedoms," Opt. Comm. 267(2), 347-355 (2006).

[67] http://www.mathworks.com/products/matlab/

[68] R. Paschotta, *Encycolpedia of Laser Physics and Technology*, 1. Ed., Wiley-VCH, Berlin, Germany, 2008.

[69] I.A. Walmsley, V. Wong, "Characterization of the electric field of ultrashort optical pulses," J. Opt. Soc. Am. B 13 (11), 2453-2463 (1996).

[70] D.J Kane and R. Trebino, "Characterization of arbitrary femtosecond pulses using frequency-resolved optical gating," IEEE J. Quantum Electron. 29(2), 571-579 (1993).

[71] C. Iaconis, I. A. Walmsley, "Spectral phase interferometry for direct electric-field reconstruction of ultrashort optical pulses," Opt. Lett. 23(10), 792-794 (1998).

[72] S. Akturk X. Gu, P. Gabolde, R. Trebino, "The general theory of first-order spatio-temporal distortions of Gaussian pulses and beams," Opt. Express 13(21), 8642-8661 (2005).

[73] J. Casas, *Óptica*, Cooperativa de Artes Gráficas Librería General, Zaragoza, Spain, 1994.

[74] G.F. Smith, "The early laser years at Hughes Aircraft Company," IEEE J. Quantum Electron. 20(6), 577-584, (1984).

[75] A. Einstein, "Über einen die Erzeugung und Verwandlung des Lichtes betreffenden heuristischen Gesichtspunkt," Ann. Phys. 17, 132-148 (1905).

[76] R.A. Millikan, "Einstein's photoelectric equation and contact electromotive force," Phys. Rev. 7, 18-32 (1926).

[77] G. Mainfray, C. Manus, "Multiphoton ionization of atoms," Rep. Mod. Phys., 54, 1333-1372 (1991).

[78] J.C. Miller, R.F. Haglund, *Laser ablation and desorption*, Academic Press, San Diego, USA (1998).

[79] P. Gibbon, *Short Pulse Laser interactions with Matter. An Introduction*, Imperial College Press, Londres, 2007.

[80] P. Drude, "On the electron theory of metals," Ann. Phys. 1(3), 566-613 (1900).

[81] http://www.newport.com/navigator

[82] A.E. Siegman, *Lasers*, 2nd ed, Oxford U. Press, London, UK, 1986.

[83] A E. Siegman, "Defining, measuring, and optimizing laser beam quality," Proc. SPIE 1868, 2-12 (1993).

[84] F.M. Dickey, S.C. Holswade, D.L. Shealy, *Laser Beam Shaping Applications*, CRC Press, Taylor& Francis Group, Boca Raton, FL, USA, 2006.

[85] J. Sabbaghzadeh, M.J. Hamedi, F. Malek Ghaini, M.J. Torkamany, "Effect of Process Parameters on the Melting Ratio in Overlap Pulsed Laser Welding," Metall. Meter. Trans. B 39(2), 340-347 (2008).

[86] http://www.schott.com/

[87] J. Ihlemann, M. Schultz-Ruhtenberg, T. Fricke-Begemann, "Micro patterning of fused silica by ArF- and F2-laser ablation,". J. Phy: Conference Series 59, 206-209 (2007).

[88] J. Wang, H. Niino, A. Yabe "One-step microfabrication of fused silica by laser ablation of an organic solution," Appl. Phys. A 68(1), 111-113 (1999).

[89] B. Hopp, T. Smausz, M. Bereznai "Processing of transparent materials using visible nanosecond laser pulses," App. Phys. A 87(1), 77-79, (2007).

[90] P.R. Herman, R.S. Majoribanks, A. Oetl, K. Chen, I. Konovalov, S. Ness, "Laser shaping of photonic materials: deep-ultraviolet and ultrafast lasers," Appl. Surf. Sci. 154, 577-586 (2000).

[91] J. Ihlemann, B. Wolf, P. Simon, "Nanosecond and femtosecond excimer laser ablation of fused silica," Appl. Phys. A 54(4), 363-368 (1992).

[92] P. Srisungsitthisunti, O.K. Ersoy, X. Xu, "Volume Fresnel zone plates fabricated by femtosecond laser direct writing," Appl. Phys. Lett. 90(1), 011104, 2007.

[93] A. Zoubir, L. Shah, K. Richardson, M. Richardosn, "Practical uses of femtosecond laser micro-materials processing," Appl. Phys. A 77(2), 311-315 (2003).

[94] W. Watanabe, D. Kuroda, K. Itoh, "Fabrication of Fresnel zone plate embedded in silica glass by femtosecond laser pulses," Opt. Express 10, 978-983 (2002).

[95] N. Bärsch, K. Körber, A. Ostendorf, K.H. Tönshoff, "Ablation and cutting of planar silicon devices using femtosecond laser pulses," Appl. Phys. A 77, 237-242 (2003).

[96] K. Venkatakrshnan, N. Sudani, B. Tan, "A high-repetition-rate femtosecond laser for thin silicon dicing", J. Micromech. Microeng. 18(7), 075032 (2008).

[97] M.J. Weber, *Handbook of Optical Materials*, CRC Press, Boca Raton, Florida, USA, 2003.

[98] K. Engelhardt, P. Seitz, "High-resolution optical position encoder with large mounting tolerances," Appl. Opt. 36(13), 2912-2916 (1997).

[99] S. Fourment, P. Arguel, J.-L. Noullet, F. Lozes, S. Bonnefont, G. Sarrabayrouse, Y. Jourlin, J. Jay, O. Parriaux, "A silicon integrated opto-electro-mechanical displacement sensor," Sensor Actuat. A-Phys., 110, 294-300 (2004).

[100] K. Patorski, "The self-imaging phenomenon and its applications," Prog. Optics 27, 3–108 (1989).

[101] G. Schirripa Spagnolo, D. Ambrosini, D. Paoletti, "Displacement measurement using the Talbot effect with a Ronchi grating," J. Opt. A-Pure Appl. Op. 4, 376–380 (2002).

[102] F.J. Torcal-Milla, L.M. Sanchez-Brea, E. Bernabeu, "Double grating systems with one steel tape grating," Opt. Commun. 281(23) 5647–5652 (2008).

[103] F.J. Torcal-Milla, L.M. Sanchez-Brea, E. Bernabeu, "Talbot effect with rough reflection gratings", Appl. Opt. 46(18), 3668-3673 (2007).

[104] L.M. Sanchez-Brea, F.J. Torcal-Milla, E. Bernabeu, "Talbot effect in metallic gratings under Gaussian illumination," Opt. Commun. **278,** 23–27 (2007).

[105] W.H.F. Talbot, "Facts relating to optical science," Philos. Mag. 9, 401–407 (1836).

[106] E. Keren, O. Kafri "Diffraction effects in moire deflectometry" J. Opt. Soc. Am. A 2, 111-120 (1985).

[107] P. Beckmann, A. Spizzichino, *The Scattering of Electromagnetic Waves from Rough Surfaces,* Artech House, Norwood, USA, 1987.

[108] A. Ogilvy, *Theory of Wave Scattering from Random Rough Surfaces*, IOP, Bristol, UK, 1991.

[109] F. Perez-Quintián, A. Lutenberg, M.A. Rebollo, "Linear displacement measurement and spckle pattern illumination," Appl. Opt. 45(20), 4821-4825 (2006).

[110] F.J. Salgado-Remacha, L.M. Sanchez-Brea, F.J. Alvarez-Rios, E. Bernabeu, "Rough Fresnel zone plates over metallic surfaces," Appl. Opt. 49(10), 1750-1756 (2010).

[111] L.M. Sanchez-Brea, F.J. Torcal-Milla, E. Bernabeu, "Variogram-based method for contrast measurement," Appl. Opt. 46(22), 5027-5033 (2007).

[112] E.G. Loewen, E. Popov, *Diffraction gratings and applications*, Marcel Dekker, New York, USA, 1997.

[113] L. Garcia-Rodriguez, J. Alonso, E. Bernabeu, "Grating pseudo-imaging with polychromatic and finite extensión sources," Opt. Express 12(11), 2529-2541 (2004).

[114] G.J. Swanson, E.N. Leith, "Analysis of the Lau effect and generalized grating imaging," J. Opt. Soc. Am. A 2(6), 789-793 (1985).

[115] A. Olszak, L. Wronkowski, "analysis of the Fresnel field of a double diffraction system in the case of two amplitude diffraction gratings under partially coherent illumination," Opt. Eng. 36, 2149-2157 (1997).

[116] J. Tu, L. Zhan, "Analysis of general double periodic structure diffraction phenomena based on the ambiguity function," J. Opt. Soc. Am. A 9(6), 983-995 (1992).

[117] D. Crespo. J. Alonso, E. Bernabeu, "Experimental measurements of generalized grating images," Appl. Opt. 41(7), 1223-1228 (2002).

[118] S. Teng, L. Liu, J. Zu, Z. Luan, D. Liu, "Uniform theory of the Talbot effect with partially coherent light illumination," J. Opt. Soc. Am. A 20(9), 1747-1754 (2003).

[119] D. Crespo, J. Alonso, E. Bernabeu, "Generalized grating imaging using an extended monochromatic light source," J. Opt. Soc. Am. A 17(7), 1231-1240 (2000).

[120] L.M. Sanchez-Brea, F.J. Torcal-Milla, E. Bernabeu, "Far field of gratings with rough strips," J. Opt. Soc. Am. A 25(4), 828-833 (2008).

[121] F.J. Torcal-Milla, L.M. Sanchez-Brea, E. Bernabeu, "Self-imaging of gratings with rough strips," J. Opt. Soc. Am. A 25(10), 2390-2394 (2008).

[122] H.G. Beutler, "The theory of the concave grating," J. Opt. Soc. Am. 35(5), 311-349 (1945).

[123] H. Haber, "The torus grating," J. Opt. Soc. Am. 40(3), 153-165 (1950).

[124] C.T. Hsieh, C.K. Lee, "Cylindrical-type nanometer-resolution laser diffractive encoder," App. Opt. 38(22), 4743-4750 (1999).

[125] X. Prieto-Blanco, C. Montero-Orille, H. Gonzalez-Núñez, M.D. Mouriz, E. López Lago, R. de la Fuente, "Imaging with classical spherical diffraction gratings: the quadrature configuration," J. Opt. Soc. Am. A, 26(11) 2400-2409 (2009).

[126] B.E. Woodgate, J. Opt. Soc. Am., 64(5) (1974) 654-661.

[127] A.V. Baez, "Fresnel Zone Plate for Optical Image Formation Using Extreme Ultraviolet and Soft X Radiation," J. Opt. Soc. Am. 51(4), 405-412 (1961).

[128] J. Kirz, "Phase zone plates for x rays and the extreme uv," J. Opt. Soc. Am. A 64(3), 301-309 (1974).

[129] F.J. González. J. Alda, B. Illic and G. Boreman, "Infrared Antennas Coupled to Lithographic Fresnel Zone Plate Lenses," Appl. Opt. 43, 6067-6073 (2004).

[130] E. Hecht, "Fresnel diffraction," in *Optics*, (Reading, MA: Addison Wesley, 2002), ch. 10, sec. 3.

[131] M.F. Modest, "Transient elastic and viscoelastic thermal stresses during laser drilling of ceramics," J. Heat Transfer 120, 892-898 (1998).

[132] J. Krüger, W. Kautek, "Femtosecond-pulse visible laser processing of transparent materials," Appl. Surf. Sci. 96-98, 430-438 (1996).

[133] J. Noack; A. Vogel, "Laser-induced plasma formation in water at nanosecond to femtosecond time scales: calculation of thresholds, absorption coefficients, and energy density," IEEE J. Quantum Electron. 35, 1156-1167 (1999).

[134] C. B. Schaffer, A. Brodeur, J. F. García, and E. Mazur, "Micromachining bulk glass by use of femtosecond laser pulses with nanojoule energy," Opt. Lett. 26(2), 93-95 (2001).

[135] S. Juodkazis, A.V. Rode, E. G. Gamaly, S. Matsuo, and H. Misawa, "Recording and reading of three-dimensional optical memory in glasses," Appl. Phys. B. 77(2-3), 361-368 (2003).

[136] V. Mizeikis, K.K. Seet, S. Juodkazis, H. Misawa, "Three-dimensional woodpile photonic crystal templates for the infrared spectral range," Opt. Lett., 29(17), 2061-2063 (2004).

[137] E.N. Glezer, M. Milosavljevic, L. Huang, R.J. Finlay, T.H. Her, J.P. Callan, E. Mazur, "Three-dimensional optical storage inside transparent materials," Opt. Lett. 21(24), 2023-2025 (1996).

[138] T. Tanaka, S. Kawata, "Comparison of recording densities in three-dimensional optical storage systems: multilayered bit recording versus angularly multiplexed holographic recording," J. Opt. Soc. Am. A 13(5), 935-943 (1996).

[139] Y. Li, Y. Dou, R. An, H. Yang, Q. Gong, "Permanent computer-generated holograms ebedded in silica glass by femtosecond laser pulses", Opt. Express 13(7), 2433-2438 (2005).

[140] I. Moreno, A. Martínez-García, L. Nieradko, J. Albero, C. Gorecki, "Low cost production of computer-generated holograms: from design to optical evaluation," J. Eur. Opt. Soc. Rap. Public. 5, 10011 (2010).

[141] S-H Cho, W-S Chang, K-R Kim, J.W. Hong, "Femtosecond laser embedded grating micromachining of flexible PDMS plates," Opt. Comm. 282(7), 1317-1321 (2009).

[142] E.G. Gamaly, A.V. Rode, B. Luther-Davies, "Ablation of solids by femtosecond laser: ablation mechanism and ablation thresholds for metals and dielectrics", Phys. Plasmas, 9, 949-957 (2002).

[143] O. Efimov, S. Juodkazis, H. Misawa, "Intrinsic single- and multiple-pulse laser-induced damage in silicate glasses in the femtosecond-to-nanosecond region," Phys. Rev. A 69(4), 042903 (2004).

[144] F. Wyrowski, "Iterative quantization of digital amplitude holograms," App. Opt.. 28, 3864-3870 (1989).

[145] F. Montiel, M. Nevière, "Differential theory of gratings: extension to deep gratings of arbitrary profile and permittivity through the R-matrix propagation algorithm," J.Opt. Soc. Am. A 11(12), 3241-3250 (1994).

[146] LC. Botten, N.A.P. Nicorovici, A.A. Asatryan, R.C. McPhedran, C.M de Sterke, P.A. Robinson, "Formulation for electromagnetic scattering and propagation through grating stacks of metallic and dielectric cylinders for photonic crystal calculations. Part I. Method," J. Opt. Soc. Am. A 17(12), 2165-2176 (2000).

[147] E.N. Glytsis, T.K. Gaylord, "Rigorous 3-D coupled wave diffraction analysis of multiple superposed gratings in anisotropic media," Appl. Opt. 28(12), 2401-2421 (1989).

[148] J.W. Goodman, *Introduction to Fourier Optics* (McGraw-Hill, New York, 1968).

[149] G.O. Reynolds, J.B. DeVelis, G.B. Parrent Jr., B.J. Thompson, *The New Physical Optics notebooks tutorials in Fourier Optics*, (SPIE Press, Bellingham,1989).

[150] F.J. Torcal-Milla, L.M. Sanchez-Brea and F.J. Salgado-Remacha, "Self-images location of amplitude/phase binary gratings," App. Opt. 48(32), 6252-6258 (2009).

[151] L.M. Sanchez-Brea, J. Saez-Landete, J. Alonso and E. Bernabeu, "Invariant grating pseudoimaging using polychromatic light and a finite extension source", Appl. Opt. 47(10), 1470-1477 (2008).

[152] W.G. Rees, "The validity of the Fresnel approximation," Eur. J. Phys 8, 44-48 (1987).

[153] M.G. Moharam, T.K. Gaylord, "Rigorous coupled-wave analysis of planar-grating diffraction," J. Opt. Soc. Am. A 71(7), 811-818 (1981).

[154] D.A. Pommet, M.G. Moharam, E.B. Grann, "Limits of scalar diffraction theory for diffractive phase elements," J.Opt. Soc. Am. A 11(6), 1827–1834 (1994).

[155] N. Chateau, J.P. Hugonin, "Algorithm for the rigorous coupled-wave analysis of grating diffraction," J. Opt. Soc. Am. A 11(4), 1321-1331(1994).

Publications and Communications

Related with this Thesis

Publications

1. F.J. Torcal-Milla, L.M. Sanchez-Brea, F.J. Salgado-Remacha, "Self-images location of amplitude/phase binary gratings," Appl. Opt. 48(32), 6252-6258 (2009).

2. L.M. Sanchez-Brea, F.J. Salgado-Remacha, F.J. Torcal-Milla, "Effect of surface defects on the self-images produced by diffraction gratings," Proceedings of SPIE "Optical Measurement Systems for Industrial Inspection VI, P.H. Lehmann, ed, 7389, 738932-1/8 (2009).

3. F.J. Torcal-Milla, L.M. Sanchez-Brea, F.J. Salgado-Remacha, "Self-images of 2D pseudo-random amplitude Ronchi gratings," Proceedings of the EOS Topical Meeting in Capri (2009).

4. J. Alda, J.M. Rico-Garcia, F.J. Salgado- L.M. Sanchez-Brea, "Diffractive Performance of Square Fresnel Zone Plates," Opt. Commun. 282(17) 3402-3407 (2009).

5. J.M. Rico-García, F.J. Salgado-Remacha, L.M. Sanchez-Brea, J. Alda, "Optimized square Fresnel zone plates for microoptics applications," Proceedings of SPIE "Modeling Aspects in Optical Metrology II, H. Bosse, B. Bodermann, R. M. Silver eds, 7390, 739011-1/8 (2009).

6. F.J. Salgado-Remacha, L.M. Sanchez-Brea, F.J. Alvarez-Rios, E. Bernabeu, "Rough Fresnel Zones Plates over metallic surfaces," Appl. Opt. 49(10), 1750-1756 (2010).

7. L.M. Sanchez-Brea, F.J. Torcal-Milla, F.J Salgado-Remacha, T. Morlanes, I. Jimenez-Castillo, E. Bernabeu, "Collimation method using a double grating system," Appl. Opt. 49(17), 3363-3368 (2010).

8. F.J. Torcal-Milla, L.M. Sanchez-Brea, F.J Salgado-Remacha, E. Bernabeu, "Self-Imaging with curved gratings," Opt. Commun. 283, 3869-3873 (2010).
9. J. Alda, L. M. Sánchez-Brea, F.J. Salgado-Remacha, J. M. Rico-García, "Diffractive optical elements with square concentric rings of equal width," Microw. Opt. Techn. Let., 52(4) 930-934 (2010).
10. F.J Salgado-Remacha, F.J. Torcal-Milla, L.M. Sanchez-Brea, E. Bernabeu, "Use of steel substrates in diffractive optics: near field of high surface quality steel tape gratings," Opt. Laser Eng., 49 356-360 (2011).
11. F.J Salgado-Remacha, L.M. Sanchez-Brea, E. Bernabeu, "Micromachining of Diffractive Optical Elements embedded in bulk fused silica by nanosecond pulses," J. Lightwave Technol., in press.
12. F.J Salgado-Remacha, L.M. Sanchez-Brea, E. Bernabeu, "Effect of fill-factor on the self-images of diffraction gratings," Appl., Opt., under revision.

Communications

13. F.J. Salgado-Remacha, "Fabrication of diffractive optical elements (DOEs) using direct laser writing" 2008 Winter College on Micro and Nano Photonics for Life Sciences, Trieste, Italy (2008).
14. F.J. Salgado-Remacha, I. Jimenez-Castillo, L.M. Sanchez-Brea, E. Bernabeu, "Diffraction gratings embedded in bulk fused silica by laser ablation," poster presentation, TNT2008 - Trends in Nanotechnology, Oviedo, Spain (2008).
15. L.M. Sanchez-Brea, F.J. Salgado-Remacha, F.J. Torcal-Milla, "Effect of surface defects on the self-images produced by diffraction gratings", poster presentation, Optical Metrology (SPIE) Munich (Germany) (2009).
16. F.J. Alvarez-Rios, F.J. Salgado-Remacha, I. Jimenez-Castillo, L.M. Sanchez-Brea, F.J. Torcal-Milla, J.M. Rico-García, E. Bernabeu, "Simulación del comportamiento óptico de metales mediante el uso de un modulador espacial de luz," 23 Bienal de Física (19 encuentro ibérico de Enseñanza de la Física), Ciudad Real, Spain (2009).
17. F.J. Torcal-Milla, L.M. Sanchez-Brea, F.J. Salgado-Remacha, "Autoimagenes producidas por redes de difracción binarias de fase-amplitud", poster presentation, Reunión Nacional de Óptica, Orense (Spain) (2009).
18. F.J. Salgado-Remacha, I. Jimenez-Castillo, F.J. Torcal-Milla, T. Morlanes, L.M. Sanchez-Brea, E. Bernabeu, "Autoimágenes producidas por redes de difracción grabadas sobre fleje de acero mediante ablación láser," poster presentation, Reunión Nacional de Óptica, Orense (Spain) (2009).

19. F.J. Torcal-Milla, L.M. Sanchez-Brea, F.J. Salgado-Remacha, "Self-images of 2D pseudo-random amplitude Ronchi gratings," 3rd EOS Topical Meeting on Optical Microsystems (OμS'09), Capri, Italy (2009).
20. J.M. Rico-García, F.J. Salgado-Remacha, L.M. Sanchez-Brea, J. Alda, "Optimized square Fresnel zone plates for microoptics applications," poster presentation, Optical Metrology (SPIE) Munich (Germany) (2009).
21. J. Alda, F.J. Salgado-Remacha, L.M. Sanchez-Brea, J.M. Rico-García, F.J. González, "Optimal phase distributions for polygonal Fresnel lenses" European Conference on Antennas & Propagation (EuCAP 2010), Barcelona (2010).
22. F.J. Salgado-Remacha, F.J. Torcal-Milla, I. Jimenez-Castillo, L.M. Sanchez-Brea, E. Bernabeu, "Diffractive Optical Elements in bulk fused silica by nanosecond pulses laser ablation," Laser Precision Microfabrication (LPM 2010), Stuttgart, Germany (2010).
23. F.J. Salgado-Remacha, I. Jimenez-Castillo, L.M. Sanchez-Brea, E. Bernebeu, "Structured photodiodes by means of Laser Ablation over silica diodes," Laser Precision Microfabrication (LPM 2010), Stuttgart, Germany (2010).

Other works

Publications

24. F. J. Salgado Remacha, S. Jarabo Lallana, "Emisión multilínea en láseres de fibra óptica dopada con erbio empleando filtros sencillos," Óptica pura y aplicada 41(1) 51-57 (2008).
25. L.M. Sanchez-Brea, F.J. Salgado-Remacha, "Three dimensional diffraction of a thin metallic cylinder illuminated in conical incidence: application to diameter estimation," Appl. Opt., 47(26) 4804-4811 (2008).
26. s, Trieste, Italy (2008).
27. F.J. Salgado-Remacha, I. Jimenez-Castillo, L.M. Sanchez-Brea, E. Bernabeu, "Diffraction gratings embedded in bulk fused silica by laser ablation," poster presentation, TNT2008 - Trends in Nanotechnology, Oviedo, Spain (2008).
28. L.M. Sanchez-Brea, F.J. Salgado-Remacha, F.J. Torcal-Milla, "Effect of surface defects on the self-images produced by diffraction gratings", poster presentation, Optical Metrology (SPIE) Munich (Germany) (2009).
29. F.J. Alvarez-Rios, F.J. Salgado-Remacha, I. Jimenez-Castillo, L.M. Sanchez-Brea, F.J. Torcal-Milla, J.M. Rico-García, E. Bernabeu, "Simulación del comportamiento óptico de metales mediante el uso de un modulador espacial de luz," 23 Bienal de Física (19 encuentro ibérico de Enseñanza de la Física), Ciudad Real, Spain (2009).

30. F.J. Torcal-Milla, L.M. Sanchez-Brea, F.J. Salgado-Remacha, "Autoimagenes producidas por redes de difracción binarias de fase-amplitud", poster presentation, Reunión Nacional de Óptica, Orense (Spain) (2009).

31. F.J. Salgado-Remacha, I. Jimenez-Castillo, F.J. Torcal-Milla, T. Morlanes, L.M. Sanchez-Brea, E. Bernabeu, "Autoimágenes producidas por redes de difracción grabadas sobre fleje de acero mediante ablación láser," poster presentation, Reunión Nacional de Óptica, Orense (Spain) (2009).

32. F.J. Torcal-Milla, L.M. Sanchez-Brea, F.J. Salgado-Remacha, "Self-images of 2D pseudo-random amplitude Ronchi gratings," 3rd EOS Topical Meeting on Optical Microsystems (OμS'09), Capri, Italy (2009).

33. J.M. Rico-García, F.J. Salgado-Remacha, L.M. Sanchez-Brea, J. Alda, "Optimized square Fresnel zone plates for microoptics applications," poster presentation, Optical Metrology (SPIE) Munich (Germany) (2009).

34. J. Alda, F.J. Salgado-Remacha, L.M. Sanchez-Brea, J.M. Rico-García, F.J. González, "Optimal phase distributions for polygonal Fresnel lenses" European Conference on Antennas & Propagation (EuCAP 2010), Barcelona (2010).

35. F.J. Salgado-Remacha, F.J. Torcal-Milla, I. Jimenez-Castillo, L.M. Sanchez-Brea, E. Bernabeu, "Diffractive Optical Elements in bulk fused silica by nanosecond pulses laser ablation," Laser Precision Microfabrication (LPM 2010), Stuttgart, Germany (2010).

36. F.J. Salgado-Remacha, I. Jimenez-Castillo, L.M. Sanchez-Brea, E. Bernebeu, "Structured photodiodes by means of Laser Ablation over silica diodes," Laser Precision Microfabrication (LPM 2010), Stuttgart, Germany (2010).

Other works

Publications

37. F. J. Salgado Remacha, S. Jarabo Lallana, "Emisión multilínea en láseres de fibra óptica dopada con erbio empleando filtros sencillos," Óptica pura y aplicada 41(1) 51-57 (2008).

38. L.M. Sanchez-Brea, F.J. Salgado-Remacha, "Three dimensional diffraction of a thin metallic cylinder illuminated in conical incidence: application to diameter estimation," Appl. Opt., 47(26) 4804-4811 (2008).